Mechanisms of Membrane Fouling by Macromolecules at Multiple Scales during Ultrafiltration

Xiafu Shi

Hertford College

University of Oxford

A thesis submitted for the degree of

Doctor of Philosophy

Michaelmas 2014

Statement of Originality

The candidate confirms that the work submitted is his own and that appropriate credit has been given where reference has been made to the work of others. This copy has been supplied on the understanding that it is copyright material and that no quotation from the thesis may be published without proper acknowledgement.

Mechanisms of Membrane Fouling by Macromolecules at Multiple Scales during Ultrafiltration

Xiafu Shi
Hertford College, University of Oxford

A thesis submitted for the degree of Doctor of Philosophy in Engineering Science
Michaelmas 2014

Abstract: The thesis aims to gain a better understanding on the mechanisms of the complicated macromolecular fouling in ultrafiltration (UF). The work is divided into three main parts. Firstly, comprehensive literature reviews on both membrane fouling and cleaning were carried out for a better overview on this problem. The findings such as the identification of the main foulants and the current knowledge on fundamental fouling mechanisms, directly contributed to further parts of the thesis.

Secondly, a multiscale approach was developed to form generalised framework for modelling complex fouling scenarios. Two complex fouling models combining multiple fouling mechanisms were derived accordingly. The models were then applied to the filtration data collected from UF experiments (constant-pressure and dead-end) on three individual macromolecular solutes, i.e., dextran blue (DB), polyethylene oxide (PEO), and humic acid (HA), respectively. During the experiments, the effect of macromolecular concentration and transmembrane pressure was investigated. Using the appropriate combined model, the overall and initial fouling behaviours and the predominant fouling mechanisms at different stages of filtration were identified. The fouling parameters in the combined models were determined and found to be consistent with the existing theories. The switch points between the dominant fouling mechanisms were assessed using two methods (integral and differential), respectively. Comparing all the information together gave a comprehensive understanding of the physics involved in the macromolecular fouling.

Finally, the effect of the deformability of a macromolecule on membrane fouling was studied. The sieving results from the experiments indicated a flux-dependent permeation during UF of the DB solution, hypothetically due to the elongational deformation of the large DB molecule (a linear polymer at 2000 kDa MWCO) under high velocity gradient at the pore entrance, allowing the molecule to adapt a smaller transversal size to enter pores at nominally 100 kDa cutoff. This not only increased the chances of permeation but also the probability of severe irreversible fouling. Subsequently, a mesoscopic model using dissipative particle dynamics (DPD) was developed to investigate the blocking event at the pore entrance in the presence of a deformable linear macromolecule. The simulation results shed lights on the threshold permeating flux at which the molecular chains start to deform.

To my parents and grandparents

Contents

List of Figures

List of Tables

Chapter 1

Introduction

1.1 Motivation and Objectives

Ultrafiltration (UF) is a type of pressure-driven, membrane-based separation technology that has been widely used in many industries, spanning from water treatment, wastewater reclamation, dairy making, juice concentration, medical usage, chemical recovery, to harvesting of cells [13]. Since the 1960s when the breakthrough in manufacturing economical and strong membranes was made, modern UF techniques have continuously developed. However, there is a long-lasting and severe problem still limiting its potential in many processes. This problem is membrane fouling, which results in an increase in operational costs, increased energy demand, additional labour for maintenance, extra needs of cleaning chemicals, and a shortened membrane lifetime. It requires effective and efficient methods for its control and minimisation. Though much investigation on fouling has been carried out since the birth of membrane technology, understanding of it is far from being complete.

The foulant, i.e., the culprit causing membrane fouling, varies with different UF applications. Numerous types have been identified. They can be roughly categorised into particles, organic matters and ions. For UF, the organic matters are arguably the most detrimental foulants and extremely difficult to deal with. For example, in water industry, natural organic matters (NOMs), which are a mixture of many different macromolecules such as humic acid (HA), polysaccharides and proteins, cause the most severe and irreversible fouling. Although there is a number of literature on the topic of membrane fouling, the study of macromolecular fouling is still an ongoing

area because they often exhibit complex fouling behaviours, still puzzling researchers over the globe.

Therefore, the work presented here focuses on understanding macromolecular fouling in ultrafiltration, particularly on the points listed below:

- Which types of the macromolecules are mostly interesting in terms of UF fouling in water industry?
- What are the mechanisms involved in their fouling process?
- Is there a comprehensive theory to model the process?
- What are the overall fouling behaviours?
- What are the fouling processes at a single pore level?
- Can the understanding of pore scale mechanisms contribute to predicting the macroscopic fouling behaviour?

1.2 Thesis Layout

The structure of this thesis is as the follows:

Chapter 1 (this chapter) contains a brief introduction to the background of the subject, the research questions and an outline for the whole thesis.

Chapter 2 reviews the existing knowledge on membrane fouling related to macromolecular ultrafiltration, including the general background on filtration, different fouling mechanisms and classical fouling models.

Chapter 3 contains a critical review on the issues in membrane cleaning, particularly regarding cleaning macromolecular fouling.

Chapter 4 discusses the theoretical development of the combined models for two complex fouling scenarios.

Chapter 5 presents the results from bench-scale experiments with three types of macromolecular feeds. The appropriate fouling model is fit to the measured data and model parameters are determined in the process. Insights of membrane fouling are gained by analysing both the experimental data and model calculations. The effect of filtration parameters such as bulk concentration and transmembrane pressure is evaluated and compared between different feeds. The evolution of fouling mechanisms is evaluated using both integral and differential methods.

Chapter 6 demonstrates the solute sieving and fouling irreversibility results obtained in the UF experiments. Discussion on the links between these results and the flow-induced deformation of polymers is included.

Chapter 7 shows the development of a mesoscopic model from the method of Dissipative Particle Dynamics to simulate the macromolecular capture and flow-induced deformation at the pore entrance. The simulation results are to be compared with the sieving results obtained in Chapter 6 to elucidate the flux-dependent event of macromolecular entrance to pores via conformational change, which fundamentally affect the fouling mechanism.

Chapter 8 concludes the whole thesis and a few remarks on future work are presented.

Chapter 2

Literature Review of Membrane Fouling in Ultrafiltration

This thesis is concerned with problems during the ultrafiltration (UF) of macromolecular solutions. Therefore, the focus is constrained to the filtration of liquids. It is worth introducing the general aspects of membrane filtration and particularly of UF before any specific problem is presented. Hence, some background information on membrane filtration of liquids is introduced in the first section, followed by a discussion of membrane fouling, which is the long-lasting problem occurring in many UF processes, in the next section. Finally, theoretical work on fouling is introduced.

2.1 Overview of Membrane Filtration

UF belongs to the family of pressure-driven membrane processes, which also include microfiltration (MF), nanofiltration (NF) and reverse osmosis (RO) [14]. In these processes, a membrane is simply a physical barrier splitting the feed stream into two parts, i.e., a retentate and a permeate fraction; and a hydraulic pressure difference is created between feed and permeate side as a driving force to push (ideally) pure solvent through the membrane, leaving unwanted molecules or particles in the retentate. This pressure difference is measured as transmembrane pressure (TMP). The distinction between these processes is somewhat arbitrary, and chiefly depends on the size of the solutes retained by the membrane, which ranges from suspended particles in MF to small molecules and ions in RO, as shown in Fig. 2.1 [15].

The differences between the four membrane processes are also manifested in their membrane structures as well as the solute retention mechanisms. UF and MF are basically similar. Their membranes have distinct pores, and the separation is largely due to the physical sieving effect as a result of the relative sizes of the solute/particles and the membrane pores. MF membranes have the largest pores and deal with suspensions containing particles and colloids in the range of 0.1 μm to 10 μm, such as microbial cells, while UF membranes, having smaller pores (1 nm to 100 nm), are mostly used for concentration and purification of macromolecules, such as protein [3]. UF requires greater TMP than MF, as a result of its smaller pore sizes. The higher pressure demand also comes partly from the osmotic pressure of the solution adjacent to the membrane, which creates an osmotic 'back pressure' that opposes the applied pressure [16]. RO membranes are very dense and do not have distinctive pores. Solute retention is not a result of sieving but of charge effects [16]. Through the matrix of an RO membrane, solvent and solutes diffuse at different rates to manifest the semi-permeability. As a result, RO has a low permeability and consequently, requires high TMP. NF occupies the transition zone between UF and RO and may be porous or non-porous depending on the material [17]. NF is usually used to remove multivalent ions and small organic compounds. Its solute-retention mechanism is complex, involving both size exclusion and charge effects [18].

Different processes involve different aspects. It is out of the scope of this thesis to cover the whole range of membrane processes. Since our interest is in UF, in the remaining chapter and throughout the thesis, unless specified, the present topics are tailored for UF.

Regarding the general operation in pressure-driven membrane processes, some terminologies are worth mentioning. The feed flows can occur normal (perpendicular) or parallel (tangential) to the membrane. The former configuration is termed *dead-end* and the latter is termed *crossflow*. The dead-end configuration is simple to implement, but it is a batch process by nature. As the retained material continues to accumulate on the membrane surface, the permeate flux eventually becomes lower than the acceptable value, at which point the process needs to stop for cleaning and restoration. However, it can be incorporated into a continuous process with certain mechanisms to limit material accumulation [16]. In crossflow, the tangential flow has a sweeping effect and re-entrains the polarised and deposited particles from the surface of a membrane by wall shear stresses [19]. In principle, a crossflow process can reach a steady state.

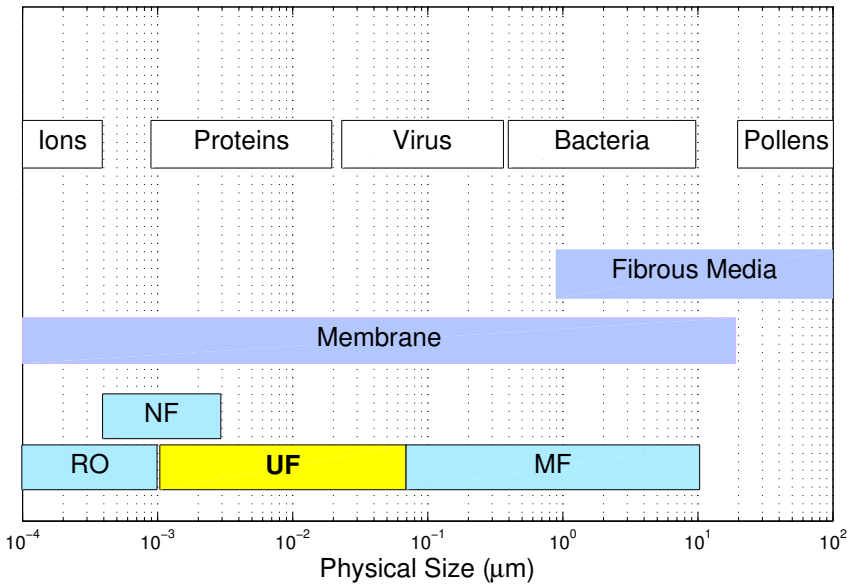

Figure 2.1: Schematic of typical pore size ranges for different types of pressure-driven membrane filtration processes compared with the relative size ranges of different solutes removed by each class of membrane (modified after [1]). Note: reverse osmosis membranes are so dense that discrete pores do not exist; instead, they can be viewed as a matrix through which molecules diffuse.

Membranes are usually installed in modules for practical use. The common designs in industries include flat sheet, spiral wound, tubular and hollow fibre [3]. In small scale operations and laboratory work, stirred cell apparatuses are frequently used [16]. A flat sheet membrane is placed in a pressurised container (the cell) and filled with feed solution. A magnetic impeller is placed just above the membrane and can be externally controlled by a magnetic stirrer to limit the concentration polarisation effect. The cell can be directly connected to the pressure source or to a fluid reservoir.

Currently, the majority of commercially available membranes are made from thermalplastic polymers, including cellulose acetate (CA), polysulfone (PS), polyethersulfone (PES), polyacrylonitrile (PAN), or polyvinyldifluoride (PVDF) [6]. During the last two decades, ceramic membranes have emerged as a major advance in UF technology [11] due to their robuster mechanical strength, higher temperature tolerance, and better chemical stability. However, they are currently more expensive, heavier, and thicker than polymeric membranes and require higher TMPs because they have greater resistance to water transport [11, 20].

Membranes have different morphologies. MF membranes are typically symmetric, with a sponge-like structure, which means that the pore size and porosity are the

same throughout the depth of the membrane. On the contrary, UF membranes are typically asymmetric, i.e., they have a thin layer of well-defined molecular weight cut-off (MWCO), supported by a thicker and highly porous layer. It is important to note that this asymmetry arises inherently from the membrane synthesis process. The permeation and sieving are mostly determined by the membrane skin layer, while the less-dense part of the membrane has little resistance to filtration flow and functions as a supporting layer to give the membrane mechanical strength [16].

2.2 Membrane Fouling in Ultrafiltration

2.2.1 Nature of Flux Decline

Under constant TMP operation, the permeate flux of a filtration process declines over time due to two important effects [9]. Firstly, concentration polarisation, which is a natural consequence of the semi-permeability and selectivity of a membrane, results in an accumulation of rejected solutes or particles in a mass transfer boundary layer (polarisation layer) adjacent to the membrane surface [9, 15, 21, 22]. In UF, this is particularly problematic during filtration of low molecular-weight solutes or macromolecules [15]. When these solutes are carried towards the membrane surface by the permeation flow, solvent molecules pass through the membrane but large solutes may be partially or even completely rejected by the membrane. For those being rejected, they are retained and concentrated over time at the upstream membrane surface, forming a concentration gradient from the membrane surface where the solute concentration is at its highest to the bulk solution where it is at its lowest [16, 23]. The concentration gradient causes back-transport (e.g. by diffusion) of solutes from the polarisation layer to the bulk. In fact, the concentration of those near the membrane surface can reach 20-50 times that in the bulk solution [3]. The accumulation of such a high amount of solute molecules at the membrane surface impedes the solvent flow through the membrane [9].

Concentration polarisation is an inevitable but reversible phenomenon that does not itself affect the intrinsic properties of a membrane [15]. The flux loss can be fully recovered by switching the feed to a pure-solvent stream. However, the resulting highly localised high concentration of the solutes may lead to macromolecular precipitation, which is relevant to the other flux-decline mechanism, i.e., the phenomenon of membrane fouling [3].

Membrane fouling, by definition, happens when the material in the feed solution leaves the liquid phase to form a deposit on either the surface (i.e., external fouling) of a membrane or inside its porous structure (i.e., internal fouling) [24]. In contrast to the reversible nature of concentration polarisation, fouling may cause irreversible loss of the permeability of a membrane. In fact, reversibility is a defining characteristic of fouling. Many studies distinguished reversible and irreversible fouling based on their relative resistance to cleaning [25, 26]. Reversible fouling can be removed easily with certain cleaning methods, while irreversible fouling still remains after the cleaning. The part of fouling that cannot be cleaned by hydraulic means is termed as *hydraulically irreversible* fouling. Similarly, the one left over after chemical cleaning is named *chemically irreversible* fouling. In general, membrane fouling is a more complicated phenomenon. It manifests in various forms during different UF processes.

2.2.2 Forms of fouling

By recognising the complex nature of fouling, the categorisation of fouling mechanisms is not universally same in literature. Following the more recent practice in Field [9], membrane fouling has generally four forms according to the nature of the solutes.

2.2.2.1 Adsorption

Adsorption occurs whenever specific interactions between solutes and the membrane surface exist. It is a consequence of surface energy, and a process of thermodynamic equilibrium. The interactions are of generally three types including weak van der Waals forces, electrostatic attraction, and chemical bonding, depending on the functional groups involved. A monolayer of solutes can adsorb on the surface of a membrane, even in the absence of a permeation flux. It occurs spontaneously and almost instantaneously. This is a common problem which occurs when separating macromolecules such as protein and humic acid (HA), and is often irreversible [15, 27]. The strong affinity of these species towards the membrane surface originates in the heterogeneity of their molecular constituents. Their molecules contain various functional groups, some of which (e.g., hydrophobic acids) make them partially lipophilic. This allows these macromolecules to participate in different surface interactions, involving electrostatic, hydrophobic, or van der Waals forces. Membranes fouled by such molecules cannot be completely restored without chemical cleaning, because desorption is thermodynamically unfavourable.

The adsorbed material on the membrane can alter its surface characteristics, such as hydrophobicity or charge [18]. For example, the adsorption of negatively charged HA was found to increase the negativity of the streaming potential of a membrane [28]. As the pore-sizes of UF membranes are comparable to that of many macromolecules, internal fouling caused by in-pore adsorption can contribute largely to the overall flux drop.

The thermodynamic nature of adsorption distinguishes it from other forms of deposition which result from body forces (e.g., hydrodynamic forces) exerted on the solutes, because the other fouling forms (discussed below) do not reach thermodynamical equilibrium [29]. Note also that a deposit of multilayers is usually not as strongly bound to the membrane as an adsorbed monolayer [24].

2.2.2.2 Pore Blocking

Pore blockage occurs when particles fully or partially seal the membrane pores [30, 31]. It usually happens rapidly in the initial stages of filtration, at which the membrane surface is free of deposits and the incoming particles can interact directly with a membrane pore.

2.2.2.3 Deposition

Particles, due to deposition, build up layer by layer on the external surface of a membrane, leading to dynamic foulant layers (secondary membrane) with an additional resistance to the permeate flow. This is often referred to as cake formation, and the extra resistance is called a cake resistance. A fouling layer or cake can consist of different types of solutes, including chemically inert colloids or active ones. The formation of an initial cake layer of inert colloids near the membrane surface prevents a direct contact between further foulants and the membrane surface, even if the later foulants can potentially bind to the membrane surface. Hence, the inert cake layer acts as a pre-filter or '*filter-aid*', which screens out those materials with a high fouling potential [32, 33]. On the other hand, active foulants may reach the membrane surface first and bridge inert deposits to it [34, 35]. This forms a more adhesive cake, and hence fouling becomes more irreversible. Sometimes, '*over-clogging*' may take place when small macromolecules enter and fill the interstices of a cake formed by large particles, leading to a greater hydraulic resistance [33, 36]. The morphology of the fouling cake dictates the flux decline, while the interaction between the cake layer and the membrane surface determines the fouling reversibility [35].

2.2.2.4 Gel Formation

For certain macromolecules, they form gel layers in the immediate vicinity of the membrane surface where the concentration of the molecules reaches its solubility limits due to concentration polarisation [3, 9, 18, 37]. The transition between concentration polarisation and gel formation occurs when the attractive forces become greater than the repulsive electrostatic forces between molecules in the layer [38]. The flux at which the gelation occurs marks the 'limiting flux' representing the maximum stationary permeation flux that the system can reach [21]. The term "gel formation" is conventionally used to describe this process of macromolecular gelation under high solute concentration.

It is necessary to clearly note the distinction between gel formation and cake formation although both form layers of foulants on the membrane surface. Cake formation is a non-specific process of particulate deposition, while gel formation specifically represents the gelation of macromolecules as a consequence of concentration polarisation. The fouling cake is bound to the membrane surface via particle-membrane interactions. The macromolecular gel layer is formed in the solution immediately above the membrane surface, which is like a blanket covering the surface. Gel layer is largely reversible due to the low interaction with the membrane surface. In some literature such as Jermann et al. [39], however, the term "gel formation" has been loosely used to describe general macromolecular deposits. In this context, gel formation strictly refers to macromolecular gelation process due to concentration polarisation. For other macromolecular depositions, they are classified as a process of general deposition (section 2.2.2.3).

In practice, typically, during filtration with complex or mixed feeds, fouling involves more than one mechanism working simultaneously. The relative importance of different fouling mechanisms will depend on the operating condition, the feed stream quality, and the membrane property [15].

2.2.3 Foulants

Foulants, the trouble-causing substances commonly found in UF, are roughly divided into four categories: particulates, macromolecules, ions, and biological substances [40]. For example, Ahn et al. [41] have analysed the composition of the fouling layers when lake water (Lake Michigan and Lake Decatur, USA) was ultrafiltered. Their

results showed that NOM, calcium and magnesium ions, and silicon of clay minerals were the main components in the fouling cake. A detailed category of common foulants is listed in Table 2.1.

2.2.3.1 Particulates

Particulates range from 1 nm to 1 μm in size and have a relatively rigid shape [19]. Depending on the ratio of the size of the particle to the size of the membrane pore, particles may completely seal, partially block or internally constrict pores [42]. Over the length of a filtration process, a particular cake layer usually dominates after pores have been blocked. Colloidal characteristics (surface charge, roughness, size, hydrophobicity, and stability) will determine the inter-particle interactions and hence the properties of the fouling cake.

2.2.3.2 Macromolecules

Macromolecular foulants range in molecular weight (MW) from around a few thousand to above one million daltons [43]. Macromolecular fouling is characterised by the functional groups in the molecules, since they contribute to the specific interactions with the membrane surface.

Protein fouling presents a major concern in the therapeutic and food industries [24, 44]. Native (non-aggregated) proteins are typically tens of nanometers in size, and have complex molecular structures with multiple charge points; the overall net charge depends on the solution pH, while the size is affected by the ionic strength and intermolecular interactions [44, 45]. Protein molecules are inherently unstable and subject to denaturation by heating, solvents or shearing. Protein rapidly and strongly adsorbs onto a clean membrane surface. The resultant fouling is largely irreversible and extremely complicated [44]; chemical cleaning is thus inevitable in most industrial applications [24].

Natural organic matter (NOM) is considered to be the major foulant type in water treatment processes. According to its origin and genesis, NOM can be categorised as: (i) allochthonous organic matter originated as flora debris from terrestrial sources; (ii) autochthonous organic matter, consisting of extracellular and intracellular macromolecules and cellular debris; and (iii) wastewater effluent organic matter (EfOM), composed of background NOM plus soluble microbial products (SMPs) derived from biological wastewater treatment units [40]. Complex chemistry is involved, as NOM consists of a heterogeneous mixture of macromolecules with a wide range in size,

Table 2.1: Examples of foulants, and their fouling modes in major membrane applications involving liquid-solid separation (modified after [9]).

Foulants	Fouling modes
Large suspended particles	Particles present in the original feed or developed due to aggregation can form a cake layer and/or block module channels.
Small colloidal particles	Colloids present in the recovery of cells from fermentation broth can form a dense cake layer. They can also block the entrance of a membrane pore or clog inside of it.
Inert macromolecules	Gel or cake formation on membrane surface.
Adsorptive macromolecules	Proteins and HAs are known for their adsorption to surfaces of membranes or in the pores.
Small molecules	Some small organic molecules tend to have strong interactions with some polymeric membranes (e.g.. antifoaming agents, such as polypropylene glycols used during fermentation, adhere strongly to certain polymeric membranes).
Biological substances	The growth of biologically active organisms such as bacteria and their excreted material (e.g. EPS) forms biofilms on membrane surfaces.
Cations	Precipitation of salts and hydroxides leads to scaling. Certain cations such as Ca_2^+ can facilitate macromolecular fouling.

functional groups and sub-structures. The majority are humic substances (HSs), representing up to 80 % of the total organic carbon in the water [46, 47]. HSs can be divided into three fractions according to their solubility in acidic solutions: humin (defined as insoluble), humic acid (HA, insoluble at pH < 2), and fulvic acid (FA, soluble at any pH, less molecular weight than HA) [48–50]. The other fractions of NOM include polysaccharides, carbohydrates, amino acids and proteins etc. [51–53]. Using robust fractionation methods and characterisation tools, Wershaw et al. [2] divided the fractions of NOM samples from a natural reservoir into nine categories, as shown in Fig. 2.2, and quantified each of them. However, the quantitative amount and the

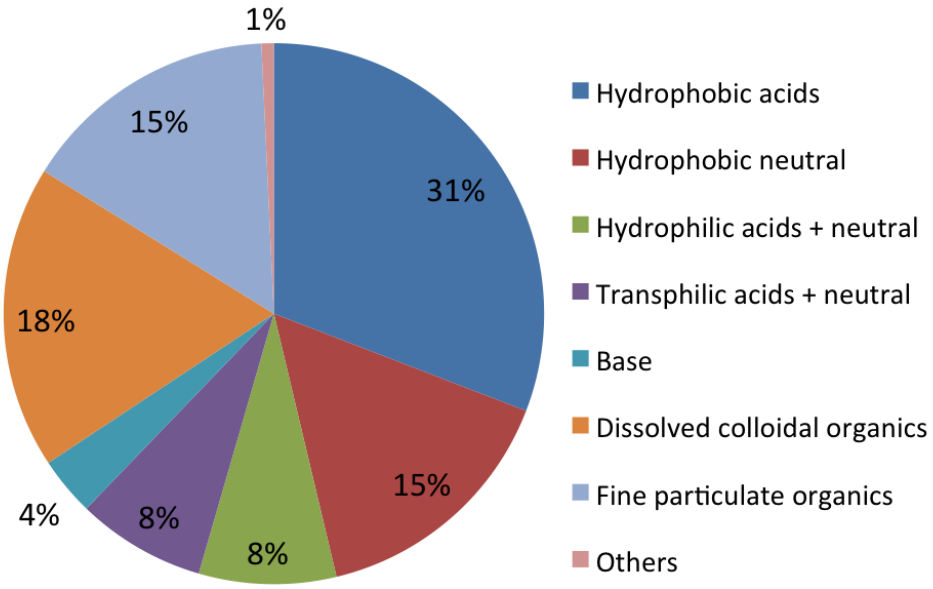

Figure 2.2: An example of the complex nature of NOM found in the Neversink Reservoir, New York, characterised by Wershaw et al. [2]. The legend "others" includes coarse particulates and solvent extractable organics.

relative percentage of each fraction is case-specific [49]. Results of experiments and studies on NOM taken from different sources showed a disagreement on the role of each NOM fraction in the rate and extent of membrane fouling. For hydrophobic membranes, some found that the hydrophilic neutral parts had a primary role in promoting fouling [54], while others found that hydrophobic portions had a higher potential to foul the membranes [27, 48, 55].

2.2.3.3 Ions

Although scaling is a more significant problem in NF and RO, metal ions may form scaling precipitates on UF membranes under certain extreme conditions. Calcium salt precipitation can appear in cheese/whey processing. Hanemaaijer et al. [56] found that the UF of pure whey salts produced considerable amounts of calcium phosphate throughout the porous structure of the membranes. This precipitation is less significant in the presence of whey proteins [29]. Coagulation agents, e.g., $Fe(OH)_3$, added from pretreament before UF, may form a slimy brown fouling layer [57]. However, cations in most UF processes are more of a concern regarding their role in fouling facilitation than foulants themselves. Divalent cations can bridge the negatively charged NOM molecules with the negatively charged membrane surface, while monovalent cations contribute to the increased ionic strength which screens out the electrostatic repulsion forces between colloids or between solutes and membrane, causing colloidal aggregation or solute adsorption [58].

2.2.3.4 Biological Substances

Biologically active organisms cause membrane biofouling, as they adhere to the membrane and grow to form biofilms. Biofouling is a major concern in membrane bioreactors (MBRs) [59]. The process starts with the formation of a conditioning film on the membrane surface by adsorption of both macromolecules originally existing in the feeds (such as proteins, HAs, and polysaccharides) and extracelluar polymeric substances (EPS) secreted from the microorganisms. The gel-like film provides an immediate additional resistance to permeate flow. After conditioning, the attachment of microorganisms onto the membrane surface occurs as patchy deposition. The convective flows and concentration gradients in the filtration system bring organics and nutrients in the feed to the membrane surface. The colonisers flourish on these and grow to form a confluent biofilm [60]. These biofilms can be heterogeneous, housing different species of microorganisms, and stratified, having different layers with aerobic populations at the top and anaerobic populations underneath [18].

2.2.3.5 Mixtures

In many situations such as NOM filtration or biofouling, it is difficult to single out an individual mechanism due to the complexity of the feeds. Sometimes, synergistic effects can occur [43]. For instance, HAs were found to bridge between alginate gel

and membrane polymers, leading to a more irreversible fouling layer [39]. HAs in the feeds may also alter the state of a colloidal particle by compressing the electrostatic double layer and facilitating colloidal aggregation [61–65].

2.2.4 Parameters Affecting Fouling

Several parameters can influence the fouling rate, including the nature and concentration of solutes and solvents, membrane materials and surface characteristics, pore size and its distribution, and hydrodynamics of the membrane modules [9, 19, 66, 67].

2.2.4.1 pH

The lower pH reduces the deprotonation of acidic functional groups in macromolecules such as protein and HAs. This will reduce electrostatic repulsion between these molecules, promoting gel formation and fouling [65, 68].

2.2.4.2 Ionic Strength

High ionic strength can compress the electrical double layer (EDL) of counter-ions, according to the Derjaguin-Landau-Verwey-Overbeek (DLVO) theory. This nullifies the repulsive energy barrier between molecules, which allows the van der Waals attraction forces to dominate [63]. This in turn causes colloidal instability and hence intensified aggregation and greater fouling cakes. High ionic strength can also compress the hydrodynamic radius of a molecule such as HA, which promotes significant diffusion of it into the pores, and this in turn results in higher pore adsorption [50].

2.2.4.3 Divalent Cations

Exacerbated membrane fouling in the presence of divalent cations (e.g., Ca^{2+} which is abundant in surface water) has been frequently reported in the literature [39, 46, 51, 68]. The negative effect of Ca^{2+} on permeate flux may be attributed to its ability to react with foulant molecules (e.g., NOM), as well as with membrane surfaces, leading to the alteration of surface chemistry for either case [69]. Ca^{2+} can form complexes with the deprotonated carboxylic groups in macromolecules and partially shield their charges, particularly at a neural pH level [70]. As Ca^{2+} has a valence of two, it can link two negatively charged functional groups together. If these two groups are in the same molecule, the complexation happens intramolecularly, rendering the molecule of

a HA into a small and coiled conformation. Otherwise, this linkage happens between two molecules, which leads to intermolecular bridging [41, 71]. Therefore, the gel layer of macromolecules becomes more compact and cohesive by the cross-linking effect of Ca^{2+} [39, 72].

2.2.4.4 Membrane Materials

Membranes are made from different materials and have different properties with respect to surface charge, degree of hydrophobicity, chemical and thermal tolerance, mechanical strength and flexibility etc. [1, 73]. These properties may affect fouling and cleaning to some extent, while, at the same time, membrane properties are influenced by fouling and cleaning procedures.

2.3 The 'Blocking' Theory of Fouling

For porous membranes, i.e. MF and UF, the pores are usually considered to be the active part of a membrane. Hence, most theories about fouling are subject to the processes involved in the reduction of the number of active pores. In this respect, 'blocking' is arguably the most frequently-appearing term used in studies about fouling mechanisms in MF and UF.

2.3.1 Classical Blocking Filtration Laws

In the 'blocking' theory of fouling, foulant and foulant aggregates are treated as particulates. When these particles contact the surface of the membrane, they cause closure of the effective pore areas in certain ways. Based on empirical observations, a series of time and filtrate volume correlations for various filtration situations were first developed by Hermans and Bredée [74], and subsequently systemised by Grace [75]. These laws include four general fouling modes: **complete blocking**, **intermediate blocking**, **standard blocking** and **cake formation** (see Fig. 2.3), with the switching between the modes depending on the ratio of the particle size to the pore opening size. After Hermia [30] derived the theoretical model for intermediate blocking, which had originally been considered as purely empirical, constitutive models for each of the four modes can now be derived from their own physics, respectively,

based on some common assumptions such as a homogeneous bulk solution and a porous filter medium to which Darcy's law;

$$Q = \frac{\Delta P A}{\mu R} \tag{2.1}$$

is applicable [30], where Q is the permeation flow rate, ΔP is the pressure difference across the porous medium, A is the surface area of the medium, μ is the solution viscosity and R is the resistance of the porous medium.

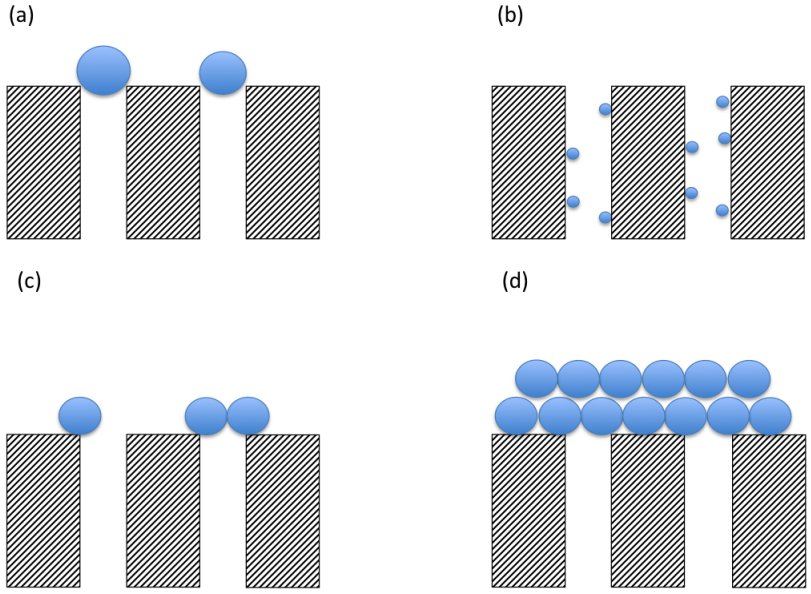

Figure 2.3: Fouling mechanisms of porous membranes: (a) complete blocking; (b) standard blocking; (c) intermediate blocking; and (d) cake formation.

2.3.1.1 Constant Pressure Blocking

In the derivation of the blocking models for constant pressure filtration, Hermia [30] showed that the respective models for the four fouling modes can all be conveniently unified into a single differential equation with only two coefficients to determine,

$$\frac{d^2t}{dV^2} = k(n)\left(\frac{dt}{dV}\right)^n \tag{2.2}$$

where t is the filtration time, V is the total filtered volume, $k(n)$ is a constant determined by fitting the equation to the experimental flux decline data, and the exponent n (called the filtration constant) characterises the filtration model, with $n = 0$ for cake filtration, $n = 1$ for intermediate blocking, $n = 3/2$ for standard blocking (also called pore constriction or filling, or internal pore blocking), and $n = 2$ for complete pore blocking [31]. In eqn 2.2, $\mathrm{d}t/\mathrm{d}V$ is the differential time needed to collect a unit differential volume of filtrate.

Given that the observed (superficial) permeate flux $J = \frac{1}{A^*}\frac{dV}{dt}$, eqn 2.2 can be conveniently converted to a form in terms of filtration fluxes [76]:

$$-\frac{dJ}{dt} = k(n)J(JA^*)^{2-n}\,, \tag{2.3}$$

where A^* is usually taken as the total membrane area for convenience. This depicts explicitly the time-dependent flux profile.

Table 2.2 lists the details of the four models. The analysis and assumptions from the derivation of Hermia [30] are described below. The complete blocking law implies the scenario that particles have a size larger than that of the membrane pores. When they arrive at the surface, they completely seal the entrances of the pores. It assumes that particles settle evenly onto the pores open at that time, without superimposition of further particles upon those already deposited. Therefore, the instant permeate flow is proportional to the number of pores still open at the time.

The assumptions for intermediate blocking are akin to those in the complete blocking case, but the restriction of 'perfect' sealing has been loosened. Instead, particles are allowed to superimpose on the deposits, which means that only a partial fraction of the particles arriving at an instant will block the pores. Hence, this scenario is also named as partial blockage.

Standard blocking, also known as pore constriction or internal fouling, happens when particle sizes are smaller than pore sizes. Particles deposit on the pore walls and are captured inside the filter medium. The governing equation in Table 2.2 is derived from the equation of Hagen-Poiseuille flow, with the assumption of straight pores that have uniform radius and constant length. Hence, the permeate flow rate decreases at a rate proportionate to the pore volume.

Cake filtration is to model the cake formation phenomenon. This law accounts for the increase of the resistance as the fouling cakes increases. The filter resistance consists of membrane intrinsic resistance R_m and a time-dependent cake resistance

R_c. The rate of the permeate flow is proportional to the change of the filter resistance.

Table 2.2: Blocking models for constant pressure filtration

Blocking modes	n	Governing equations	k	Flow rate equations
Complete	2	$\frac{\mathrm{d}A}{\mathrm{d}t} = -k_b A$	$k_b = J_0 C_b \sigma$, $[s^{-1}]$	$Q = Q_0 exp(-k_b t)$
Standard	3/2	$\frac{\mathrm{d}r_p^2}{\mathrm{d}t} = -k_s r_0^2 Q$	$k_s = \frac{\phi C_b}{N_p \pi r_{p0}^2 \delta_m}$, $[m^{-3}]$	$Q = \frac{Q_0}{(1+k_s Q_0 t)^2}$
Intermediate	1	$\frac{\mathrm{d}A}{\mathrm{d}t} = -k_i A^2$	$k_i = \frac{J_0 C_b \sigma}{A_0}$, $[m^{-2}\, s^{-1}]$	$Q = \frac{Q_0}{1+k_i A_0 t}$
Cake filtration	0	$\frac{\mathrm{d}R_t}{\mathrm{d}t} = \alpha C_b \frac{\Delta P}{\mu R_t}$	$k_c = \frac{\alpha C_b \mu}{\Delta P A_0^2}$, $[s\, m^{-6}]$	$Q = \frac{Q_0}{\sqrt{1+2k_c Q_0^2 t}}$

1. Relationship with $k(n)$ in eqn 2.2: $k(2) = k_b$, $k(3/2) = k_s Q_0^{1/2}$, $k(1) = k_i/J_0$, and $k(0) = k_c$
2. Physical meaning: σ is the blocked area per unit mass of particles being filtered, $[m^2\, kg^{-1}]$; ϕ is the volume of particles, deposited onto the pore wall, per unit weight of solutes being filtered, $[m^3\, kg^{-1}]$; and, α is the specific cake resistance, $[m\, kg^{-1}]$
3. The subscript 0 means the physical quantity at its original state, e.g. Q_0 is the flow rate through a fresh membrane.

As we can see from the assumed mechanisms related to each law, they are purely physical and mostly extreme situations. The filter medium has been treated as ideal with a perfect geometry, where pores have uniform size and distribute evenly over the whole membrane area. The size distribution of the solutes is also assumed to be ideally narrow. Nevertheless, due to their simplicity, these laws have been extensively used in the analysis of the clogging behaviours of pore-flow membranes during liquid filtration [77].

2.3.1.2 Blocking Laws for Other Operational Conditions

When the flux is kept constant, TMP increases as fouling grows. Based on a similar analysis to the above, one can readily derive blocking equations for the constant flux filtration. For the four blocking modes mentioned previously, there is a common characteristic form analogous to eqn 2.2 for the time dependence of the pressure

necessary to maintain constant flux during operation [78];

$$\frac{\mathrm{d}^2 t}{\mathrm{d}(\Delta P)^2} = k' \left(\frac{\mathrm{d}t}{\mathrm{d}\Delta P} \right)^{m'} \tag{2.4}$$

Alternatively, the characteristic form can be written as a function of the pressure and the permeate volume [79]

$$\frac{\mathrm{d}^2 \Delta P}{\mathrm{d}V^2} = k'' \left(\frac{\mathrm{d}\Delta P}{\mathrm{d}V} \right)^{m''} \quad . \tag{2.5}$$

The original blocking laws (eqn 2.2) are limited to dead-end operation, because they do not include the mechanism of particle removal induced by the cross-flow. Field et al. [76] first incorporated removal terms into the classical blocking laws by assuming that the permeation flux tends to have a value of J^* in the long term. Equation 2.3 will then have the form:

$$\frac{dJ}{dt} = -K(n) J^{2-n} (J - J^*) \tag{2.6}$$

The coefficient $K(n)$ equals $(A^*)^{2-n} k(n)$, where $k(n)$ is the coefficient used in eqn 2.2. The value of J^* can be considered as the 'steady-state' flux, since crossflow filtration tends to a pseudo-steady state in the long run. The new equation is valid for all n values except for $n = 3/2$, i.e. the pore constriction, because this form of fouling is not affected by the back-diffusion induced by the crossflow shear forces [76]. The standard blocking law will be the same in both dead-end and crossflow operations.

Blocking laws can also be extended to non-newtonian fluids, for example, in the case of a power-law model where the viscosity is proportional to some power of the shear rate $\dot{\gamma}$;

$$\eta = M \dot{\gamma}^{N-1} \quad , \tag{2.7}$$

with the two correlational parameters, M and N, depending on a particular power-law fluid. Thus, the flow velocity through a cylindrical pore is obtained as [30]:

$$v = \frac{N}{3N+1} \left(\frac{\Delta P}{2LM} \right)^{1/N} r^{(N+1)/N} \quad . \tag{2.8}$$

where L and r are the length and radius of the pore, respectively. Hermia [30] showed

that the two parameters, k and n in eqn 2.2 could accommodate power-law rheological model in an elaborate way according to each fouling mode, except in the intermediate blocking case.

2.3.2 Combined Blocking Models

The four classical blocking models are extreme cases of fouling, and are overly idealistic as judged by today's knowledge [80]. In practice, membrane fouling is far more complicated, especially with complex feeds. The underlying physics are difficult to identify. It is usually too ambiguous to determine a classic blocking mode for many real cases by simply plotting a $t - V$ graph and fitting any classic mode of blocking to it.

Many studies have shown that the flux decline in membrane filtration consists of multiple steps: for example, pore blockage and/or pore constriction at the initial stage, followed by cake filtration in the long term [77]. In fact, complete and intermediate blocking laws are both frequently present during the initial stages of cake filtration [77]. Bowen et al. [81] showed that the value of the filtration constant n in eqn 2.2 varied with the progress of filtration during MF of BSA solution. Similar trend in particulate microfiltration was observed in a study by Hwang et al. [82].

In spite of the complex nature of most fouling, the concept in the derivation of the classic blocking laws is still useful in formulating more advanced fouling models. Recently, there has been a trend towards combining various fouling laws to construct more comprehensive models, to account for the complex nature of fouling with which multiple processes may develop either simultaneously or sequentially during filtration. The first such example is the work conducted by Ho and Zydney [83]. They assumed that during MF of protein solution, the filter got blocked by protein aggregates first, and until a certain time when sufficient pore areas were blocked, further deposits built on the blocked pores to form cakes gradually. Hence, based on classical blocking analysis, they combined complete blocking and cake filtration models consecutively to describe the two-step fouling processes . Their results, by comparing with the experimental data, confirmed a nice transition from one mechanism to the other on a double logarithmic plot of $\mathrm{d}^2t/\mathrm{d}V^2$ versus $\mathrm{d}t/\mathrm{d}V$ [83]. Thereafter, Taniguchi et al. [84] successfully applied this model to NOM fouling in UF.

Different fouling modes may also occur simultaneously. For example, fouling may develop inside pore structures and on the surface of membranes at the same time. This increases the complexity of the system to an even greater extent. However,

classical blocking laws come in handy in this case as well. Bolton et al. [85] derived several formulas resulting from two concurrent mechanisms of classical laws. Their scheme originated from Darcy's law (eqn 2.1), in which different variables may vary according to respective mechanisms. Under constant pressure filtration, complete or intermediate blocking contribute to the reduction of the effective area, A, by sealing the open pores, while pore constriction and cake filtration have an effect on the increase of the filter resistance R. By comparing the time-dependent flow rate $Q(t)$ with the initial flow rate through the clean membrane Q_0;

$$\frac{Q(t)}{Q_0} = \left(\frac{A(t)}{A_0}\right)\left(\frac{R_0}{R(t)}\right) , \tag{2.9}$$

from which it is possible to combine, for example, complete and standard blocking since they contribute to the variation of the different items in the equation. Similarly, if the filter can be idealised as a bundle of N capillaries with uniform diameter D and length L, the normalised flow rate in eqn 2.9 can be expressed using the Hagen-Poiseuille equation [86]:

$$\frac{Q}{Q_0} = \left(\frac{N}{N_0}\right)\left(\frac{D}{D_0}\right)^4\left(\frac{L_{eff0}}{L_{eff}}\right) \tag{2.10}$$

where L_{eff} accounts for the tortuous paths through which the flow passes, and the subscript t for time dependence is omitted for clearance. This equation separates the contributions of different fouling mechanisms into three variables. For example, the effect of pore constriction can be explicitly represented in the second term on the right, since the pore diameter reduces while materials deposit onto the pore walls; cake filtration increases the L_{eff}; and both complete and intermediate blocking reduces the N. Equation 2.10 works with consecutive combined fouling as well, by simply assuming the contributions of fouling mechanisms are additive when they happen sequentially. Using this, Cheng et al. [86] demonstrated that the same form as the approximate solution in the work by Ho and Zydney [83] can be derived for the consecutive model of pore blocking and cake filtration. Similarly, assuming that the contributions of different fouling mechanisms are additive, de Bruijn et al. [87] used a weight coefficient W_n to explicitly account for the different degrees of participation of the four classical blocking laws. The accumulated permeate volume could then be

expressed as:

$$V = \sum_{n=1}^{4} W_n V_n \tag{2.11}$$

where V_n accounts for the permeate volume obtained under the nth blocking laws, and the sum of all weight coefficients is unity.

An important assumption in the analysis of both Bolton et al. [85] and Cheng et al. [86] is that the fouling phenomena happen homogeneously over the membrane surface. However, the surface heterogeneity may significantly affect the interaction between particles and membrane locally [80]. In fact, Ho and Zydney [83] have taken into account the heterogeneity of the occurrence of protein deposit over the whole membrane surface in their 'absolute' solution. They assigned a critical time for the transition of mechanisms occurring in the local region so that this characteristic time varied over the whole surface area. This means fouling modes occur consecutively at local areas but overall blocking and cake filtration can occur simultaneously at different regions. Based on Bolton and Ho's derivation, Duclos-Orsello et al. [88] derived a three mechanism model combing pore constriction, blocking, and cake filtration for MF cases. Their results were compatible with experimental data for both protein and colloidal particles.

2.4 Conclusions

The relevant literature on the fouling of UF membranes has been reviewed. This area is important for many industries and has been extensively studied. Macromolecules have been identified as the major foulants in many UF applications and its fouling is recognised as a highly complicated process. The underlying mechanisms are not completely understood currently and remain exceptionally challenging to study. Theoretically, the macromolecular fouling (mostly during the filtration of protein solutions) has been approached by the classical blocking laws. Different fouling models were combined in either series or parallel to form complex models in order to address the dynamics of the fouling curves. From the review, the development of comprehensive models to simulate the complex behaviours in macromolecular fouling is still in a rudimentary stage and there exists the need for theoretical techniques to address the finer details of a particular fouling problem.

Chapter 3

Literature Review: Cleaning of Membrane

3.1 Introduction

It may be possible to prevent severe fouling before its occurrence by methods such as pre-treatment of the feed streams, chemical modification to improve the anti-fouling properties of a membrane, and optimisation of the operational conditions. However, periodic membrane cleaning is still inevitable currently. As an integral part of the modern membrane processes in most industries, cleaning must be regularly carried out to remove the fouled materials and restore the productivity of the operation [24].

Study of membrane cleaning has often been a complement to developing deeper knowledge of fouling. The dedicated literature on membrane cleaning is notably less than that on fouling studies [89]. Many previous cleaning studies were actually subsidiary to that of relative fouling, and for which the study was far from comprehensive. However, owing to the greatly improved understanding of fouling in the last two decades, there have been an increasing number of dedicated studies on membrane cleaning. In particular, systematic studies have been made in many respects in recent years.

A quick scan in bibliographic databases (Scopus and Web of Science) showed that the number of research papers with respect to membrane cleaning has boomed in the last decade. This corresponds to the large expansion of UF processes in industries such as water, wastewater, food and biotechnology at the same time. The up-to-date

information of membrane cleaning is constantly in demand because it is a vital part for any operation of most membrane systems. An updated review is therefore timely and useful.

The comprehension of membrane cleaning involves gaining the knowledge in many patches and of the linkages between them. It should include the target (common fouling problems in these industries), removal (various cleaning methods), results (cleaning effectiveness and any side effects such as membrane damage) and optimisation (effect of operational parameters). Since UF fouling is introduced in the previous chapter, we will start to discuss the general concepts about membrane cleaning below, followed by cleaning methods including both conventional and non-conventional means. A discussion of the cleaning processes, important operational variables and general considerations for optimisation is presented afterwards. Finally, the side effects of cleaning are discussed.

The material of this chapter has been published in the journal paper: [90] X. Shi, G. Tal, N. P. Hankins, V. Gitis, *Fouling and cleaning of ultrafiltration membranes: A review.*

3.2 Principal of Membrane Cleaning

Cleaning can be defined as "a process whereby material is relieved of a substance that is not an integral part of the material [91]". Membrane cleaning should result in a membrane that is physically, chemically and biologically clean, and thus can provide adequate flux and separation [92]. It should do so, while also meeting following criteria: (1) restoring of the initial flow through a pristine membrane without adversely changing its surface; (2) keeping dislodged foulants in dispersion or solution, to prevent re-fouling of already cleaned surfaces; (3) being compatible with both the membrane and other system components, such as joints and spacers; (4) being compatible with water; (5) possessing good buffering capacity and stability with time; (6) promoting disinfection of the wet surfaces; and (7) being available and cost effective.

There are many ways to clean a fouled membrane. Generally, they can be divided into two categories: physical and chemical methods, based on whether any chemical agent is applied in the procedure. Physical cleaning changes hydrodynamics, applies turbulence or varies temperature to the system in order to kinetically force foulants to leave the membrane material. Chemical cleaning applies chemical agents to modify the solution chemistry and change the EDL in favour of electrostatic repulsion between

foulants and membrane material, or rapidly react with the foulants to decompose them into the liquid stream. In practice, physical and chemical methods are often applied together to enhance the cleaning effectiveness. However, there are always limitations of conventional methods preventing them from achieving good results in some difficult cases. Therefore, innovative ways to do the job more effectively or economically are in demand. Some emerging techniques studied and developed in recent years, such as applications of ultrasonic and electrical fields, have shown the potential.

3.3 Physical Cleaning

Physical cleaning generally involves applying physical forces such as hydraulic, mechanical and electrical forces to remove foulants. Both hydraulic and mechanical cleaning alternate the shear forces on the membrane surface, in order to loosen and dislodge the deposits. The way to achieve this includes reversing TMP (e.g. backwashing), increasing turbulence (e.g. rotating disks), or applying mechanical scouring (e.g. air, sponge balls). Electrical cleaning is achieved by applying a voltage across the membrane, thus pushing charged deposits away [93]. In current industry, hydraulic and mechanical methods are more widely used, while electrical cleaning, as a non-conventional method, is not commonly applied at large scale. Another innovative method, ultrasonic cleaning, is discussed under the category of mechanical cleaning.

3.3.1 Hydraulic cleaning methods

3.3.1.1 Relaxation

Relaxation is basically a non-continuous operation of the membrane, giving break for concentrated foulants at the membrane surface to diffuse away via the concentration gradient [59, 94]. This is a simple yet effective method for removing reversible fouling [95], allowing filtration to be maintained for longer periods before the need for further cleaning [59]. The removal efficiency of this method can be further increased when air scouring is applied during relaxation [94]. However, relaxation is only suitable for higher membrane surface. It also requires sufficient relaxation time and hence lowers the overall production. If the relaxation time is too short, increased membrane fouling may occur [96].

3.3.1.2 Surface flushing

Surface flushing/rinsing, in principle, removes surface deposits with a turbulent cross-flow through the membrane surface facing the retentate side [97]. The rinsing flow can be pumped in the forward direction as that of a feed stream in filtration or in its reverse direction. Rinsing is, in practice, often employed to rinse off the debris loosened by other cleaning methods, e.g., backwash and chemical cleaning. Feed water may be used as the rinsing solution to save the usage of clean water [98].

3.3.1.3 Backwashing

Backwashing is performed with a reversed flow pushed from permeate side to the feed side of a membrane. The reversed flow dislodges the deposits in the membrane pores and loosens fouling cakes on the external side [99]. Backwashing typically requires a working flux at least two times higher than the typical filtration flux. It should be executed carefully to avoid membrane damage, and therefore, it is usually used for capillary and ceramic membranes which can withstand a reversed permeate flow [3].

Backwashing employed for submerged membrane systems such as MBRs is able to remove most of the debris blocking the pores as well as loosely attached sludge cakes [59]. Backwashing has been found to be more effective than forward flushing in many cases but it requires more energy [98, 100].

A typical regime for backwashing capillary fibre modules is to close the permeate port and apply crossflow as shown in Figure 3.1, such that a differential pressure is established across the length of the membrane. At the higher pressure end of the module, the feed water flows through the membrane and permeate is produced; at the lower pressure end, the permeate produced earlier becomes a backflushing solution and flows through the membrane to the feed side. If the direction of the feed flow is reversed, the other half of the module will undergo backwashing, and hence the whole membrane is cleaned [3]. This regime has a minimal interference to the normal operation but is limited by the maximum flow rate and backwash pressure achievable [101].

The compositions of backwash solution affect the cleaning efficacy. UF permeate is commonly used as backwash media. However, studies have indicated ions in the permeate reduces the removal efficiency of NOM fouling [102]. It is hence better to use demineralised water to do the cleaning [102, 103], because the reduced ionic strength in demineralised water helps restore the electrical double layer on the surfaces of the

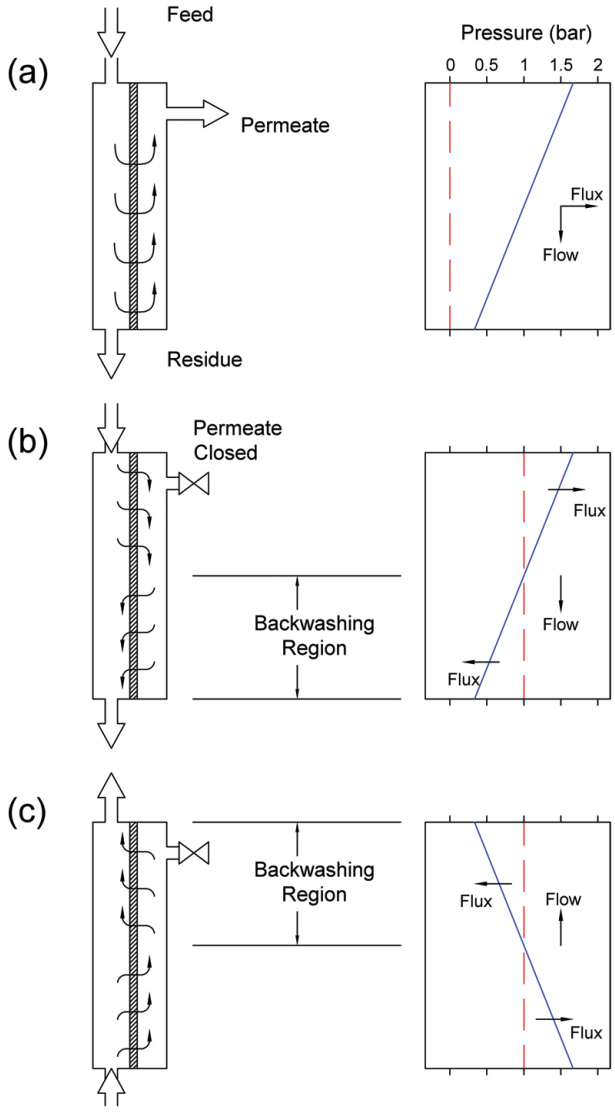

Figure 3.1: Example of a backwashing regime for the crossflow module: (a) Normal filtration; (b) Forward flow backwashing; and (c) Reverse flow backwashing. During backwashing, the permeate port is closed. The blue solid line stands for the feed pressure across the membrane module and the red dashed line for the permeate pressure. Modified after [3].

membrane and the foulants (both are negatively charged at the common pH range occurring in UF) and hence enhance electrostatic repulsion between them [58, 104].

Backwash effectiveness also depends on the fouling it deals with. The more adherent foulants require higher forces to remove. In the study conducted by Katsoufidou et al. [72], backwashing was found to be more effective in reviving the membrane fouled by sodium alginate than that by HA. Therefore, for more robust cleaning, chemicals need to be dosed into backwash solution. This is discussed in Section 3.4.2.

Backwashing, in industry, has now been made fully automatic, initiated either when TMP increases to a set point or at a fixed interval of operation [105]. For example, backwashing with the permeate only has been set at regular intervals (10 - 120 min) for UF processes in German water companies [106]. Generally, UF backwashing needs to be performed every 15 min to several hours of normal operation for a duration of 30 s to 5 min [101].

3.3.2 Mechanical cleaning methods

3.3.2.1 Sponge ball scouring

Sponge balls are only applicable to big tubular membranes due to their size limitation. They can effectively scrape deposits off the membrane modules, but the method is time-consuming and may cause scratches on the membrane surface [3]. Therefore, their usage has been limited in practice and can only be found in the early electrocoat paint recovery and some small-scale studies in conjunction with other cleaning methods [3, 107, 108].

3.3.2.2 Pneumatic cleaning

The application of compressed air to a filtration system (e.g. air sparging [97], air scrabbling [109], etc.) varies with the way of injecting or incorporating air into a membrane module, either intermittently or continuously, through retentate side or permeate side, for capillary or flat-sheet membranes, etc.

As a cleaning method, air can be used in a surface flushing and backwashing medium. However, air backwashing is not usually applicable in UF because the typical size ranges of air bubbles (from hundred nm to μm) are about two orders of magnitude higher than the average pore sizes in UF membranes. Therefore, in UF, air is usually periodically introduced into flushing stream for removal of particulates on the surface, before backwash takes place. Compared to hydraulic surface flushing, the injected air

bubbles promote higher turbulence at the membrane surface and hence can improve the removal effectiveness under the same conditions [97]. Pneumatic cleaning has been proved effective to clean fouling during UF of natural and simulated surface water [108]. In a pilot-scale experiment where an inside-out hollow-fibre UF module had been filtering water spiked with synthetic colloids, the rate of colloidal removal during cleaning was improved by 30% to 130% (the variation was due to the difference in the hydrodynamic operating conditions) with air enhanced flushing compared to pure hydraulic cleaning, while its energy consumption was kept at almost the same level as that using only regular backwashing [110]. Air sparging has also been used in biological processes. In experiments with an MBR operated in an outside-in mode [111], cleaning with air sparging alone maintained the membrane permeability at approximately 50% of the initial value after 5-days operation, which was almost 30% more than that achieved by conventional backwash. Moreover, the best results of no flux decline for one week were obtained by sequentially using air sparging and backwashing together under a low TMP [111].

Air sparging can be used as a continuous fouling control or flux enhancement method to maintain the filtration process with good productivity. For this, air is continuously pumped into the feed stream to form a gas/liquid two-phase flow parallel to the membrane surface [112], reducing concentration polarisation and colloidal settlements under a certain degree [113, 114]. Technically, this method can be applied to crossflow but not to dead-end configuration in UF [110].

Currently, there are challenges and drawbacks in applying pneumatic cleaning in practice. Firstly, it is difficult to achieve an equal distribution of air flow over/through the whole membrane module [97]. Secondly, compressed air has the potential to cause membrane damage and rewetting [59]. Thirdly, its mechanism of particle removal is not yet wholly clear. Parameters such as the membrane module, the duration to inject air, the velocity of air passing over/through the membrane and the size and direction of the air bubbles have effects on the removal efficiency [99, 109, 110, 112]. More fundamentally, studies are required to understand the cleaning mechanisms in the solid-liquid-gas interfaces in order to more efficiently utilise the air bubbles.

3.3.2.3 Ultrasonic cleaning

Ultrasonic membrane cleaning uses high frequency sound waves to agitate the aqueous medium that in turn acts on the foulants adhering to the membrane surface. This offers several advantages compared to conventional methods. For example, it can be

incorporated in the filtration process without interrupting the production flow, while backwashing or chemical cleaning requires a stop to the normal operation; since it does not use chemicals and backwashing water, it avoids the difficulties of chemical costs, waste disposal and environmental concerns.

An ultrasonic cleaner consists of an ultrasound generator and special transducers. The produced ultrasonic pressure waves propagate through the liquid medium, resulting in a cyclic succession of compression and rarefaction (expansion) phases. Compression exerts a positive pressure and pushes the liquid molecules together, while rarefaction cycles exert a negative pressure and pull the molecules apart. When the negative pressure amplitude exceeds the tensile strength of the liquid in the rarefaction phase, small vapour-filled cavities known as cavitation bubbles are formed [115]. The cavitation bubble pulsates with its size under the propagation of ultrasound. This sets the surrounding fluid into small amplitude oscillatory motion, known as *micro-streaming*. Otherwise, the cavity can grow to a size at which the surface tension of the liquid cause it collapse on itself [116]. Consequently, this asymmetric collapse results in an inrush of liquid to fill the void, forming a high-speed liquid jet, referred to as *micro-jets* [117]. These two phenomena both apply to a short distance on the order of microns. In favour of the occurrence of cavitational collapses, the frequencies between 21 and 620 kHz are used in membrane cleaning [116]. On the membrane surface, cavitation bubbles that form at nucleation sites may travel along ribbon-like tortuous pathways to a mutual location (e.g., antinodes) [115]. Their motion can be much faster than that of the surrounding fluids. This phenomenon is called *micro-streamers* [118]. At a macroscopic scale, strong convective currents, known as *acoustic streams*, resulting from the absorption of acoustic energy, circulate from the transducer to membrane surface [119]. These four effects mentioned above lead to mechanical scouring over the fouling layers and breaking down of particles and macromolecules, and are recognised as the main cleaning mechanisms.

There are also chemical effects when an ultrasonic field applies. Radical species may be formed from, for example, the sonolysis of water molecules during cavitation [115]. Their effects on membrane cleaning are not yet clear.

Owing to the recent improvement in the transducer technology, application of ultrasonic field in membrane modules is now more feasible and plausible. Within the last fifteen years, membrane systems coupled with ultrasonic devices have been extensively studied in the lab to simulate UF and MF in dairy industry [120, 121], water [122–124] and wastewater [125] treatment. Most studies were tested in flat sheet

systems [119, 120, 126] due to easy placement of the transducers. Lately, ultrasonic field has also been applied to hollow-fiber UF membranes [127].

In recent studies, the use of ultrasound has been found to improve the cleaning efficiency by $5 - 10$ % in treating PS membranes fouled by dairy whey solutions [126]. A sonication period of approximately 10 min achieved the optimum cleaning results. Further exposure did not improve cleaning [120]. Experiments also demonstrated that the ultrasonic effect is only remotely influenced by temperature and TMP, and increases linearly with ultrasonic power [126]. Increasing the power level which reaches the membrane can improve the cleaning efficiency.

Although studies have shown great potential for ultrasonic membrane cleaning, it must prove to be cost effective to be a viable option, regarding both the capital cost (e.g., instalment of transducers) , and the operating cost (e.g., energy consumption). In order to overcome the potentially high costs throughout longer production periods, Muthukumaran et al. [120] advised the use of an intermittent series of short pulses instead of continuous operation. It was also observed that adding surfactants to the system during sonication could substantially improve the flux recovery [120].

Technically, membrane disintegration is a major concern for ultrasonic cleaning. Firstly, ultrasound can only be applied to membranes synthesised from one type of polymer, because it can disintegrate composite membranes. Secondly, the mechanical forces created from the collapses of cavities and the radicals formed from sonolysis can erode the membrane surfaces. Masselin et al. [128] found that PES flat-sheet membranes were damaged after 5 min of exposure to a 47 kHz stream of ultrasound. Li et al. [127] observed similar damage in a PS hollow-fibre membrane after exposure to ultrasonic irradiation with low frequency and high intensity. Even for ceramic membranes (most reported are MF), changes in membrane structure were found under different power and frequency of ultrasound irradiation [129]. However, other studies [120, 121, 130] showed it was safe to apply ultrasound on flat-sheet membranes such as PS [120, 131], PAN [130]. No damage and change in intrinsic permeability of the membranes were observed. The significance of the tolerance of a membrane to ultrasonic irradiation is listed in Table 3.3 for different materials. However, this information is limited in literature and difficult to compare in parallel, due to lack of a standardised testing protocol [116].

3.3.3 Electrical cleaning methods

Electrical cleaning utilises an electric field generated across a membrane by placing two electrodes on either side of a membrane to enhance the permeation flux and prevent fouling in UF. The process is sometimes known as electrofiltration [132]. Sometimes only one electrode is used when a membrane itself can act as an electrode if it is made of conductive materials [133]. The applied electric field can induce charged molecules or particles to move towards the electrode with the opposite sign. This effect is referred to as *electrophoresis*. By this, an electrostatic force lifts the deposits from the membrane surface and carries them away [134]. This is the main mechanism on which the electrical membrane cleaning is based. The other electrokinetic effect, *electro-osmosis*, where a liquid is caused to move relative to a charged surface (e.g. of a membrane pore), may also contribute to an increase in the flux, although with minor importance in the case of membrane cleaning.

The limitation in conventional electrofiltration is the high energy demand for continuous application of an electric field, which could be up to 10 kWh/m^3 of permeate [135]. In order to save energy, modern electric membrane cleaning often utilises the intermittent (pulsed) operation of an electric field and the advance in electrodes and modular design in recent years makes the process more efficient. Therefore, the energy consumption can be lower than 1 kWh/m^3 [136].

It is usual to apply the electric fields with direct current (DC) in UF because it is of a great effect for the foulants with a uniform charge. Otherwise, an alternating (AC) field can be used, which can cause the vibration of charged particles in the fouling layer or membrane pores , enhancing fouling removal [137]. Electrodes can be installed for flat-sheet and tubular membranes. Operation usually takes place in crossflow configurations, but can apply to the dead-end as well [138].

An important parameter in the operation of electric fields is the electric field strength (E). An effective cleaning requires E is high enough to achieve a negative net migration of particles towards the membrane [133]. The electrophoretic forces on particles increase when E increases. There exists a critical E value above which the electrophoretic forces become greater than the convective forces, as the increase of electrophoretic forces corresponds to the rise in E. Below the critical value, the membrane permeate flux depends on the strength level. However, once above it, the permeate flux will not change much with further increasing E level [133, 138, 139]. This means that, by reaching the critical E, the resistance due to fouling or concentration polarisation has been reduced to its minimum. After that, a further increase in E has minor effect on increasing the flux.

Other parameters such as frequency, feed conductivity, properties of the solutes (concentration, zeta potential and charge), and membrane materials also have effects on electric cleaning.

Protein is the common target to test the effect of electrical cleaning [140, 141]. Tarazaga et al. [142] studied this using a ceramic (ZrO_2-TiO_2) membrane fouled with bovine plasma in a tubular crossflow module. The pH was set above the isoelectric point of the proteins, so that they were negatively charged in the solution. The membrane itself was charged to be the cathode with a wire through the centreline of the channel as the anode. Their results showed an electric field, intermittently applied for 2 to 3 min after the permeate decreased to a constant plateau, achieved more than 100% flux recovery as long as the applied voltage was above certain values, such as 15 V for 0.5 wt% solution in their cases. The higher the voltage, the better the flux recovery and the faster the cleaning. They also found the concentration of the feeds affected the cleaning results. Under the same voltage, the higher the concentration, the less effect of the cleaning.

Electric fields have been recently applied to MBRs [139], resulting in a novel system named EMBRs (Electric-field attached MBRs). Akamatsu et al. [143] applied an intermittent electric field ($E = 6\,\mathrm{V/cm}$; switching on and off every 90 s) to MBRs, which replaced any air sparging. Their results indicated that the negatively charged sludge particles were removed from the membrane surface by electrostatic repulsion, once the electric field was turned on for enough duration. The intermittent operation was as effective as the continuous application of the same electric field strength. By operating intermittently, the energy consumption could be kept lower than that in a conventional aeration system. Positive results about this application were also obtained by other researchers such as Liu et al. [136], who used newly configured electrodes to apply an electric field at very low strength (0.036 and 0.073 V/cm). This kept energy consumption at very low level, despite occasional air bubbling. Although currently the studied EMBRs were all equipped with MF-sized membranes, similar results were expected in UF.

The most obvious advantage of an electrical cleaning is an incorporated in-line technique, like ultrasonic cleaning, keeping filtration running without interruption. Electric fields may be used in conjunction with other cleaning methods, e.g. chemical cleaning. For example, when charged surfactant micelles accumulated on a crossflow UF membrane, an external DC electric field helped lift them back to the flow region and break the gel layer [144]. However, it requires a substantial capital instalment. Its cleaning effectiveness has also limitation. It may be effective in removing reversible

foulants [140, 142], which have to be charged in order for electrophoresis to take place. For irreversible fouling, the effect of electric fields may not be great. This requires more research, as currently there is a lack of clear information. Electric fields are also of little use for feed streams with relatively low conductivity.

The imposed electric fields may result in Joule's heating which can be substantial. It also impacts the chemistry in the feed, due to the electrochemical effects such as electrolysis and pH shifting. Their effects in membrane filtration are not fully understood. The literature contains limited information about them. Sometimes, the effect can be positive. For example, gases generated during electrolysis are considered to have a positive scouring effect on the membrane surface [145]. However, at other times, electrolysis imposes serious problems such as electrocoating on membranes and corrosion of the electrodes [137]. Electric fields also affect biological activities. The applied electricity may stimulate the secretion of EPS from cells; this has been observed in EMBRs [136]. Before this technique can be scaled up to large-scale application, these issues need to be studied more thoroughly.

3.4 Chemical cleaning

Chemical cleaning of fouled membranes is based on chemical reactions between the chemical agents and the foulants. Chemical cleaning is generally applied to hydraulically irreversible foulants, i.e., to the tough parts of fouling. It can be carried out *in situ*, also known as cleaning-in-place (CIP), by replacing the original feed with cleaning solution in the membrane module, or *ex situ*, referred to as cleaning out of place (COP), by taking the membrane out of the main process stream and placing it into an off-site tank to soak with chemicals [146, 147]. Chemical cleaning can be done statically without circulation of the cleaning solution or kinetically with flow. A selective list of recent studies on UF chemical cleaning is presented in Table 3.1

A cleaning agent works by dissolving, displacing or chemically modifying the foulants or the fouling layer [71]. From a process point of view, it usually takes six stages to complete the cleaning [89, 93, 164]: (1) bulk dispersal and formation of cleaning agents; (2) transport of the agents to the fouled surface; (3) transmission through the fouled layers; (4) chemical reactions; (5) transport of reaction products back to the interface; and (6) transport of products back to the bulk solution. The mass transfer stage of the cleaners to the fouling layer may become the limitation of the whole process.

Table 3.1: Selective lists of studies on UF chemical cleaning in recent publications

Application	Fouling types			Membrane	Cleaning agents							References
	Organic	Inorganic	Microbial		Acid	Alkali	Chelate	Oxidant	Surfactant	Enzyme	Blend	
Milk	+			PS	+	o	+	+	+		o	[148]
Skim milk	+			PES	+	+				+	+	[149]
Glutamic fermentation broth	+		+	PS	+	+		+	+		+	[150]
Protein	+			PES, PVDF					+			[151, 152]
Protein	+			PES						+		[153]
Protein	+			PES, PVDF		+		+	+		o	[154, 155]
Tea solutions	+			PS		+						[156]
Pulp effluent	+			PES		+		+	+	+	o	[107]
NOM	+			PES	+	+			+			[157]
DOM	+			PVC		+						[158, 159]
Surface water	+	+	+	PAN				+				[160]
Algal-rich water	+		+	PVC	+	+	+	o				[161]
Municipal wastewater	+	+	+	PES							+	[100]
Activated sludge effluent	+	+	+	PVDF	+	+	+	o	o	o	+	[162]
Spent sulphite liquor	+	+		PES, PS		+					+	[163]

Notes: "o" – optimal; "+" – tested

3.4.1 Cleaning agents

Six categories of cleaning agents, shown in Table 3.2 are commonly used: acids, alkalis, oxidants, surfactants, chelants and enzymes [91, 148]. Commercial cleaning products are often mixtures of these compounds, but the actual composition is often proprietary and unknown in the public domain [71]. Chemical agents, particularly oxidants, are also used for disinfection to maintain the system free of microorganisms.

Acids Acids are mainly used to dissolve precipitates of inorganic salts or metal oxides and hydroxides [29, 91]. Mineral acids such as hydrochloric (HCl), nitric (HNO_3), and sulphuric (H_2SO_4) acids can perform efficiently and effectively for this. HNO_3, especially, is increasingly favoured in many plants to remove calcium precipitates [24, 29]. Besides this, HNO_3 is a strong oxidising agent, and in some cases, used to clean many organic and biologic foulants by nitration.

However, the major drawback of strong acids is their great impact on pH of the solutions. Too low pH can threaten the integrity of membranes. In this respect, weak acids are usually preferred as cleaning agents in membrane plants. Phosphoric acid (H_3PO_4) and some organic acids, such as citric acid, are good buffers in maintaining pH during cleaning, and therefore much less corrosive. Many of weak acids are also chelating agents, extremely effective at removing metal cations. However, they have

Table 3.2: Common cleaning agents and possible interactions between cleaning agents and foulants

Family	Examples	General functions	Concerns
Acids	Strong: HCl, HNO_3, Weak: H_3PO_4, Citric	pH regulation, dissolution of inorganic precipitates, acidic hydrolysis of certain macromolecules	Strong ones corrosive; Weak ones expensive; Possible insoluble products
Alkalis	Strong: NaOH, KOH, Weak: Na_2CO_3	pH regulation, alteration of surface charges, alkaline hydrolysis of proteins, catalysing saponification of fats	Strong ones caustic; Weak ones may form insoluble salts
Oxidants	NaClO, H_2O_2	Oxidation of organics; Disinfection	Membrane disintegration; chlorination by-products; H_2O_2 explosive; high consumption
Surfactants	Anionic: SDS, Cationic: CTAB Non-ionic: Tween 20	Dispersion/suspension of deposits	Long cleaning time; surface adsorption; re-fouling
Chelants	EDTA	Complexion with metals, removal of mineral deposits	Environmental concerns; legislation; costs
Enzymes	Proteases , Lipases	Catalysing lysis of specific substrates (e.g., proteins, lipids)	Costs; effectiveness

relatively high cost [165]. It may also be a concern that some reaction products of HNO_3 and H_3PO_4 are of limited solubility, which may cause re-deposition.

Alkalis Hydroxide solutions, such as sodium hydroxide (NaOH), potassium hydroxide (KOH) or their mixtures, can promote rapid hydrolysis of proteins and polysaccharides into small amides and sugars; efficient neutralisation of acidic organics; expansion of HA molecule to reduce its bond to the membrane surface; saponification of fats and oils and hence solubilisation of the cleaning products; dispersion/emulsification of colloidal material; and regulation of pH to the effective working condition for other chemical cleaners (e.g. oxidants on breakdown of HAs) [24, 89, 157, 166]. A drawback with these hydroxide solutions is their lack of a buffering capacity (or hydroxide reserve). Therefore, most cleaning must begin with high pH levels of 11 - 12 in order to sufficiently neutralise all the acidic components and saponify all fats [24, 29].

Weak bases such as soda ash (sodium carbonate (Na_2CO_3)) and sodium metasilicate (Na_2SiO_3), as opposed to those strong bases, is of high alkaline reserve with comparatively mild pH values, making them less caustic. Polyphosphates, another types of weak bases, sometimes included in some built detergents, has an additional

chelating capability [24]. However, one disadvantage of these mentioned weak bases is that they may form insoluble salts with divalent metal ions. For complex phosphates, there are also environmental ramifications to bear in mind, due to the concern over water source eutrophication.

Oxidants Oxidants are strong cleaners such as sodium hypochlorite (NaOCl), hydrogen peroxide (H_2O_2) and peracetic acid ($CH_3COCOOH$). Their primary role is for disinfection to eliminate all pathogenic microorganisms. Water and wastewater treatments need disinfection frequently to reduce biofilm growth, while the food and dairy industries require their membranes to be disinfected on a daily basis and the pharmaceutical manufacturers require their process systems to be sterilised prior to each use. Therefore, the usage of oxidants is almost inevitable in many industrial membrane systems.

Sodium hypochlorite (NaOCl) is the most commonly used oxidant, which hydrolyses in water rapidly to form hypochlorous acid (HOCl), a weak acid that dissociates depending on pH. HOCl possesses high microbicidal activity especially at low pH which preserves HOCl undissociated. Besides its oxidising capability, hypochlorite may cause membrane swelling [13], and this assists in flushing out material that may be lodged within the pores [167]. However, these agents can oxidise the membrane surface and cause a partial scission of the membrane polymers, thus shortening the membrane lifetime by causing changes in membrane functional groups, mechanical properties, physical structure and hence hydraulic and retention performance. More information on membrane damage is discussed in later section. The by-products of the chlorination of NOM can have health and environmental concerns. Therefore, industrial users are looking for alternative cleaning methods to reduce the usage of NaClO [168].

The other oxidants, H_2O_2 and $CH_3COCOOH$, are compatible with almost all membranes and are easy to rinse off. $CH_3COCOOH$ can be used for many biological applications, for example, cleaning hemodialysis membranes for subsequent reuse, since it decomposes into the non-toxic acetic acid [29]. However, the consumption of them in membrane cleaning (e.g., for MBR) is very high. They also possess safety issues as both of them are explosive, and therefore expensive safety precautions are required for their storage in plants [168]. They were chosen as surrogates for NaClO in a large scale MBR plant in Germany, but found not as effective [168].

Sometimes, a reducing agent, such as sodium metabisulphite ($Na_2S_2O_5$) and sodium bisulphite ($NaHSO_3$), is used to neutralise any unwanted free chlorine in

the membrane system. These reducers were considered for disinfection in oxidant-sensitive membranes as well [169]. However, their reaction takes too long and may be of little effect on bio-activity. A study on PAN spiral-wound membranes showed immersion with the $Na_2S_2O_5$ solution for 24 hours had no impact on biofouling [160].

Surfactants Surfactants are amphiphilic compounds which can lower the interfacial tension between two liquids or between liquids and solids. They may act as dispersants, emulsifiers, detergents, wetting agents and biocides. They help to solubilise and disperse deposits such as proteins, and improve the wettability and rinseability of the membrane surface [91, 170, 171]. Consequently, surfactant cleaning can reduce the rinsing time and water consumption.

The functional properties of surfactants are due to their amphiphilic nature, i.e., their molecules containing both hydrophilic and hydrophobic groups. They diffuse in water and adsorb at interfaces, e.g., between air and water, or foulants and water. When the concentration of surfactant is greater than the critical micelle concentration (CMC), the surfactant molecules aggregate in aqueous solution to form micelles, with the hydrophilic 'shells' in contact with surrounding water and the hydrophobic 'cores' tucked into the centre, . In membrane cleaning, surfactant concentration is usually kept above CMC and the micellization process has been recognised as a key component in the cleaning process [151]. A mechanistic model was developed by Naim et al. [151] for surfactant cleaning above its CMC. It starts with the formation of micelles at the air-water interface, followed by their transfer towards membrane surface, where the micelles start to partially disassemble and release surfactant monomers which are bound to the foulants. This causes "roll-up" of the foulant, which is lifted away from the membrane into the bulk solution. However, it is possible that over time surfactants will adsorb onto the available membrane surface where the foulants have left. This will eventually cause a more hydrophilic membrane surface and attract free micelles to form a cake layer reducing the flux. The micelle migration towards the membrane surface is quite slow, the speed of which was estimated at about 2×10^{-5}m/hr [151]. Therefore, it has suggested that surfactant cleaning is controlled by its transfer limits.

Chemically, surfactants have four main subgroups: cationic, anionic, nonionic, and zwitterionic (or amphoteric) [91]. Cationic surfactants such as cetyltrimethylammonium bromide (CTAB) have a positive charge and consist of an amino or quaternary nitrogen group. They can be used with acid cleaners, but are generally insoluble in alkali solution. Their main disadvantage is that they can strongly

adsorb onto a negatively charged membrane, the latter often being the natural membrane state under near-neutral pH conditions [29]. Anionic surfactants have negative charges when dissociated in water. Typical examples include household soaps (often salts of carboxylic acids), alkyl sulphates (e.g., sodium dodecyl sulphate (SDS)), alkyl sulphonates and phosphates [24]. Nonionic surfactants (e.g., polysorbate 20, commercially branded as Tween 20) usually have long chains of hydrophilic groups in combination with alcohol, alkyl phenyl or polypropylene oxide chains. Nonionics are unaffected by metal cations, and thus can be used in hard water. They are stable in both acidic and alkali solutions, and are therefore commonly used in the blended cleaners formulated for organic fouling. They are also low foaming and easy to rinse off, but are usually less effective than anionic agents [91]. However, like cationics, many nonionic agents can strongly adsorb onto a negatively charged membranes. Naim et al. [151] confirmed the adsorption of Tween-20 on PES and PVDF membranes by testing their contact angles through the cleaning and it altered the hydrophobicity of both membranes from slightly hydrophobic before cleaning to obviously hydrophilic after. The adsorption of surfactant cleaners may be detrimental to filtration as these cleaners can cause severe re-fouling, just like those surfactants naturally present in some filtration streams, such as fatty ester, polyols and silicones, which can cause severe irreversible fouling [91, 172].

Chelants Chelants or sequesterants such as ethylenediamine tetra-acetic acid (EDTA) form strong complexes with multivalent metal ions such as calcium and dispersal minerals in general [29, 89]. Thus, EDTA is effective in destroying the otherwise tough, cross-linked Ca^{2+}-HA fouling layer by taking Ca^{2+} away via a ligand exchange reaction [71]. Moreover, EDTA is often blended into proprietary cleaning agents (e.g., P3 Ultrasil 11) as an enzyme disruptor and studies have demonstrated the latter inhibits biofilm reformation [93]. The cleaning efficiency of EDTA is pH dependent, as the number of deprotonated carboxylic groups in EDTA is a function of pH [71]. However, there are environmental concerns and legislation limits about using EDTA, for example, in water industry [89]. This is because EDTA is persistent in the environment although it has low toxicity. Chelating cleaners have also relatively high cost. Therefore, their usage in membrane cleaning is generally limited.

Enzymes Enzymes are selective catalysts, designed for specific targets. For example, protease, an enzyme that can degrade proteins by cutting the molecular chain at strategic points, has been used to remove protein foulants in industrial UF

[24, 153, 173]. Their reaction is highly efficient. In a study conducted by Argüello et al. [174], a greater than 90% cleaning efficiency was achieved, when dealing with ceramic membranes fouled with whey protein solutions, and the efficiency was influenced by pH, enzymic concentration, cleaning duration, the operation of permeate recycling. Their maximum efficiency can be achieved at high pH and at temperatures below 60 °C[171]. Increasing pH by addition of alkali can permit hydrolysis of proteins, which can further favour the cleaning [174]. After enzymatic cleaning, it is effective to apply detergents to solubilise any small loose protein fragments [173].

Enzymatic cleaning has many advantages over other types of cleaning agents [24, 29]. For example, it prolongs membrane life, because enzymatic reactions take place at low temperature, mild pH ranges and enzymes themselves are safe for most membranes. Therefore, they are suitable for membranes that are unable to withstand elevated temperature, extreme pH values, or strong chemicals. Their reactions are very efficient and require less rinsing, which cuts chemical cost and produces less waste water. They don't require high temperature, which saves energy. They are also biodegradable and environmentally friendly. However, its cost efficiency is difficult to control [24] because there exists an optimal enzymatic concentration that maximises the chain scission effect. Lower amounts of enzyme can result in low cleaning efficiency or high cleaning duration, whereas a higher enzymatic concentration does not necessarily increase cleaning efficiency but does increase costs and even causes further membrane fouling [173, 174].

Enzymatic cleaners are especially useful for biofilm removal, since they break down proteins at bacterial attachment sites. Most alkaline or acid cleaners struggle to do this.

3.4.2 Physical and chemical cleaning combined

One of the current trends is towards merging physical and chemical cleaning, for example, a chemically enhanced backwashing (CEB), to improve cleaning efficiency. A CEB usually follows the steps of a normal backwash, except the backwashing solution is dosed with chemicals [175]. The choice of dosing chemicals is process-oriented, typically involving an acid or base combined with an oxidant, normally chlorine [101, 176]. During CEB, a soaking step for 5 - 20 mins is usually applied to allow thorough chemical reactions [175]. Alternatively, the membrane is soaked for several hours and air sparging may be employed during soaking.

Compared to cleaning-in-place (CIP) where the cleaning solution flow is conducted across the membrane surface, CEB needs less equipment and interrupt the filtration process less, despite that CIP allows the use of elevated temperatures and special cleaning agents. A survey of 83 UF plants in Germany [106] showed that these plants with a routine CEB required chemical CIP once every 1-5 years at maximum, while those without CEB needed CIP at least 1-4 times per year. However, CEB cannot be performed at any installation. And it is high energy demand, which makes the gain not always obvious.

3.5 Evaluation of Cleaning Efficiency

3.5.1 Evaluation by flux measurement

The most common way to evaluate the effectiveness of a cleaning process is to compare the pure water flux through fresh and cleaned membranes under the same operating conditions. For example, the flux recovery (FR) is defined as the ratio of the water flux of the membrane after cleaning (J_c) to the flux through the virgin membrane (J_0) at the same TMP.

$$FR = \frac{J_c}{J_0} \quad . \tag{3.1}$$

Based on this, Astudillo et al. [177] proposed an upgraded characterisation parameter named "membrane performance recovery (MPR) ". It is defined as the ratio between the average membrane flux after cleaning and the average value of the original membrane flux:

$$MPR = \frac{\int J_c \, \mathrm{d}\Delta P}{\int J_0 \, \mathrm{d}\Delta P} \quad . \tag{3.2}$$

As the flux is averaged out over a range of TMP, this parameter can provide more information than the FR value at a particular TMP.

However, the evaluation method based on measurements of pure water flux may not be reliable because a good water flux does not necessarily assure a good operational flux [145]. Even when the permeate flux is fully restored after cleaning, it may drop immediately after a new filtration cycle starts [178]. Moreover, many physical and chemical properties of a membrane can change with the cleaning process, especially those on its surface since this has direct contact with foulants and cleaning chemicals. Flux measurement does not necessarily reflect the changes. Nev-

ertheless, FR or MPR is a good indicator for cleaning effectiveness due to the quick, non-invasive, and simple nature of this method.

3.5.2 Membrane autopsy

For a more comprehensive evaluation of cleaning performance, it needs not only the immediate cleaning result represented by flux recovery, but also information on the effect of cleaning on membrane properties and fouling removal. Therefore, the more sophisticated way of studying the cleaning performance is membrane autopsy with different material characterisation techniques. By saying autopsy, we mean the membrane needs to be removed from its normal filtration module and characterised *ex situ*. Sometimes, it is even necessary to break the membrane for sampling and testing. This way is intrusive, complicated and often expensive, but it does generate extra information relating to the membrane and fouling residuals, and brings more insights into the cleaning efficiency and mechanisms, for example, identifying which foulants remain on the membrane after cleaning and indicating any damage caused by cleaning. Some methods, particularly those involving imaging techniques, may also be applied *in situ* without moving the membrane. This reduces unknown effects on the membrane or fouling layer during removal, but the techniques require specially designed membrane modules, i.e., modifications to the filtration process, which means they are still invasive [179]. However, compared to *ex situ* methods, their impact has been kept minimal and therefore, they may be referred to as quasi-non-invasive [180]. Moreover, most of the *in situ* techniques are only applicable to bench-scale studies and not to the full-scale operation. For real-life analyses in a membrane plant, the only *in situ* testing possible is perhaps the flux measurement.

The membrane properties can be determined through several parameters such as charge, hydrophilicity, strength and thermal stability. The measurement of the streaming potential of a membrane is a convenient means to indicate the changes in the surface charge of a membrane. Experiments have shown that a change in streaming potential is highly dependent on the interactions between the membrane and foulants or cleaning chemicals [163]. Hence, it is an important tool in determining the quality of a cleaning. The hydrophilicity of a membrane top surface can be determined by measuring contact angles. After cleaning by NaClO, PVDF membranes tend to become more hydrophilic [181]. These changes may be attributed to the fact that either foulants or cleaning chemicals, or both of them have modified

the membrane surface. Membrane's mechanical strength can be measured by material stress tests, including valuing the ultimate tensile strength (i.e., the amount of force required to pull a filter apart), ultimate elongation (i.e., the degree to which the filter stretches before it breaks), and Young's modulus [182]. Their change in value (normally decreasing) reflects the deterioration in the material integrity. The thermal stability of a membrane is examined by thermogravimetric analysis (TGA). Modern UF membranes often have a double layered structure (a thin active semi-permeable layer on top of a thick supporting layer). The analysis of thermal-mechanical stability of a membrane ideally requires measurement on each layer separately in order to gain accurate results [7].

Fourier Transform Infrared (FTIR) spectroscopy in conjunction with attenuated total reflectance (ATR) sampling technique has been widely used to analyse the surface chemical composition on a membrane. It can detect the changes in the functional groups of the membrane polymers after being fouled or cleaned [181, 183]. By using this technique, Arkhangelsky et al. [6] observed a reduction of the number of C−S bonds in chlorine-treated PES membranes, indicating the breaking-down of some chains between phenyl and sulfonyl groups in PES polymers.

Besides characterising membrane materials, the fouling residues on the membrane are the other important factor to be delineated. The surface chemistry analysing tool, ATR-FTIR, can identify remaining organic foulants such as protein on the membrane surface and even quantify it, given that the protein has been well determined as the only fouling-causing material [184]. Energy dispersive X-ray spectroscopy (EDX or EDS), often coupled with scanning electron microscopy, is an elemental analysis technique [184–186]. It can determine mineral foulants on the membrane [187].

Imaging techniques such as electron microscopy can achieve nanometre resolutions, which makes them suitable for works in the UF range. For example, scanning electron microscopy (SEM) can reveal the morphology of the membrane surface and its cross-sections and has become a common tool to identify and visualise macromolecular (e.g. protein) depositions on the surface or within the matrix of the membrane [188]. SEM requires membranes being removed from the module and to undergo special treatments before imaging, and it cannot, generally, differentiate the species, for instance, if fouling is caused by a mixture of proteins [179].

An alternative to electron microscopy is fluorescence microscopy, for example, confocal laser scanning microscopy (CLSM). It produces 3D images with resolutions close to the SEM. It requires foulants and/or membranes labelled with fluorophores before filtration experiments, but it can distinct between foulants with different dyes

[189]. With specially designed membrane module, CLSM can be used in-situ [189]. Although it has been used in studying protein fouling, there is as yet no information about its usage in evaluating membrane cleaning. While CLSM uses a single high-energy photon to evoke fluorescence, multi-photon microscopy (MPM), a similar fluorescence technique, uses two or more photons excitation, which increases the photon penetration and reduces sample damage [189]. As MPM can be designed as a non-intrusive, *in situ* tool, it can visualise the development of a cleaning process. It has successfully captured the re-fouling of a membrane after a prolonged cleaning by the previously removed foulant (ovalbumin) present in the cleaning solution [190].

Atomic force microscopy (AFM) is a type of scanning probe microscopy, i.e., it uses a probe (cantilever) to measure the interactions between its tip and the sample surface. By scanning a sample area, the measured interactions from different points can be mapped spatially into a high-resolution 3D surface topography, e.g., of a pristine or fouled membrane. Unlike SEM, AFM does not need special sample preparation and can be performed in liquid environment, which means it can operate *in situ* [191]. AFM has been used to quantify the reduction in intermolecular adhesion between foulants and membrane surface during cleaning [71, 185]. However, AFM pictures may not be clear for comparing cleaning results [185].

Among the less traditional characterisation methods is membrane staining (or dye tests), which is a qualitative colorimetric assay to help determine the existence and location of proteins on the membrane. The membrane needs to be stained with dyes for certain amount of time and then distained several times [192]. This leaves the protein fouling area a darker colour than other areas. However, the sensitivity of this method is affected by undesired background staining [193]. Nevertheless, by changing the dye from Coomassie blue [192, 193] to Amido black [194], the background staining can be reduced. Therefore, it was proven to be capable of identifying any remaining protein foulants and adsorbed surfactant cleaners on the cleaned membranes [194]. The staining method also provides an interesting insight regarding the traditional flux measurement when they are both used in the analysis. Membranes that had recorded similar fluxes were found containing different amounts of protein residues [194]. Thus, it is yet more proof that the flux measurement is not always representative of the degree of membrane fouling.

In summary, most cleaning characterisation techniques are also methods that can be used for studying membranes and fouling. In the scope of this review, it is unrealistic to include all the information about these techniques and their usage. For

more details, there are more focused review papers available, for example, by Chan and Chen [188] and Chen et al. [180].

3.6 Cleaning Process and Operating Parameters

3.6.1 Common practice

Membranes in industry are regularly maintained and cleaned in place. At industrial scale, a typical cleaning-in-place (CIP) practice requires several stages including, (1), emptying the filtration rack from the liquid on both permeate and feed sides, followed by water rinsing to remove product residues and reversible foulants; (2), chemical cleaning which often consists of multiple steps in sequence for addition of different agents with/without rinsing in-between but definitely with water rinsing at the end to eliminate chemical agents and foulant residues; (3), disinfection and rinsing (maybe with the addition of sodium bisulphate).

However, the permeate flux and productivity will gradually deteriorate to a level unrecoverable by CIP. CIP is relatively simple and convenient but its effectiveness is limited. An intensive COP is usually required periodically. Although MBRs usually incorporate an online backwash system, chemical cleaning can only take place off-line for submerged systems where membranes are installed in the main reactor. During cleaning, membrane modules are taken out of the reactor and immersed in a separate washing basin filled with cleaning solution. For an MBR with a separate membrane tank, cleaning agents can be injected to the tank after the sludge has been drained out [195]. As better and better cleaning strategies are applied nowadays, this intensive COP process can be delayed now for years, for example, in some large scale municipal MBR plants [168].

3.6.2 Cleaning steps

The requirement of different cleaning steps is process-oriented. The sequence of these steps affects the overall cleaning efficacy [89, 91]. For example, backwash followed by forward flushing was observed more effective than the reverse sequence [98]. It is not difficult to envisage that backwash dislodges the otherwise difficult-to-reach foulants in the pores and then forward wash helps remove them from the stream. As for the sequence of adding chemicals, an alkaline cleaning followed by an acid step is

widely used in diary and surface water industry in order to remove macromolecular and mineral foulants respectively [24, 89, 149]. This order has proven more effective than the reversed in several studies [89, 149].

However, the acid clean step was thought to be redundant and not effective in cleaning protein fouling if no minerals present in the fouling layer. Acids such as HNO_3 and HCl can not remove irreversible protein residuals at all (based on ATR-FTIR results) [149]. Therefore, it is vital to determine the composition of foulants before constructing a cleaning strategy. Then, a 'standard' cleaning process can be tailored to a particular case for optimisation.

In order to simplify the process, multiple cleaning steps may be cut into a single stage by using an optimised cleaning solution [183]. The first choice of all is the right cleaning agents for a particular job. It is critical to the cleaning effect and efficiency and depends on the filtration system components, including both membrane and foulant, of which the complexity of the latter increases with the number of species or functional groups involved. Currently, the choice is usually done empirically [183]. For example, a combined NaOH (0.02N) and NaClO (100 mg/L) solution was shown optimal in a study to clean a membrane fouled by algae-rich reservoir water [98]. More advanced and theoretical methods include correlating the interfacial energy to the fouling-removal capability of a cleaning solution for formulating more chemically efficient solution [183].

3.6.3 Cleaning frequency

More frequent cleaning means a shorter period of filtration. This usually causes a less condensed fouling layer liable to be removed by simple physical forces, leaving only small amount of irreversible foulants scattering over the membrane. Therefore, membrane properties, such as porosity, surface roughness, and expression of end groups, become the major controlling factors in the cleaning process [163]. On the other hand, less frequent cleaning allows more time for the condensation of fouling layers, which may be difficult to rinse off. Therefore, the membrane is possibly covered with fouling layers when chemicals are applied. Then, the reaction between cleaners and foulants, rather than membrane properties, becomes the control factor to a cleaning practice.

3.6.4 Cleaning duration

For chemical cleaning stages, a minimum cleaning duration should be set so as to allow chemical reactions within fouling layers to be completed, while an up-limit should also be determined for an optimal cleaning efficiency. There are currently two concepts of the maximum time of cleaning in the literature [155]. They are cleaning to the maximum flux restoration or cleaning up to the level when the flux after cleaning will be equal to that of a fresh membrane. The former view suggests cleaning should continue till membrane is completely clean and the flux restores to a steady-state maximum value if the cleaning efficiency continues to increase as the cleaning time lasts. Therefore, the longer the cleaning, the cleaner the membrane. The latter considers a shorter cleaning period should be performed if short and long cleanings are equally effective. It can be postulated that the cleaning efficiency passes through a peak value to a lower stable level. This secondary drop during the later stage of cleaning may be caused by redeposition or denaturation of the foulants on the membrane surface.

The re-fouling phenomena were observed in some studies, e.g., the one with protein determined by the MPM technique [190]. Some researches [196, 197] have suggested that the re-fouling is caused by the decomposition of large flocs, previously dislodged, into smaller segments due to a prolonged cleaning. As foulants become smaller, they have higher chance of entering membrane pores and plugging them.

Prolonged exposure to certain chemicals can induce membrane disintegration as well [181, 198]. This is discussed in the next section.

Operational time is important for water rinsing as well. It should be sufficient so as to make sure the outlet stream is clean from permeate and foulants [199], especially for solutions containing surfactants [183].

3.6.5 Chemical concentration

Concentration affects the rate and the equilibrium of a reaction. The concentration of the cleaning agents in bulk solution does not necessarily reflect the effective amount engaged in the reaction with the foulants because the foulants have indeed left the liquid phase into a solid-like state on the membrane surface. Therefore, reactions between cleaning agents and foulants occur in the liquid-solid interface. There exists a mass-transfer boundary controlling the amount of reagents entering the fouling layer [200]. Hence, the dosage must be higher enough to overcome this mass-transfer barrier as well as to maintain the reaction in a reasonable rate.

As formerly mentioned, the previously accepted consensus that an increase in the agent's concentration results in an improvement in the cleaning efficiency has been proven incorrect. Researchers have repeatedly shown that there is an optimum concentration, above which cleaning efficiency does not improve and at times may , on the contrary, cause deterioration [201, 202]. For example, in cleaning a UF membrane fouled with whey protein concentrate (3 wt%), the membrane flux recovered by NaOH solution at mass fraction of 0.2 % was almost two times higher than those by 0.3 % and 0.5 % solutions [203]. Similar trend was observed in the work of Väisänen et al. [185] on a PA (50 kDa) membrane. In their work, the optimal concentration is even at lower value of 0.075 wt% though their whey protein solution has as high a concentration as 16 wt%. It was suggested that the higher concentration of NaOH could have enhanced the swelling of the deposits, resulting in additional pore blockage [203].

Interestingly, while investigating the optimum concentration of NaClO on cleaning PVDF membranes, Puspitasari et al. [198] reported the repeated cleaning with 0.5% NaClO was as effective as a single clean performed with 1%.

3.6.6 Physical conditions

The physical conditions such as hydrodynamics and temperature of the system affect the cleaning efficacy as well. Hydrodynamic conditions that promote contacts between cleaning agents and fouling materials during the cleaning are favoured. Dynamic cleaning can be more effective than static soaking of membranes with chemicals with respect to mass-transfer. Under static conditions, diffusion dominates the transport mechanism. It may not be efficient in many cases such as the internal fouling within the membrane matrix. Mass transfer can be enhanced dramatically by circulating cleaning solution through the system, which convects chemicals to the foulants at a faster pace.

For crossflow operation, the flow parallel to the membrane surface can provide a constant shear force with the effect of carrying away reversible foulants. Some studies concluded that, for a good mechanical cleaning effect, CFV is recommended to be higher, and the TMP lower, than those values used during normal operation [204]. Other studies found that hydraulic and chemical cleaning bear a negligible relationship to CFV [92, 201]. In practice, the pump capacity and mechanical forces on the membranes limit the possible increase to the flow rate.

It is recommended that permeate flux is kept lower in the cleaning process than that used during normal filtration, in order to prevent dislodged foulants from penetrating and adsorbing or compacting within the pores [169, 201]. Some studies have been carried out on cleaning with as low as possible a transmembrane flux, which can eliminate any possibility of redeposition within the pores.

An elevated temperature can increase the kinetics of the reaction. The higher the temperature, the more soluble both the foulants and the cleaning agents become. Higher temperature also improves diffusion and reaction rates. However, temperature has a non-linear effect on the cleaning efficiency. Whilst increasing temperature, one must keep in mind two major drawbacks: the membranes may be susceptible to high temperatures [29], and the possibility that the fouling will become less amenable to loosening and breakup [24, 201]. It is suggested that temperature is kept at around 50 °C and not higher for cleaning [24, 197].

3.6.7 Optimisation

A cleaning process can be optimised in order for: (i) improving and maintaining the cleaning efficiency, (ii) lengthening the service life, (iii) reducing the consumption of chemicals, water and energy, and (iv) minimising the environmental impact of the waste effluent. If the first two goals are fulfilled while chemical usage can be reduced, it will beneficially cut down the total cost and emission of unwanted substances into the effluents, and minimising the plant downtime, labour input and hazards to plant operators [168]. There are many studies about optimising membrane cleanings from almost every means. However, at current state, chemical cleaning is still inevitable in most practical cases

Optimisation is usually studied by adjusting one chemical or physical condition at one time. However, given the complex nature of fouling, cleaning involves many variables such as process sequence, hydrodynamic conditions, solution temperature and pH, chemical dosage, and cleaning duration etc. Apparently, by the one-parameter-each-time method, a comprehensive understanding of them requires a large number of experiments to cover all of the parameters for a specific membrane application [89]. To reduce the total workloads, researchers have started to use multi-variables statistical methods recently [100]. In these methods, full factorial experiments are designed to aid identifying the major independent parameters affecting cleaning efficiency and their optimal conditions as well as the interactions between factors. The experimental results can be analysed by the analysis of variance (ANOVA) method. Chen et al.

[100] first designed a factorial experiment to study the chemical cleaning efficiency in a spiral-wound UF of the secondary effluent of municipal wastewater. Porcelli et al. [205] factorised concentration, soaking time and temperature with Box-Behken design to study chemical cleaning on a biofouling case with upland surface water. They later incorporated a cost model into their factorial experiments [206].

3.7 Membrane disintegration

3.7.1 Membrane properties

Membranes possess mechanical strength, thermal stability and chemical resistance, which depend on the material of construction. And it is not necessarily the membrane that is stable against one of the factor can perform well against all of them. The mechanical, thermal and chemical factors regarding these materials are listed in Table 3.3.

CA membranes are naturally hydrophilic with low binding to proteins, but have limited range of operational pH. A lower pH can degrade the β-glucosidic linkages in the backbone of the cellulose polymer, reducing the effective molecular weight and eventually causing loss of structural integrity. At higher pH values, CA membranes will deacetylate [29]. Free chlorine higher than 1 ppm for long term applications or higher than 50 ppm in short term applications will oxidise and damage the membrane [207].

PAN membranes have good tolerance to organic solvents and, hence, been widely used in treatment of industrial wastewater.

PES and PS membranes have high rigidity and good chemical resistance due to their structures consisting of phenylene rings connected by sulfonyl (SO_2) groups. Operating temperature for these membranes can reach as high as 75 °C. Operating pH can range from 1 to 13 [3]. These membranes have strong alkali resistance. However, PS and PES membranes are susceptible to oxidising agents, such as chlorine or hydrogen peroxide. The maximum allowed chlorine concentration is up to 200 ppm for short term applications and 50 ppm for long term applications [207].

PVDF membranes are even more stable than PES and PS ones. They usually have remarkable chemical resistance and can be repeatedly autoclaved, and thus are suitable for food and pharmaceutical applications. However, in alkaline streams with pH greater than 12, PVDF can dehydrofluorinate [29].

In many practices, increased hydrophilicity of a membrane is favoured. Then, polymeric additives such as polyvinylpyrrolidone (PVP), which is mostly used, are often blended into or grafted onto these polymeric back-bone matrices [4].

It is worth mentioning that even small differences in the chemical composition of the base polymer, the presence of blended-in polymeric additives, the specific membrane casting processes, or the use of any post formation modification, can cause significant differences in its chemical and mechanical stability. Thus, detailed information on the operational limits for different membranes should be obtained directly from the manufacturer [24].

Besides these polymeric membranes, ceramic membranes have emerged as an major advance in UF technology during the last two decades [11]. Compared to their polymeric counterparts, ceramic membranes have robuster mechanical strength, higher temperature tolerance, better chemical stability [20], despite the fact that they are currently more expensive, heavier and thicker than polymeric membranes and require higher TMP because they have greater resistance to water transport [11]. Consequently, they generally have higher tolerance to ultrasonic irradiation as shown in Table 3.3 [116]. However, they may still be impaired by ultrasound cleaning based on limited published results [129, 208, 209].

Proper cleaning procedures should not exceed the limits of any of these properties. Excessive cleaning may accelerate wear or damage to the membrane structure, resulting in enlarged pore sizes, fractured surfaces, or compromised and even broken fibres [10, 210]. This implies that the membrane gradually loses its functionality during the course of cleaning, which manifests as a reduction in the quantity or quality of the filtrate products, or a mechanical failure such as fibre embrittlement [211]. In practice, membranes need to be monitored regularly to ensure its integrity. An average annual fibre failure rate in hollow fibre membrane plants was found to be around 1-10 per million fibres [210].

Table 3.3: Mechanical, thermal and chemical resistances of common membrane materials of UF. Sources from [10–12].

	CA	PAN	PES	PS	PVDF	Ceramic
Mechanical strength	good	good	good	good	good	excellent
Thermal limit, °C	30	40	80	75	40	high
pH	4 - 8	2 - 10	2-12	1-13	2 - 10.5	superior
Oxidant tolerance	moderate	moderate	good	good	excellent	superior
Ultrasonic irradiation [116]	moderate	moderate	poor	good	good	excellent

3.7.2 Chemical degradation

There are many factors affecting the failure in membrane integrity in a membrane plant. For example, manufacturing fault, incidents and the shocks caused by the accumulation of air in the system can all lead to physical damage [210]. Most importantly, contact with chemicals during membrane cleaning can alter the functional groups in the membrane materials [6]. It is only recently this effect on membrane integrity has been systematically studied by various characterisation techniques such as membrane thermo-mechanincal strength and chemical composition analyses. Most focuses are on the effects of hypochlorite cleaners. Prolonged exposure to them has been revealed to be the primary cause of chemical degradation in membrane polymers (e.g., PVDF [181, 198] and PS [4, 212]) The degradation rate depends on total chlorine dosage (concentration $\times$ time) and pH [4]. Excessive dosage of NaClO has been found to cause the enlargement of pores in PAN membranes [213] and pitting and cracking on the surfaces of PES membranes [7]. These changes were clearly displayed in SEM images. As a consequence, these changes affect the filter behaviour in terms of flux and filtrate rejection and also alter foulant-PES interactions. A denser protein fouling layer was observed in the membrane with determined PES scission after extreme NaClO exposure [214]. Furthermore, the degradation was found as a surface process with no obtainable effect on the supporting layer [7].

It has been proposed that these changes are due fundamentally to the reactions between the cleaners and some specific functional groups. These reactions cause breakdown of membrane polymers and attachment of new end groups. This process is often described as a chain scission phenomenon. Chemical analyses have revealed the formation of various functional groups (e.g., carboxyl, aldehyde and ketone) on the skin layer of cellulose membranes [215] and the oxidation of sulphonyl ($-SO_2$) groups to sulphonate acids ($-SO_3^-$) in PES chains [6] after prolonged exposure to NaClO solution, the latter being shown in Fig. 3.2. The mechanism in Fig. 3.2a was proposed by Thominette et al. [5] and later Arkhangelsky et al. [6] based on their analyses results. However, Yadav et al. [7] detected the chlorine element in membranes aged at pH 9 (in contrast to pH 12) from EDS analysis, so that a different chain scission mechanism (see Fig. 3.2b) was suggested at pH 9, where one end of the broken PES chain is still terminated with a sulphonic acid group but the other broken end has now a phenyl-Cl group. The pH value affects the concentration between ClO^- and HClO in aqueous solution, with a acid dissociation constant (pK_a) value of, e.g., 7.58 at 20 °C[216]. These two species are known to have different oxidising potential,

with a higher value for HClO [7, 217]. Therefore, the chain scission phenomenon may be controlled by pH. More studies need to address the details.

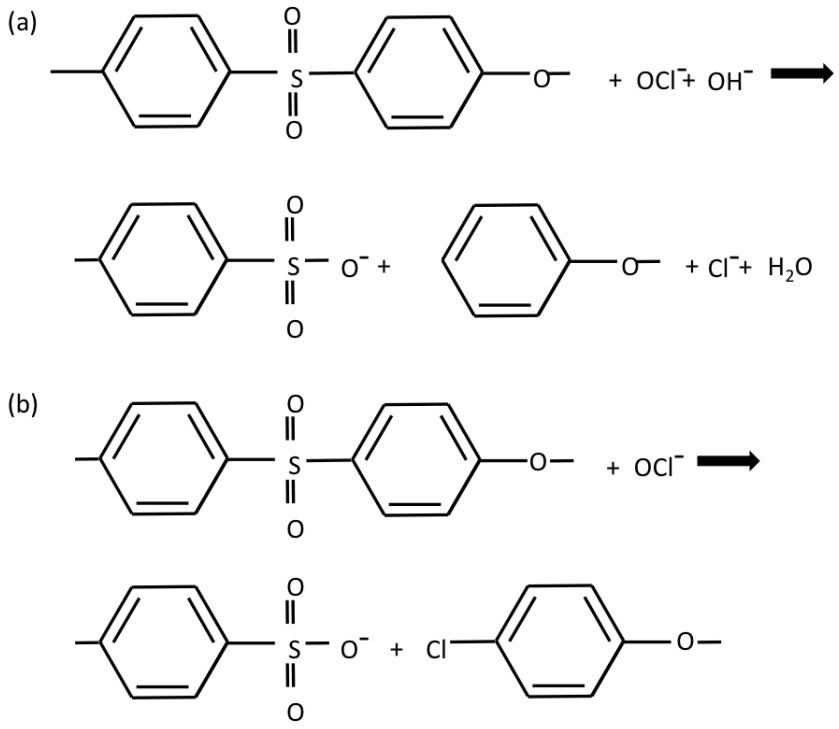

Figure 3.2: The mechanisms of chain scission in PES membrane after prolonged exposure to hypochlorite (a) proposed in Refs. [4–6], and (b) in Ref [7].

The coexistence of HClO and ClO^- in the solution, i.e., around pH 7 to pH 8, may induce the formation of hydroxyl radicals ($HO^{\cdot}$) [218]. The formed $HO^{\cdot}$ can attack the sulphonyl group, which may become the cause of chain scission [212]. The repeating isopropylidene groups in PS monomers are also susceptible to free radicals and can be oxidised into an alkene group [4].

Radicals are also responsible for chain scission in PVP, the additive used in PES membrane manufacturing [4, 218]. PVP degradation in contact of NaClO has been observed in various membranes such as PS/PVP [4, 219], PAN/PVP [213], CA/PVP [220]. Pellegrin et al. [217] found the worst degradation of PES/PVP membranes at pH 8. With a comprehensive analysis protocol, they found it was related to the PVP chain scissions due to radical attack and being washed away from the membrane matrix. They didn't observe the PES chain scission but the evident PES oxidation was found within a thin layer from the surface (40 μm) in the presence of PVP or PVP degraded products. Thence, in their case, they concluded that the membrane integrity

loss was due to a radical induced PVP degradation. Prulho et al. [221] fundamentally studied the hypochlorite and radical effect on PVP, PES and PES/PVP blended films, separately. Their findings agreed well with the aforementioned results.

Prolonged exposure to NaClO have also been observed to cause alterations in PVDF membranes, leading to changes in structure, compromised filtration performances and weakened mechanical properties [181, 198], although PVDF membranes have been considered one of the most stable membranes amongst the other commercially available polymeric membranes [210].

Most membrane disintegration studies, sometimes referred to as ageing experiments, are conducted in the laboratory by soaking the membrane under static conditions at an elevated concentration of oxidants [4, 6, 7]. Although the experimental dosage (ppm $\times$ days) could be set comparable to on-site operation, the question is whether these accelerated lab-scale experiments can represent the real situation in the plants. Pellegrin et al. [217] studied the impact of hypochlorite concentration on membrane degradation while the eventual dosage was kept the same by varying the exposure duration. The results showed higher concentration obviously worsened the degradation. Therefore, accelerated ageing experiments using higher concentration and shorter exposure time may overestimate the real situation.

3.8 Conclusions

This chapter presented a comprehensive review of membrane cleaning in UF applications. The goals, methods, mechanisms and processes of membrane cleaning were discussed in great detail. The principal findings are listed as following:

- Membrane cleaning is a vital step in maintaining the permeability and selectivity of the membrane. It is also necessary to return the plant to its original capacity, to minimise bacteriological contamination and to produce acceptable products.

- There are as many types of cleaning regimes as there are fouling types and mechanism. Generally, the commercially popular means include groups of physical and chemical methods. Non-conventional methods, including ultrasonic and electrical cleaning, are alternative and innovative means under study.

- A cleaning process can include several steps, depending on the fouling situation. Common cleaning protocols adopted by various industries consist of a hydraulic

wash prior to and after chemical/biological cleaning. However, in order for optimisation, the detailed cleaning flow has to be specially designed for a particular job.

- Cleaning process parameters include choosing suitable cleaning agents and their concentration, order and duration of cleaning steps, system hydrodynamics and operation temperature.

- The methods of evaluation of cleaning efficiency are listed, especially, containing a number of modern characterisation techniques (mainly microscopic methods) which help gain more insights into the results, impacts and mechanisms of cleaning process.

- Membrane disintegration is revealed as membrane structure changes, embrittlement of membrane fibres and compromised filtration performance. The mechanism mostly studied is the polymeric chain scission occurring in membrane materials, owing to the attacks from the oxidants in the cleaning solution.

Chapter 4

Theoretical Developments of Combined Fouling Model

4.1 Introduction

The classical blocking laws dissect membrane fouling into four extreme but simple scenarios. However, in reality, the phenomena of membrane fouling is a far more complex, involving multiple mechanisms that may emerge in series or in parallel. The overall behaviour is dictated by a certain combination of these mechanisms.

The aim of this chapter is to develop suitable models for complex fouling processes. Here, we use a 'bottom-up' multiscale approach to the problem. Fouling dynamics are resolved first at an individual pore randomly chosen on a membrane and then statistically averaged over the whole membrane area.

To begin with, a description is given of the complex nature of the relevant fouling phenomena. Subsequently, the multiscale approach is used to form complex models from the classical blocking laws for, respectively, two fouling scenarios commonly encountered in UF of macromolecules.

4.2 Complex Membrane Fouling

Fouling, in many situations, consists of a set of physicochemical processes, occurring either consecutively or concurrently. The mechanisms responsible for each process cooperate in a certain way, dictating the overall behaviour of the fouling.

4.2.1 Consecutive Fouling Mechanisms

Multiple consecutive steps have been frequently observed on the flux-decline curve of a filtration process. The progression from one step to the other is manifested in the noticeable variation of the decline rate of the flux. This phenomenon is often considered to be the evidence of the evolution of a fouling process, where membrane fouling develops into different stages as filtration proceeds. These stages may be characterised by distinctive fouling mechanisms.

For UF of macromolecules, the common fouling stages involved are illustrated in Fig. 4.1. The first stage represents a rapid process of macromolecular adsorption

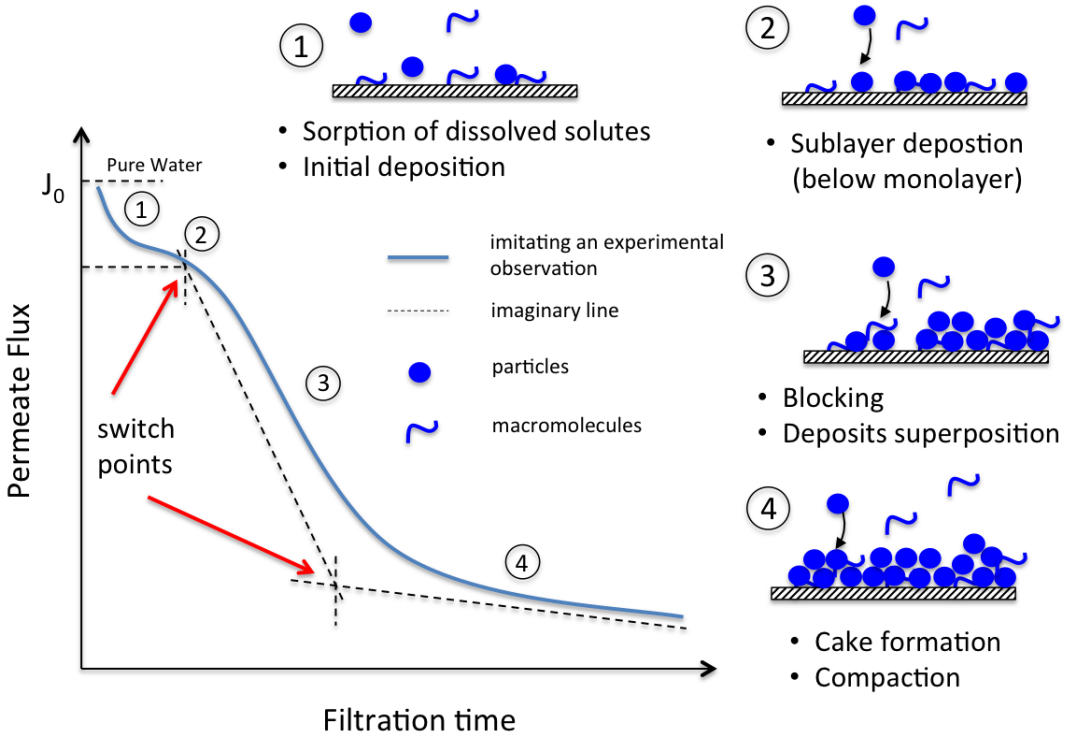

Figure 4.1: Schematic of concepts of multiple-stage fouling behaviour.

onto the exposed membrane surface. This causes a sharp decline in permeate flux. However, if the macromolecules are inert with the membrane material, adsorption will not happen; or when the molecules are larger than the pore size, size exclusion occurs [83]. After most of the binding sites are occupied, the first sublayers or the first few patches of foulants start to build up at some regions of the membrane surface (stage 2, Fig 4.1). The flux declines rather slowly in this stage but it will not last long since solutes continue to accumulate onto the surface, leading to the inevitable pore blocking. The blocking process (stage 3, Fig 4.1) usually takes place in an

exponential rate and dramatically reduces the passage for the solvent. This manifests a steep decline in the flux curve. Subsequently, patches of these sublayers grow together into multiple layers and cover the whole membrane surface, forming the fouling cakes. While the cake continues to grow thicker, the layers are compressed under TMP (stage 4, Fig 4.1). Eventually, the particles of the deposits are rearranged into a more densified state. This is usually a slow process and the decline of permeate flux will become more gradual. Flux tends to a pseudo-steady state. There are, of course, exceptional cases, but such a flux-decline pattern has been found in many studies [19, 81, 83, 88, 222, 223]. Belfort et al. [19] also considered a non-Newtonian viscous effect as a further stage taking place after cake compaction for filtration of mixtures of macromolecules and particles.

4.2.2 Concurrent Fouling Mechanisms

Every so often, more than one fouling mechanism may occur at the same time in a filtration stage [77], especially when the feed solution contains a mixture of foulants. For example, a mixture containing small and large fractions can cause simultaneous internal fouling and external deposition [224]. In such a case, even during cake filtration stage, pore blockage may still take place because small solutes may reach the membrane surface through the interstices of a coarse cake layer composed of large particles [225].

Based on the classical blocking models, Bolton et al. [85] and Duclos-Orsello et al. [88] have both derived a combined blocking model to account for the decrease of the unblocked membrane areas under the simultaneous standard (internal) and complete blocking;

$$\frac{\mathrm{d}A_{open}(t)}{\mathrm{d}t} = -\sigma C_b J_{open}(t) A_{open}(t) \tag{4.1}$$

where $J_{open}(t)$ is the superficial flux through the open pore areas, given by the standard blocking model:

$$J_{open}(t) = \frac{J_0}{(1+\beta C_b Q_0 t)^2} \tag{4.2}$$

where the coefficient β $[kg^{-1}]$ is equal to the part of k_s in Table 2.2 with C_b removed;

$$\beta = \frac{k_s}{C_b} = \frac{\phi}{A_0 \delta_m} \tag{4.3}$$

Hence, the area containing opening pores (i.e. the effective membrane surface) can

be explicitly expressed as the function of the filtration time:

$$\frac{A(t)}{A_0} = exp\left(-\frac{\sigma C_b J_0 t}{1+\beta C_b Q_0 t}\right) \quad . \tag{4.4}$$

In fact, the model of the classical intermediate blocking may be interpreted as a situation where complete pore blocking and cake formation simultaneously contribute to the apparent flux decline. As described in the classical model, the particles have an even probability to fall onto the open pores or onto the previously settled deposits. Therefore, the particles, which directly contact the pore entrance, contribute to the pore blockage mechanism; others, superimposing on the first sublayer, contribute to cake growth. This concept is shown in Fig. 4.2.

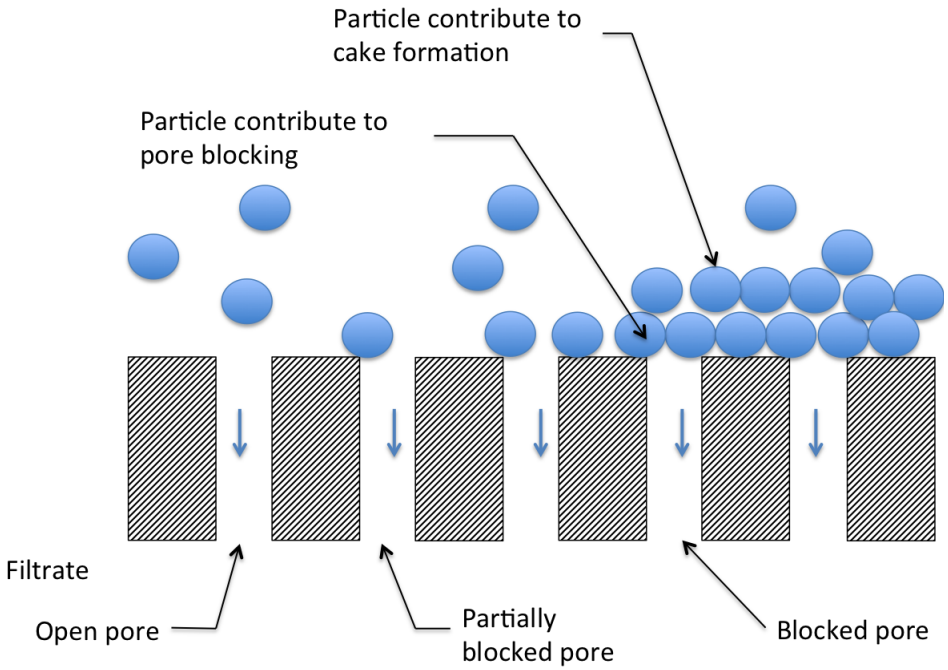

Figure 4.2: Schematic diagram for a case of simultaneous pore blocking and cake formation.

4.3 Fouling Dynamics at Pore Scale

The study of fouling at pore scale is to zoom into the local region of a single pore on a membrane to see how solutes or particles interact with the pore locally. Once the

fundamental mechanisms at pore scale are resolved, it is only a matter to upscale to the macroscale.

The pore size in a UF membrane typically ranges from 10 nm to 100 nm. In fluid systems, this range is within the mesoscale, where flow is still treated as continuum but solutes are commonly modelled as particles. By analysing all the forces acting on the particle, its trajectory and its deposition can be studied from the first principal. However, this method can rarely give analytical solutions, and often requires expensive computing to produce simulation results.

On the contrary, the classical phenomenological blocking laws are computationally simple and easy to implement in the pressure-driven filtration. Although these classical models were derived semi-empirically for the phenomena observable at the macroscale, their derivation [30] was deeply established in the analysis of the mass transport at about the pore scale. The assumption of uniform pore arrays in the membrane serves key for simplification in the classical theory. By the assumption, the classical models essentially represent the average behaviour of the many pores constituting the membrane and the parameters used are statistically averaged over the whole membrane area.Thus, the following context shows the development of a dynamic model based on the classical blocking theory to predict the permeability of an individual pore being randomly chosen.

Under classic blocking theories, fouling either causes membrane to lose the effective pore areas via either pore blockage or pore constriction, or adds extra resistance to the membrane by forming cake layers on the upstream surface of the membrane.

The ratio of the particle size to that of the pore determines where the particle will be captured by the pore, either outside or in the pore channel. When the size of the particles are much smaller than the pore diameter, pore constriction (internal fouling) takes place if the surface of the pore channel is attractive to the particles. With the assumption of straight channel in which Hagen-Poiseuille flow can develop, the normalised permeability[1] of the pore has an expression following the standard blocking model in Table 2.2 as

$$p_n(t) = \frac{1}{(1 + \beta C_b Q_0 t)^2} \ , \tag{4.5}$$

where βC_b equals to the constant k_s as described in eqn 4.3. Pore constriction causes the relative permeability a gradual decline along the filtration time.

[1] The permeability of a medium is the inverse of its resistance; the normalised permeability is the temporal permeability normalised by its initial value.

Unlike the pore constriction, the pore blocking has a sudden effect on the local permeability of a single pore. Pore blocking happens when the size of the particles are comparable to the pore diameter. It seals the pore gateway completely or partially. In the macroscopic model, the effect of pore blockage is reflected by an increase in the average membrane resistance, which can be attributed to $\langle R_b \rangle$ (note that bracket $\langle ... \rangle$ means average), and the closure of pore entrance contributes to the loss of the membrane porosity. While $\langle R_b \rangle$ is the mean value averaged over all the pores on the membrane, for each pore, there is a local resistance, denoted by R_b, representing the local effect of pore blocking on a single pore. If it is completely blocked, R_b tends to infinity. However, due to the imperfect shape of both the particles and the pore in many practical cases or due to the porous body of the blockage material, for instance, in the case of many naturally coiled polymers [226], R_b is likely to be a finite number, which resembles a pore being partially blocked. Hence, blocked pores exclude large particles to enter pore channel but still allow water or small solutes to pass through the interstices between the pore surface and the plugging particles.

Another fouling mode in the single-pore dynamics is the accumulation of solutes above the pore entrance. Though it usually happens for particles with size apparently larger than the pore's to form gel or cake layers above the membrane upstream surface [227], smaller particles ($d_s < d_p$) can also build up on the pore entrance according to computational studies on MF [228], in which particles deposit on the edge of the pores first and then bridge across the pore through certain interactions such as electrostatic forces when further particles from the bulk continuously deposit onto each other [229]. Cake formation above a single pore contributes to an additional resistance, R_c, locally, while the effect of the cake on the entire membrane is expressed as the overall cake resistance which is an average value over the whole surface area, denoted by $\langle R_c \rangle$. Note that the relationship between the resistances at pore scale and that at macroscale is far more complex in reality due to factors such as inter-particle interactions. Assuming Darcy's law is applicable to the pore under study, the local total resistance $R_t(t)$ is simply derived from the governing equation for cake filtration in Table 2.2 by assuming the rate of increase in total resistance is proportional to the instant flux through the area:

$$\frac{\mathrm{d}R}{\mathrm{d}t} = \alpha C_b J(t) \ . \tag{4.6}$$

Integrating the equation above with Darcy's law, one can obtain:

$$R_t(t) = R_t(t_0) + R_c(t) = R_t(t_0)\sqrt{1 + \frac{2\alpha C_b \Delta P}{\mu R_t(t_0)^2}(t - t_0)}\ . \tag{4.7}$$

where R_t is the total local resistance and $R_t(t_0)$ is the local resistance at t_0 when cake formation starts. The normalised permeability of the pore can be obtained from

$$p_n(t) = \frac{R_m}{R_t(t)} \tag{4.8}$$

and it gives by combining eqn 4.7 and 4.8;

$$p_n(t) = \frac{R_m}{\sqrt{R_t(t_0)^2 + \frac{2\alpha C_b \Delta P}{\mu}(t - t_0)}}\ . \tag{4.9}$$

With the three basic pore-level fouling modes mentioned above, it is possible to construct models for complex particle-capturing dynamics at pore scale.

4.3.1 Model A: Sequential Pore Blocking and Cake Filtration

This model is developed for constant pressure filtration. In its scenario, the solutes are inert and have sizes comparable to the pore diameter so that the pore constriction is unlikely to happen. Initially, the solvent flows freely through the pore channel until an oncoming particle of the solute blocks the pore at time τ, which abruptly increases the overall local resistance by an additional R_b. The value of R_b is assumed to be finite given that the pore blockage is likely to be incomplete as described previously. As a result, the solvent flow continues at a reduced rate, so that solutes from the bulk phase can further deposit onto the blocked areas and gradually build up a fouling layer above the entrance, exerting an additional resistance $\langle R_c \rangle$ on the flow.

Since the cake filtration only takes place after the pore is plugged, its growth can only start after the blocking time τ. Therefore, τ is the value of the initial time for cake formation, t_0, in eqn 4.7, i.e., the cake growth being delayed by an amount of τ from the initial filtration time. Meanwhile, the total pore resistance at the onset of cake formation ($t = \tau$) includes the resistance due to pore plugging (R_b) in addition to the intrinsic resistance (R_m) and can be represented in a resistance-in-series fashion

[9], i.e.,

$$R_t(t_0) = R_t(\tau) = R_m + R_b \, . \tag{4.10}$$

Combining all the mechanisms in a sequence, the normalised permeability can be generalised as a single expression in terms of the filtration time, t, as

$$p_n(t, \tau) = p_{n1}(t)H(\tau - t) + p_{n2}(t - \tau)H(t - \tau) \tag{4.11}$$

in which $H(x)$ is the Heaviside function defined as:

$$H(x) = \begin{cases} 1 & \text{if } x \geq 0 \, , \\ 0 & \text{if } x < 0 \, . \end{cases} \tag{4.12}$$

The blocking time τ accounts for the transitional moment from one mechanism to the other. Function p_{n1} acts during filtration before the blocking, when $t \in [0, \tau)$; while function p_{n2} commences after pore blocking, when $t \in [\tau, \infty)$. In this present scenario, $p_{n1} = 1$ is the normalised permeability of a clean pore channel before a particle blocks the pore, while p_{n2} is a decay function of the permeability due to cake formation, given by eqn 4.9. Applying their expressions to eqn 4.11, one can obtain the specific expression for the normalised permeability of model A as a function of t:

$$p_n(t) = H(\tau - t) + \frac{R_m}{\sqrt{(R_m + R_b)^2 + \frac{2\alpha C_b \Delta P}{\mu}(t - \tau)}} H(t - \tau) \quad . \tag{4.13}$$

which is a two-steps curve on a $p - t$ plot shown as p_A in Fig. 4.3.

4.3.2 Model B: Sequential Pore Constriction, Blocking and Cake Filtration

In model B, the solutes in the feeds are assumed to have a wide size distribution, containing not only big colloids, which can block the pores like in the scenario of model A, but also a portion of small macromolecules which can cause pore constriction. Therefore, before the pore is blocked by any large particle, small macromolecules can enter the pore channel to cause internal fouling. Such a fouling scenario has been

observed during filtration of protein solutions, where small protein monomers coexist with large protein aggregates [88, 230].

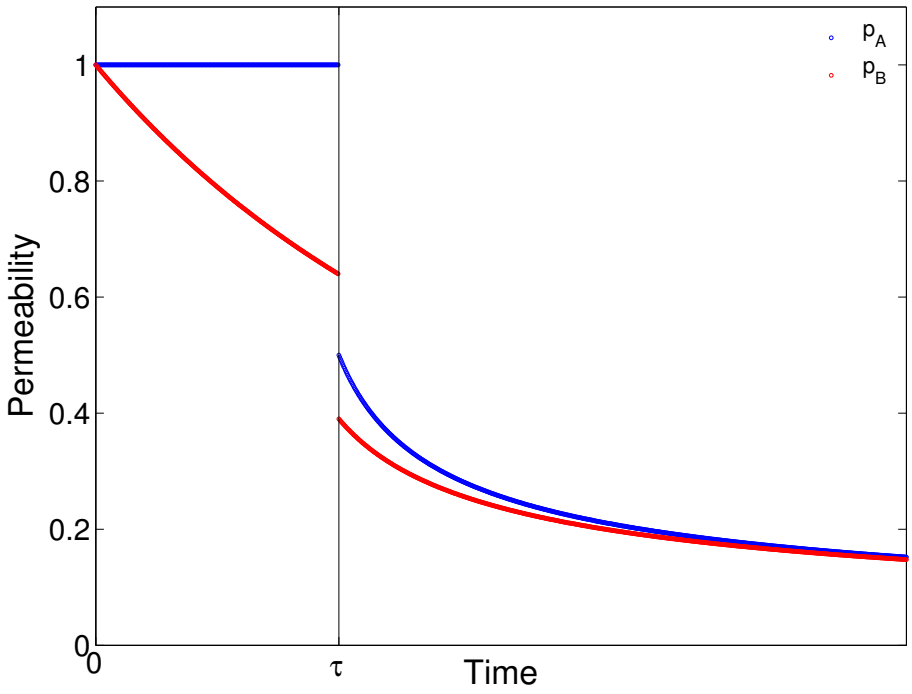

Figure 4.3: Schematic of the local normalised permeability function in a single pore for model A (p_A, eqn 4.13) and model B (p_B, eqn 4.15), respectively. The time τ is the 'switch' time when the pore becomes partially blocked. Model A refers to the sequential pore blocking and cake filtration model and model B to the sequential internal and external fouling.

By using similar assumptions to those in Model A, one can readily derive the dynamics in an individual pore with for model B. The expression of p_{n1} in eqn 4.11 adopts the form of eqn 4.5 for pore constriction model; while p_{n2} still uses eqn 4.10 but $R_t(\tau)$ is modified as

$$R_t(\tau) = R_m(1 + \beta C_b Q_0 \tau)^2 + R_b \tag{4.14}$$

which means that the initial resistance for cake formation at the transitional moment, when cake filtration just starts, includes not only the clean membrane resistance but also the effects of pore constriction (the factor $(1 + \beta C_b Q_0 \tau)^2$) and pore blocking ($R_b$). Thus, the relative permeability is again given as a function of filtration time

with specific components relative to model B:

$$p_n(t) = \frac{1}{(1+\beta C_b Q_0 t)^2} H(\tau - t) + \frac{R_m}{\sqrt{[R_m(1+\beta C_b Q_0 \tau)^2 + R_b]^2 + \frac{2\alpha C_b \Delta P}{\mu}(t-\tau)}} H(t-\tau) \tag{4.15}$$

which is shown as p_B in Fig. 4.3.

4.4 Probability of Switch Time

In the last section, the dynamics of fouling in a single pore has been modelled with multiple mechanisms combined in sequence. In this section, the linkage from a single pore to the whole membrane is built to develop macro-scale combined models for predicting the observable flux decline behaviour during the filtration.

The general form of fouling dynamics at pore level (eqn 4.11) is applicable to all pores in the membrane. In the equation, the switch time τ, at which the cause of fouling transitions from one mechanism to the other, is a random variable. It varies between pores at different location. Under the assumption that membrane consists of an array of independent pores, the overall permeability of a membrane is essentially an average over all the pores within it.

In both model A and B, the cause of the switch is pore blocking. In classical blocking laws, Therefore, the distribution function of τ is related to

The cause of switch is due to pore blockage. Moreover, the governing equations for classical complete and intermediate blocking laws (see Table 2.2) give the decay function of the effective pore areas. This means the total number of the blocked pores is a function of the blocking time if still holding the approximation of membrane structures to an array of microfluidic channels. Since the classical intermediate blocking model is considered as a special case of combining complete blocking and cake formation mechanisms, the derivation below has only used the complete case.

For model A, the total number of blocked pores at time τ is obtained in percentage over the total pore numbers , using the classical complete blocking model, as

$$F = 1 - exp(-k_b \tau) \tag{4.16}$$

where $\tau \in [0, \infty)$ and

$$k_b = \sigma C_b J_0 \ . \tag{4.17}$$

For a single pore, F is the probability that pore blockage happens at time τ. Then, eqn 4.16 represents the cumulative distribution function of the random variable τ that stands for the switch time at which a pore enduring a transition from one fouling mode to the other.

The distribution density function of τ, denoted by $f(\tau)$, is, hence,

$$f(\tau) = \frac{dF(\tau)}{d\tau} = k_b exp(-k_b \tau) \tag{4.18}$$

which stands for the number of pores being blocked at a particular point of τ. The two probability functions for model A are portrayed in Fig. 4.4.

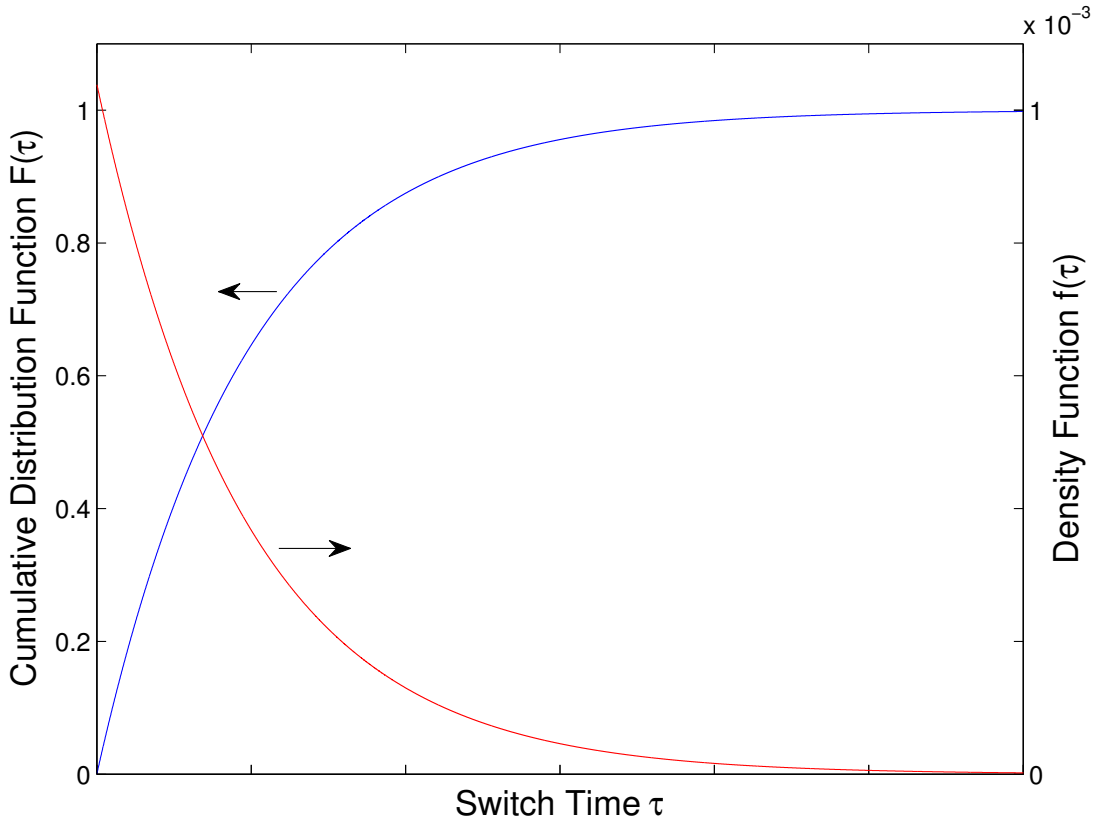

Figure 4.4: Schematic of the cumulative (eqn 4.16) and (eqn 4.18) density distribution functions of switch time τ.

For model B, which is the sequential standard, complete and cake blocking, the cumulative distribution function of τ takes the form from eqn 4.4:

$$F = 1 - exp\left(-\frac{\sigma C_b J_0 \tau}{1 + \beta C_b Q_0 \tau}\right) , \tag{4.19}$$

since the pore blocking rate will be affected by the internal fouling as discussed in the concurrent fouling models (see section 4.2.2). And the density function hence is

$$f = \frac{\sigma C_b J_0}{(1 + \beta C_b Q_0 \tau)^2} exp\left(-\frac{\sigma C_b J_0 \tau}{1 + \beta C_b Q_0 \tau}\right) . \tag{4.20}$$

4.5 Consecutive Models of Multiple Blocking Mechanisms

With the mechanisms-switching model for an 'averaged' individual pore and the switch time distribution density function obtained, the sequentially combined 'microscale' models are to be correlated to macroscale, i.e., application from a single pore to the whole membrane, in this section.

The procedure is to add up the contributions from all the pores to calculate the total flow rate through the whole membrane relative to the filtration time, t. As the assumption of uniform pores is kept valid here, the difference between fouling in different pores is due to the variety of τ. Since the distribution function for τ was obtained in eqn 4.18, the overall flow rate $Q_n(t)$ (normalised by the initial flow rate Q_0) can be calculated from the mean permeability, p, at a particular filtration time, i.e.

$$Q_n(t) = \int_0^\infty p(t, \tau) f(\tau) \, \mathrm{d}\tau \tag{4.21}$$

where $p(t, \tau)$ and $f(\tau)$ are eqn 4.11 and 4.18 respectively. The integration in the above equation accounts for the temporal heterogeneity of the switching time from p_{n1} to p_{n2} in eqn 4.11 and the resultant Q_n is an average over all the possible τ.

Using eqn 4.13, 4.18, and 4.21 , we can derive the macroscale equation for model

A scenario,

$$Q_n(t) = exp(-\sigma C_b J_0 t) + \int_0^t \frac{\sigma C_b J_0 R_m}{(R_m + R_b)\sqrt{1 + \frac{2\alpha C_b \Delta P}{\mu(R_m+R_b)^2}(t-\tau)}} exp(-\sigma C_b J_0 \tau)\, \mathrm{d}\tau \ . \tag{4.22}$$

where the first part accounts for the flow through the open-pore area while the latter for that through the blocked area. This expression agrees with the model, for the same scenario, derived by Ho and Zydney [83] using purely phenomenological arguments.

For model B, using eqn 4.15, 4.18 and 4.21 it derives

$$\begin{aligned} Q_n(t) = & \frac{1}{(1+\beta C_b Q_0 t)^2} exp(-\frac{\sigma J_0 t}{1+\beta C_b Q_0 t}) \\ & + \int_0^t \frac{R_m \frac{\sigma C_b J_0}{(1+\beta C_b Q_0 \tau)^2} exp\left(-\frac{\sigma C_b J_0 \tau}{1+\beta C_b Q_0 \tau}\right)}{(1+\beta C_b Q_0 t)^2 \sqrt{[R_m(1+\beta C_b Q_0 t)^2 + R_b]^2 + 2\frac{\alpha C_b \Delta P}{\mu}(t-\tau)}}\, \mathrm{d}\tau \ . \end{aligned} \tag{4.23}$$

Compared to the model A, this one has an extra parameter, k_s, to determine. It's a model containing three sequential fouling mechanisms and four parameters and equal to the one derived by Duclos-Orsello et al. [88].

4.6 Conclusions

A multiscale approach to complex fouling scenarios has been postulated and demonstrated with examples in this chapter. In this approach, the membrane is idealised to contain only independent pores. The fouling dynamics are resolved first at a single pore with average properties. The resultant microscopic (strictly the pore scale is at the mesoscale) model is then statistically summarised over the whole membrane to derive the macroscopic model to be comparable to experimental observations. The generalised framework is flexible to incorporate different mechanisms.

The application of the approach has been demonstrated in two proposed complex scenarios, which are later used to represent for the macromolecular fouling experiments in the following chapters. In these two scenarios, the microscopic fouling models consist of multiple steps and a switch time is given for changing the mechanisms. The switch time is a random variable and has a probability distribution function over different pores, dictating how many pores are blocked at a particular time. The informations then lead to the derivation of the macroscopic models. The

detailed derivation involves combining the relevant classical blocking models. Benefiting from the simplicity of those models, the final expressions for the two scenarios are easy to implement computationally.

Compared to conventional approaches which incorporate multiple mechanisms, the multiscale approach proposed here is a more general scheme. The generalised equation 4.11 can be adapted to wider fouling scenarios. The multiscale scheme has also a more sound physical meaning, which can produce more accurate solution.

Chapter 5

Investigation of Dilute Macromolecular Fouling in UF

5.1 Introduction

The main purpose of this chapter is to understand the general fouling behaviour during UF of dilute macromolecular solutions via the theory developed in Chapter 4. The conducted work involves mainly obtaining the primary data from bench-scale UF experiments with three different macromolecular feeds, verifying the applicability of the combined models to the measured data, and evaluating the fouling mechanisms behind. Two series of experiments were designed to study the different fouling behaviours under various bulk concentration and under different TMPs. The flux-volume-time data were obtained and further analysed with the fouling models. The fouling mechanisms were evaluated using two methods, i.e., integral and differential, over the filtration time.

5.1.1 Chapter Outline

The rest of the chapter starts with the section introducing the materials and methodology used in the present work, and outlining the filtration protocol and the model numerical scheme. The following section presents the results from both experiments and numerical stimulations. Two sets of the results on the study of bulk concentration and TMP are included in Section 5.3.3 and 5.3.4 for each macromolecular feed,

respectively. The models have been fit to the experimental results and are presented along with them. The resultant model parameters are discussed in Section 5.3.4.2. There are also some non-trivial parts from the experiments reported here, including the determined size distribution of the humic acid, one of the three macromolecules under study (Section 5.3.1); and the verification of an invariant bulk concentration under the experimental condition (Section 5.3.2). Subsequently, the evolution of the fouling mechanisms and its evaluation methods are presented in Section 5.3.5. At last, a summary concludes the findings in this chapter.

5.2 Materials and Methods

Three model feeds, representing two common types of macromolecules encountered in water treatment, i.e., polymeric and humic substances, are used in a dead-end filtration protocol. Two polymers, blue dextran and polyethylene oxide, were used to model sequential pore blocking and cake filtration, while commercial humic acids with a wide distribution of molecular weight were tested to perform the sequential pore constriction, blocking and cake filtration model.

5.2.1 Macromolecular Samples

The chosen polymers are dextran blue (DB) (MW = 2000 kDa, Blue Dextran 2000, GE Healthcare), a neutral polysaccharide, and polyethylene oxide (PEO) (MW = 100 kDa, Sigma-Aldrich). They are both linear flexible macromolecules, being neutral, stable and water soluble, not interacting with most of the material of UF membranes. Both of the polymeric samples were dissolved in filtered deionised (DI) water (MilliQ, Millipore) and continuously stirred for 24 hours at room temperature (22 °C) before the solution pH was adjusted to the range between 7.0 and 7.5 by doping small amounts of 0.1 M HCl or NaOH solution, to make the 1.0 g/L stock solutions. Commercial humic acids (HA) (Sigma-Aldrich) were used as model surrogates of humic substances. Pre-weighed HA powder was dissolved in DI water (1 g/L) with the aid of an increasing pH (to about 8 - 9) and constant stirring for 24 hours. The pH values were measured using an Jenway 3345 ion meter (Bibby Scientific, UK). All stock solutions were stored at 4 °C in the dark. The properties of materials were summarised in Table 5.1.

Prior to filtration experiments, stock solutions were directly diluted with DI water to prepare the working solution at the designated concentrations and the working solutions were left in the environment for enough time to reach the working temperature. The pH of the working solution was checked and kept at 7.25 ± 0.25. Except for the HA stock, it was pre-filtered through 0.22 μm filter (PVDF, Millipore) to remove non-dissolvable large particular debris before making any trial samples. The pre-filtration of 1 L raw HA solution was conducted under TMPs between 30 and 50 kPa in a stirred cell (Model 8200, 63.5 mm diameter, Millipore) at a stirring speed of 275 rpm. After the filtration, the filter that contained rejected portions from the HA raw stock, was carefully removed from the filtration rig, and dried at 105 °C for 3 hours in a furnace and cooled in a desiccator. After it has been dried, the fouled filter was weighed on an analytical balance (repeatability $<= \pm 0.1mg$, Model ED224S, Sartorius), from which the weight of the fresh filter, predetermined before filtration, was then taken out to derive the net weight of the rejected portion of the HA raw stock. Based on this, a $200mg/L$ prefiltered HA stock solution was made from the collected filtrate and pH was adjusted to $7.0 - 7.5$.

The concentration of DB was determined using UV/Vis spectroscope (UV1800, Shimadzu, Japan) at 620 nm wavelength, while that of PEO was evaluated by the total organic carbon (TOC) analyser (TOC-VCPH, Shimadzu, Japan) using the purgeable organic carbon (NPOC) method. The TOC analyser was calibrated externally with the solution of potassium hydrogen phthalate. The concentration of HA solutions was determined spectroscopically at 254 nm wavelength and correlated with TOC measurement.

The apparent molecular weight distribution of the HA samples was measured using a membrane fractionation method originally developed by Aiken [231]. 50.0 mg HA powders were dissolved in 1 L DI water for 24 hours and 50 ml of the sample solution was then sequentially filtered by 0.22 μm PVDF microfilter, followed by PES 300 kDa (Millipore) and RC 100, 50, 30 and 10 kDa ultrafilters (Ultracel YM, Millipore). The filtration was performed in a stirred cell (Model 8050, capacity 50 ml, Millipore) at dead-end mode under 50 kPa for the micro-filter, 100 kPa for the 300 kDa membrane and 200 kPa for all the other UF membranes, respectively. A stirring speed of 275 rpm was employed for all the filtration in the fractionation process. The fractional amount within each MWCO range was calculated from the difference in the UV absorbance between adjacent HA filtrate samples.

Table 5.1: Summary of materials used in the constant pressure UF experiments

Model material	Dextran Blue	Polyethylene Oxide	Humic Acids
Source	GE Healthcare	Sigma	Aldrich
Molecular Weight (kDa)	2000	100	<100 (ca. 70%)
Membrane	RC, 100 kDa, hydrophilic, Millipore		
Solution condition	pH 7.25 ± 0.25, 22 °C		
Concentration measuring	TOC	UV 623nm	UV 254 nm, TOC

5.2.2 Filtration Setup and Protocol

All filtration experiments were conducted in a stirred cell (Amicon 8050, 43 mm diameter, 50 ml capacity, Millipore) with an effective membrane area of 13.4 cm^2. The feed solution was stored in a metallic pressure vessel (5 L max. capacity, Millipore) that was connected to the cell unit.

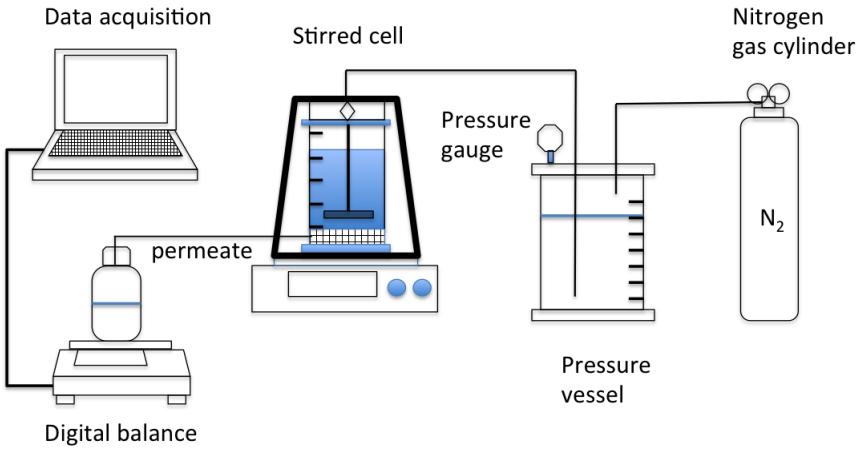

Figure 5.1: Set-up of constant-pressure ultrafiltration

The UF unit was operated in the dead-end mode at a constant TMP, supplied and controlled by a nitrogen gas cylinder, without stirring for all experimental trials. The avoidance of stirring in the cell is to minimise re-lifting of macromolecular deposits from the membrane to the bulk phase by eliminating any removal forces at the membrane surface, since the models to be verified assume that deposits will not be released from the membrane. However, without stirring, the complete or partial blocking process is promoted while pore constriction is reduced since large particles will block the pores more easily. On the contrary, stirring can create shear forces on

the surface to remove large particles so that small particles will have more chances to enter the pores.

TMPs were monitored using a pressure gauge. Permeate weight was monitored continuously over the course of filtration and recorded in a known time interval via a digital balance (Model FX-2000i, capacity 2200 g, readability 0.01 g, AND, Japan) with a data-acquisition software (WinCT, AND, Japan) onto a computer (see Fig. 5.1). The experimental trials were all conducted at $22 \pm 1\,^{\circ}\mathrm{C}$ in a temperature controlled room.

The membranes used are made of composite regenerate cellulose (RC) with a MWCO of 100 kDa (Ultracel YM, Millipore). This RC membrane is chosen for its relatively low macromolecular binding and uniform structure, which serves better for verification of the models proposed in Chapter 4, in spite of the fact that PES and PVDF membranes are currently dominating the UF market. For each filtration trial, fresh membranes were used. The new membranes were rinsed several times and soaked in DI water overnight to remove the wetting agent before conducting filtration experiments.

A typical UF protocol [84, 232] shown in the schematic of Fig. 5.2 was employed to study the change of flux over the time as well as test the fouling reversibility for different macromolecular feeds. At the beginning of each trial, fresh membrane was first filtered with DI water at TMP of 200 kPa to allow membrane to be compacted for about 2 hrs till the permeate flux became stable. Then, DI water filtration was conducted sequentially at TMPs of 200, 150, 100 and 50 kPa respectively. The temporal permeate flow was then calculated from the permeate weight measured every $10s$ and the average flow rate over 30 min filtration under each TMP was used to deduce, by linear regression, the hydraulic resistance of the clean membrane (R_m).

Afterwards, the feed solution in the pressure vessel was switched to macromolecular samples while the stirred cell was still filled with DI water. Resuming the hydraulic pressure to the working TMP and keeping it constant, macromolecular UF started. The permeate weight was again measured at the time interval of $10s$ and the macromolecular concentration in the permeate were examined at certain filtration time. Most of the macromolecular filtration experiments were conducted for up to 4 hrs unless the accumulated permeate weight was over the capacity of the balance.

After the filtration of sample feeds, the cell and vessel were emptied and refilled with DI water and repressurised to the same working TMP to conduct water filtration for evaluating the hydraulic resistance of a fouled membrane. The fouled membrane

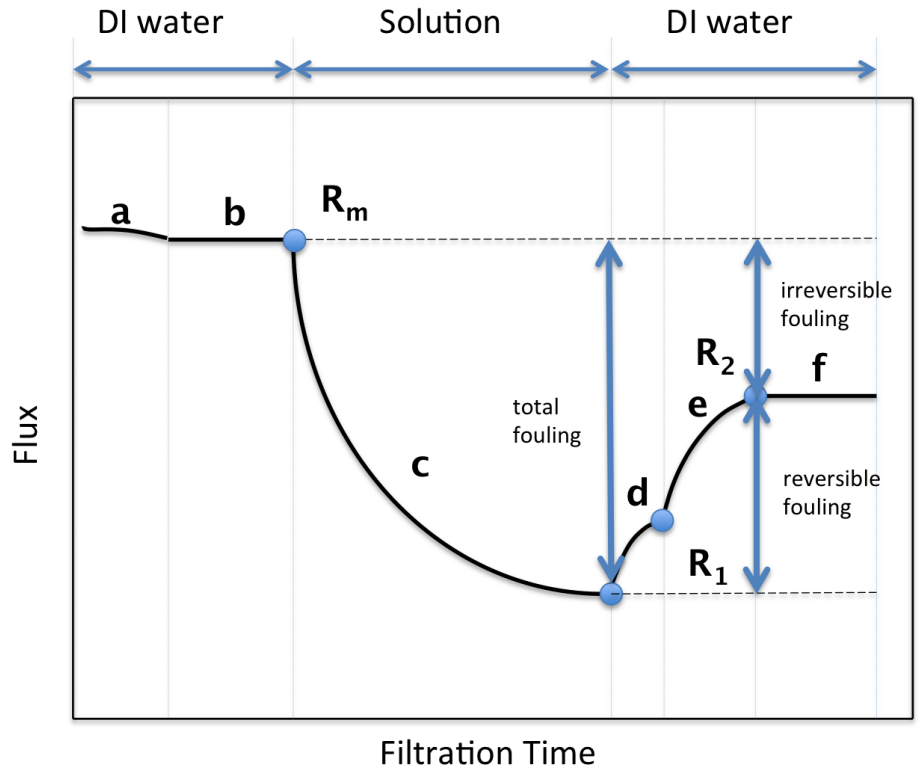

Figure 5.2: Filtration protocol: (a) compaction; (b) stable DI water permeability test; (c) model feed filtration; (d) repressurising with DI water; (e) DI water backwashing; (f) water permeability test

was then taken out of the cell, rinsed with DI water and placed back to the cell in a reverse orientation on a glass microfibres paper (as a supporting layer protecting the membrane's thin film from scratching). Backwashing at 250 kPa took place to physically clean the membrane for a time sufficient to pass 1 L DI water and the permeate concentration at the end was checked to make sure that a thorough cleaning had been done. Then, the membrane was reoriented to its original position and the hydraulic resistance to DI water permeation was again measured at the working TMP.

5.2.3 Bulk Concentration Measurement

In order to examine whether the bulk concentration changes during filtration under the protocol used in this thesis, parallel filtration experiments were conducted for taking the sample from the bulk at real time. A house-made stirred cell (25 mm diameter, 16.5 ml capacity) with an extra outlet at the retentate side [233] replaced the Millipore 8050 cell in the process train. Except this, all other experimental conditions and protocols were kept same to replicate the situation in the experiments discussed in section 5.2.2. During UF of macromolecular feeds, the point when the TMP reached the designated value was counted as the start of filtration and 5 ml retentate each time was collected from the middle height of the cell to a TOC vial at certain volume intervals and the concentration was measured externally in either spectrophotometer or TOC machine, depending on the feed type.

5.2.4 Model Numerical Scheme

The expressions of the complex fouling model took two forms depending on whether or not there is pore constriction. The prediction of the permeate flux as a function of filtration time is given by eqn 4.22 for Model A and by eqn 4.23 for Model B. Both the equations involve a convolutional integration. In general, analytical solutions are not available. Therefore, a numerical scheme of Euler integration was employed to solve the equations; while the model coefficients were determined using the least square curve fitting method by minimising the sum of the squared residuals between the selected set of experimental flux-time data and the model calculations. For efficiency, the time step in most cases was set at 1.0 s.

5.3 Results and Discussion

5.3.1 Molecular Size Distribution of HA

The goal of molecular size evaluation by the filtration fractionation method [231] was to characterise the size of sample HA relative to the pore sizes of the membranes used rather than to yield the absolute measures of the molecular weight. This technique has been frequently used to evaluate the size distribution of NOM [68, 84]. A 50 ml unfiltered HA sample of 50 mg/L was filtered through a series of MF and UF membranes in an order of descending pore sizes. The volume of each filtrate and its concentration of HA were measured to evaluate the differences in the fraction of HA passing successive membranes. This yielded a discrete size distribution of the HA sample shown in Fig. 5.3.

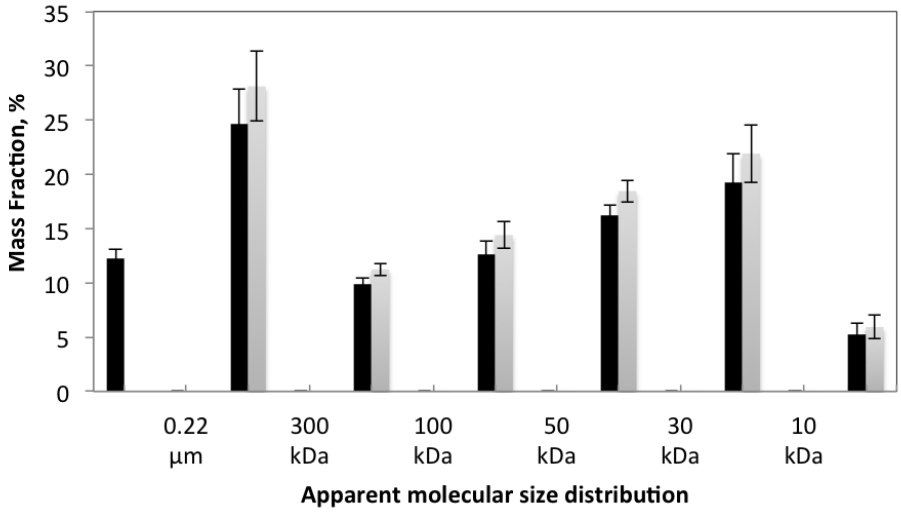

Figure 5.3: Apparent molecular weight distribution for commercial humic acids samples (Sigma-Aldrich) against various MWCO. Each bar represents the fraction of HA retained by the membrane to its right with smaller MWCO but passing the membrane to its left with larger MWCO. Black filled bars represent the fractional distribution calculated from HA rejection by the whole series of membranes and the grey filled bars represent the distribution calculated after removing the fraction rejected by the 0.22 μm Isopore filter. The error bars represent the standard deviation over three trials.

About 13% of the weight of the original HA sample was rejected by the 0.22 μm filter. On the other hand, approximately 87% HA passing the MF membrane made up of the prefiltered HA samples that would be used in the flux decline experiments. For convenience, the molecular weight distribution was also calculated after taking

out the fraction rejected by the microfilter, represented by the grey bars in Fig. 5.3. Therefore, more than 60% weight of HA in a prefiltered feed could pass the 100 kDa UF membrane, of which the MW mainly lay between 50 and 10 kDa (approx. 40% of the total weight), while 27% of the HA mass in the prefiltered feed would be rejected by 300 kDa membrane.

5.3.2 Bulk Concentration during Filtration

Bulk concentration is assumed constant during filtration courses in the consecutive fouling model, type A (eqn 4.22) and B (eqn 4.23), developed in Chapter 4. Therefore,

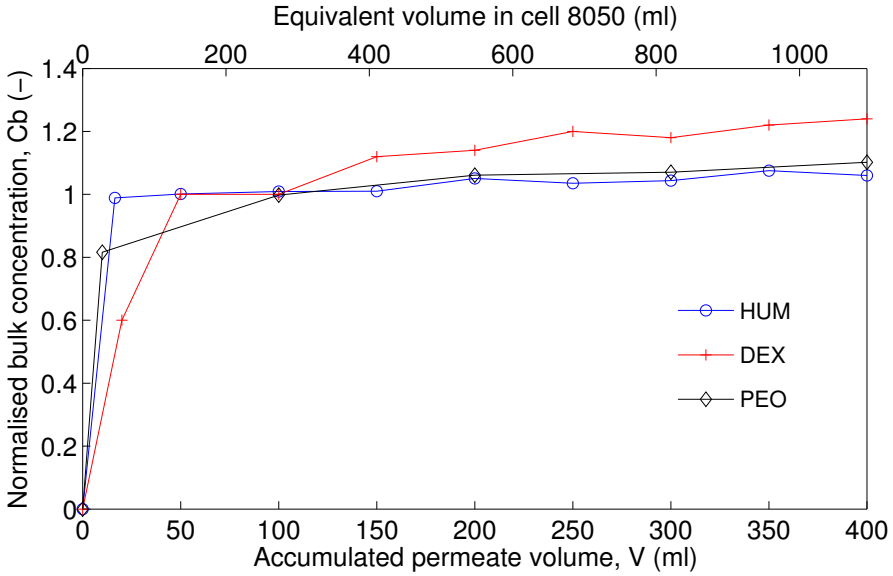

Figure 5.4: Bulk concentration in the house-made filtration cell during UF trials with three different feed types (HUM - humic acid; DEX - dextran blue; PEO - polyethylene oxide), as a function of the accumulated permeate volume. The three individual experiments were kept at same conditions (100 kPa TMP, 50 mg/L feed solution, 100 kDa RC membrane and no-stirring). The bottom x-axis is the permeate volume through the current cell (4.9 cm^2 membrane area) while the top x-axis is the equivalent permeate volume corresponding to the Millipore 8050 cell (13.4 cm^2 membrane area) by assuming the permeate volume per unit membrane area is same in the two cells. Bulk concentration was sampled at the middle height of the retentate side of the cell and normalised by the feed solution concentration.

stirring was omitted in the filtration cell during our experiments in order to hold this assumption, since this should prevent creating any mechanical forces above the membrane upstream surface, which might release particles from the deposits. Although

deposited macromolecules may still return to the bulk phase via diffusion, this is not likely to happen under high TMPs such as those involved in the experiments here ranging from 50 to 200 kPa, given that the osmotic pressure of the macromolecules is much less to be considered. For the size of the membrane pore and the macromolecules, used in the current experiments, the dead-end filtration is assumed.

Before the main set of fouling experiments started, the assumption of constant bulk concentration under our UF protocol was evaluated in a specially designed filtration cell [233], which has a capacity of 16.5 ml. The measurement of the bulk concentration during selected UF experiments, covering all three feeds, is shown in Fig. 5.4. After the DI water in the cell passed through the membrane within the first 20 ml permeate, the bulk concentrations in the cell rose to the value of the feed solution in the external vessel. Afterwards, the concentrations were kept relatively stable for all three cases during a considerably long filtration course, where 400 ml (i.e., equivalent to over 1000 ml in Amicon 8050 cell with 50 ml capacity) solution was filtered.

The bulk concentration during UF of DB solution had a slight increase from 50 mg/L to approximately 60 mg/L at the end of filtration, while changes in the other two cases were even less noticeable. The relatively small variation in the bulk concentration over a long filtration time was also observed by Sarkar [223] in their dead-end UF experiment of polysaccharides (pectin), where the feed concentration was 3 g/L and stirring speed was set at zero. Therefore, the evaluation results should verify the assumption that a constant bulk concentration held during filtration under the experimental protocol used in this work. The value for the feed concentration can be taken as the constant value for the bulk concentration during a filtration.

5.3.3 Effect of Bulk Concentration on Fouling

The effect of bulk concentrations of macromolecules on fouling was studied during UF of sample solutions containing a single type of macromolecules. Meanwhile, the consecutive fouling models were applied to compare with experiments and the model parameters were determined for the three feed types respectively.

UF experiments were conducted in a filtration cell with a 50 ml capacity (Amicon 8050, Millipore)to evaluate the effect of bulk concentration on the behaviour of flux decline for the three types of feeds, respectively. All UF trials carried out under this investigation shared some common conditions, i.e., single type of membrane (RC 100 kDa) and one fixed TMP (100 kPa), except for varying the bulk concentration. The subject of this study requires the macromolecular solution to be dilute to avoid

polymeric entanglement or aggregation of humic acids, and to allow a macromolecule to be treated as a single particle. Therefore, the upper limit of the feed concentration was set at 500 mg/L for DB and PEO solutions and 200 mg/L for HA. For each condition, the filtration experiments were conducted in duplicates.

The resistance of a fresh membrane was determined first for each trial. The mean value of the intrinsic membrane resistance for the batch of the RC 100 kDa membrane based on 48 samples was calculated to be $8.24 \pm 0.49 \times 10^{11}\ m^{-1}$. The steady-state pure water flux under 100 kPa TMP was also determined in the meantime. Due to the inherent membrane variability, the pure water fluxes for different trials varied, but, within a relatively small range.

After the water flux was determined, the external reservoir was switched to a fresh macromolecular working solution. In order to avoid any pre-deposition or adsorption, the filtration cell would be left filled with DI water.

During UF of macromolecular feeds, the accumulated permeate weight was recorded every 10 s to constitute the raw volume-time data set. Then, the permeate flux was derived numerically using a Savitzky-Golay filter [234] to take the derivative of a series of piecewise cubic polynomials fitting to the primary V-t data, in order to reduce the noise existing in the raw data. The deduced permeate flux data were then normalised by the initial pure water flux.

It took about 10-20 s to reach the designated TMP in the filtration cell after the gas valve was switched on, which led to a flux-increase at the initial moment. Therefore, the starting time for an experimental run was chosen at the moment when the peak flux was achieved. This peak value was in close agreement with the pure water flux at the same working TMP.

5.3.3.1 Case for Dextran Blue

The results for DB solutions are shown in Fig. 5.5. Its top plate displays the normalised permeate fluxes (J_n) as a function of the filtration time for five trials with different DB bulk concentrations (C_b). Generally, the scattered data points for each trial at a particular C_b appear to resemble an exponentially decaying curve and can be generally divided into two stages. The normalised flux declined rapidly at the initial stage of the filtration, with an increased declining-rate at higher bulk concentration. At later stage, i.e., towards long times, the flux tended to drop more gradually, and even approach quasi-steady values for the higher C_b case. These curves were highly

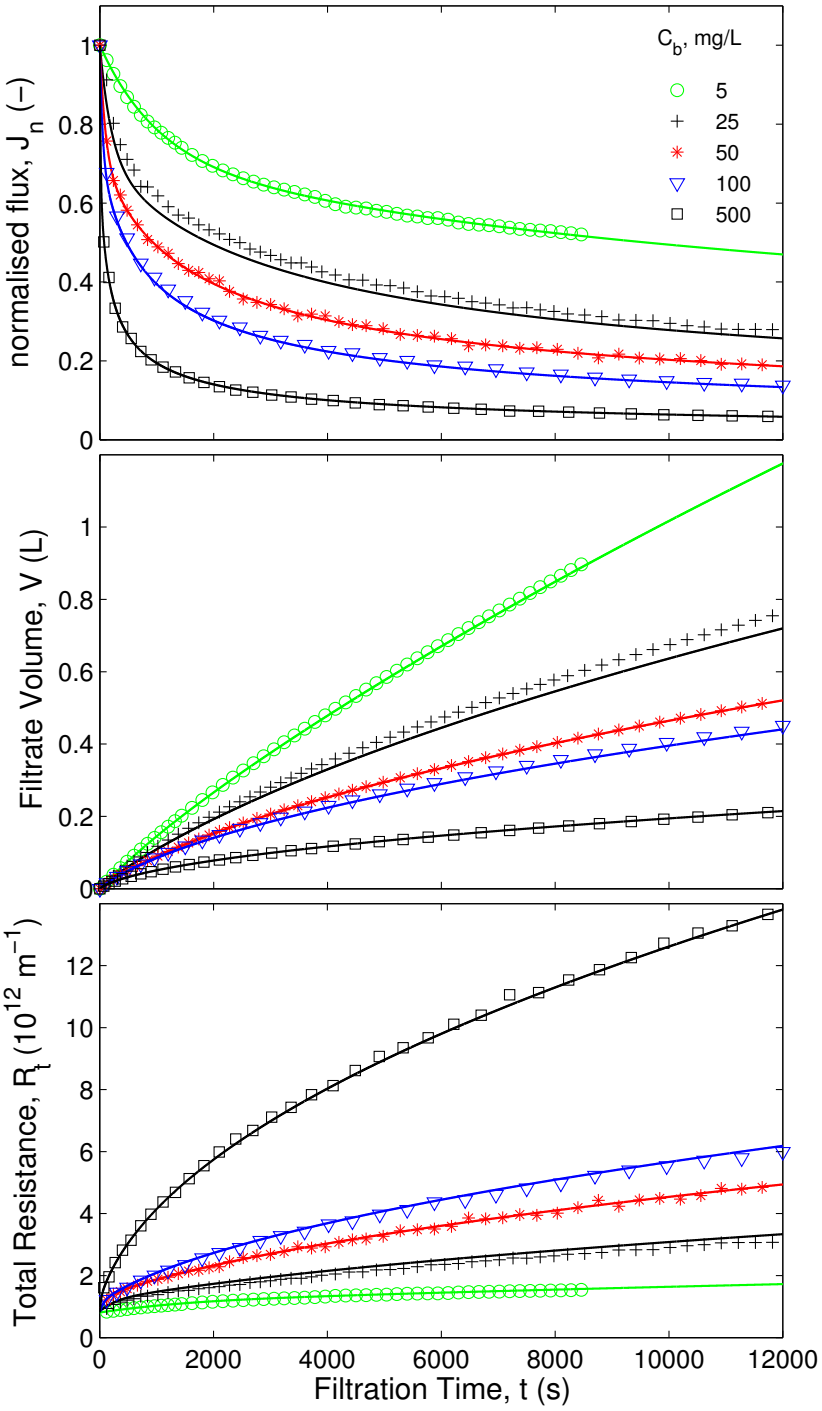

Figure 5.5: UF of Blue Dextran (MW = 2000 kDa) solutions at different concentrations by RC membranes (MWCO = 100 kDa) under 100 kPa TMP. Plots of variables as functions of filtration time: (a) Top plate: normalised flux (J_n); (b) Middle plate: accumulated permeate volume (V); (c) Bottom plate: total resistance (R_t). Solid curves are model calculations using eqn 4.22 with parameters determined by best-fitting to the $J - t$ data.

reproducible, with the data from repeat experiments differing by less than 10% for almost all sample points on the $J-t$ plot. For clarity reason, only one of the duplicates at each bulk concentration was selected to display.

Since the nominal size of the DB samples (MW = 2,000 kDa) is much larger than the membrane MWCO of 100 kDa, the DB molecules are less likely to enter membrane pores to cause internal fouling. Therefore, the potential fouling mechanisms are limited to consecutive pore blocking and cake formation (Model A). Hence, the solid curves in the $J-t$ plot of Fig. 5.5 are the model calculations using eqn 4.22. The values of the model coefficients, including the blocking constant (σ), the additional blockage resistance (R_b), and the specific cake resistance (α) are determined by best fitting to the experimentally measured permeate flux data in Fig. 5.5a. For each $J-t$ curve (one C_b condition) in this plot, a set of the three coefficients are produced. The average value of each coefficient and its standard deviation are calculated among the five curves and the results are listed in Table 5.2. This approach hence shows that the model curves are almost perfectly fitted to each set of data in Fig. 5.5a since the coefficients are chosen for each set (of different C_b). The verification of the model is based on evaluation of the individually determined fouling coefficients in Table 5.2. Under same TMP, for each macromolecular type, the coefficients are expected to be independent of the change of C_b.

It is worth mentioning that not all of the measured data (originally obtained at every 10 s) were used during the procedure of curve fitting in order to preserve the shapes of the curve, because the two stages of flux decline were not equal in length. For most trials, the early stage, that is characterised by the rapid flux decline, lasts less than one-fifth of the total filtration time in Fig. 5.5, although the majority of flux decline, in fact, takes place in this stage. In order to have the characteristic shape of the rapid flux decline well preserved in the model, it is desired for curve fitting to have a more balanced data sets, where the respective data points in the two stages should be more or less equal. Therefore, most of the data points at the early stage were kept, while the number of points at later stage were reduced. An automatic data selection protocol based on volume-steps was developed for the purpose. In this protocol, it only reads the data at a point when the amount of permeate volume increased from the last selected point exceeds the required critical value, which was set typically between 20 and 30 mL. Hence, Fig. 5.5 only shows these selected measures.

The model results show a very good agreement to the experimental data over the entire filtration time for all five trials in Fig. 5.5. The model accurately describes a rapid flux decline at the early stages of the filtration and a more gradual decline

towards the long time. Moreover, all of the three best-fit parameters were consistent among the five trials, respectively. Their mean values along with standard deviation were listed in Table 5.2. This proves these three parameters are all independent of the bulk concentration, complying with the theory [30].

Table 5.2: The mean fouling model parameters from the best-fitting to the sets of UF at constant pressure of 100 kPa with varying bulk concentrations.

	$\sigma\,(\mathrm{m^2/kg})$	$\mathrm{R_b/R_m}$	$\alpha(\mathrm{m/kg})$	$\beta\,(\mathrm{kg^{-1}})$
DB (Fig. 5.5a)	$1.7 \pm 0.3 \times 10^3$	0.46 ± 0.04	$1.6 \pm 0.2 \times 10^{14}$	0
PEO (Fig. 5.6a)	$3.1 \pm 0.6 \times 10^2$	2.2 ± 1.6	$4.1 \pm 0.5 \times 10^{13}$	0
HA (Fig. 5.7a)	81 ± 26	0.44 ± 0.31	$4.2 \pm 1.2 \times 10^{13}$	$7.2 \pm 5.5 \times 10^3$

The middle plate in Fig. 5.5 displays the accumulated permeate volume (V) against the filtration time (t). The sample points are the raw experimental data at the selected time. The solid curves represent the theoretical calculations obtained from integrating the simulated $J - t$ curves in the top plate of the same figure. As it displays, the model results fit well to the experimental data. Generally, the $V - t$ curves steadily rise but are gradually concave downward, deviating more and more from the pure water curve towards the long time. For trials with higher bulk concentration, this deviation is more obvious, i.e., the higher C_b the lower V. This complies with the trend in the flux curves since lower fluxes lead to less permeation. At the end of the filtration experiment, more than 1 L solution was filtered in the trial with C_b equal to 5 mg/L, while only about 0.2 L solution passed through the membrane in the one at 500 mg/L.

The filtrate flux data can be replotted as the total filtration resistance using the relationship,

$$R_t = \frac{\Delta P}{\mu J}. \tag{5.1}$$

The results are shown in the bottom plate of Fig. 5.5, with the solid lines representing the derived data from the fouling model calculations. Higher DB concentration led to greater and faster increase in R_t, especially in the early stage. Towards the later stage of the filtration, all five curves are concave down, which means the growth of the resistance has become more gradual. As clear as those on the $J - t$ plots, the transitions from early to late stages are easily identified. This is especially apparent for the curve with 500 mg/L bulk concentration.

Since the curves in the three graphs of Fig. 5.5 became more linear at the later stage of filtration, the changes in the filtration status, then, tended to be slower.

Based on the model, this indicated the majority of membrane pores would have been closed at the late stage and cake filtration played the major role in fouling. More details on evaluation of fouling mechanisms were discussed later.

5.3.3.2 Case for PEO

The same experiments have also been conducted with solutions of PEO. The results are shown in Fig. 5.6. Due to the size of PEO molecules (MW = 100 kDa) used was about the size of the membrane pore size (MWCO = 100 kDa), the pore constriction mechanism should not play any important role. Hence, the fouling model used here was still A type (eqn 4.22) same to that employed in the case of DB, with two possible mechanisms, i.e. pore blocking and cake filtration participating, and three fouling parameters to determine.

Overall, the effect of bulk concentration on PEO fouling is similar to that in the DB cases. Basically, higher concentration leads to more flux decline, less collected permeate volume, and higher hydraulic resistance. However, in detail, the shapes of their fouling curves were not exactly the same between PEO and DB cases. The difference has been made quite clear on the $J-t$ and $R-t$ plots, which lies mainly at the initial stage. The fluxes of PEO trials declined more rapidly at the early stage than those DB counterparts at the same bulk concentration. For the trial with 100 mg/L bulk concentration, the permeate flux dropped to approximately 30 % of its initial value within 10 min of filtration. The decline was even more dramatic for the trial at $C_b = 500$ mg/L, where the flux had plunged more than 80 % its original value in less than 5 min. After this dramatic early stage, the flux decline turned into a much slower and more steady phase, especially for trials at higher bulk concentrations, which had a very sharp change in their curves. For example, the normalised permeate flux in the 100 mg/L case was approximately 0.20 at the end of the 200 min filtration; while it had already been about 0.26 by 20 min filtration. This means the last 3 h filtration had only approximately 6 % contribution to the overall decline, which was marginal compared to over 70 % drop in the first 15 min. Although when the bulk filtration is lower than 50 mg/L the fouling curves are relatively smoother, the transitions between the fast and slow decline stages in PEO trials were generally sharper than those in the case of DB at each bulk concentration. This was exhibited in both the $J-t$ and $R-t$ plots. On the other hand, the $V-t$ plots didn't reveal the distinctive difference between PEO and DB trials, partly due to the present time scale, where a comparatively long filtration course (up to 200 min) is displayed. The other part of

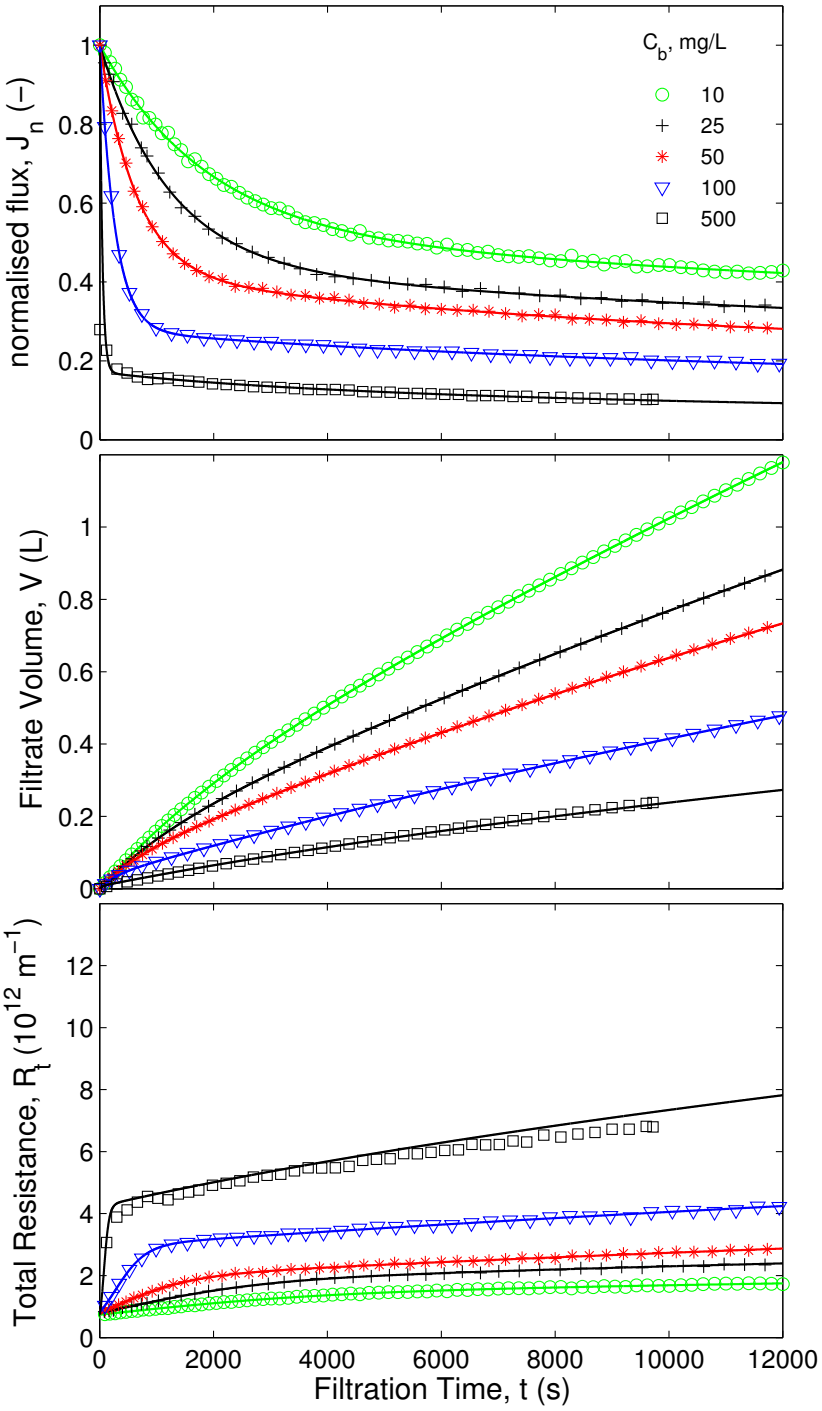

Figure 5.6: UF of PEO (MW = 100 kDa) solutions at different bulk concentrations through RC membranes (MWCO = 100 kDa) under 100 kPa TMP. Plots of variables as functions of filtration time: (a) Top plate: normalised flux (J_n); (b) Middle plate: accumulated permeate volume (V); (c) Bottom plate: total resistance (R_t). Solid curves are model calculations using eqn 4.22 with parameters determined by best-fitting to the $J - t$ data.

the reason is due to the intrinsic character of the permeate volume data, which will be elaborated in Section 5.3.5.1.

Although PEO trials have more dramatical flux drop at early stage, DB trials generally had lower fluxes at long times, comparing trials at the same feed concentration. This trend is revealed more clearly on the $R - t$ graph. Comparing the 500 mg/L trials from Fig. 5.5 and 5.6, the total resistance (R_t) of the PEO trial was twice as much as that of the DB trial by 15 min. However, the increasing rate of the resistance then slowed down greatly in the PEO trial, while the resistance growth in DB trial decelerated as well but much more gradually and eventually became higher than its counterpart until the end. Thus, at the end of the 200 min filtration, R_t of DB filtration became 7 times of its initial value and almost double the final value in the PEO trial.

The fouling model (type A) fitted well to PEO experimental data on the graphs, but one of the best-fit parameters, the additional blocked-pore resistance, R_b, had apparently greater variance between the values for each curve than that determined in DB cases (see Table 5.2), of which the standard deviation was up to 73% of the mean value; while the blocking rate, σ, and specific cake resistance, α, still had small deviations in their values. The great deviations in the R_b values are possibly due to the fact that the nominal size of the PEO molecules used in the study are of the same order of magnitude with that of the pores in the RC membrane used. This might cause a great varity in the way that a particular pore got blocked by the molecules, which is an interesting topic by itself.

Comparing the mean values of the three parameters between the two types of polymeric feeds, PEO trials resulted in greater R_b but smaller σ and α than DB trials. The mean R_b value is nearly 5 times that in the DB cases, although its blocking constant is about 5 times lower. Moreover, the R_b values of the PEO trials were larger than the intrinsic membrane resistance while those of the DB trials were smaller. This might be the reason for the great decrease in PEO fluxes occurring at the early stage of filtration.

5.3.3.3 Case for Humic Acid

Besides these two polymeric macromolecules were used in experiments, HA solutions were also filtered for comparing the effect of feed concentration. The results were depicted in Fig. 5.7. However, the fouling model in this case was type B assuming the participation of an additional blocking law, i.e. pore constriction, since the HA

samples had a big fraction ($> 70\%$) could not pass the 100 kDa membrane. The model fitted well to the experimental data in all the three plots of Fig. 5.7. The values of the four best-fit parameters between trials at different bulk concentration are, respectively, in good agreement. Their mean values were listed in Table 5.2 along with those in DB and PEO cases.

Due to the low solubility of the HA at neutral pH, the feed concentration was only tested up to 100 mg/L. Similar to the cases of DB and PEO, the fluxes of HA trials declined constantly over the whole course and more rapidly at the beginning for those with higher bulk concentration. However, comparing the trials at the same bulk concentration across different feeds, trials of HA had overall higher fluxes, higher volumes of permeate and lower total resistance than the other two feeds. Moreover, in terms of the shape of the curves, HA trials have smoother transition between fast decline at early time, and gradual decline being almost linear at late times, especially when high concentrated trials are compared. For HA trials at low feed concentrations, such as 10 mg/L, its flux decline curve cannot be staged in terms of the gradient, which is almost in a nearly linear fashion over the whole filtration course. Its volume-time and resistance-time curves have the similar linearity.

In order for better comparison across the three feed types, trials at 50 and 100 mg/L feed concentration, regarding all feed types, were all plotted in Fig. 5.8. At both concentrations, HA trials maintained their fluxes higher than the other two feeds, respectively. Therefore, they passed more permeates since the very beginning of filtration as shown in the $V - t$ plot.

All the $J - t$ curves seem to possess multiple stages. The early stage is characterised by its great and rapid flux descend. The curve is at its steepest in this stage. The later stage is marked by the small and gradual decline in flux with a flatter curve. PEO trials have clearly the most distinctive breakpoints between early and later stages. They have the steepest descend at the early stage and most flat curves afterwards. The switch between the stages is very sharp and sudden. The curves look like being snapped into two almost straight sections. Especially for the curve after the breakpoints, it has a good linearity ($R^2 > 0.99$). HA trials do not have a clear switching to divide curves into two distinctive phases on the graph. Their curves are overall smoothest among all present curves. Therefore, the range of the fluxes in HA trials is the least wide. DB curves have a shape, overall, similar to those of HA trials, with gradual and continuous switch between stages, but they have great negative gradients coinciding with the PEO curves at the beginning of filtration. Comparing at 100 mg/L bulk concentration, the DB trial had as rapid flux decline as the PEO

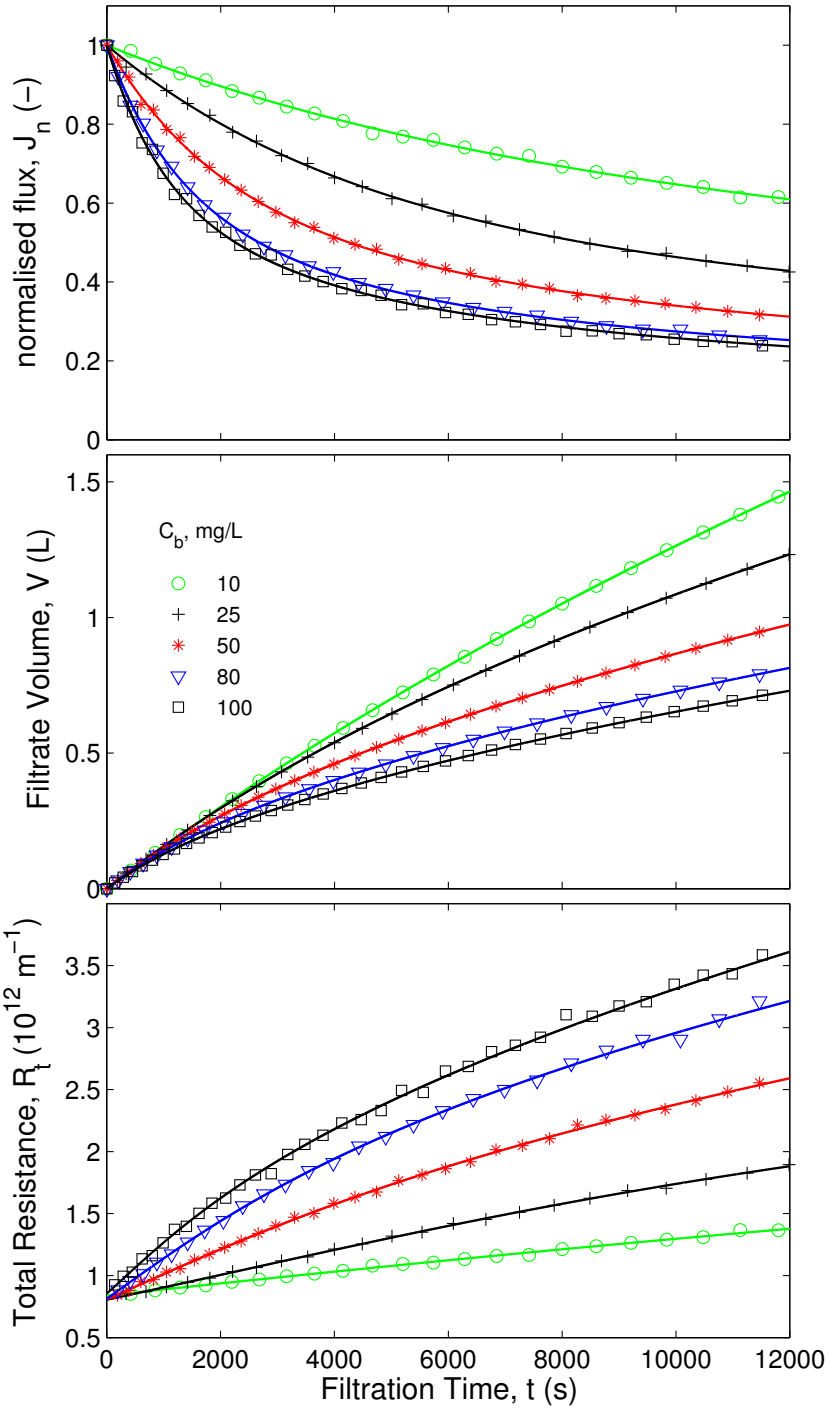

Figure 5.7: UF of prefiltered HA (MW distribution shown in Fig. 5.3) solutions at different bulk concentrations filtered by fresh RC membranes (MWCO = 100 kDa) under 100 kPa TMP. Plots of variables as functions of filtration time: (a) Top plate: normalised flux (J_n); (b) Middle plate: accumulated permeate volume (V); (c) Bottom plate: total resistance (R_t). Solid curves are model calculations using eqn 4.23 with 4 parameters determined by best-fitting to the corresponding $J - t$ data.

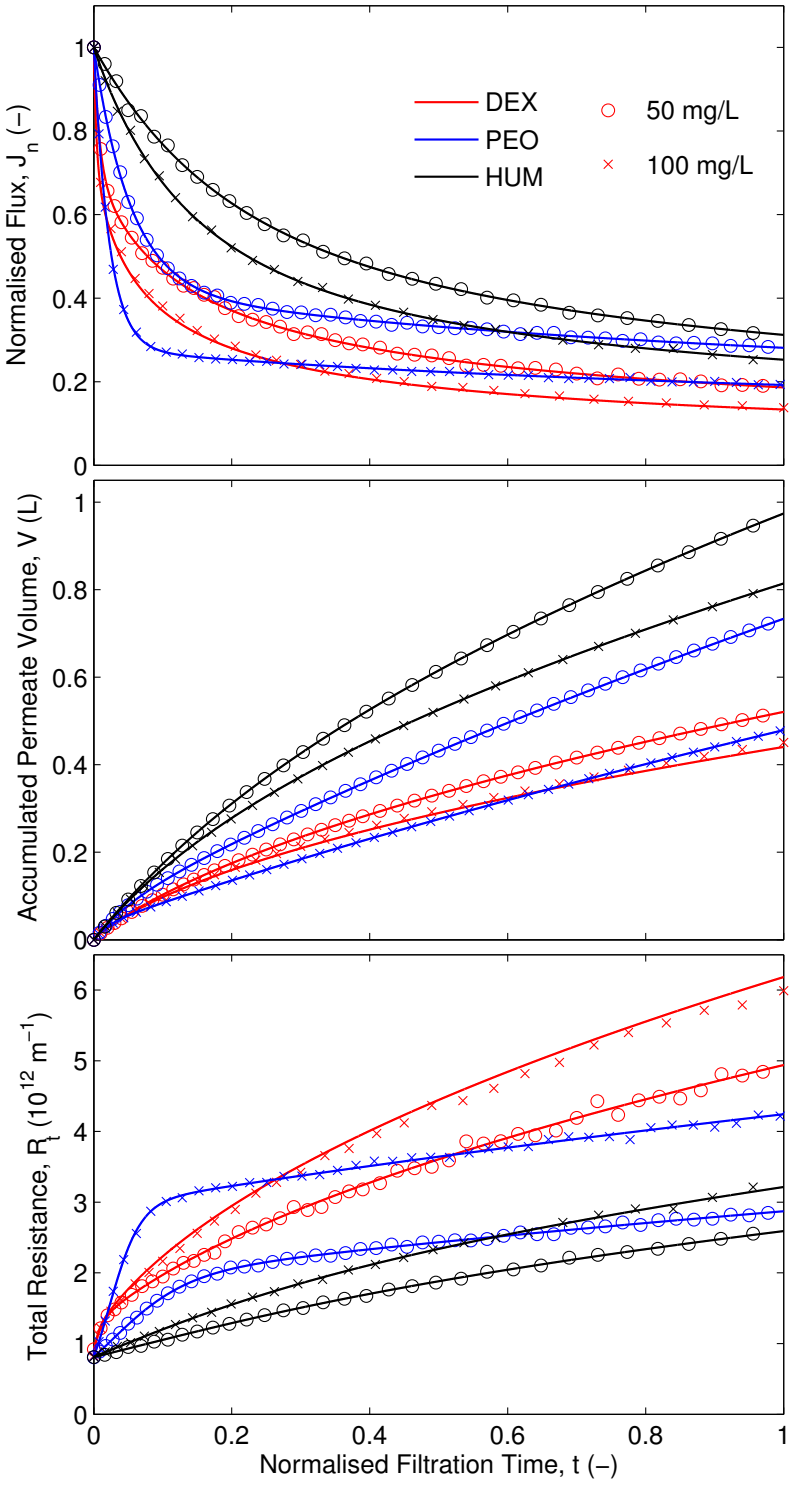

Figure 5.8: Filtration variables as functions of filtration time (a) top: normalised flux; (b) middle: accumulated permeate volume; (c) bottom: total resistance, showing trials of DB, PEO and HA solutions at 50 and 100 mg/L, respectively.

at the first 5 min of filtration and then it slowed down and gradually switched to its later stage. Hence, its flux was higher than that of the PEO trial after the first 5 min, but this didn't last long. As the PEO trial proceeded into the slow-decline stage at around 20 min, its rate of decline became, in fact, smaller. Although the flux-decline rate in the DB trial gradually decreased till the end of 200 min filtration, it was still higher than that of the PEO trial at the end. Therefore, at nearly 60 min, the DB trial eventually dropped its flux lower than the PEO. The $R-t$ curves basically inverse to the $J-t$ ones have similar trends.

Comparing the mean values of fouling model coefficients σ, R_b, α and β in Table 5.2 for all three feeds, trials with HA had the least pore blocking coefficient (σ) while DB cases had the highest. A hypothesis for the high σ in DB cases is that since the size of DB molecules is much larger (MW=2000 kDa) than the membrane pore size (MWCO = 100 kDa), it should be completely rejected by the membrane and therefore contribute more to the surface coverage. The feed rejection was checked during filtration, which had confirmed no trace of DB was detectable in the permeate from the start to the end of filtration (10 ml each collected at certain time interval). In terms of the membrane retention, HA was the least feed type among the three. At the beginning, almost 50% weight of HA passed through the membrane with flow. PEO had The 100 kDa PEO had the modest pore blockage rate on 100 kDa RC membrane, but caused the highest resistance ($1.7 \pm 1.1 \times 10^{12}\ m^{-1}$) when blocking the pores, about 5 times greater than those in DB and HA cases where they had similar values ($3.9 \pm 0.3 \times 10^{11}$ and $3.6 \pm 2.5 \times 10^{11}\ m^{-1}$ respectively). Based on the molecular size ratio hypothesis, PEO molecules can enter the depth of a membrane pore since its size is close to the membrane's while DB molecules cannot, which causes R_b from UF of PEO molecules becomes greater than R_m of the membrane used. However, PEO is not completely rejected by the chosen membrane, especially, at the initial stage of filtration. The determined specific cake resistances, α, were similar between PEO and HA feeds, but 3 times higher in DB cases. This attributed to the lowest fluxes achieved in DB trials at the end of a long filtration.

5.3.3.4 Effect of Bulk Concentration on the Blocking Time

In order to see better the effect of bulk concentration on fouling, the density function (eqn 4.18) and the cumulative distribution function (eqn 4.16) of the switching time τ between different fouling mechanisms were depicted in Fig. 5.9 and 5.10 using the parameters for DB cases.

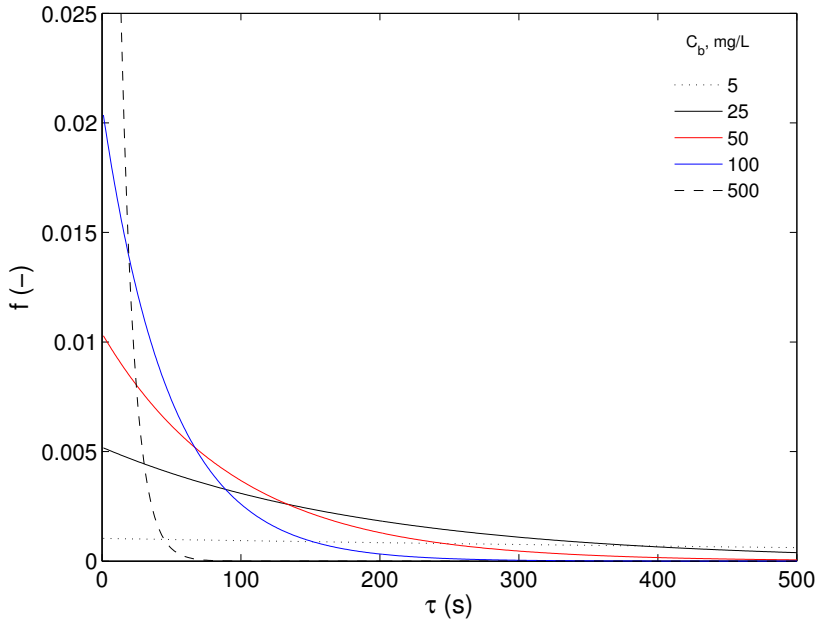

Figure 5.9: The effect of the bulk concentration on the probability density function (eqn 4.18) of the blocking time τ using the mean value of σ for DB in Table 5.2.

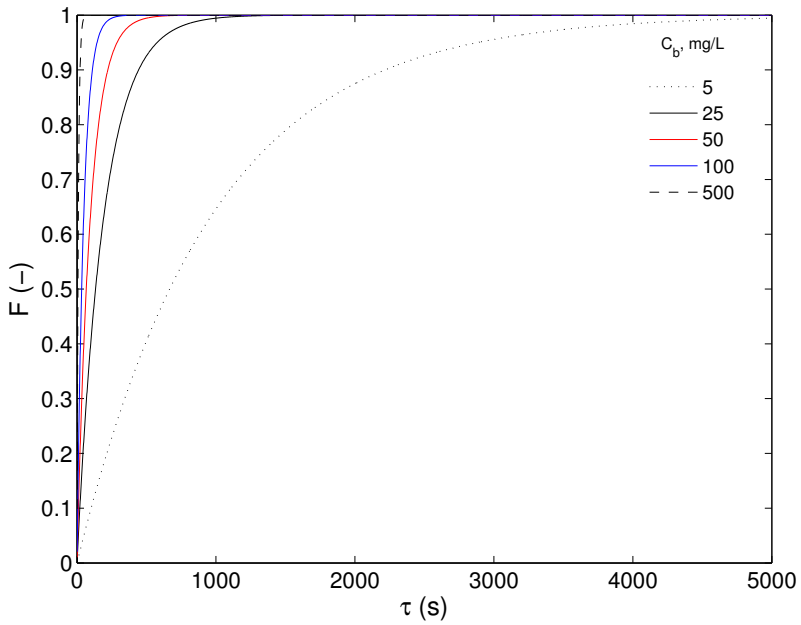

Figure 5.10: The effect of the bulk concentration on the accumulated distribution function (eqn 4.16) of the mechanisms-switching time τ using the mean value of σ for DB trials in Table 5.2.

Physically, the density and cumulative distribution functions represent the blocking rate, i.e. the number of pores being blocked at time τ and the blocked portion, i.e. the number of blocked pores by the time τ normalised by the total pore numbers, respectively. Since the distribution function took the form from the classical complete blocking law, pore blocking has taken place very fast and the blocking rate has decreased exponentially against the filtration time as shown in Fig. 5.9 while the percentage of the blocked pores increased exponentially with the time as shown in Fig. 5.10. According to these two figures, the bulk concentration has significant impact on the blocking rate and percentage. For the feed solution at 5 mg/L, the initial rate was very low so that only 1% pores would be covered at the very beginning and afterwards decreased very gradually, almost levelling for the first 9 min. It took more than 80 min to cover more than 99% areas in this case. On the other hand, for the trial with 500 mg/L bulk concentration, the initial blocking rate was 10.3%, 100 times (exactly the ratio between the two C_b values) that of the trial with 5 mg/L. It only took 1.2 min for the whole area being covered by the dextran deposits and its blocking rate had an sharp exponential decay within such a short period for the high concentrated trial. In order to quantify the impact of the bulk concentration, we introduce a statistical term, i.e. the mean blocking time, $\langle\tau\rangle$, which is the average time before a random pore is blocked. It can be calculated as

$$\langle\tau\rangle = \frac{1}{k_b}. \tag{5.2}$$

This yielded 994, 199, 100, 50 and 10 s for trials at 5, 25, 50, 100 and 500 mg/L, respectively. This leads to the great divergence between curves of $C_b = 5$ and 500 mg/L in Fig. 5.10.

The distribution of the blocking time affects the growth of fouling cakes over the membrane surface. The interplay between these two mechanisms is illustrated in Fig. 5.11 for the trial with 25 mg/L DB solution. The total membrane resistance, R_t, at each filtration time t was evaluated as a function of the blocking time τ using eqn 4.7 with $t_0 = \tau$ and the two parameters α and R_b previously determined in Fig. 5.5, and then normalised with $R_m + R_b$ in order to show only the contribution of the fouling cake. The blocked portion of the whole membrane area, F, was evaluated using eqn 4.16, as a function of τ as well. These two quantities were then related to each other via τ and drawn onto the same graph.

Figure 5.11 shows that the normalised resistance falls when the blocked portion rises at every time during filtration. This reflects the calculation from the eqn 4.16

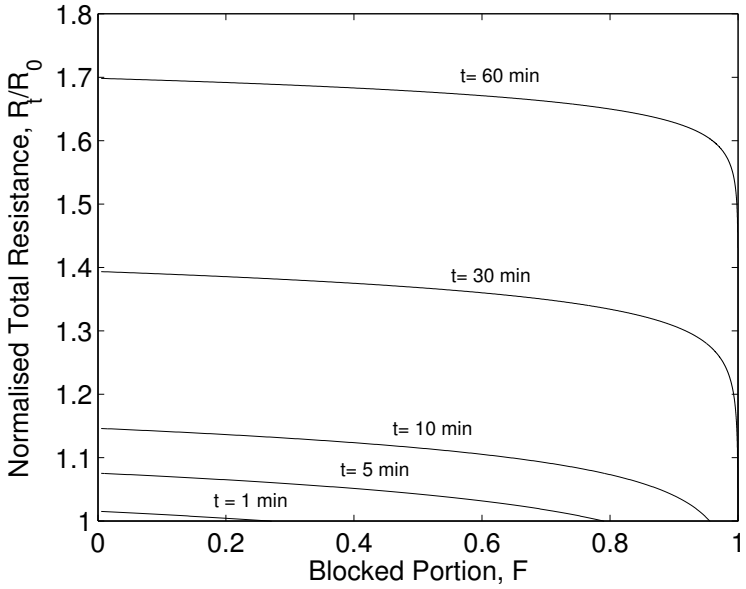

Figure 5.11: Model calculations of total resistance R_t normalised with $R_0 = R_m + R_b$ as a function of the blocked portion, F, using best-fit parameters obtained in Fig. 5.5 for 25 mg/L DB solution filtered through RC 100 kDa membrane at TMP 100 kPa.

and 4.7, i.e. the fraction of the blocked areas becomes larger when the blocking time τ delays, while the cake resistance is lowered. The value for the total resistance during cake-controlled fouling varies from the maximum at the region being blocked at the very beginning when $\tau = 0$, to the minimum, $R_m + R_b$ at the region where the pores are just blocked at $\tau = t$. When the filtration time is short, large areas of the membrane (approx. 78%) remained open in Fig. 5.11. The effect of cake filtration was minor. Until after 10 min filtration, the majority of the membrane was blocked. By 30 min filtration, all areas had been blocked. This figure also tells that since the early stage, the inhomogeneity of the cake resistance over the membrane surface existed. Area blocked earlier had the highest resistance over the whole filtration time. As the filtration ran longer, the variation of the resistance between different regions became larger (see the difference between the curves at $t = 1$ min and $t = 30$ min), although the resistance was fairly close over much of the membrane surface. The most difference occurred at areas only recently got blocked. Ho and Zydney [83] observed similar trends in their protein MF experiments and explained that the cake growth should be a self-levelling process, i.e., pores blocked first would have the greatest resistance and thus the lowest flux, leading to the slowest rate of deposition of new foulants.

5.3.3.5 Sensitivity Analysis of Fouling Parameters

The three fouling parameters (σ, α, and R_b) determined in this section are evaluated using local sensitivity analysis. For each parameter, its sensitivity to the output of the model, i.e., normalised flux, is evaluated individually by varying its value around its optimised value shown in Table 5.2, while keeping all other parameters constant.

Figure 5.12 shows the sensitivity results for the pore blocking coefficient σ. The

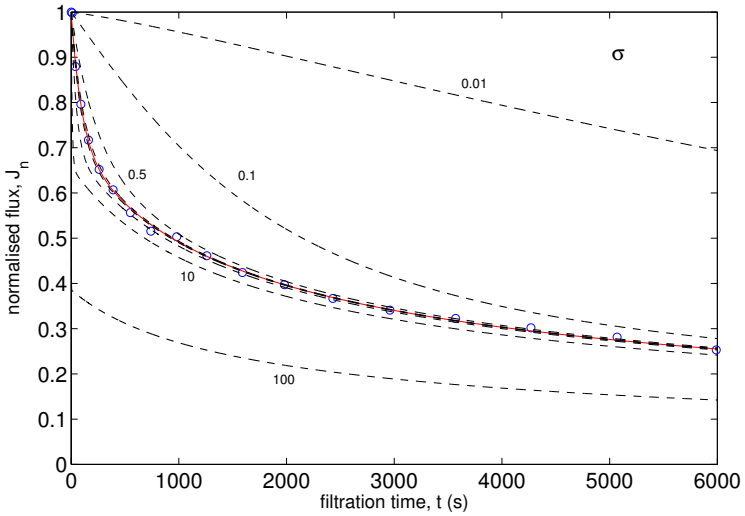

Figure 5.12: Local sensitivity analysis for the pore blocking coefficient, σ, in the case of 50 mg/L DB filtration at 100 kPa. The dotted points are the original experimental data, while the red solid line is calculated using the optimised value determined in Table 5.2. The dash lines represent the outputs calculated at variant σ values. The numbers next to these dash lines show the scale factors of σ.

effect of σ mainly contributes to the initial stage of flux decline. High values of σ causes sharper and faster decline, while small values can have longer effect during filtration although the flux decline curve shows less obvious transition between fouling mechanisms. Small degree change of σ (10% difference, i.e. between 0.9 times and 1.1 times) does not change the shape of the curve visibly. When σ becomes 2 times larger or half times smaller, the curves are affected visibly during the first 1000 s of filtration, but are negligibly affected towards long time. However, once the change becomes larger than 1 order of magnitude, the effect is apparent.

Figure 5.13 shows the results for the coefficient of specific cake resistance α. It affects the later stage of filtration and the overall degree of flux decline. Its value does not affect the filtration performance at a short period but flux becomes more

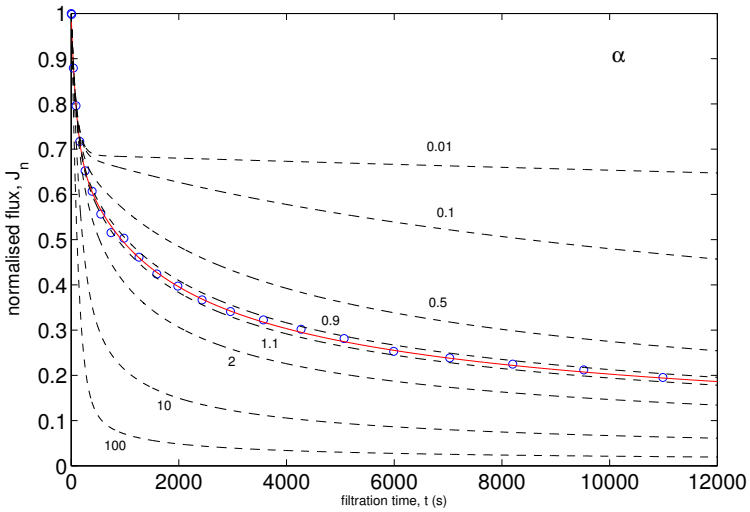

Figure 5.13: Local sensitivity analysis for specific cake resistance, α, in the case of 50 mg/L DB filtration at 100 kPa. The dotted points are the original experimental data, while the red solid line is calculated using the optimised value determined in Table 5.2. The dash lines represent the outputs calculated at variant α values. The numbers next to these dash lines show the scale factors of α.

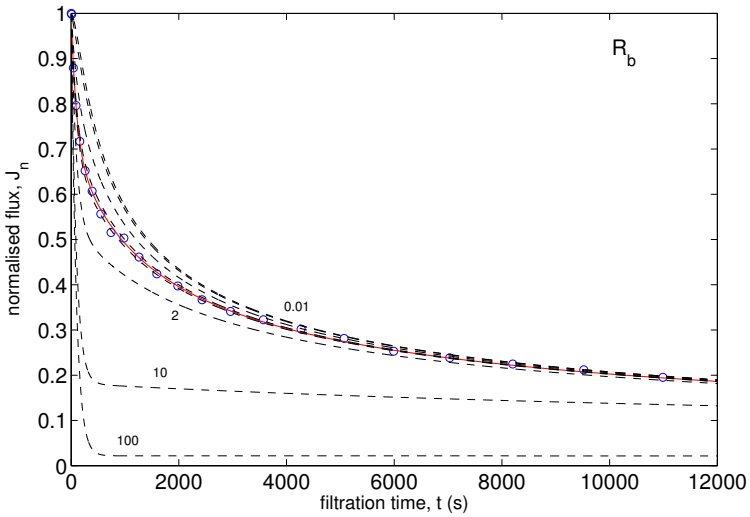

Figure 5.14: Local sensitivity analysis for the pore blocking coefficient, R_b, in the case of 50 mg/L DB filtration at 100 kPa. The dotted points are the original experimental data, while the red solid line is calculated using the optimised value determined in Table 5.2. The dash lines represent the outputs calculated at variant R_b values. The numbers next to these dash lines show the scale factors of R_b.

sensitive to the variance of α at long time. 10% difference in its value has visible effect on the flux values after approximately 2000 s filtration.

Figure 5.14 displays the effect of additional resistance of pore blocking, R_b, on the overall flux decline curve. The effect of R_b is similar to that of σ since they are both caused by pore blocking process. Small variations between 0.01 times and 2 times do not affect the long term flux but have apparent impact on the flux in the short time. The larger R_b becomes, the greater and faster flux decline appears. The flux decline is relatively less sensitive to small R_b values but greater to large values. When R_b becomes 2 order of magnitude larger, the flux decline process is controlled by it. Flux at R_b at 100 times its optimal value drops to as low as approx. 0.03 after the first 500 s of filtration.

5.3.4 Effect of TMP

5.3.4.1 Experimental and Model Results

Figure 5.15 shows the effect of the TMP on the normalised filtrate flux, accumulated permeate volume and membrane total resistance during the constant pressure filtration of 50 mg/L Blue Dextran solutions, respectively. Before macromolecular filtration, the pure water fluxes were determined at a wide range of TMP. The results showed the RC 100 kDa membranes were almost incompressible within the test range achieved up to 200 kPa and the pure water fluxes were reproducible after re-applying the working pressure. Once macromolecular filtration started, the initial fluxes descended more rapidly at higher TMP. Particularly, the flux decreased to less than 30 % of its initial value within the first 5 min of filtration at TMP 200 kPa. Then, the decline of the fluxes became more gradual towards longer filtration time. Especially for the trials with TMPs above 100 kPa, their curves almost reached a flat slope, which were similar to those of the trials with high concentrations at 100 kPa. The differences between the normalised final flux values at the end of the experiments became narrower between those with high TMPs. The smallest gap occurred between runs at 150 and 200 kPa, where fluxes dropped to approximately 15 % and 10 % of their respective initial values.

On the $V-t$ plot, the total volume of filtrate didn't differ much between different trials over the whole course of 200 min. Initially, these trials with higher TMP cumulated more permeates at the same filtration time, indicating that they had higher absolute fluxes at the beginning. However, higher pressure also caused higher decline

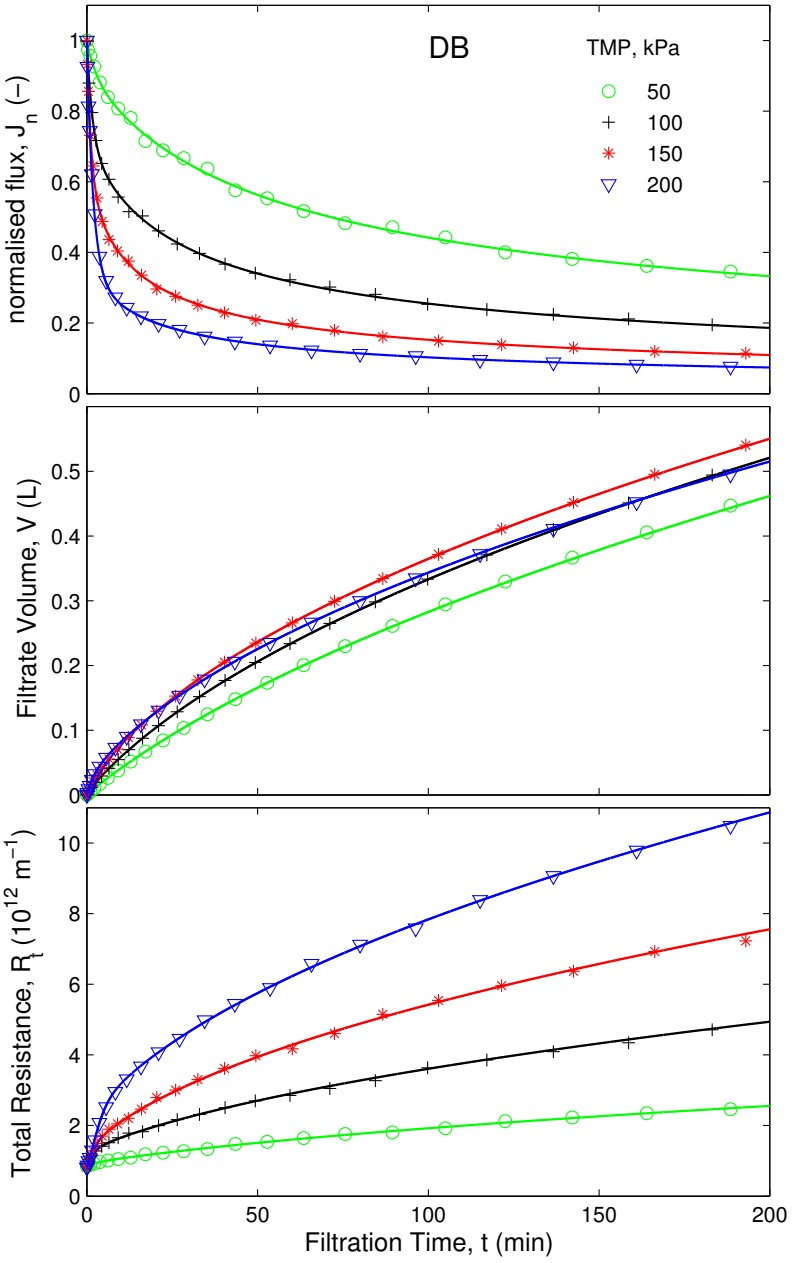

Figure 5.15: Effect of TMP on UF of 50 mg/L DB (MW = 2000 kDa) solutions through fresh RC membranes (MWCO = 100 kDa). Plots of variables as functions of filtration time: (a) top: normalised flux (J_n); (b) middle: accumulated permeate volume (V); and (c) bottom plate: total resistance (R_t). Dots are sample date acquired from their respective experiments and solid curves are model calculates using eqn 4.22 with 3 parameters determined by best-fitting to the corresponding $J - t$ data.

rate in flux as indicated in the $J-t$ plot above, the slope of the volume-accumulating curves became less steep, especially for the one with highest TMP. The total amount of the permeate through the membrane at 200 kPa became less than that at 150 kPa after only 30 min filtration and the gradient of its curve further decreased to be the lowest among the whole sets. The 200 kPa trial collected even less volume than that at 100 kPa at the end of the 200 min experimental run.

The effect of TMP on the total resistances became clearer when the filtration ran longer as the discrepancy between each trial at different TMPs became larger and larger with increasing filtration time. Due to the relatively small variance in intrinsic membrane resistances, the initial values of R_t lay almost at the same position on the y-axis in the scale presented in Fig. 5.15(c). Then, higher pressure led to more rapid increase in R_t. Within merely 5 min, the value doubled for the run at 200 kPa. Although the great rate reduced soon after for the same set, the R_t still kept increasing. To the end of 200 min, R_t at 200 kPa increased almost 10 times of its initial value, and it was approximately 30 % greater than that at 150 kPa. In comparison, the trial with the lowest TMP, i.e., 50 kPa had the least increase in R_t, of which the end value is only about 1.5 times its initial value.

The solid curves in Fig. 5.15 represent the model calculations using eqn 4.22 of the A model of the consecutive blocking scenario. Model parameters for each TMP cases were determined by best-fitting to its corresponding $J-t$ data. The model results fit experimental data points well for all three graphs.

Similarly, Fig. 5.16 and 5.17 show the effect of TMP on the UF of PEO and HA solutions, respectively. Both of their trials were at 50 mg/L bulk concentrations same to those DB trials. The range of TMPs was between 50 and 200 kPa for all cases.

5.3.4.2 Comparison of Model Parameters

Figure 5.18 depicts the values of the four best-fit parameters as a function of TMPs, for all trials shown in Fig. 5.15, 5.16 and 5.17. DB trials had the highest pore blockage rate (σ) over those of other feed types in the range of TMPs tested. It decreased almost linearly with increasing TMPs, of which the lowest value occurred at 200 kPa, i.e. about one third of the peak value at 50 kPa. The blocking constants for PEO trials were almost unaffected by the change of TMPs, which had a mean value of $282.4 \pm 19.8\ m^2/kg$, while those for HA trials had the lowest values, although they slightly increased from only 11.9 m^2/kg at 50 kPa to 184.6 m^2/kg at 200 kPa.

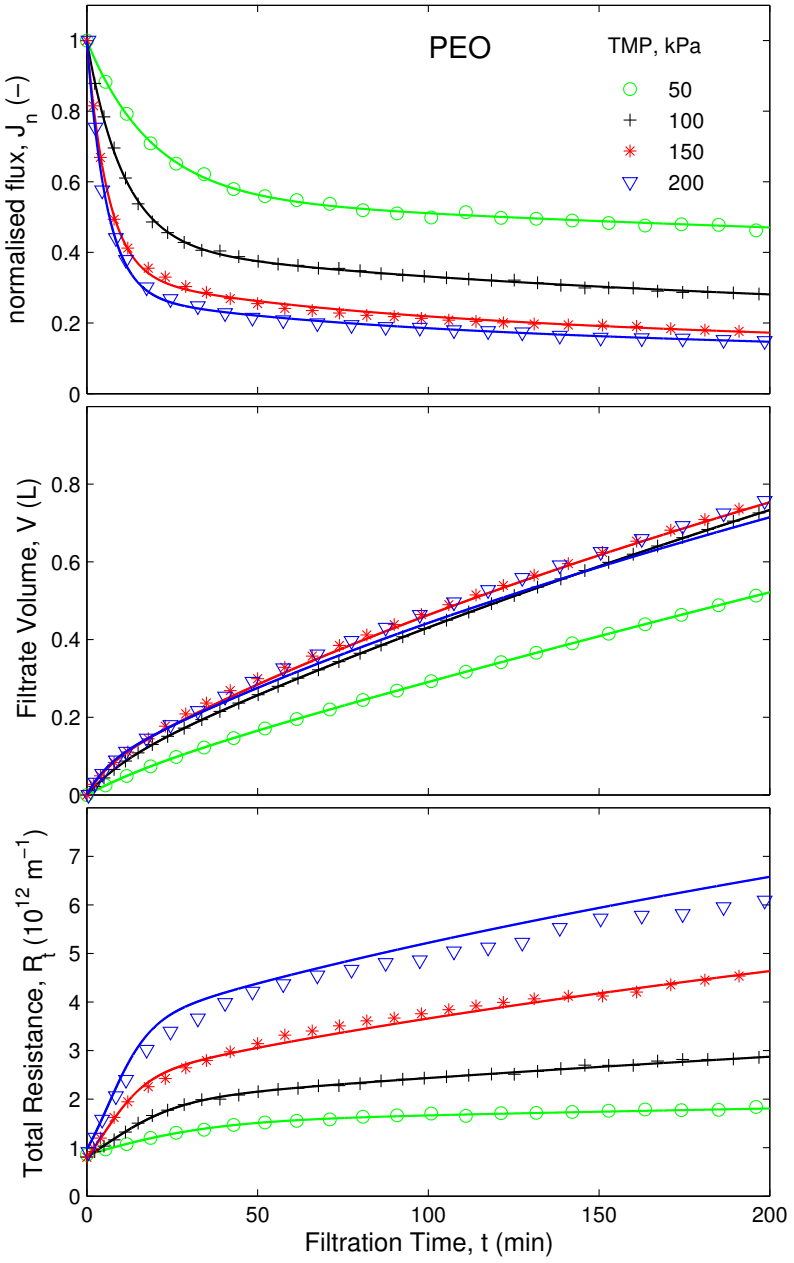

Figure 5.16: Effect of TMP on UF of 50 mg/L PEO (MW = 100 kDa) solutions through fresh RC membranes (MWCO = 100 kDa). Plots of variables as functions of filtration time: (a) top: normalised flux (J_n); (b) middle: accumulated permeate volume (V); and (c) bottom plate: total resistance (R_t). Dots are sample date acquired from their respective experiments and solid curves are model calculates using eqn 4.22 with 3 parameters determined by best-fitting to the corresponding $J - t$ data.

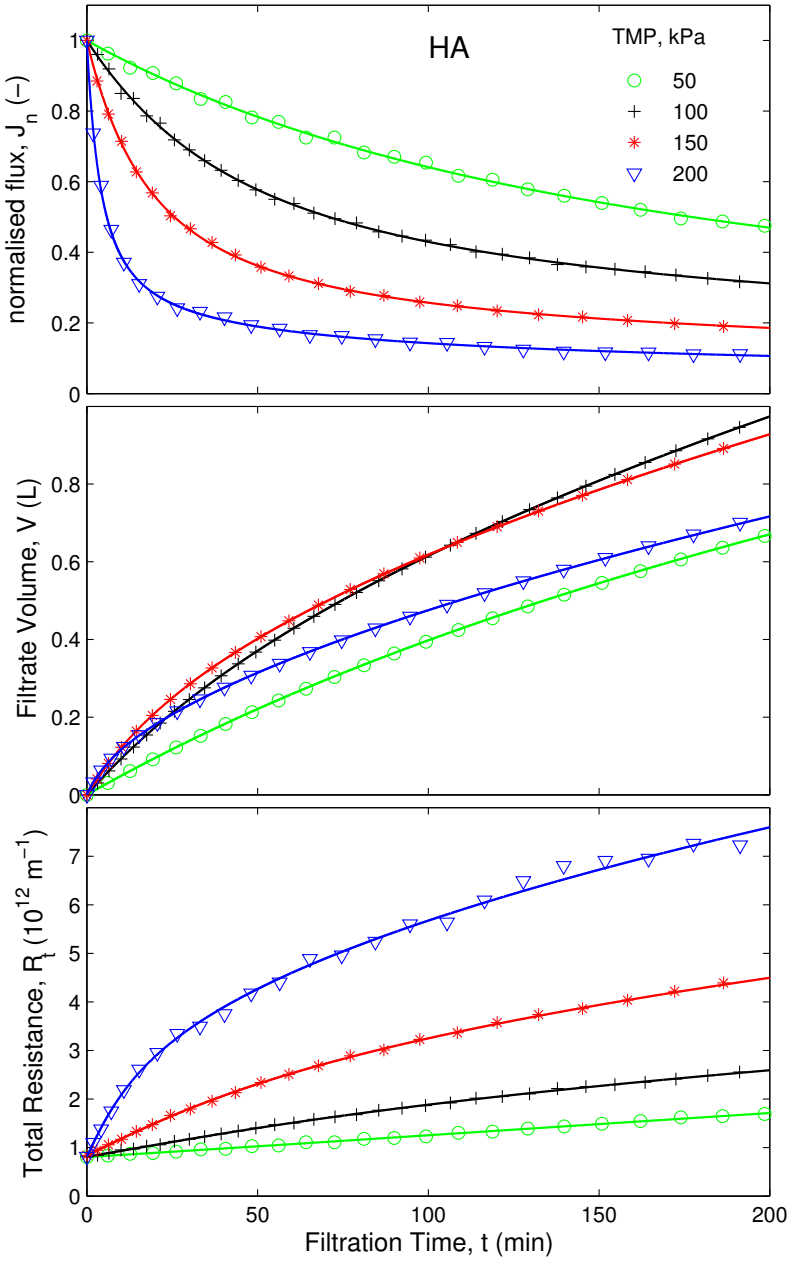

Figure 5.17: Effect of TMP on UF of 50 mg/L prefiltered HA (approx. 60 % <= 100 kDa) solutions through fresh RC membranes (MWCO = 100 kDa). Plots of variables as functions of filtration time: (a) top: normalised flux (J_n); (b) middle: accumulated permeate volume (V); and (c) bottom plate: total resistance (R_t). Dots are sample date acquired from their respective experiments and solid curves are model calculates using eqn 4.22 with 3 parameters determined by best-fitting to the corresponding $J-t$ data.

Overall, the difference on blocking rate between trials with different feeds became narrower with higher TMPs.

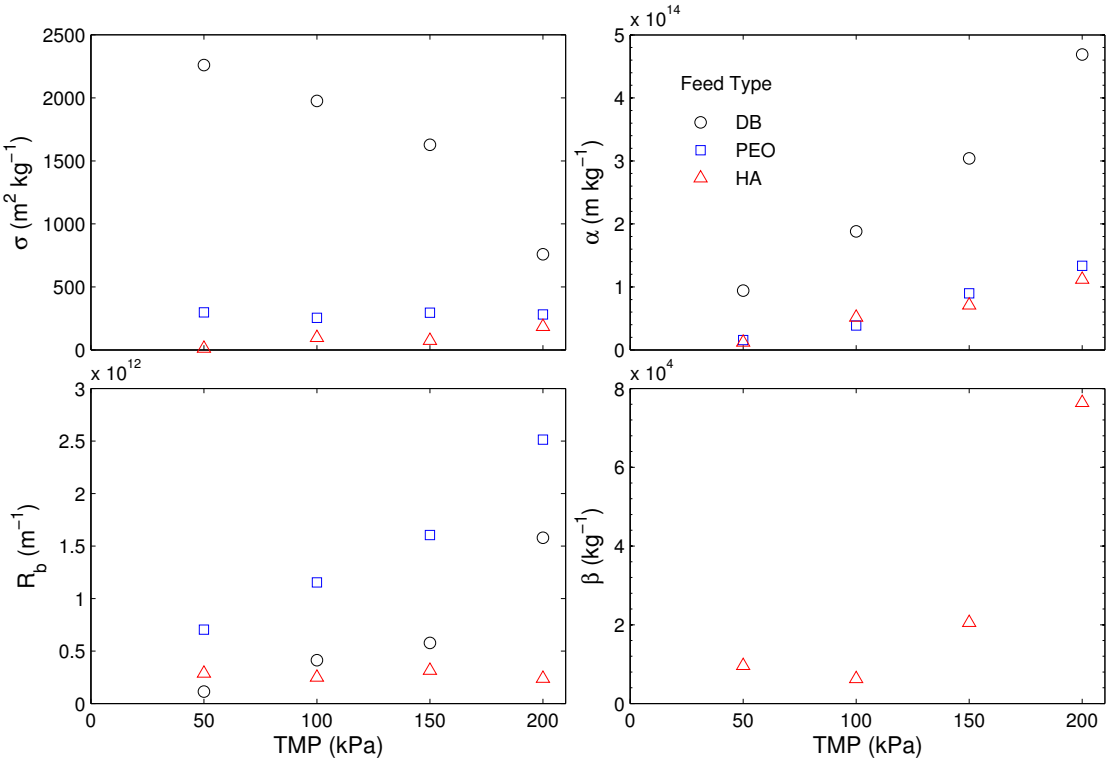

Figure 5.18: The best-fit parameters determined for trials with 50 mg/L bulk concentration at different TMP values. Parameters were presented as a function of TMPs: (a) top left: pore blocking rate, σ ; (b) top right: specific cake resistance, α; (c) bottom left: the additional resistance caused by particles blocking a pore, R_b, and (d) bottom right: pore constriction coefficient, β, only applicable to HA trials.

The additional resistance caused by pore blocking (R_b), increased with increasing TMPs in a similar fashion for both PEO and DB trials. PEO molecules, the one with smaller sizes, caused higher resistances at each TMPs. Different from the two polymeric feeds, HA caused the least resistance when it partially closed the pores at most TMPs except for 50 kPa, where it had a slightly higher value than that for DB trial. For HA trials, the additional resistance was almost invariant to the change of TMPs.

The specific resistance of cake filtration (α) increased with increasing TMPs for all three feed types. Over the whole pressure range, the highest values were obtained in DB trials, while PEO and HA trials had similar values. The increasing rate of the cake resistance was also higher in DB trials than those of the other two.

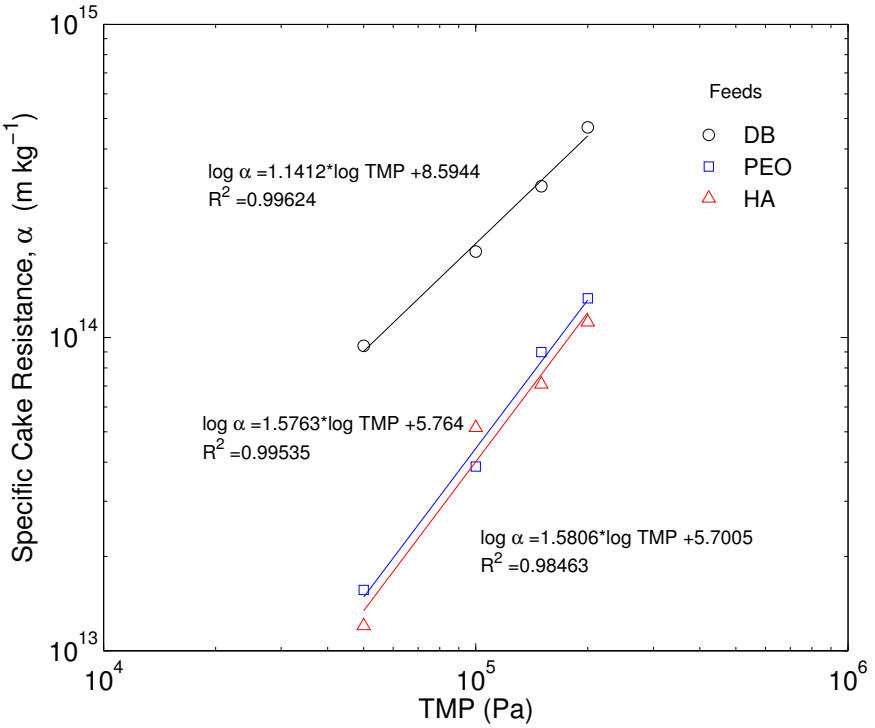

Figure 5.19: Specific macromolecular surface layer resistance (α) as a function of transmembrane pressure. Circle markers represent the best-fit results from the flux decline curves of the DB trials; squares are for PEO; triangles for HA. The solid lines are linear regression based on eqn 5.3, respectively.

The specific cake resistance data for the three macromolecular deposits are all highly linear when plotted on a log-log graph in Fig. 5.19. This is consistent with the commonly used power law relationship [16]:

$$\alpha = a(\Delta P)^s \tag{5.3}$$

where a and s are empirical constants. The multiplier a is related to the size and shape of the particles within the deposits, while the power s represents the cake compressibility [83]. By linear regression, s and a have the values of 1.1 and $3.9 \times 10^8\ m\,kg^{-1}\,Pa^{-1.14}$, with correlation coefficient $r^2 = 0.996$. For both PEO and HA trials, they had almost same $s = 1.6$ and very close a values, i.e. 5.8×10^5 and $5.0 \times 10^5\ m\,kg^{-1}\,Pa^{-1.6}$, respectively.

5.3.5 Fouling Mode Determination

In the frame of classical blocking laws, the filtration constant, n, in eqn 2.2 determines the fouling mode or mechanism according to the blocking laws. Numerical differentiation of experimental data is sensitive to minor changes in the shape of the data sets, since differentiation describes the slopes of a function at a point, i.e. a microscopic property of a function. Any small noise in the original data can easily be enlarged in its differential derivatives. Due to this inherent sensitivity of differentiation, the Savitzky-Golay filter had to be used to smooth the flux data in the previous section. Since eqn 2.2 is a second order differential equation, direct calculation from the original volume-time data may cause a large deviation from the truth. Therefore, two methods are tested using here, integral analysis by integration of the original data or differentiating the polynomial resulting from the fitted model.

5.3.5.1 Integral Method

Integral analysis was recently proposed by Field and Wu [31]. The concept is to avoid differentiation of the flux data. Since integration describes an overall or macroscopic property of a function, it is not sensitive to minor changes in the shape of a function. Equation 2.6 is rewritten into the integral form below,

$$\int_{J_0}^{J} \frac{-\mathrm{d}J}{J^{2-n}} = K(n) \int_0^t (J - J_n^*)\,\mathrm{d}t = K(n)(v - J^*(n)t) \tag{5.4}$$

where J^* stands for a 'steady-state' flux obtained when t towards infinity and its value depends on the fouling mode, i.e. the n value. The v is the volume of permeate per unit area defined in $V = Av$. The left-hand side (LHS) of eqn 5.4 is an integral function of J and n, which has the integrated expression in terms of each n value listed in Table 5.3.

Table 5.3: Expression in terms of absolute flux J or normalised flux J/J_0 after integration of LHS of eqn 5.4 for all four fouling constant n, respectively

n value	2	1.5	1	0
$\text{fn}(J, n)$	$J_0 - J$	$J_0^{0.5} - J^{0.5}$	$\ln(J_0/J)$	$1/J - 1/J_0$
$\text{fn}(J/J_0, n)$	$1 - J/J_0$	$1 - (J/J_0)^{0.5}$	$1 - \ln(J/J_0)$	$J_0/J - 1$

The first step is to qualitatively evaluate the existence of any change in mechanisms during the filtration by assuming that J^* tends to 0 and checking the linearity on the plots of $\text{fn}(J, n)$ vs v. If the filtration is a single-mechanism process, the plot should show a straight line according to eqn 5.4. Otherwise, any non-linear behaviour on the curve ($\text{fn}(J, n)$ vs v) indicates more complex fouling mechanisms. Field and Wu [31] have shown that 'artificial' fouling data involving consecutive two mechanisms will manifest two sections of straight line with a breakpoint dividing them. For the present experiment, the 50mg/L PEO filtration data under four different TMP are evaluated in this way as shown in Fig. 5.20, which depicts non-linearity in the curves for all four sets. The changing in the slopes of the curves in Fig. 5.20(a)-(c) is apparent, while in Fig. 5.20(d) it is subtle. Therefore, Fig. 5.20 graphically shows the fact that complex mechanisms are involved in the fouling and for all four subplots in Fig. 5.20, the data towards the long term present a relatively straight line for each TMP. However, it is still hard to tell which mechanisms are exactly involved.

Since the flux data at long time tend to be linear, they are plotted as $\text{fn}(J, n)/t$ against v/t to extrapolate the J^* value. This is the second step in the integral analysis. One of them (DB trial under TMP 200 kPa) is shown in Fig. 5.21. The fit for all four n values are apparently all very good. From the gradient and intercept of the linear regression , the long term flux, J^* can be obtained in terms of different n values. For the 200 kPa DB case, the values for J^* are 78.4, 74.5, 71.7, and 13.4 $Lm^{-2}hr^{-1}$ for $n = 2$, 1.5, 1, and 0, respectively. However, the fluxes derived from the primary data had clearly the values below 70 $Lm^{-2}hr^{-1}$, which rules out the lines for n with values other than 0. Therefore, the membrane in the 200 kPa DB case is likely to experience cake formation at the late stage of filtration.

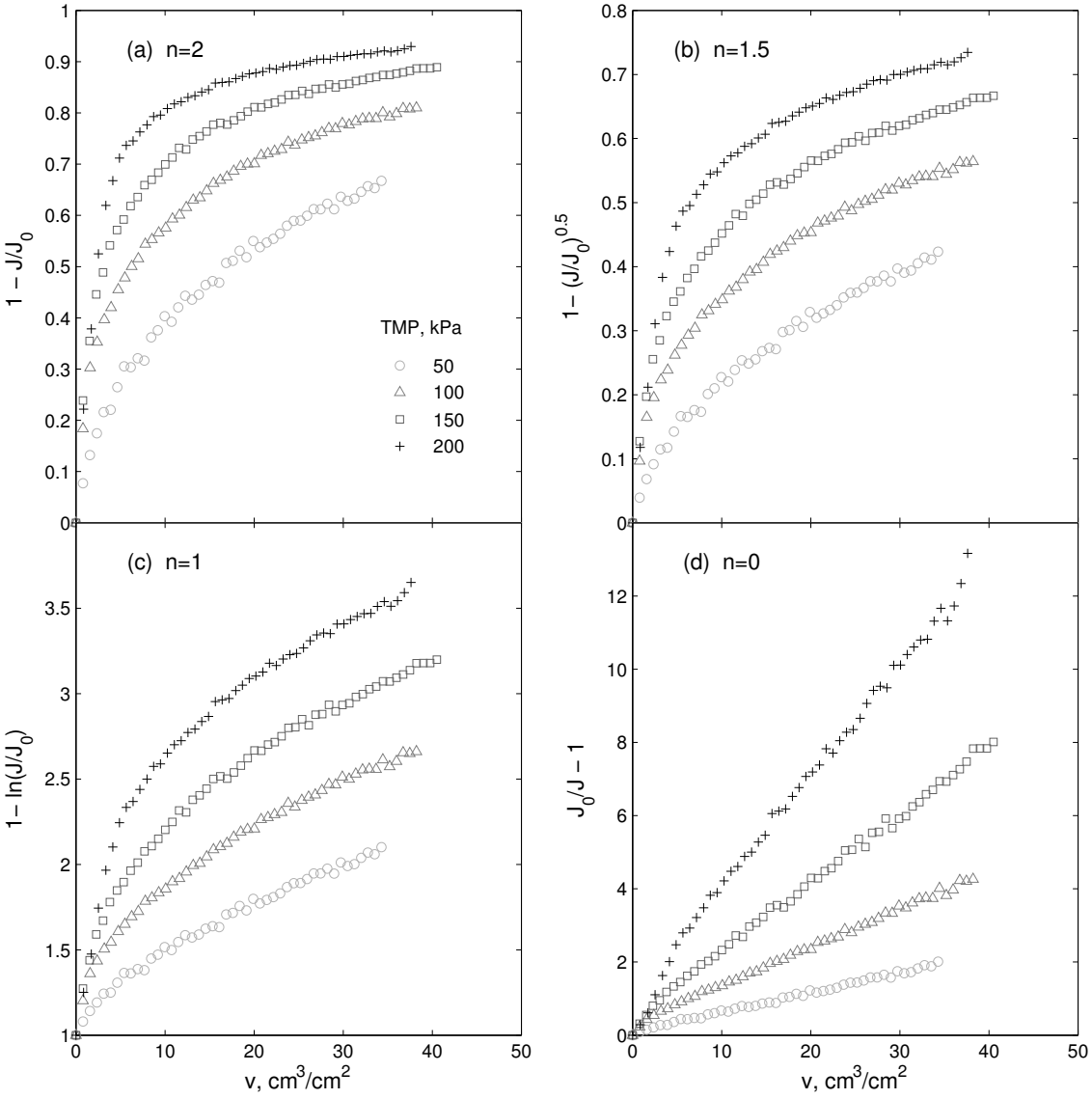

Figure 5.20: Plots of normalised expressions of LHS of eqn 5.4 for different fouling constant n vs. volume of permeate per filter area; First step in the integral analysis to determine the breakpoint for trials of 50 mg/L DB solutions under various TMPs.

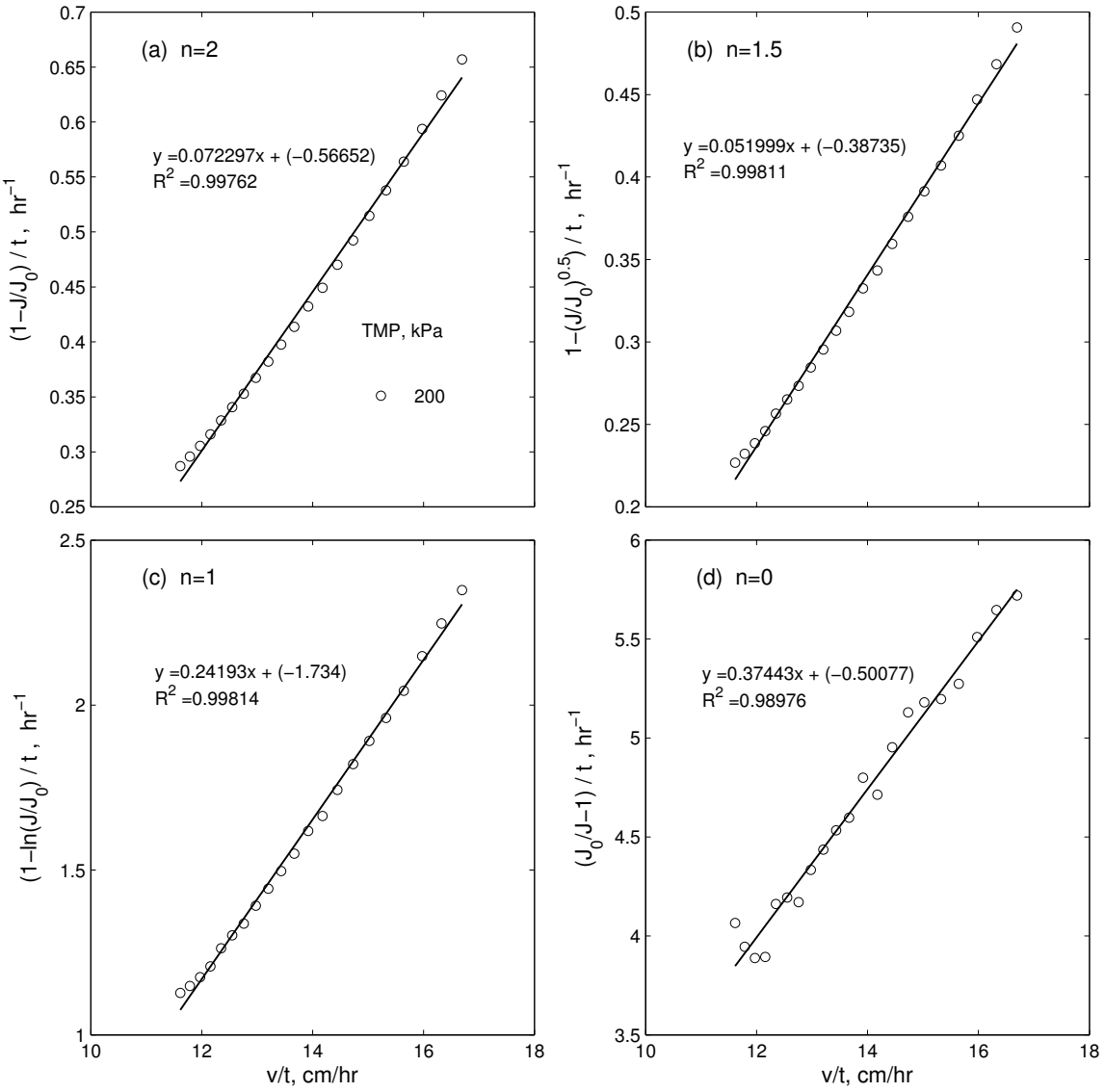

Figure 5.21: Plots of the normalised expressions of LHS of eqn 5.4, at different n values, divided by the corresponding filtration time respectively, against the volume of permeate per filter area divided by the filtration time using the time-volume-flux data after the switch point determined in Fig. 5.20 (200 kPa 50 mg/L DB trial) ; The dotted points represent the calculations from the measured data; the solid lines represent the linear regression to the measured data.

In conclusion, integral analysis is a neat tool to qualify and visualise whether more than one mechanisms involved during filtration. It may also give a quick evaluation on the mode of fouling. It better uses the primary data obtained from filtration experiments by avoiding the need to differentiate. Therefore, it barely requires computational power. However, there lacks of physical meaning on the variables in the plots. It is limited when there is no clear separation between different fouling mechanisms. For fouling at the initial stage, this method cannot distinguish the exact modes.

5.3.5.2 Differential Method

By calculating the two derivative terms in eqn 2.2 from filtrate flux data, the constant n can be calculated as:

$$n = \frac{d[\log(d^2t/dV^2)]}{d[\log(dt/dV)]} \tag{5.5}$$

The required derivatives can be evaluated in terms of the filtrate flow rate;

$$\frac{dt}{dV} = \frac{1}{Q} \tag{5.6}$$

$$\frac{d^2t}{dV^2} = -\frac{1}{Q^3}\frac{dQ}{dt} \tag{5.7}$$

with dQ/dt being a second-order derivative.

Direct differentiation on the experimental $V - t$ data may enlarge the noise to a great extent, especially at the second order. Therefore, the $Q - V - t$ data, used in this analysis, are from the model calculations, with the parameters predetermined, since the fouling models have been proven capable of accurately predicting the flux (or flow rate) and permeate volume with respect to the filtration time. Then, the second derivative, dQ/dt, was evaluated numerically by taking the derivatives of many third-order polynomials, piecewisely fitted to the simulated $Q - t$ dataset, instead of analytically differentiating the equation of the curve.

Figure 5.22, 5.24 and 5.26 show $\frac{d^2t}{dV^2}$ against $\frac{dt}{dV}$ in log-log scale for both experimental and simulated data of DB, PEO and HA trials presented in Sections 5.3.3 and 5.3.4, while Fig. 5.23, 5.25 and 5.27 show the evolution of filtration constant, n, calculated from Fig. 5.22, 5.24 and 5.26, respectively.

In Fig. 5.22(a), the values for d^2t/dV^2 reached a maximum value at low dt/dV, corresponding to the early time of filtration. After the peak value, d^2t/dV^2 started to

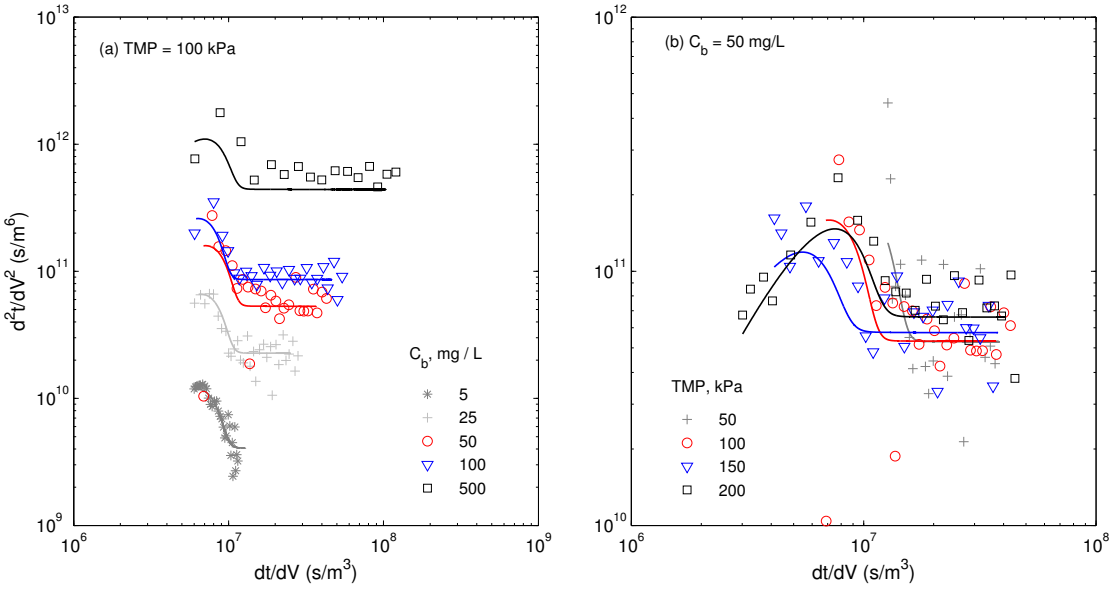

Figure 5.22: Plots of $\frac{d^2t}{dV^2}$ versus $\frac{dt}{dV}$ for DB trials: (a) at various C_b but same TMP (100 kPa) from Fig. 5.5; (b) at various TMPs but same C_b (50 mg/L) from Fig. 5.15. Dots represent experimental data. Solid curves represent model calculations.

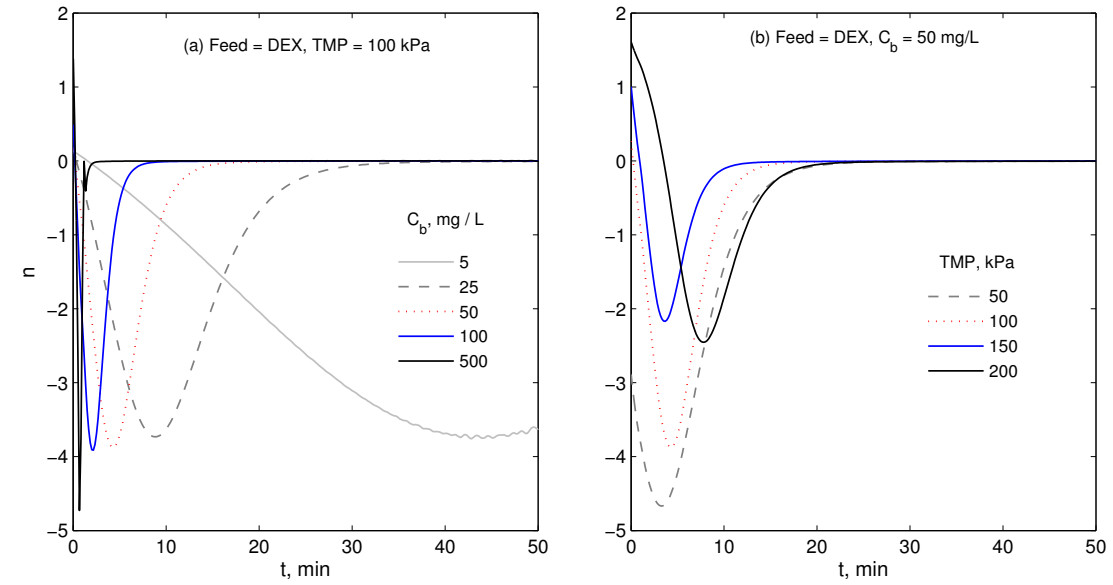

Figure 5.23: The change of filtration constant, n against filtration time, calculated from the simulation using model A for DB trials: (a) at various C_b (same 100 kPa TMP) ; (b) under various TMP (same 50 mg/L C_b).

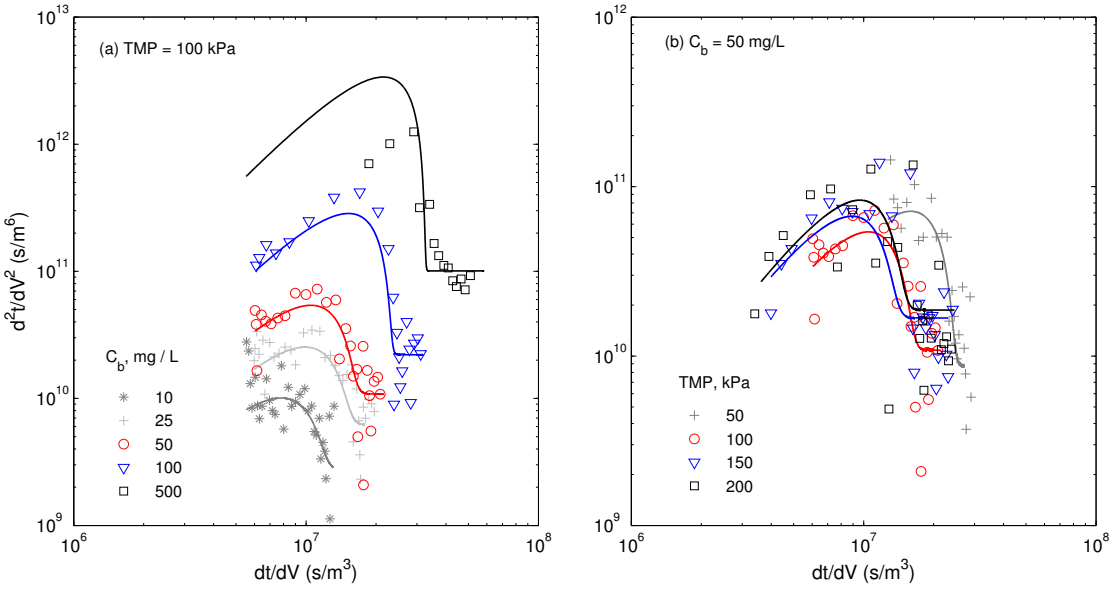

Figure 5.24: Plots of $\frac{d^2t}{dV^2}$ versus $\frac{dt}{dV}$ for PEO trials: (a) at various C_b but same TMP (100 kPa) from Fig. 5.6; (b) at various TMPs but same C_b (50 mg/L) from Fig. 5.16. Dots represent experimental data. Solid curves represent model calculations.

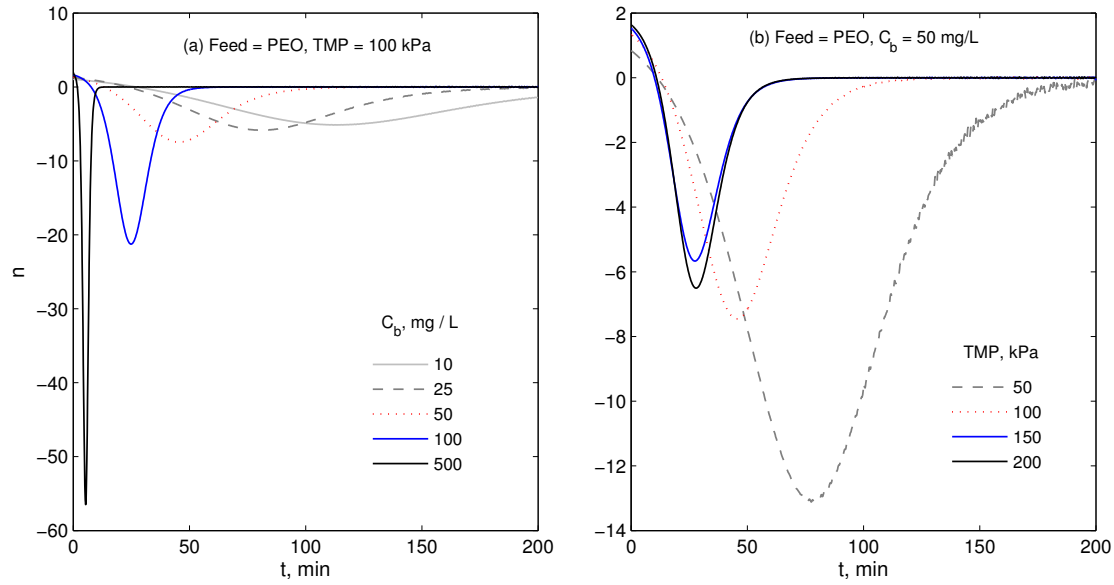

Figure 5.25: The change of filtration constant, n against filtration time, calculated from the simulation using model A for PEO trials: (a) at various C_b (same 100 kPa TMP) ; (b) under various TMP (same 50 mg/L C_b).

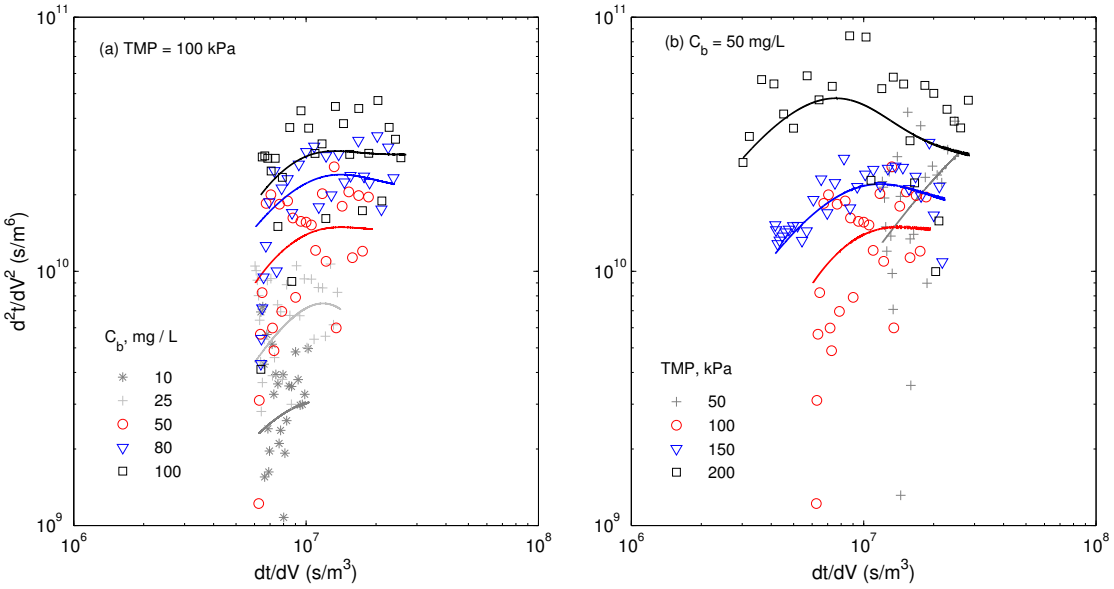

Figure 5.26: Plots of $\frac{d^2t}{dV^2}$ versus $\frac{dt}{dV}$ for HA trials: (a) at various C_b but same TMP (100 kPa) from Fig. 5.7; (b) at various TMPs but same C_b (50 mg/L) from Fig. 5.17. Dots represent experimental data. Solid curves represent model calculations.

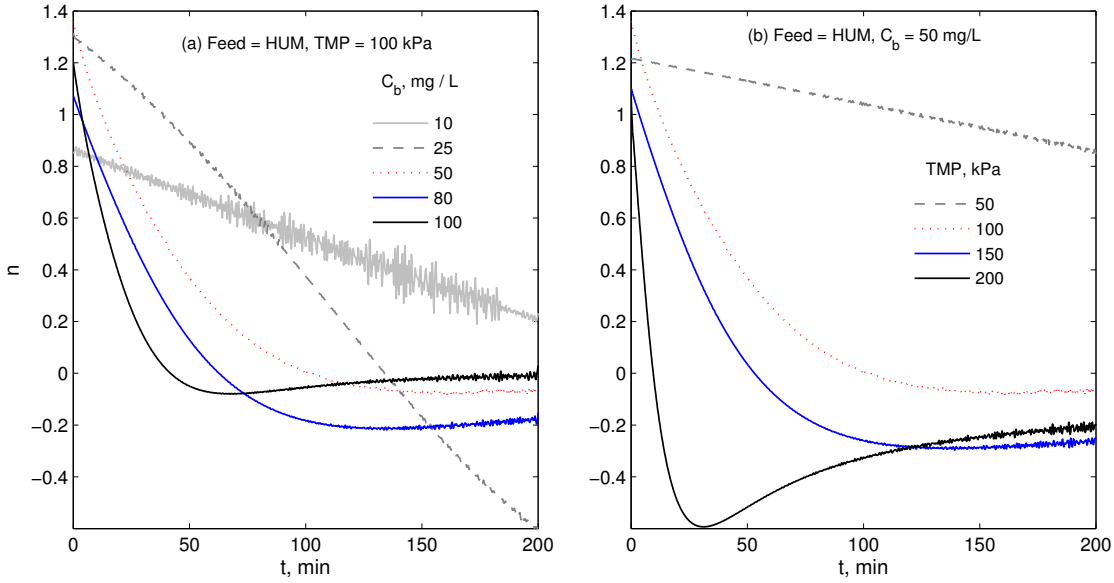

Figure 5.27: The change of filtration constant, n against filtration time, calculated from the simulation using model B for HA trials: (a) at various C_b (same 100 kPa TMP) ; (b) under various TMP (same 50 mg/L C_b).

decrease, resulting in a negative slope, i.e., a negative filtration constant n in eqn 2.2. At the later stage, the curves reaches an asymptotic plateau in the plot for all the cases, at which the filtration reaches a 'pseudo-steady' state, where the ratio between dQ/dt and Q^3 becomes constant. This typical pattern of the curves (the maximum and asymptote) was also observed during MF of protein solution by Ho and Zydney [83], and Duclos-Orsello et al. [88]. The derivations from experimental primary data (scattered points with markers) matched relatively well with those from simulation (solid curves), although more noises appeared in the former.

The difference between trials with different feed concentration manifested in the position and the shape of the curves. Higher bulk concentration caused faster fouling, higher flux decline rate, dQ/dt (see Fig. 5.5), and lower absolute fluxes in most times, hence, leading to higher d^2t/dV^2 in eqn 5.7. Therefore, curves with higher bulk concentration are generally at higher positions in Fig. 5.22. The initial fluxes between the trials of different C_b were almost same since these trials were all conducted under the same TMP, while the long-term fluxes became much lower in the trials with higher C_b since fouling was more severe under higher C_b . Therefore, the difference between initial and long-term fluxes became larger when bulk concentration was higher. Hence, the data range, corresponding to higher C_b, spreads wider on the axis of dt/dV. Furthermore, the asymptotic plateau of the 'pseudo-steady' state at high dt/dV was also across larger range of dt/dV for higher C_b trials.

The filtration constant n in eqn 2.2 were plotted in Fig. 5.23 against filtration time, which was calculated from the slopes of the curves in Fig. 5.22. The initial n values were 0.14, 0.18, 0.27, 0.49 and 1.4 for feed concentrations at 5, 25, 50, 100 and 500 mg/L, respectively. None of them approached to 2.0, i.e., a pure complete blocking case. From the beginning of filtration, n values kept decreasing till a lowest value well below 0. After the bottom stage, n rose back and held constant at a value approximate to 0 for the rest of filtration time, indicating cake filtration dominant in the long run. However, none of the initial and negative n values could be explained by any single mode of classical blocking laws, indicating that these filtration trials underwent complex fouling phenomena. Based on the consecutive complex fouling model developed in Chapter 4, the irregular n values were likely to result from the simultaneous interactions between different mechanisms, i.e. pore blocking and cake filtration. However, since the coefficient n is calculated by differentiating twice V with respect to t (eqn 5.5), the possible errors in the model used to generate the data can have large impact on the values of n.

Bulk concentrations affect the duration of the transition from the initial positive n values to eventual 0. Higher concentration has the shorter transitional time. For example, $500mg/L$ filtration took less than 4 min to reach a constant n value, while the $5mg/L$ run needed more than 180 min. This was the reason that the curve for 5 mg/L solution in Fig. 5.22(a) had a short plateau at high values of dt/dV, corresponding to later filtration time, since the recorded filtration lasted only 200 min while the transition took 180 min to reach the pseudo-steady state.

Given that the assumption of no back transport of deposits, the total weight of deposits was simply calculated from the corresponding permeate volume collected at the time, times the feed concentration. At the time when n approximated to 0, the amount of DB deposits were between $5-10$ mg for all the five cases in Fig. 5.23a.

Fig. 5.22b and 5.23b show the comparative results for 50 mg/L DB trials under different TMPs. Since the initial fluxes changed under different pressures, these fouling curves started at different dt/dV. The data obtained at the higher TMPs started at lower values of dt/dV due to the higher initial flux. At low TMP, e.g, 50 kPa, the curve does not have the characteristic peak plateau, where its slope transits from positive values to negative; instead, it starts with a negative slope ($n = -2.9$) at the beginning of filtration. On the other hand, the other curves, representing the trials with TMPs higher than 100 kPa, all had the transitional peaks in their shape. Especially at 200 kPa, both experimental data and model calculations showed a more distinctive linear increase of d^2t/dV^2 in terms of dt/dV on the log-log graph during early stage of filtration. The resultant slope for the first 150 s filtration was equal to 1.23 calculated from linear regression of the limited experimental data points with a correlation coefficient, $r^2 = 0.994$. It is known that the slope should be equal to 2 given that the filtration is controlled by only complete pore blocking. Apparently, this is not the case. After approximately 25 min filtration, the fouling was dominated by the cake filtration for all the four trials. The period of mechanisms transition is similar between trials under different TMPs in Fig. 5.23b, which is different from the C_b-varying case in Fig. 5.23a. The fouling curves at high TMPs (150 and 200 kPa) have a slightly less steep decline between the peak and the asymptotic values of d^2t/dV^2 . This corresponds to generally less negative n values in Fig. 5.23b.

In comparison with the DB cases, the fouling curves for PEO trials in Fig. 5.24 also show the characteristic peak and asymptotic plateaus. However, PEO curves have more distinctive steady-increase in d^2t/dV^2 at the low dt/dV range corresponding to early filtration time. This trend is more noticeable in curves associated with high C_b or high TMPs, since the degree of flux decline at high C_b (see Fig. 5.6) or high TMP

(see Fig. 5.16) was greater, leading to a longer rising stage of the curves at small dt/dV values in Fig. 5.24. The steady increase appears almost linear in the log-log scale. Fouling curves at higher C_b or higher TMP possess more positive slopes. For example, the initial n value calculated using eqn 5.5 is nearly at 2 for the 500 mg/L case (see Fig. 5.25a), which is a strong indication of the classical complete pore blocking since it predicts a slope at 2 on the same type of plot. The derivatives from experimental measure in the 500 mg/L trial were not placed around the corresponding theoretical curve in Fig. 5.24a. This is due to the fact that the fouling in this case took place too fast (within the first 10s, its permeate flux had dropped 70 %) to be recorded in the experimental condition used here (the interval between each record was set at 10 s). For other PEO trials, the theoretical derivatives coincide relatively well with experimental derivatives.

Similar to DB cases, the temporal n values in Fig. 5.25, calculated from the theoretical curves in Fig. 5.24, reveal the intrinsic difference between the different trials. At high bulk concentration, the fouling exponent index n drops faster and deeper in Fig. 5.25a, corresponding to the fact that the curves of d^2t/dV^2 vs. dt/dV, at higher C_b in Fig. 5.24, have steeper slopes at the transition from the peak to the asymptotic plateau. It appears that the filtration at 10 mg/L and 100 kPa has not reached the pseudo-steady state at the end, since the derived n index did not reach the stable value at 0 yet in 200 min filtration, shown in Fig. 5.25a. For the trials at 50 mg/L, the difference in TMP causes the variance in the n profiles in a similar way as those in DB cases. The index n varies greater at low TMP. However, unlike those in DB cases, the trials of PEO at low TMP requires more time to approach to the eventual 0 point.

Figure 5.26 and 5.27 depict the fouling curves for HA filtration. The curves in both figures have generally different shapes to those of DB and PEO trials. In Fig. **??**, the fouling curves of HA trials only show a diminished hump. For the smaller dt/dV, the second-derivative term slowly increases and gradually flattens out so that the positive slope decreases. For the trial at $C_b = 100$ mg/L, after a vague peak, the curve dip marginally and level off eventually, and for trials at $C_b < 100$ mg/L, their curves have not yet held steady at the end of 200 min filtration; while for trials at $C_b = 10$ mg/L or TMP = 50 kPa, their curves have only a rising stage within the studied range.

The flattened shape of HA fouling curves is reflected in the corresponding n profiles in Fig. 5.27, which do not display the nearly symmetric 'U' shape like those in PEO and DB cases, but, instead, a drop to certain values slightly below 0 at a moderate

rate followed by a gradual bounce back towards 0. However, for bulk concentrations lower than 50 mg/L, n profiles only consist of a constantly declining curve within the 200 min filtration. It is only in the curve associated with conditions of 50 mg/L feed solution and 200 kPa TMP that a relatively sharper transition can be observed.

The unique pattern in the fouling curves and n profiles in the case of HA ultrafiltration, compared to the other two large macromolecular cases, is likely due to the smaller size of the HA molecules, which allows the pore constriction to process gradually and longer, and prevents the fast complete blocking process. Therefore, the transition between different phases of fouling is less dramatic in the case.

5.4 Summary and Remarks

Macromolecular fouling is a complex phenomenon even when only one type of macromolecules existing in the feed. In order to describe the process preciously, the combined blocking models formulated in Chapter 4 were employed to fit experimental filtration data for three types of feeds, including Dextran Blue (DB), Polyethylene Oxide (PEO), and Humic Acid (HA), to obtain a better understanding of the fouling mechanisms involved in UF of dilute macromolecular solutions under constant TMP.

There were several findings concluded in the three main areas as follows:

5.4.1 Model Applicability

In the study, size exclusion is assumed to be the main filtration mechanism. Then, the relative size of the macromolecule to the pore size of the membrane is the criterion to choose the form of the model.

For DB and PEO molecules, they have sizes larger than or comparable to the pore size. Their fouling behaviours were expected to be similar, which was indeed verified in the work. For them, the model (namely Model A), then, comprises two blocking laws, i.e., pore blocking and cake formation, with three coefficients to be determined by curve-fitting, namely pore blocking rate (σ), additional resistance (R_b), and specific cake resistance (α).

The HA used in the study has a broad size distribution, with main portions smaller than the pore size of the 100 kDa membrane. The model for this case (namely Model

B) has one additional mechanism, i.e., pore constriction, including an extra coefficient, i.e., pore constriction rate (β).

Models were fit to the experimental flux-time data to determine the coefficients. The results showed a good fit between the model and experimental data, on the flux-time, volume-time, and resistance-time plots for each feed type, respectively. The consistency in the values for each coefficient determined under conditions of various bulk concentration (C_b) has been proven good, especially, in the case of DB.

5.4.2 Filtration Parameters

The effect of bulk concentration (C_b) and TMP was investigated in the experiments, respectively. Generally, higher C_b or higher TMP is found to cause faster pore closures. In the flux decline graph, trials under these conditions have faster and greater decline at the early stage, and hence more obvious transitions between early and late stages.

The four model coefficients are dependent of the macromolecular type. In theory, they are expected to be independent of C_b which are well verified in the case of DB but there are rather large variations in some coefficient values in the case of DB and HA, for example, R_b of DB and β of HA. Some coefficients also change with a varying TMP. For example, the effect of TMP on the specific cake resistance (α) has been shown following a well-known power-law correlation for all three feeds.

Moreover, for other coefficients, TMP has inconsistent effects for different feeds. For instance, DB case has the pore blocking rate (σ) decreasing under an increasing TMP, while the PEO and HA cases have constant σ within the tested TMP range (50 - 200 kPa). The increase in TMP also results in an increasing R_b in the case of DB and PEO, but does not affect that in HA case. The specific functions for the coefficients, σ, R_b and β, are not totally clear. In general, the four model coefficients are determined by the characteristics of the feed macromolecules.

5.4.3 Evolution of Fouling Mechanisms

Experimental results showed multiple stages during flux decline and resistance rise in UF of any one of the three feeds. The explanation, based on the complex fouling scenarios related to the models, is due to the sequential change of dominant fouling mechanisms through the filtration course.

At the pore scale, Model A predicts that pore blocking takes place first and then further deposits can build upon the blocked areas to form fouling cakes, while Model B, being essentially a more general case of Model A, assumes that small particles deposit inside the membrane pore before it is blocked by large particles, i.e., pore constriction can happen only before the pore is closed. Over the whole surfaces, spatial variance exists, which permits different areas in the membrane surface to be in different stages.

Applying integral analysis to the primary experimental data clearly showed the breakpoint of fouling mechanisms switching and helped determine the dominance of cake filtration at the later stage of filtration. Differential method using the model calculations confirmed this finding, and further revealed that the early stage of fouling is a complex situation, controlled by the interplay of different mechanisms at the same time. This mixture of mechanisms at the macroscopic level is due to the spatial variation, represented by the blocking time distribution in the models.

Differentiation on the model calculations can explicitly determine the fouling index n used in the classical blocking theory, and hence can be considered superior in terms of fouling mechanisms study. However, integral analysis avoids complicated numerical computation and prevents amplifying the noise existing in the experimental data, and is really useful when there is a clear cut in the data. Therefore, integral analysis is preferable for being a quick and neat tool to check the raw data at the first place.

Chapter 6

Examination of Macromolecular Deformation in UF and Its Impact on Fouling

6.1 Introduction

In the last chapter, membrane fouling was analysed using combined fouling models. The determined fouling parameters indicate the changing in the experimental conditions may trigger behavioural changes in the macromolecules, leading to some specific impacts on fouling. The large macromolecules used in this work, including both DB (MW = 2000 kDa) and PEO (MW = 100 kDa), are linear polymers, possessing flexible long chains in their molecular structure. In general, such molecules are well known for their deformability in a flow field [235]. There have been a few extensive studies both theoretically and experimentally on the relative flow-induced transformation of linear chains. Although some researchers [236–239] have observed the forced permeation of macromolecules in UF during recent years, none of them have studied linkage between the polymeric deformability and membrane fouling. Therefore, in this chapter, the effect of macromolecular deformability on UF fouling will be discussed in the light of some observations during experiments conducted in the previous chapter. Before presenting our results, a brief review of the literature regarding UF of deformable macromolecules is introduced. Note that the present work is restricted to dilute macromolecular solutions.

6.2 Review on UF of Deformable Macromolecules

From a pure steric viewpoint of UF, regardless of any specific interactions between solutes and the membrane, the solutes with smaller sizes than the pores can pass through the membrane while those of a size comparable to or larger than the pore sizes will be retained by the filter. This is true for rigid solutes with fixed shapes. For example, protein typically having a globular structure with relatively little molecular flexibility is often treated as a rigid sphere in UF studies [240]. In the dilute regime, therefore, the parameter that controls the passage of a macromolecule is the ratio λ of the molecular dimension to the pore size. For $\lambda > 1$, the macromolecule will be excluded by the membrane. For $\lambda < 1$, macromolecules can enter the pores and may eventually transfer into the permeate side, and their transport in the pores has been well studied using the *hydrodynamic hindrance theory* by assuming each macromolecular solute as a hydrodynamic particle enduring hindered movement in the confined space, i.e., a pore [241–243].

However, this theory does not work well with deformable macromolecules when they have $\lambda > 1$ in a filtration process due to some other aspects related to their characteristic molecular structures. For example, their non-spherical molecular shape solutes will cause them to sacrifice rotational freedom [244], and their flexible nature will lead them to sacrifice conformational freedom to enter the channel [245]. This will come at an entropic energy cost which can greatly reduce the partitioning effect at the pore entrance, i.e., the probability to enter membrane pores [246].

Moreover, soluble polymeric macromolecules naturally adopt a conformation of random coils and are tightly filed in a static and dilute condition. Their molecular chains undergo random motions in the solution, and hence, the random variations in their molecular shapes are constant.

Furthermore, these randomly-coiled polymeric chains are well-known to be flexible, which can deform when they are perturbed. For example, when such a macromolecule is exposed to a shear flow, its molecular shape may be distorted because of the difference in velocity between the two sides of the random coil [247]. In theory, the conformation of a deformable linear polymer chain can change from a random coil to a stretched one under a flow velocity gradient if the product of the strain rate and the largest relaxation time of the unperturbed chain is larger than a certain threshold [236]

In UF, a relatively fast converging flow field will exist at the pore entrance when a TMP applies. If the flow is fast enough to set up a sufficiently high longitudinal

gradient at the pore entrance, a flexible macromolecule will be stretched in the flow direction to such a point that the macromolecule arrives at the pore entrance with a transversal section smaller than the entrance diameter [248]. Then, this macromolecule may enter and eventually pass through a pore much smaller than its unperturbed size. This phenomenon is often regarded as the flow-induced translocation of linear polymer chains.

According to the theory of de Gennes [249], a linear polymer chain can undergo a sharp transition from coiled to stretched state when its surrounding velocity gradient reaches a 'critical' value. Such phenomenon has been observed in several experimental studies. For example, Perkins et al. [235] and Smith et al. [250] observed the conformational change of a single DNA molecule in an elongational and a steady shear flow field, respectively. Although the 'sharpness' of the transition is still in debate, the theory essentially guided to develop the 'affine stretching model' to describe the penetration of linear polymer chains into cylindrical pores driven by solvent flow. To apply their theoretical calculation to membrane filtration case, Nguyen et al. [247] assumed that:

- The membrane surface has only circular, uniform, equidistant pore openings.
- The polymer adsorption on the solid surface is negligible.
- The flow near the membrane surface is laminar, unperturbed and of negligible inertia.
- The fluid is not agitated

Using the scaling approach [249], Daoudi and Brochard [248] evaluated the static partition coefficient (i.e., the ratio of the solute concentration inside the pore to the solute concentration outside) of polymers in a good solvent for both dilute and semi-dilute solutions.

Hirasaki et al. [251] examined DNA filtration through membranes with mean pore diameters of 15 and 35 nm. They observed that the fractional transmission for the DNA was significantly larger than that for globular proteins of comparable molecular weight and transmission of larger linear DNA increased with increasing TMPs. The high transmission of the DNA was attributed to the elongation or deformation of the DNA molecules due to the shear stress associated with the filtrate flow.

Recently, Jin and Wu [236] observed a discontinuous transmission during UF experiments of flexible linear polymer chains (Polystyrene, $\lambda > 1$) using a specially-designed double-layered membrane, which was specially designed to prevent interaction among flow fields generated by different pores. This was the first experimental proof of the predicted 'first-order' transition by de Gennes [249]. Then, the flow-dependent permeation of long linear macromolecules of high molecular weight through small pores has also been reported during UF of dextran (2000 kDa) [238], PEO (1000 kDa) [239], and biopolymers such as DNAs [237, 240, 252]. It is worth mentioning that the later experiments were conducted on common polymeric membranes and the results showed a gradual change in polymeric permeation by varying the permeate flux instead of a sharp change observed by Jin and Wu [236].

6.3 Experimental Observations on Sieving and Fouling

During the experiments presented in the last chapter, the permeate concentration, C_p, was measured by collecting 5 ml permeate at particular time points during a filtration. Then, these data were used to calculate the observed sieving coefficient;

$$S_o = \frac{C_p}{C_b} \tag{6.1}$$

where the bulk concentration, C_b, has been proved to be same as the feed concentration. This type of information was commonly used in other studies [237–239] to evaluate the flow-induced transmission of large polymers in UF, while in the present work, this information was used to investigate the relationship with the membrane fouling, particularly, pore blocking phenomena at the early stages of filtration.

6.3.1 Macromolecular and Pore Size Estimations

Firstly, the dimensions of the macromolecules and membrane pores were quantified in order to show the size comparison between them.

The Ultracel RC 100 kDa membrane used in the present experiments has been estimated to have porosity (φ) at 0.5 in several studies [252, 253]. The thickness of

the membrane skin layer (δ_m) was estimated as 1.0 μm [252]. The mean pore radius (r_p) was then calculated using the Hagen-Poiseuille equation as :

$$r_p = \left(\frac{8\delta_m L_p}{\varphi} \right)^{1/2} \tag{6.2}$$

where the membrane hydraulic permeability was determined using

$$L_p = \frac{1}{R_m} = \frac{J\mu}{\Delta P} \tag{6.3}$$

from the DI water filtration experiments conducted for each fresh membrane, which gave a mean value at $1.22 \pm 0.07 \times 10^{-12}$ m. The mean pore radius is thus estimated to be approximately 4.4 nm. The estimated value depends upon the assumptions and varies between 1.6 and 7.0 nm when it is calculated using assumed thickness from 0.2 to 1 μm and porosity from 20 to 80 %.

The dimensions of polymers in solution are usually measured using the radius of gyration, r_g, and hydrodynamic radius, r_s. They are both statistical averages over the many configurations of the molecule due to its random motion. For the two polymers, DB and PEO, used in this work, their sizes were estimated using empirical correlations in the literature.

For general dextran solutions, the following correlation was used to estimate the hydrodynamic radius [238, 254]:

$$r_s = 0.0282(MW)^{0.47752} \tag{6.4}$$

with r_s in nm and MW in Da. Hence, the dextran blue used in the work with a nominal molecular weight (MW) of 2×10^6 Da was calculated to give r_s equal to 28.8 nm, and its radius of gyration (r_g) was then estimated from the r_s value according to the Zimm model [8, 238] to approximately 45.0 nm. These two estimated values were in good agreement with those recorded in the literature [255].

For the PEO (MW = 1×10^5 Da) used here, the following relationship [256] was used to determine the hydrodynamic radius;

$$r_s = 0.0145(MW)^{0.57} \tag{6.5}$$

which gave r_s equal to 10.3 nm. Then, from the Zimm model [8], the radius of

gyration was estimated approximate to 16.1 nm.

6.3.2 Effect of TMP on Sieving Coefficient

6.3.2.1 Temporal Variation of Sieving Coefficient

Fig. 6.1 shows that the observed sieving coefficient, S_o, changes during 50 mg/L DB filtration experiments under different TMPs. At the beginning of the filtration, higher sieving coefficients were observed in trials under higher TMPs. For trials under 50 kPa TMP, negligible amounts of DB molecules passed through the membrane at all times, but the sieving coefficient reached almost 0.7 and 0.6 for trials under 200 and 150 kPa, respectively.

From the estimation, the molecules of DB samples used in this work have a considerable larger size than that of the pores. Therefore, if the molecule is not deformed, it should not be able to pass the pores, and instead, it will block the pores when arriving at the membrane surface. At 50 kPa, it appears that the hydrodynamic forces related to the flow field are not able to elongate the macromolecular chains to a shape with a transverse section smaller than the pore diameter. Therefore, no DB could pass through the membrane to the permeate side at all times. On the contrary, there may be forced permeation of DB chains happening when TMP is larger than 50 kPa at the beginning of filtration. Higher TMP caused apparently more DB molecules permeating through the membrane at 2 min of filtration as shown in Fig. 6.1. The difference in S_o between the 50 and 200 kPa trials reached about 70 %.

After 20 min filtration, the membranes in all trials became almost impermeable to the DB molecules. This is likely due to the pore blocking developed over time, which is discussed and shown following. The fractions of blocked pores, F, are plotted in Fig. 6.2 using eqn 4.16, with the coefficients determined from Fig. 5.15. It shows that the membrane pores have been fully blocked by 20 min filtration for all trials. The blocking curves for 50 kPa has the slowest growth rate so that it takes nearly 15 min to reach >99 % pore coverage. For other curves, their membranes have almost all been blocked by 10 min. This is mainly because of the smaller value of J_0 arising from a lower TMP in the combined blocking parameter k_b equal to $\sigma C_b J_0$ defined in eqn 4.16. Hence, in general, higher TMP causes a faster increase in F, except for the curve at TMP equal to 200 kPa, which apparently had a slightly slower trend than those at TMP equal to 100 and 150 kPa. This exception is caused by the other

component in k_b, i.e., the blocking rate σ (see eqn 4.17), since σ decreases as TMP increases (see Fig. 5.18).

At high TMP, the molecules are more likely to be stretched under the elongational flow field just above the pore entrance. DB molecules have higher probability to enter the permeate side, and hence less chance for pore clogging taking place. At the same time, since the stretched DB molecules more easily enter the membrane pores, they may form deep bed clogging inside the pores, instead of surface clogging. This may be the cause for a higher blocking resistance, R_b, at high TMP in Fig. 5.18.

Figure 6.3 shows the decline of the sieving coefficient S_o during 50 mg/L PEO filtrations under different TMPs. Similar to those in DB case, the S_o is apparently higher at the beginning of each trial. Then, it drops as membrane fouling proceeds. Unlike the DB case, there are still fractions of PEO molecules in the permeate at the beginning of filtration under TMP equal to 50 kPa. This is likely due to the close sizes between the PEO molecules and the membrane pores, allowing easy passing of unstretched PEO molecules through the membrane at low TMP.

Figure 6.4 gives the total blocked areas (F) of a membrane in the case of PEO discussed above in Fig. 6.3. Compared to the filtration of DB solutions, the blocking rate is generally smaller in PEO cases. For example, it took almost 120 min to achieve more than 99 % pore blockage at TMP equal to 50 kPa. In higher TMP cases, the fastest case is with TMP equal to 200 kPa, which still needs more than 30 min to reach a full blocking coverage.

Unlike the DB case, there is no exception to follow the general trend that the higher the TMP, the higher the rate of the increase of F in this case. The curve associated with 200 kPa is the one that rises fastest and approaches earliest to unity. The explanation is that the blocking rate, σ, is not significantly affected by the change of TMP, which can be seen in Fig. 5.18 of the previous chapter; and therefore the change of pore blocking constant, k_b, according to eqn 4.17, is mainly controlled by the change in J_0 between curves, which monotonically increases with the rise of TMP.

Similar to the DB case, Fig. 6.3 also shows the difference between the S_o curves from trials under different TMP. In general, higher TMP leads to a higher S_o at the initial stage until 30 min of filtration, when the trial at TMP equal to 150 and that at 200 kPa have their S_o values dropping below those from the curves at TMP equal to 50 or 100 kPa. This may correspond to the fact that the majority of the pores for the cases with higher TMP ($\geq$ 150 kPa) had been clogged by 30 min shown in Fig. 6.4, while trials at lower TMP ($\leq$ 100 kPa) still had significant fractions of pores

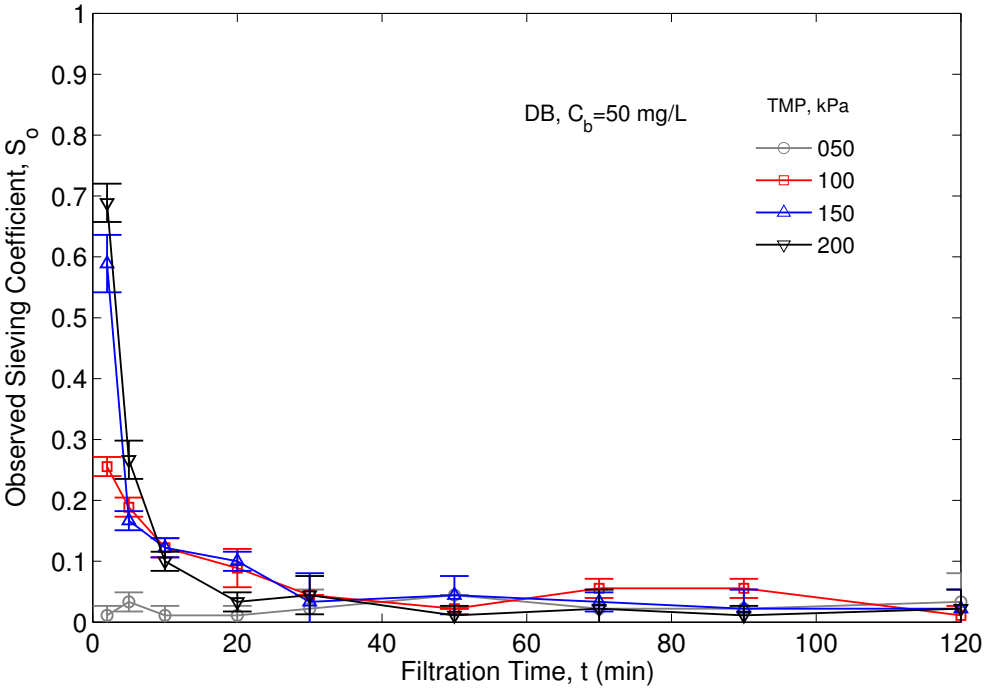

Figure 6.1: Obsersved sieving coefficient, S_o, as a function of the filtration time during UF of 2000 kDa DB through the 100 kDa RC membrane at 50 mg/L feed concentration and various TMPs.

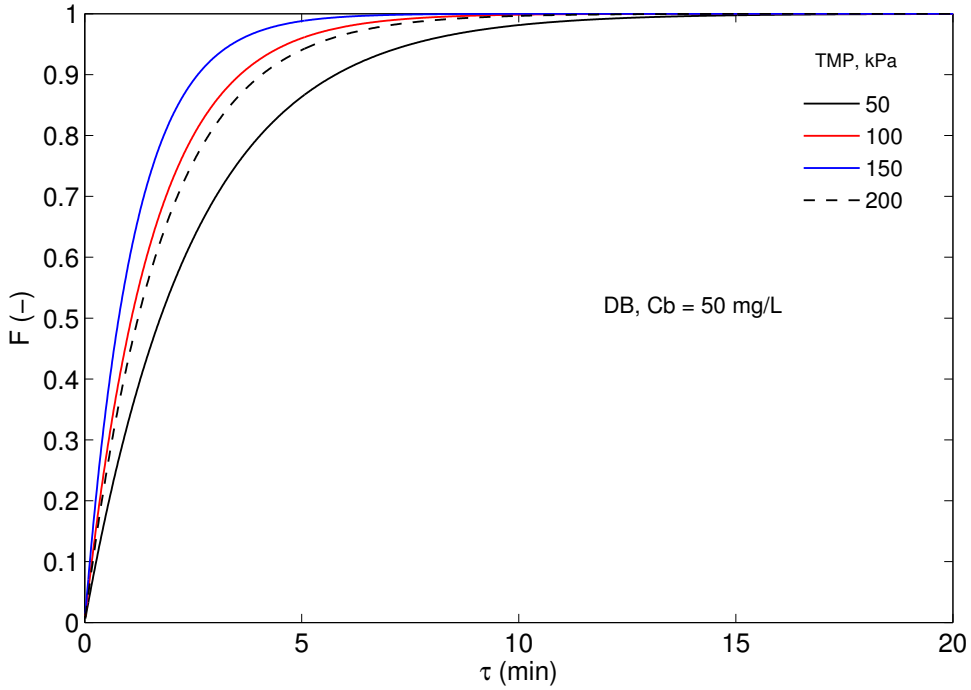

Figure 6.2: Fractions of blocked pores as a function of the filtration time during UF of 2000 kDa DB through the 100 kDa RC membrane at 50 mg/L feed concentration and various TMPs.

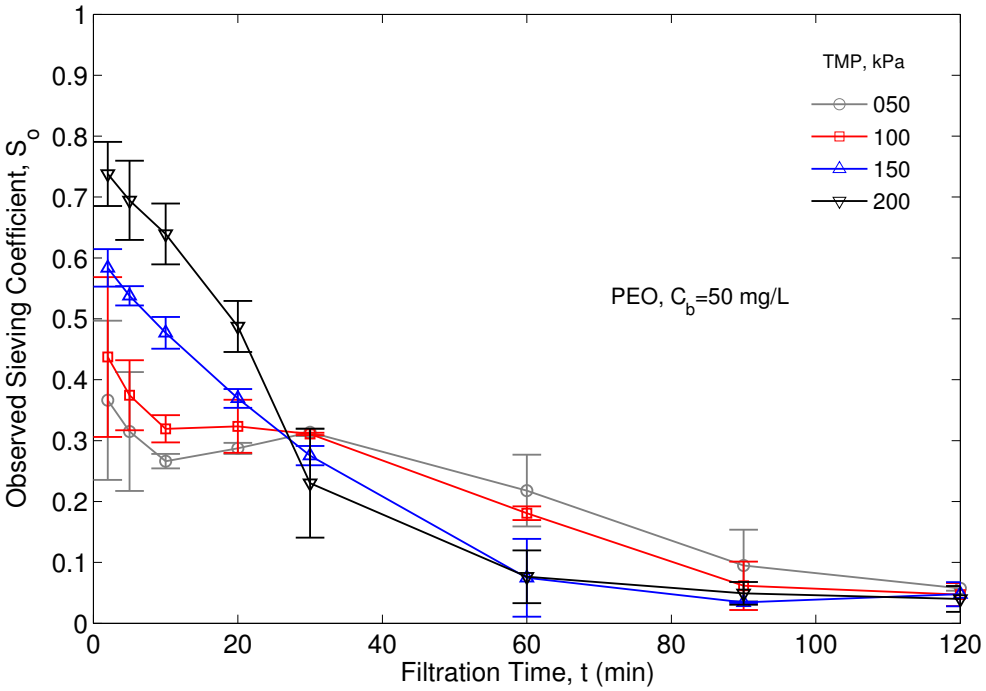

Figure 6.3: Obsersved sieving coefficient, S_o, as a function of the filtration time during UF of 100 kDa PEO through the 100 kDa RC membrane at 50 mg/L feed concentration and various TMPs.

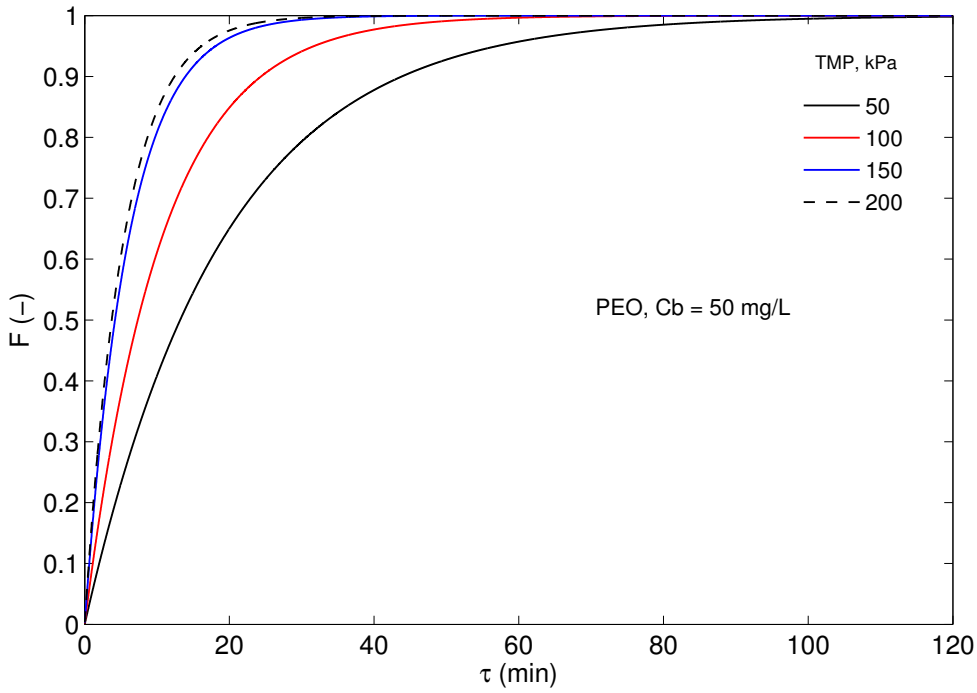

Figure 6.4: Fractions of blocked pores as a function of the filtration time during UF of 100 kDa PEO through the 100 kDa RC membrane at 50 mg/L feed concentration and various TMPs.

remaining open. After 30 min, the 50 kPa trial has the highest PEO permeation, just followed by the 100 kPa trial, until the end of 120 min when membranes in all four conditions become almost all impermeable to the solutes. In fact, both the 150 and 200 kPa trials have nearly reached the bottom of S_o by 60 min.

Comparisons were drawn between the sieving results of the two feeds (see Fig. 6.1 and 6.3). In general, PEO trials have higher sieving coefficients than the counterpart trials in the DB case in most of the time shown in these two figures. This is much expected since DB has much larger sizes than those of PEO and membrane pores. In fact, if there were no deformation of DB macromolecules, the permeation in all DB trials should have be insignificant just like the one at 50 kPa in Fig. 6.1. However, in the actual results, the S_o of the DB trial at high TMP (150 or 200 kPa) is very much comparable to that of the counterpart in the PEO case by 2 min of filtration.

6.3.2.2 Permeate Flux vs Sieving Coefficient

Figure 6.5 collates and displays the observed sieving coefficients (S_o) by the end of 2 min of every trial depicted in Fig. 6.1 and 6.3 versus the corresponding permeate fluxes at the same time. For the DB case, the results from extra experiments under 30 kPa TMP with C_b equal to 50 mg/L are included. Instead of showing the mean values, data from the duplicates conducted under the same condition are both plotted in the graph. Fig. 6.5 is a semi-log graph with the x-axis, representing the permeate flux, in log scale. Shown in the graph, the sieving coefficient is a strong function of the permeate flux in the case of DB filtration, with S_o having increased by more than 70 % when J_t increases from approximately (55 to 133) μm/s (corresponding to TMPs from 50 kPa to 200 kPa). At lower TMPs of (30 to 50) kPa, i.e., flux lower than 55 μm/s, the sieving coefficient was not significant ($S_o < 0.02$). By linear regression of the data corresponding to trials above 50 kPa TMP, the intercept on the x-axis gives a flux value of approximately 60 μm/s, equivalent to a shear rate at the inner wall of the pore channel ($\dot{\gamma}$) of around 5.45×10^4 s^{-1} (using the relationship of $\dot{\gamma} = 8v/d$, where d is the average diameter of a membrane pore and v, the linear velocity, equals to the average flux). This is an important quantity which is related to the threshold between passing or non-passing of a polymer, undergoing the flow-induced deformation, through a small pore, which is discussed in detail in next section.

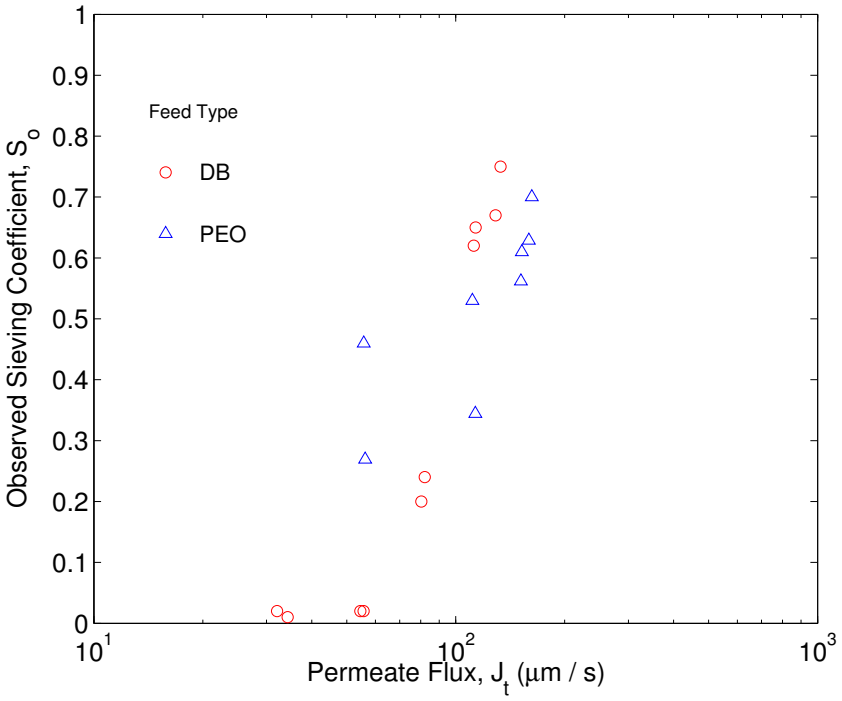

Figure 6.5: Plot of observed sieving coefficient (S_o) against the permeate flux (J_t) for both DB ($\circ$) and PEO ($\triangle$) trials at the bulk concentration of 50 mg/L. Both quantities were obtained at the 2^{nd} min of each filtration. Data from duplicate experiments were plotted together.

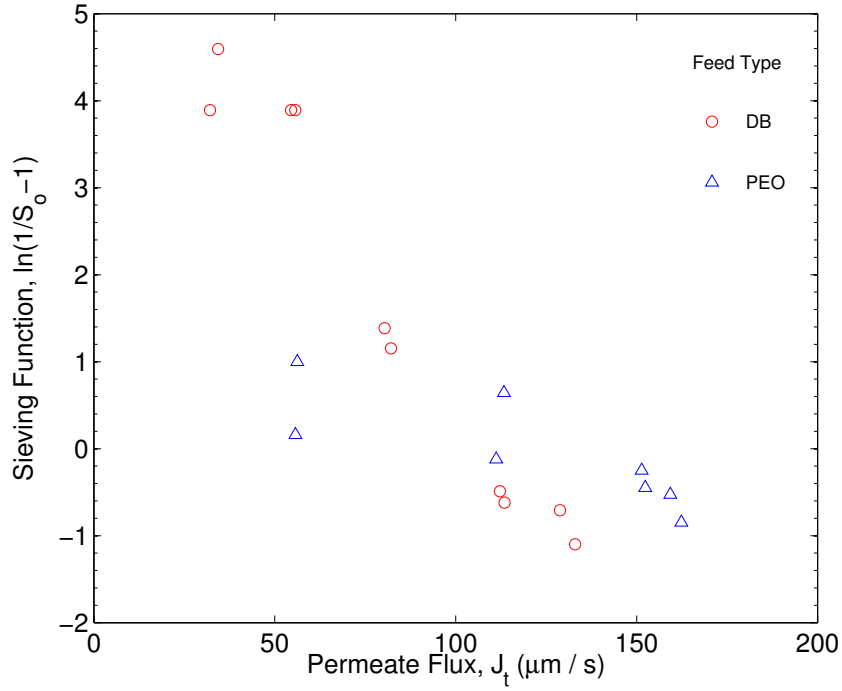

Figure 6.6: Plot of $ln(1/S_o - 1)$ against the permeate flux (J_t) for data in Fig. 6.5.

For the PEO case, the sieving coefficient increases with the permeate flux in general. For high fluxes corresponding to 150 and 200 kPa TMPs, such increasing trend appears quite linear on the graph. However, at low fluxes corresponding to 50 and 100 kPa TMPs, there are large deviations in sieving coefficient between duplicate trials. Within the range of TMPs tested, some PEO transmission is present in all trials. This is partly due to the similar dimensions between the pores and macromolecules. Although the calculated values of the hydrodynamic radius of PEO is about 2 times larger than the mean radius of the membrane pores, PEO chains are flexible enough to enter the pores or at least those larger ones, and go through.

It should be noted that in the present experiments, no mechanical agitation was applied during filtration. Therefore, on top of the effect of forced permeation, the effect of concentration polarisation on the sieving coefficient should not be neglected. Using the classical 'stagnant film theory' [242], the membrane sieving coefficient can be expressed as;

$$S_o = \frac{S_a}{(1 - S_a)exp(-J/k_m) + S_a} \tag{6.6}$$

where S_a is the actual sieving coefficient, equal to C_p/C_m, i.e., the ratio of the permeate concentration to the solute concentration at the upstream surface of the membrane; J is the permeate flux; and k_m is the mass transfer coefficient averaged over the membrane surface. By rearranging eqn 6.6, it can obtain:

$$ln\left(\frac{1}{S_o} - 1\right) = ln\left(\frac{1}{S_a} - 1\right) - \frac{J}{k_m} \tag{6.7}$$

According to this equation, the sieving and flux data from Fig. 6.5 were plotted as $ln(1/S_o - 1)$ and J in Fig. 6.6. From the plot, the change in the $ln(1/S_o - 1)$ term is roughly linear with the flux change at the low TMP range but it appears non-linear towards high flux range for both DB and PEO cases. This increase in sieving coefficient with increasing permeate flux may not be solely contributed to the concentration polarisation effect. The flow-induced deformation of the macromolecules is likely to be one of the cause.

6.3.3 Fouling Reversibility and Macromolecular Deformability

Fouling reversibility is evaluated using the indices [39] deduced from the flux data obtained in experiments. Referring to the filtration protocol in Fig. 5.2, the initial DI water flux was measured using DI water (stage b) just before solution filtration and referred to as J_0; the permeate flux achieved at the end of the macromolecular filtration (stage c) as J_f; and the DI water flux determined after backwashing (stage f) as J_c. The index for the total fouling is:

$$TF = 1 - \frac{J_f}{J_0} \tag{6.8}$$

representing the total flux decline at the end of the fouling experiment; while the index for the irreversible part of fouling is expressed as:

$$IF = 1 - \frac{J_c}{J_0} \tag{6.9}$$

representing the unrecoverable part of the flux loss after backwash. One can also normalise IF with TF to obtain:

$$nIF = \frac{IF}{TF} \times 100\ . \tag{6.10}$$

Therefore, nIF represents the percentage of hydraulic irreversible fouling with respect to the total fouling.

The reversibility tests were routinely conducted for the set of fouling experiments running in the course of 200 min. Results for DB and PEO trials at C_b equal to 50 mg/L are shown in Fig. 6.7. In general, higher TMP leads to a more irreversible fouling for both feed types. This is obvious in the case of DB. At low TMP ($<$ 100 kPa), DB fouling is relatively reversible but, at high TMP ($>$ 100 kPa), it is much more irreversible. The gap between the trials at 50 kPa and 200 kPa is more than 40 %. For PEO trials, their fouling has relatively high irreversibility ($>$ 50 %) at the whole range of TMPs. The differences between all PEO trials are subtle and within a range less than 10 %. Hence, the disparity in nIF between DB and PEO trials at the same TMP narrows down as TMP increases. At 200 kPa, the irreversibility indices are both slightly above 60 %, with the one for PEO being marginally a little

bit higher.

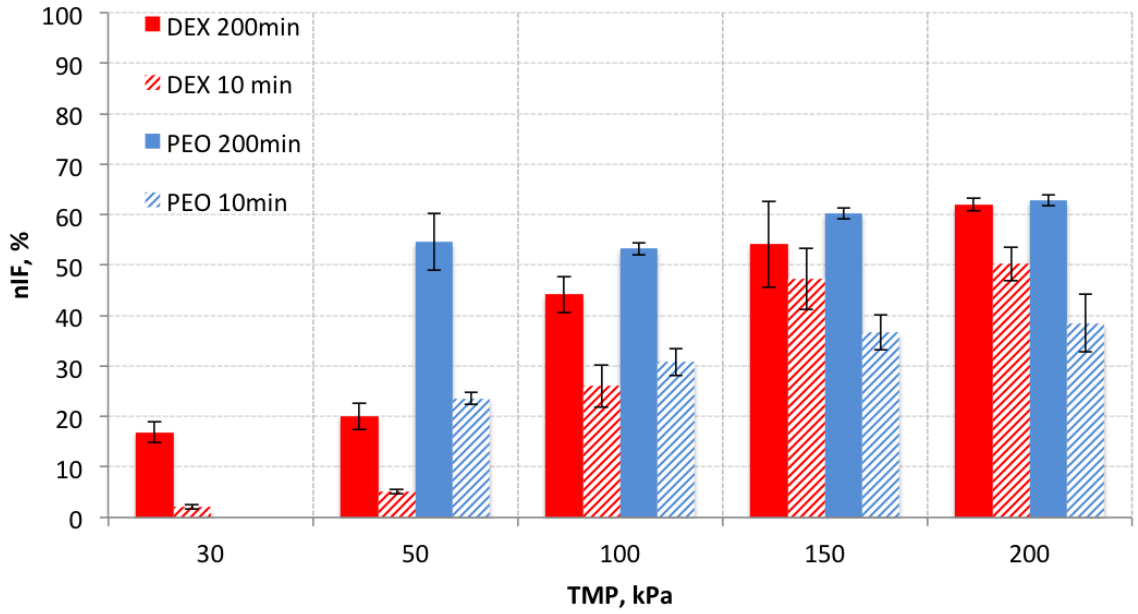

Figure 6.7: Normalised fouling irreversibility index (nIF) determined for 50 mg/L DB and PEO filtration trials at different TMPs and different filtration duration. No data available for PEO trials at 30 kPa.

Another set of timely shortened experiments, where the macromolecular filtration (stage c in Fig. 5.2) was only run for 10 min, were conducted in order to investigate the degree of the contribution of the initial stage of filtration to the irreversibility of fouling. Results of this set are also included in Fig. 6.7 for both DB and PEO. It appears that the shortened filtrations generally lead to less irreversible fouling than their corresponding 200-min filtration trials, especially for those at low TMPs. For DB, the 10-min fouling at 30 kPa and 50 kPa is almost totally reversible (nIF < 5 %), but when TMP increases above 100 kPa , the irreversibility of the fouling increases dramatically to a level not too shy of those of the 200-min correspondents. In the PEO case, the fouling irreversibility also increases with increasing TMPs but within a smaller range from approximately 23 % at 50 kPa to 38 % at 200 kPa. Comparing the two feeds in the 10-min set, DB fouling is apparently less irreversible at low TMP (50 kPa and 100 kPa), while it becomes more than that of the PEO correspondents at high TMP (150 kPa and 200 kPa). This is slightly different to the comparison results in the 200-min set, where PEO fouling is consistently more irreversible from 50 kPa to 200 kPa.

In summary, TMP appears to have more impact on the fouling reversibility in the DB case. The increase in TMP apparently causes the DB fouling to become more irreversible in both short and long filtration experiments. In the PEO case, the percentage of irreversible fouling with respect to the total fouling is relatively consistent against TMP changing for both filtration durations.

The initial stage appears to have more profound impact on the fouling irreversibility in the DB fouling at higher TMP (> 100 kPa) since the nIF difference between these results is narrow. In order to clearly show this, the corresponding absolute irreversibility indices (IF) are displayed in Fig. 6.8 for all normalised data shown in Fig. 6.7. The results are consistent between the two figures. At the high TMP range, the majority of irreversible fouling is attributed to the first 10-min filtration for DB experiments.

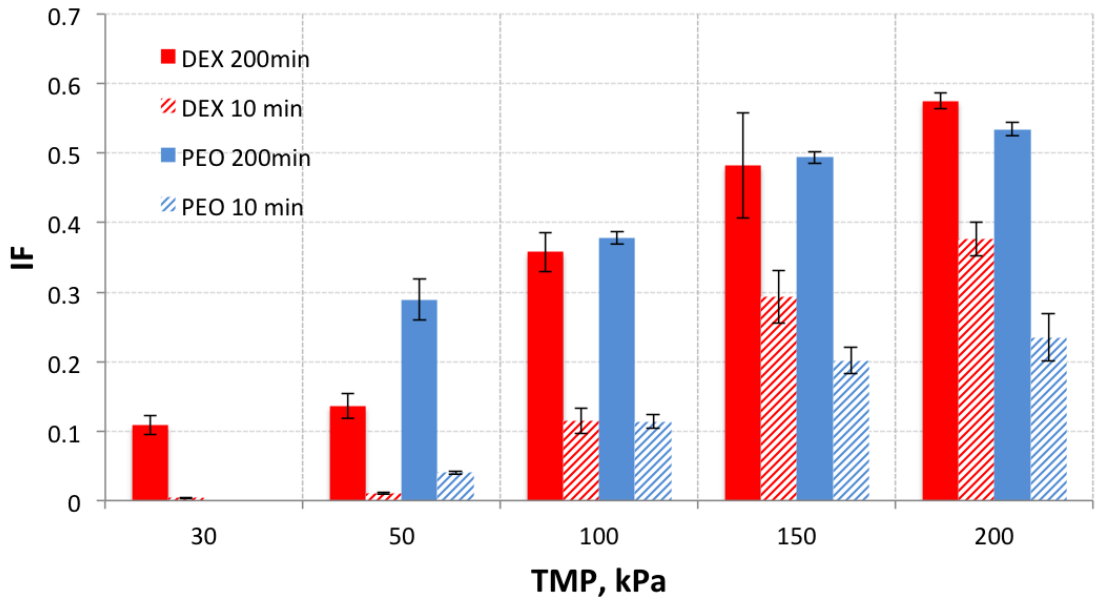

Figure 6.8: Fouling irreversibility index (IF) determined for 50 mg/L DB and PEO filtration trials at different TMPs and different filtration duration.

6.4 Impact of Macromolecular Deformation on Fouling

The flow-dependent permeation and highly irreversible fouling of DB filtration at high TMP ($\geqslant$ 100) likely stem from the macromolecular deformation under a high

shear flow. Theory [248] suggests that the onset of the macromolecular deformation occurs at a critical filtrate flux. Below this value, filtration is simply governed by size exclusion. The large DB molecules are retained on the membrane surface. However, once above the threshold, the converging flow at the pore mouth theoretically can sustain a strong elongational flow field to stretch the macromolecule to a transversal diameter smaller to that of the pore opening. A macromolecule would then be able to permeate through the pore with an opening size smaller than the unperturbed size of the molecule. The sieving results of DB have shown such a turn in Fig. 6.5 from a nearly impermeable state at small fluxes to appreciable permeation at high fluxes. The critical flux is roughly determined at 6×10^{-5} m/s from the turning point in the sieving curve.

With respect to the critical deformation-flow theory, a hypothesis can then be formed to regard the macromolecular deformability to membrane fouling. It states that a high flow field can induce the deformation of a linear flexible macromolecule and drag the stretched molecule into a pore which is usually too small for it to enter, and this phenomenon increases the permeation as indicated by the sieving coefficient as well as increases the opportunity of internal fouling. Since membrane pores are not perfectly shaped, the irregular pore geometry may cause trap of the 'squeezed' macromolecule inside the pore structure. Moreover, a pore radius in the present UF membrane is within 10 nm while a pore length can be 100 times larger since the effective membrane thickness is at a few μm. Such large difference in the two dimensions may allow enough space for the chains to recoil, returning from a stretched state to a coiled conformation. Therefore, when the large macromolecules are not deformed, they can only cause the surface pore blockage; while when they are stretched by the hydrodynamic force, they may be captured inside the pore matrix, causing severe internal pore clogging. This deep-bed type of fouling is more difficult to recover than surface blockage.

Therefore, high TMP corresponding to high extensional flow field can cause a more irreversible fouling as depicted in Fig. 6.7. The process of internal pore clogging takes place quickly at the beginning of fouling when the permeate flux is at its highest. This was shown in the irreversibility results for the 10 min filtration. At high TMPs, 10 min filtration of DB solution could cause irreversible fouling comparable to the 200 min filtration. At the early filtration time, the sieving results (see Fig. 6.1) were also high for DB filtration under high TMPs since macromolecules were dragged into the pores, they have both probabilities to clog or pass through. At low TMPs, i.e. 30 and 50 kPa (the corresponding fluxes were lower than the threshold shown in Fig. 6.5),

most of the DB molecules cannot enter the membrane pores, and hence, can most likely only cause surface blockage. Therefore, fouling in these cases are more reversible especially for a short period. For long-term filtration, the consolidation in the fouling layers via certain mechanisms may have contributed to some of the irreversibility in the fouling. These mechanisms involving the entangled macromolecules (no longer in dilute regime) are more complicated to determine.

For PEO cases, since their sizes are comparable to the pore sizes, they can more easily enter the pores, even without the requirement of molecular deformation/elongation for entrance. The TMPs and the strength of the flow field do not affect them as much as they do to DB molecules. Therefore, their fouling irreversibility does not vary too much between different TMPs.

In practice, there are numerous pores in a filter and their sizes are not exactly same. The macroscopic flux is only an average value over the many pores. Sometimes, although the macroscopic flux is below the threshold, there may be a fraction of the pores passing flow at a speed greater than the critical value to stretch macromolecules. Therefore, the true value of the critical flux may be in fact higher than the one determined purely based on the sieving results.

6.5 Conclusions

The sieving and fouling irreversibility results have been presented for the two large polymers, i.e., the DB and PEO used in the experiments. For DB, noticeable permeation was only observed under high TMPs ($\geq$ 100 kPa) and at the very early stage ($<$ 10 min out of 120 min) of the filtration. For PEO, the molecular permeation was also found to be affected by TMPs but less noticeable. Permeation was observed under all TMPs conditions and decreased more gradually than that in the DB case. The decrease of the sieving coefficients as the filtration proceeds coincides with the build-up of membrane fouling. Given that the mean pore radius of the membrane is estimated at 4.4 nm and the hydrodynamic radius for DB (MW = 2000 kDa) and PEO (MW = 100 kDa) samples are at 28.8 and 10.2 nm, respectively, the low permeability at low TMPs is due to the size exclusion. However, the variance in the characteristic sizes allows a fraction of PEO molecules to pass through the membranes naturally.

The initial sieving coefficients have been demonstrated to depend on the fluxes with only exceptions in the DB case when fluxes are low. The change from being impermeable to permeable for DB occurs at a certain value of the flux, which can

be roughly determined from curve fitting. This agrees with the profile of the conformational change of a polymer molecule suggested by the 'coil-to-stretch' theory [248, 249].

The results of the fouling irreversibility have also demonstrated that DB fouling is more susceptible to the TMPs change. At low TMP, DB fouling is totally reversible after 10-min filtration and only slightly irreversible after 200-min, while at high TMP, its fouling becomes much more irreversible since the initial time. In contrast, PEO fouling is less affected although it is not totally independent of the TMPs change.

The increased irreversible fouling in the DB case is, hypothetically, caused by the flow-induced deformation of the macromolecules. The high permeate flux leads to an elongational velocity gradient at the pore entrance which can deform the coiled molecule to a stretched state, when the flux is higher than a certain threshold. The elongated molecules are much easier to enter the pores. This leads to high permeation while also enables the molecules to be engaged in the internal pore clogging.

Chapter 7

Mesoscale Simulation of Pore Blocking

7.1 Introduction

Solute molecular deformation due to the elongation flow near the pore entrance may change the state of the filtration process, or the extent of fouling; Chapter 6 has proposed that a transition between surface fouling and possible internal fouling under a high converging flow at the pore entrance may occur during UF of macromolecules. In order to determine the relationship between the macromolecular fouling and flow-induced deformation, a mesoscale model using Dissipative Particle Dynamics (DPD) was built for investigation. Choice of this method is because of the particularly small scale involved at the pore entrance, where the flow field is important for the flow-induced deformation of macromolecules, and may dramatically affect the fouling behaviour. At such a small scale, numerical simulation can provide detailed information on flow and molecular conformations [257].

7.1.1 The Physical Scale

The observable behaviour of membrane fouling and flux decline is affected in a fundamental way by many non-trivial details at the smaller scales. Following the previous chapters, macromolecules capture and size exclusion at the pore entrance are considered to be particularly important in UF fouling. Therefore, we zoom into the

confined region surrounding the opening of an individual pore on the surface of a UF membrane and study the physic-chemical processes at this scale, affecting the fouling behaviour. Given that the chemical and electrostatic interactions can be neglected for the present, the focus is on the permeate flow at this region and how the macromolecule behaves in the flow and interacts with the pore wall.

The model system should consist of the pore, the solvent and the macromolecule. The pore in the UF membrane studied in the thesis has a diamerter typically ranging from 1 nm to 10 nm. The macromolecule has size at the same order to the pores. For a dilute solution, one molecule studied at a time is adequate.

To simulate the flow, the first choice is the continuous fluidic dynamics (FD) using the Navier-Stokes equation. It can well describe a simple fluid passing through a pore in a phenomenological manner without consideration of any microscopic detail, but it may not suit the system of present interest. Firstly, the continuum assumption may no longer be held when the length scale is smaller than 10 nm. Secondly, it is difficult to couple the dynamics of the macromolecule into the FD, since the molecule is too large in the system to neglect its conformational effect. Alternatively, it may resort to a simulation on the atomistic level. Molecular dynamics (MD) is such a tool modelling single atoms in a system by following the position and momentum of every particle [258, 259]. It can be extremely useful in the simulation of small numbers of particles and has been scaled up to model even large biomolecules via improved algorithms [260]. However, MD is restricted to a small space-time domain, typically for dimensions smaller than 100 nm and time intervals less than 5 ns [261]. Attempts to apply MD to large systems often consume unrealistic computational powers.

Both atomistic (microscopic) and continuum methods are not ideal for our system. What one needs is a model that can study both hydrodynamics and thermodynamics of a system and bring out the infromation on the flow and the molecular conformation together. This is where the mesocopic models come into play. The mesoscale is larger than the atomistic scale but smaller than the continuum scale in the temporal and spacial chart. A mesocopic system can have the length between 10 nm and 1 μm and the characteristic time from 10 ns to 1 s. In mesoscopic models, the macromolecule will be modelled with coarse-grained particles, i.e. a cluster of many atoms, and the atomic interactions are omitted since the exact structure of the molecule is not of interest. The relevant phenomena can then be assumed to only occur above the mesoscopic scale and nothing of interest should occur faster than the characteristic time [262].

7.1.2 Introduction of the DPD method

In general, the DPD method as a mesoscopic modelling technique bridges microscopic simulation methods such as MD and macroscopic approaches involving the solution of the fluid flow equations [263]. DPD can model both thermodynamics and hydrodynamics. It can obtain both atom-like and fluid-like effects. Therefore, DPD can be used to simulate systems that are too large to be simulated by MD but small enough for thermal fluctuations to play an important role. Important examples include polymer solutions, gels, small particle suspensions and membranes. In these applications inter-particle and intra-molecular hydrodynamic interactions are automatically included.

In form, DPD closely resembles MD. Both are particle methods. A DPD system is made up of off-lattice, discrete, and free particles. They have continuous spatial positions and velocities though updated discretely in time according to Newton's law of motion. This differs from other mesoscopic methods such as Lattice-Boltzman and lattice Monte Carlo methods [264, 265], where the particles are restricted to a set of discrete positions.

Fundamentally, DPD is different from MD in the concept that each DPD particle is a soft sphere and represents a large number of solvent or polymeric monomer units, and might be better thought of as a carrier of momentum [266, 267]. In a three-dimensional space, they are associated with constant masses and interact pairwise over a range that is usually of the same order as their diameters. DPD particles, being 'soft', do not have hard-sphere repulsions, like the Lennard-Jones interaction used in MD, with each other. As a result, they can overlap with each other to a significant degree. Then, the distance between two overlapped particles is less than the sum of radii of their interaction range.

DPD obtains the hydrodynamics because it is Galilean invariant so that momentum is conserved via the laws of pairwise interaction. Compared to computational fluidic mechanics, particle methods are much less computationally efficient than grid based numerical solution of the Navier-Stokes equation, and they have been used less extensively, particularly for engineering applications. However, they have important advantages in respect of (1) rigorous mass and momentum conservation; (2) being isotropic ; (3) being simple to simulate flows with moving boundaries; (4) easy coupling of fluid flow with other physical phenomena such as a phase separation; (5) no need for explicit interface tracking and capturing; and (6) relatively simple code development.

The history of DPD models is not long. The concept was first introduced in 1992 by Hoogerbrugge and Koelman [266], as an alternative method for the mesoscopic simulation of complex fluids on physically interesting length and time scales. Later, Espanol and Warren [268] proposed a constraint on the coefficients and weighting functions of the dissipative and random forces, satisfying the fluctuation-dissipation theorem. Groot and Warren [263] contributed to the next major step in its development, which established an integration algorithm for Newton's equations of motion, and made the first theory-based argument for the value of the conservative force coefficient.

DPD is a relatively young mesoscopic method and is still under development, whereas this method has been adopted by a number of researchers who recognised that the form of this model would allow for a great deal of flexibility in building complex molecules and systems. Most applications of DPD involve systems of either large, inter-connected particle structures immersed within fluid, or fluid flow through complex surfaces. Willemsen et al. [269] used frozen particles to build a wall exhibiting no-slip boundary conditions, later using the method to simulate pressure-driven flow in a chromatography channel. Clarke [270] developed DPD models for performing shear and planar elongational flow over a wide range of strain rates. The results showed that the polymer molecules were significantly deformed only at high strain rates, which complied well with other experimental and theoretical works. Guo et al. [271] used DPD to model the flow-induced permeation of a polymer chain through a small pore.

7.2 Model and Methods

In this chapter, DPD simulations of the deposition of a single macromolecule onto a permeable membrane surface in a normal flow field were performed. In a sense, it is similar to particle deposition studies in the continuum domain (MF range) [228, 229], where the flow field was modelled as a continuum predicted by the Navier-Stokes equation directly, and the particles were modelled as rigid spheres and their motions were described by the phenomenological forces, such as the Stokes hydrodynamics force [229]. However, in the present work, the physical scale in UF of the macromolecule is much smaller than the colloidal system in those MF studies. It is at the mesoscopic scale, therefore, that significant contributions from molecular interactions are expected.

The DPD method was used to study the dynamics of a linear flexible macromolecular chain in the converging flow field above a narrow pore in a three dimensional space. The DPD simulation code was developed based on a Fortran code for the DPD model named DL-MESO [272], with case-specific modifications as required.

7.2.1 Outline of the DPD Method

This work follows standard DPD protocol. The model consists of an ensemble of N point-particles existing in continuous space. Each particle has its associated vector position ($\mathbf{r}_i$), velocity ($\mathbf{v}_i$) and its mass (m_i) registered in the system, where i is the index to distinguish between particles. The mass of a particle is usually set constant during a simulation; while its position and velocity vectors are temporally updated according to Newton's second law of motion:

$$\frac{\mathrm{d}\mathbf{r}_i}{\mathrm{d}t} = \mathbf{v}_i \tag{7.1}$$

and

$$\frac{\mathrm{d}\mathbf{v}_i}{\mathrm{d}t} = \frac{\mathbf{F}_i}{m_i} \tag{7.2}$$

The total force on a particle i is simply a sum of all distinct forces applied to this particle;

$$\mathbf{F}_i = \sum_{i \neq j} \mathbf{f}_{ij} + \mathbf{F}_i^{ext} \tag{7.3}$$

where $\mathbf{f}_{ij}$ is the interparticle force on particle i exerted by particle j, and $\mathbf{F}_i^{ext}$ represents other external body forces.

7.2.1.1 Pairwise Interactions and Thermostat

In any DPD system, $\mathbf{f}_{ij}$ consists of three distinct forces: a conservative force ($\mathbf{F}^C$), a dissipative (drag) force ($\mathbf{F}^D$), and a random force ($\mathbf{F}^R$), which are all assumed to be pairwise additive;

$$\mathbf{f}_{ij} = \mathbf{F}_{ij}^C + \mathbf{F}_{ij}^D + \mathbf{F}_{ij}^R \tag{7.4}$$

Between a pair of particles, these forces are always equal and opposite, so that momentum is conserved both locally and over the entire system. The summation in eqn 7.3 runs over all particles found within a cutoff radius designated by r_c.

The three basic forces have the usual forms [268]:

$$\mathbf{F}_{ij}^{C} = -\frac{\partial V_{ij}}{\partial r_{ij}}\hat{\mathbf{e}}_{ij} \tag{7.5}$$

$$\mathbf{F}_{ij}^{D} = -\gamma_{ij}\omega^{D}(\hat{\mathbf{e}}_{ij}\cdot\mathbf{v}_{ij})\hat{\mathbf{e}}_{ij} \tag{7.6}$$

$$\mathbf{F}_{ij}^{R} = \sigma_{ij}\omega^{R}\theta_{ij}\Delta t^{-1/2}\hat{\mathbf{e}}_{ij} \tag{7.7}$$

where V_{ij} is a two-particle interaction potential; $\hat{\mathbf{e}}_{ij}$ is the unit vector in the direction of the interparticle vector $\mathbf{r}_{ij} \equiv \mathbf{r}_i - \mathbf{r}_j$; both ω^D and ω^R are distance-based screening functions (i.e. weighting functions), relating the interparticle distance r_{ij} (equal to $|\mathbf{r}_{ij}|$) to the magnitude of the forces respectively.

The pairwise conservative force is to generate local thermodynamics. Its interaction potential is often chosen as:

$$V_{ij} = \frac{1}{2}a_{ij}r_c\left(1-\frac{r_{ij}}{r_c}\right)^2 \tag{7.8}$$

where a_{ij} is the interaction strength, i.e., the maximum repulsion between the two particles; The interaction distance r_{ij} is set no more than the cutoff r_c so that the conservative interaction is purely repulsive. Note that it is not forbidden in DPD to use other kinds of potential, e.g., the Lennard-Jones, which is commonly used in MD [258] and has both attractive and repulsive terms in its form.

Inserting eqn 7.5 into eqn 7.8 with the cutoff constraint gives rise to the form of the conservative force:

$$\mathbf{F}_{ij}^{C} = \begin{cases} a_{ij}\left(1-\frac{r_{ij}}{r_c}\right)\hat{\mathbf{e}}_{ij} & \text{if } r_{ij} < r_c, \\ 0 & \text{if } r_{ij} \geq r_c. \end{cases} \tag{7.9}$$

The resultant $\mathbf{F}_{ij}^{C}$ is a 'soft' (i.e. weakly) repulsive force set to be finite at very small separation distances. This allows for large time steps in computing [267]. In comparison, the Lennard-Jones force (in MD) approaches infinity at small particle separations, limiting the permissible timesteps to very small values. Therefore, DPD can usually simulate in larger time scales than MD. Moreover, it is possible for two DPD point masses to coincide, since the maximal repulsion achieved at $r_{ij} = 0$ is large but finite.

The most distinctive feature in DPD is its thermostat consisting of the pairwise dissipative and random forces. The thermostat couples a DPD system to a heat bath so that system momentum can be conserved correctly.

The dissipative force $\mathbf{F}_{ij}^{D}$ acts in such a manner as to reduce the relative velocity, $\mathbf{v}_{ij}$ between two particles and hence drain the kinetic energy from the system. This force originates from the friction between the particles that pass each other. A particle moving more slowly receives momentum from a faster particle, and in return, the faster one is slowed down. The constant γ in eqn 7.6 is the frictional coefficient controlling the force amplitude, and is an important parameter in determining the viscosity of the fluid [262]. A large value of γ will produce a system sensitive to fluctuations in temperature, which relaxes quickly [263, 273].

The random force $\mathbf{F}_{ij}^{R}$ is a stochastic force originated from the Brownian motion. It can be understood as the random fluctuations of the fluid due to the local temperature [262]. In a DPD system, it counteracts the dissipative force to provide the system with energy. By viewing the DPD particle as a coarse-grain of many atomistic particles, it can be interpreted that the energy flows from the invisible microscopic entities which DPD ignores into the mesoscopic DPD grains. The strength of the random force is governed by the coefficient σ. The randomness in eqn 7.7 is contained in θ_{ij}, which generates Gaussian random numbers with zero mean and unit variance [262], and Δt is the timestep size.

The strength of the random force is related to that of the dissipative force by the fluctuation-dissipation theorem [268], which ensures the balance between the energy resulting from the two forces and hence brings the system to the desired equilibrium temperature ($k_B T$) over time. This brings out the following correlations between the two forces in order for thermodynamic equilibrium to be achieved:

$$\sigma^2 = 2\gamma k_B T \tag{7.10}$$

$$(\omega^R)^2 = \omega^D \tag{7.11}$$

The form of the weighting functions are not specified by the model itself. A common choice [263] is

$$\omega^D = (\omega^R)^2 = \begin{cases} (1 - \frac{r_{ij}}{r_c})^2 & \text{if } r_{ij} < r_c, \\ 0 & \text{if } r_{ij} \geq r_c. \end{cases} \tag{7.12}$$

The combination of the dissipative and random forces comprise the DPD thermostat. It connects the model system to a heat bath so that a highly controllable environment is created to allow a finite number of spherical beads to model complex fluids with accuracy. The effect can be analogous to bouncing balls in a can: by filling the can with water and skating it consistently, the movements of the balls become more stable and predictable [267].

7.2.1.2 External Forces

An external body force can be explicitly exerted on DPD particles of interest, as shown in eqn 7.3 in addition to the pairwise interactions.

$$\mathbf{F}_i^{ext} = \mathbf{g}_i \hat{\mathbf{e}}_i \tag{7.13}$$

where g is the modulus of the body force, and $\hat{\mathbf{e}}_i$ is a unit vector in the force direction for particle i. The body force can represent the constant acceleration that the particles receive under an external force field, for example, a gravitational or electric field [272]. By this, a pressure-driven Poiseuille flow, for example, can be generated [257]. Application of the body force can be used to investigate a system in non-equilibrium.

7.2.1.3 Integration Algorithm

The simulation is performed by iterating the Newtonian equations of motion for DPD particles (eqns 7.1 and 7.2) through a series of timesteps to obtain the instantaneous position, velocity and acceleration of all particles at each timestep. The integration algorithm uses a modified velocity-Verlet (DPD-VV) scheme [263]:

$$\mathbf{r}_i(t+\Delta t) = \mathbf{r}_i(t) + \mathbf{v}_i(t)\Delta t + \frac{\mathbf{f}_i(t)}{2m_i}(\Delta t)^2, \tag{7.14}$$

$$\tilde{\mathbf{v}}_i(t+\Delta t) = \mathbf{v}_i(t) + \lambda \Delta t \frac{\mathbf{f}_i(t)}{m_i}, \tag{7.15}$$

$$\mathbf{f}_i(t+\Delta t) = \mathbf{f}(\mathbf{r}_i(t+\Delta t), \tilde{\mathbf{v}}_i(t+\Delta t)), \tag{7.16}$$

$$\mathbf{v}_i(t+\Delta t) = \mathbf{v}_i(t) + \frac{(\mathbf{f}_i(t) + \mathbf{f}_i(t+\Delta t))}{2m_i}\Delta t. \tag{7.17}$$

The steps are as follows: (1) forces are applied to particles at each timestep, depending on their position and velocity at the instant, t; (2) the velocity $\tilde{\mathbf{v}}_i$ serves as an intermediate guess for the velocity at $t + \Delta t$, and λ is an empirically-introduced parameter, for which Groot and Warren [263] found an optimal value at 0.65; (3) the total force (acceleration) at the next timestep is then calculated using eqn 7.4, based on the updated position, and the intermediate velocity vectors; and (4) the velocity at the next timestep is recalculated using half the forces from the previous timestep and half from the current timestep.

The introduction of the intermediate velocity $\tilde{\mathbf{v}}_i$ allows the calculation of the dissipative force (eqn 7.6), since it depends on the particle velocity, which is the main modification to the original velocity-Verlet algorithm widely used in the conventional MD simulation [259]. However, this algorithm is not a self-consistent procedure because of the cyclic dependence between the dissipative force and the velocity [272]. This also means that the DPD-VV is not time-reversible due to the calculation of the stochastic force, involved in each time step [274]. Hence, the effective equilibrium temperature depends on the time step used in the scheme [275]. Therefore, the maximum attainable Δt is limited in order not to compromise the stability of the system. Extra care is required for the choice of the timestep size.

During simulation, the convergence of the algorithm is constantly monitored through each timestep by checking the system temperature with the desired value.

7.2.1.4 Units in DPD

The DPD code uses fundamental units for mass, length and energy. For the convenience of editing, their units are reduced using the respective characteristic scales in the system [263]. The unit of length is defined by the cutoff radius, r_c, since DPD contains no other inherent length scales. This cutoff radius also represents the size of a particle.

The unit of mass is defined to be the mass of a DPD particle, m_i. The unit of energy is set as $k_B T$, i.e., two-thirds of the kinetic energy per particle.

The time unit in the DPD system is the result of the three fundamental units. A unit time is then:

$$\hat{t} = r_c \sqrt{\frac{m_i}{k_B T}} \tag{7.18}$$

which represents the time in the system being scaled such that a particle with speed $v = 1$ will move a distance r_c in one unit time.

7.2.2 Model Configuration

The model configuration here is similar to those in the previous studies [236, 271, 276] of flow-induced translocation of a polymer through a narrow pore. Instead of trying to pull the polymer through the pore [276], the relationship of the hydrodynamic force to fouling is studied here. A state of fouling is defined as that occurring when a polymer is captured by the pore and stopped entering further. Therefore, in this fashion, the goal of the present model is to study the surface fouling phenomenon, i.e., the deposition of a macromolecule onto the pore mouth, which is the mode of the pore blocking as described in the classical blocking theory. Furthermore, fouling is assumed to be caused purely by steric effects so that other effects such as electrostatics are not considered.

7.2.2.1 System Geometry

The system is modelled in a rectangular simulation box, with a square base in the x-y surface and its longitudinal direction along the z-axis (see Fig. 7.1). Within the box, there are three components: the pore structure (denoted by W), the solvent fluid (S), and the macromolecule (P).

The pore structure represents a small surface portion in a UF membrane, containing a single pore. The pore wall extends in the x and y-axes and is placed in the middle of the simulation box. It divides the flow space into two regions: the upstream feed side and the downstream permeate side. A straight cylindrical pore with a radius of r_p is then dug through the membrane wall material to connect the flow regions. During this work, two values of r_p, i.e., 1.0 and 2.0 (units normalised by r_c), are investigated respectively. The length of the pore channel, l, is fixed at 8.0, i.e., the thickness of the membrane in the system. The ratio of l to r_p here is not realistic (UF membranes have their thickness typically more than 100 times their pore radius). The choice is for the sake of the limited computational power. A large chunk of the pore channel is actually omitted in the present work. Therefore, this simulation work is limited to studying pore blocking phenomena at the pore entrance region. It is not suitable for an internal fouling study.

The pore wall is constructed with layers of frozen DPD particles which are set stationary during the simulation but can still interact with all other particles. The wall particles are placed in a lattice with its grid size determined by the particle number density (ρ).

At the wall surface, the no-slip boundary condition is assumed. In order to avoid the freely-moving particles penetrating the solid walls, the density of the wall particles ($\rho_W = 8$) is set higher than the density of the fluid particles ($\rho_S = 3$) in the free flow space. No extra bounce-back rule is set at the surface, since the goal is to study macromolecular deposition.

The flow is later created from the $-z$ direction so that the inlet of the system is at the upstream boundary and the outlet the downstream in Fig. 7.1.

The length of the simulation box, L, varies slightly in different simulation runs, depending on the size of the macromolecule in the system, because the centre of the molecule is always placed at a distance of 15.0 r_c in the z-direction away from the centre of the pore entrance and the size of the molecule was varied in the study.

7.2.2.2 Fluid and Flow

The fluid in the system is modelled with unbounded DPD particles. Its particle density is required to be enough to fill the entire system to ensure plentiful short-range interactions in the system in order to accurately control the temperature and form incompressible fluid. If there is an abundance of free space, particles will move freely without experiencing dissipation. Also in consideration of the minimal computational cost, most DPD studies have chosen the number density between 3 and 4 [270]. In the present work, the number density of the fluid particle is chosen at $\rho_S = 3$, the same as that in a previous pore-flow simulation [271] Then, the total number of fluid particles is determined by multiplying ρ_S by the free volume (not occupied by the wall) in the simulation box.

DPD obeys the Navier-Stokes equation [277] so that hydrodynamic flow can be generated within the model. However, unlike continuum methods, it is not an easy task to assign a given pressure difference in a stochastic particle method. Strictly, it requires to specify (statistically) appropriate chemical potentials at the two ends of the fluidic system in the grand-canonical ensemble [278]. Technically, the chemical potential is maintained by continuously creating and deleting particles in the source (inlet) and sink (outlet) regions respectively. However, this method is prone to instabilities and cumbersome to implement in practice [279].

Alternatively, the reflecting boundary method [280], setting a biased boundary condition to allow the particles to freely cross from one side but partially reflect those from the other side according to a probability, can also lead to the effect of a pressure difference. This method is technically simple and can coincide with the periodic

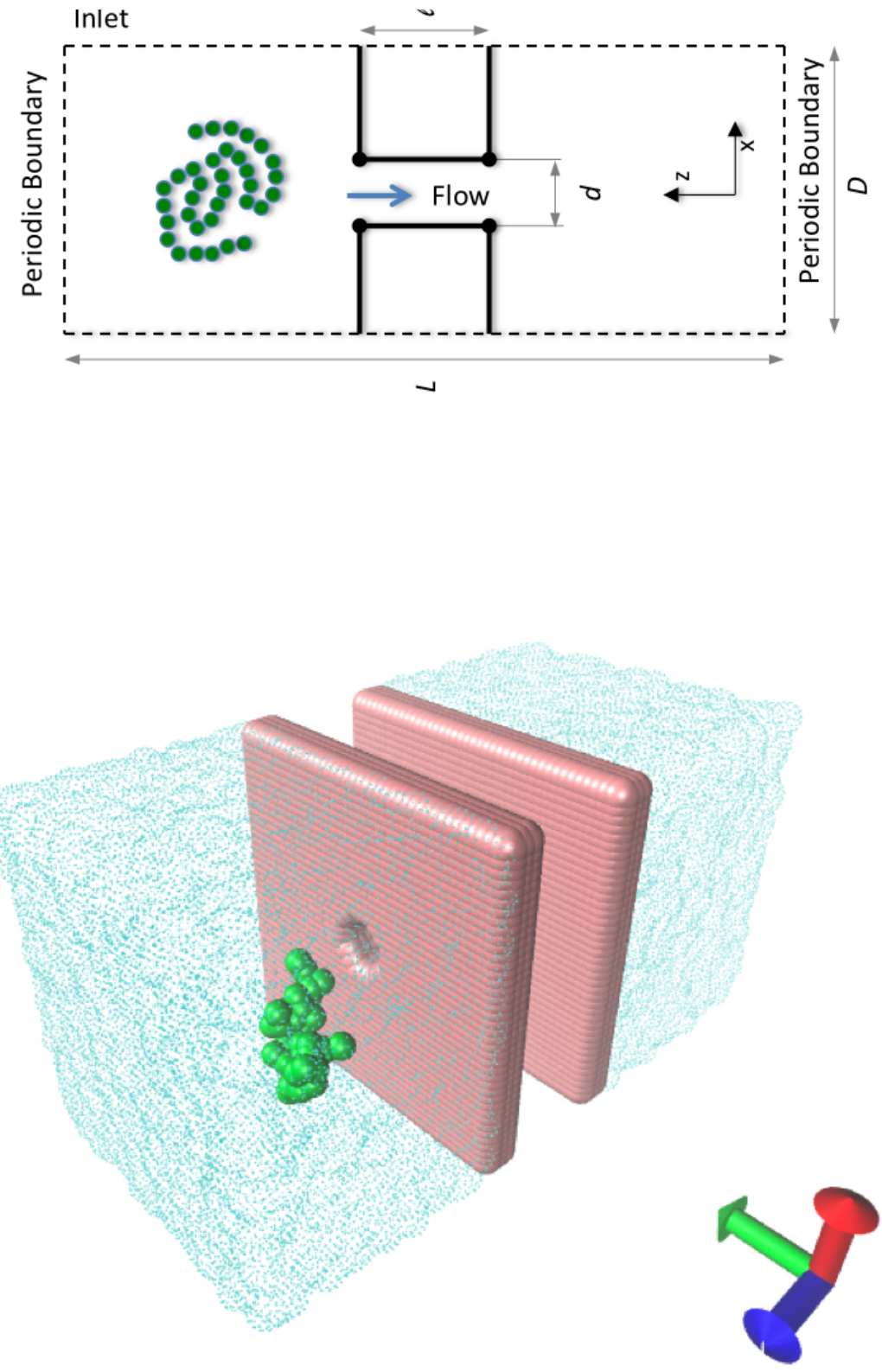

Figure 7.1: Schematics of the DPD simulation setup for the study of a linear polymeric chain blocking a cylindrical membrane pore.

boundaries, but it is difficult to achieve a desired flow field by simply adjusting the reflection probabilities [279]. These 'reservoir' methods [280] may be further modified with some smart 'water pumping' mechanisms, but the steady flow is difficult to maintain in these methods.

Therefore, in this work, the flow generation is simply resolved with the application of an artificial acceleration field to every flow region of the system [271, 281]. In this method, a constant body force, $\mathbf{F}_i^{ext}$ (eqn 7.13), in the $-z$ direction is imposed directly on each solvent particle to force them to flow in a uniform direction. A constant pressure gradient can be generated in this fashion. By carefully choosing the magnitude of the body force, a steady state Poiseuille flow is expected in the pore region. This scheme is simple, effective and computationally efficient, but there are also some artefacts in it. Firstly, the body force has to be unrealistically large compared to the earth gravity in order to generate an appreciable flow in DPD system. Secondly, effects on local dynamics induced by constant acceleration are different from those induced by pressure gradient, which have microscopic spatial and temporal fluctuations associated with molecular collisions. Thirdly, the flow near the complex geometry such as the membrane structure in the present simulation will deviate from the Navier-Stokes equation. Hence, it may not faithfully model the flow region next to the solid surface away from the pore entrance in the present simulation geometry. However, since the flow region at the pore entrance is of the main interest, this method is currently the most suitable.

Periodic boundary conditions [258] are applied to the six surfaces of the orthorhombic simulation box. The fluid particles leaving one end are instantly placed back to the box from the opposite side. Hence, the total number of the DPD particles are conserved.

7.2.2.3 Macromolecules in DPD

It is straightforward to incorporate macromolecules into the DPD simulation using the bead-spring model. A linear polymer is represented by a freely-jointed chain, which consists of N number of DPD particles. These beads are connected consecutively by massless spring-like bonds. The bond imparts an elastic constriction to the two beads it connects. Each bead in the chain represents a monomer of the polymer. This simple model does not allow any tertiary forces, e.g. hydrogen bonding. It is a coarse-grained description of the macromolecule, omitting the details at the atomic

level. A dilute solution of macromolecules can then be formed by immersing a single chain into a sea of fluid particles.

The bonded interaction between monomers contributes to the total force calculation in eqn 7.3, in addition to the basic DPD forces [263]. In the present work, it is represented by the harmonic (Hookean/Fraenkel) force [271, 276], expressed as

$$\mathbf{F}_{ij}^{bond} = H(1 - \frac{r_{ij}}{r_0})\hat{\mathbf{e}}_{ij} \tag{7.19}$$

where H is the spring constant governing the strength of the force, and r_0 is the equilibrium bond length between the two connected beads.

In order to avoid chain-crossing, we firstly need the bead particles to become impenetrable [282], and therefore the soft potential in the conservative force expression (see eqn 7.5) is modified. A segmental repulsion model has been adopted to mix a hard and a soft potential in sequence [283, 284], i.e., adding a hard core to the polymer beads. The Morse potential [271] is used to model the strong repulsion at the adjacent space of the particle centre, of which the corresponding force is expressed as

$$\mathbf{F}_{ij}^{M} = 2D_e\nu\left(e^{2\nu(2r_e - r_{ij})} - e^{\nu(2r_e - r_{ij})}\right)\hat{\mathbf{e}}_{ij} \tag{7.20}$$

where D_e is the well depth of the Morse potential, ν controls the 'width' of the depth, and r_e is the equilibrium bond distance representing the radius of the core of the particle, which is set at 0.30 r_c. The Morse force is assumed only effective within the distance, r_e, and then the modified conservative force has segments as follows:

$$\mathbf{F}_{ij}^{CM} = \begin{cases} \mathbf{F}_{ij}^{M} + \mathbf{F}_{ij}^{C} & \text{if } r_{ij} \leqslant 2r_e, \\ \mathbf{F}_{ij}^{C} & \text{if } 2r_e < r_{ij} \leqslant r_c, \\ 0 & \text{if } r_{ij} > r_c. \end{cases} \tag{7.21}$$

Secondly, an extra topological constraint is added to the system to prevent chain crossings. [282] has demonstrated that chains crossing cannot occur if the bond length r_0 in eqn 7.19 and the core radius r_e of the polymer particle satisfy the following relationship:

$$r_0 < 2\sqrt{2}r_e \ . \tag{7.22}$$

Geometrically, this is easy to prove as r_0 represents the maximum length that a bond

can reach, while $2r_e$ represents the minimum distance that a bond can be compressed to. Therefore, r_0 is set to $0.70r_c$ herein according to the preset value of r_e [271] .

7.2.2.4 Choice of Paramters

The choice of DPD parameters is made based on a combination of physical rationalisation and practical computational necessity.

The parameters in the pairwise particle interactions can be specified for each species pair in DPD. The strength coefficients of dissipative forces, λ, and random forces, σ, are set to 4.5 and 3.0 for all pairs in the system, respectively. The combination satisfies the relationship in eqn 7.10 and has been chosen in many studies in the literature [257, 263, 271, 285].

The value for the conservative coefficient, a_{ij}, is chosen for each species in the system with care. Note that we use subscriptions, S, W, and P to denote the species of solvent, wall, and polymer beads respectively.

In order to set the compressibility of the fluid to the correct value for water under room temperature, Groot and Warren [263] found that the parameter between two water particles, a_{SS}, should satisfy:

$$a_{SS} = \frac{75k_BT}{\rho_S} \quad . \tag{7.23}$$

Since ρ_S is set to 3.0 and k_BT to 1.0, a_{SS} should be equal to 25.0 . This value will be kept constant through a simulation.

For stationary wall particles, the coefficient between them, a_{WW}, is set to 10.0. Given that the interaction between unlike particle pairs can be estimated from

$$a_{\alpha\beta} = \sqrt{a_{\alpha\alpha}a_{\beta\beta}} \tag{7.24}$$

where α and β represent the denotations for two different species, the coefficient for interactions between solvent and wall particles is given as $a_{SW} \equiv a_{WS} = 15.81$, which is slightly lower than a_{SS}. This means the repulsion between wall and fluid particles is softened in the simulation, which can help reduce the distortion of the particle density near the wall boundary [257].

For the interaction between polymer beads, a_{PP} is set to 25.0. Then, the conservative coefficient for interactions between the molecule and the fluid, a_{PS}, is given by eqn 7.24 as 25.0. This is a reasonable value for freely jointed polymer chains in a good

solvent [286]. Between the wall and the polymer particles, the repulsive coefficient, a_{PW}, then has a value of 15.81.

The well depth and width in the Morse potential for the polymer beads are set to $D_e = 500.0$ and $\nu = 0.50$, respectively, and the spring constant, H, governing the bond interactions is set to 500.0, to reinforce the rigidity in the respective properties of a polymer chain, according to a previous study [271].

The external body force is added to all solvent particles in the system. Its direction is set parallel to $-z$ axis. Its strength, g, is set between 0.001 and 1.0 to investigate its effect on the macromolecular deposition.

The time step, Δt, in the modified velocity-Verlet algorithm is set at 0.01. The desired energy (temperature) is set to 1.0 k_BT and assumed to be uniform over the entire system.

7.3 Results and Discussion

In the simulations, two system variables are studied: polymer chain lengths N ranging from 25 to 250; and external body force g from 0.01 to 1.0.

For each simulation, the general procedure is to build the pore geometry, add fluids and equilibrate, relax and add a polymer chain, re-equilibrate, and then, add the body force to solvent particles, set the polymer free when a steady flow field is generated, and, finally, allow the resulting hydrodynamic flow to drive the chain towards the pore entrance. The instantaneous position of each bead of the chain is recorded at each time step.

At the end of the simulation, the polymer either travels through the pore or fails to do so. In these failure cases, if the polymer mostly resides at the pore entrance because of the size exclusion, these cases are then defined as fouling cases.

For each experimental condition, 100 independent simulations were conducted. In each run, the initial conformation of the polymer was set completely randomly. For each set, the number of runs which successfully translocates the polymer and the number of runs where fouling occurrs were recorded.

7.3.1 Pore Flow

The membrane in this study consists of about 10,000 frozen particles ($\rho_W = 8.0$). The exact number slightly varies with the choice of the pore radius. After the pore

structure is built, the system is filled with water particles at the number density of 3.0 ($\rho_S = 3.0$). The total number of these unbounded solvent particles is around 36,000.

The polymer molecule is initially placed near the system inlet and fixed at its centre point. After solvation, the external body force is applied to the solvent particles. The hydrodynamic flow is, then, generated in the pore channel. After an equilibrium of $160,000$ timesteps (i.e. 1,600 $\hat{t}$), a steady-state Poiseuille flow in the pore channel is achieved for each applied body force ranging from 0.01 to 10.0. Figure 7.2 shows an example of the velocity field achieved in the simulation with the application of a body force at 0.1 with a standard DPD unit. The parabolic shape of the velocity profiles indicate a Poiseuille flow. Note that, when the body force is lower than 0.01, the effect of transverse diffusion is too large to form an appreciable uniform flow in the pore channel.

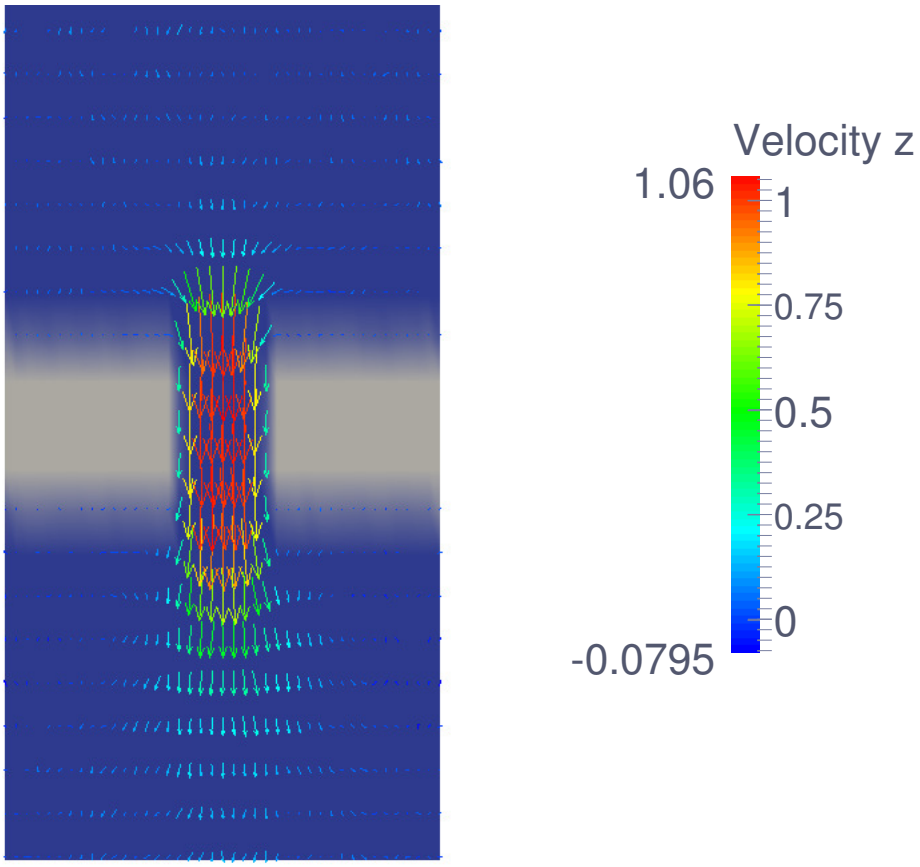

Figure 7.2: 2D vector field of the velocity in the z direction for the middle plane of the simulation box. Poiseuile flow is achieved after equilibrium for simulation with a body force of 0.1.

The average convective flux $< j_z >$, through the pore is calculated as the mean flow velocity in the z direction over the cross-section of the pore and averaged over 4,000 timesteps after the steady-state flow is achieved. It is found that increasing the body force can effectively increase the convective flux. A power-law relationship is obtained between $< j_z >$ and the strength of the corresponding body force, g, and depicted in Fig. 7.3. The exponent is found at about 0.883.

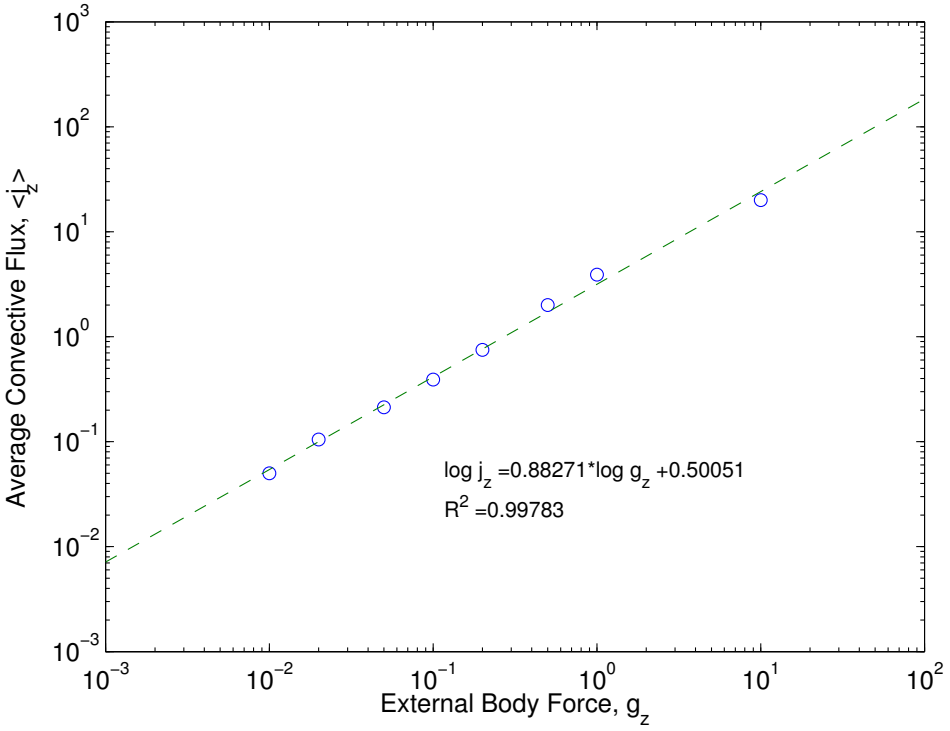

Figure 7.3: The steady-state mean convective flux through the pore as a function of the strength of the constant body force applied to the system.

7.3.2 Macromolecular Pore Blocking

The macromolecular model is represented by a freely jointed chain, which is constructed by connecting particle beads with a harmonic bond of length, r_0. These constituent beads are modelled as unique beads. The interactions between these beads are only derived from the basic DPD forces (conservative, dissipative and random) and the bond interaction. Other intramolecular interactions, such as electrostatic forces, are neglected in the present model.

Differently sized polymer chains are constructed by varying the number of constituent beads, N. Therefore, for convenience, N is used to represent the size of the chain. After construction, the polymer chain is immersed in the simulation box filled with water particles to equilibrate. The equilibrated polymer possesses a randomly coiled shape. The unperturbed size of the polymer chain is then determined as the root of the mean-square radius of gyration, $< R_g^2 >^{0.5}$ over 10,000 samples. The results are shown in Fig. 7.4. Compared with the theoretical results [8], the model

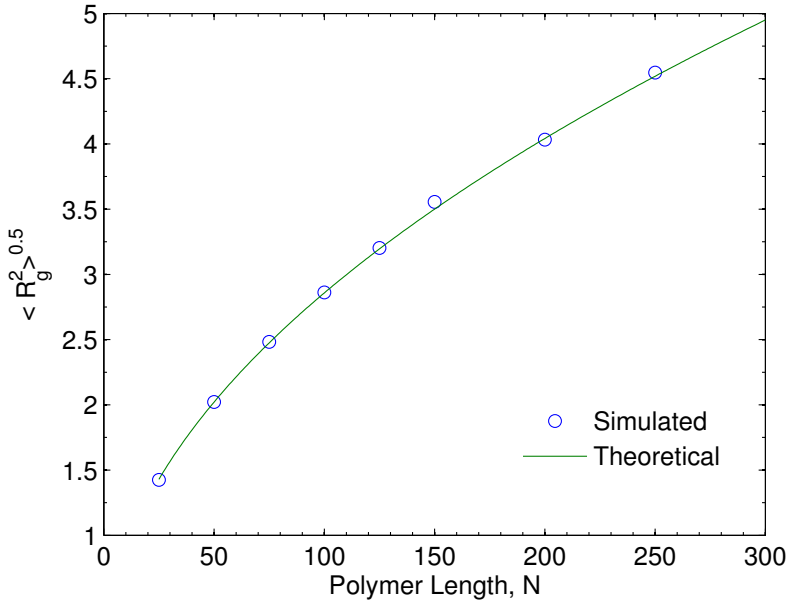

Figure 7.4: The root of the mean-square radius of gyration as a function of the length of the polymer. Dotted data were obtained from simulation and the curve stands for the theoretical values obtained from $< R_g^2 >^{0.5} = (\frac{1}{6} N r_0^2)^{0.5}$ for a freely jointed polymer model [8].

behaves well as an ideal flexible polymer.

The ratio of the unperturbed radius of the polymer to the pore radius, λ, is an important parameter during pore blocking. Since the model pore has a radius of 2.0, this means $\lambda \approx 1.0$ when the polymer has $N = 50$.

The equilibrated polymer chain is added to the near-inlet end of the simulation box and its molecular centre is fixed at the same spot until a steady flow is generated in the pore channel. The polymer chain is, then, set free to be carried away by the flow towards the pore entrance. For most runs, the molecule drifted in the flow direction, i.e., the longitudinal direction. However, under smaller body forces ($g < 0.1$), the intermolecular interactions (i.e. mainly attributed to the random force) are

strong enough to cause slow diffusion of the polymer in the transverse sections of the simulation box. Therefore, it usually takes a longer simulation time for the molecule to approach the pore entrance under a small body force.

When the polymer chain arrives at the region just above the pore entrance, the strong converging flow field creates a pulling force on the chain beads. If the chain diameter is smaller than the pore diameter ($\lambda < 1$), the molecule enters the pore and is eventually transferred to the permeate side of the simulation box. Otherwise, if the chain has a larger diameter ($\lambda > 1$), the size of the pore becomes a physical barrier for it to pass through to the other side. Thus, the polymer has a higher probability to be retained on the feed side and, due to a continuous push by the water particles coming from the inlet, the polymer would be likely to dwell at the pore entrance and hence partially block the pathway of the water particles. Note that this blockage is only partial because the molecule is not completely solid in the model and allows water particles to continue travelling to the permeate side but at a reduced rate. When such blockage is observed in a simulation, the run is marked as a fouling case. For each simulation condition, i.e. various combinations of the imposed body force and polymer size, a total of 100 runs were conducted. The number of cases where the pore blockage occurred are recorded and presented as the fouling probability, P_{block}. The results are plotted in Fig. 7.5.

According to the simulation results, when the external body force is small and the resultant water flux in the channel, measured when it is still fully open, is low (i.e. $\langle j \rangle < 0.2$ corresponding to $g_z < 0.05$), the size exclusion phenomena are more frequently observed, especially for longer chains (i.e. $N > 100$). For chains with N equal to 250, a total of 99 out of 100 simulation runs experience pore blocking at the lowest flux, $\langle j \rangle = 0.05$ (i.e., at $g = 0.01$), used in the experiment, while for chains with N less than 75, there is no blocking ($P_{block} = 0$) observed in all the simulations because their size is too small to be retained by the pore used in the simulations. In fact, small chains with N equal to 25 and 50 does not demonstrate blocking through the whole range of pore fluxes studied.

When the imposed body force increases, the average water flux through the open pore increases. For small chains, it does not have a large effect since the blocking cases are already rare at low fluxes. However, in general, an increased flux dramatically reduces the occurrence of pore blocking. When the fluxes are higher than 1.0 (i.e., $g > 0.2$) , fouling is only observed in less than 10 % of simulations for long chains ($N > 100$). When the fluxes are even higher ($\langle j \rangle = 2.0$ at $g = 1.0$), there are only a

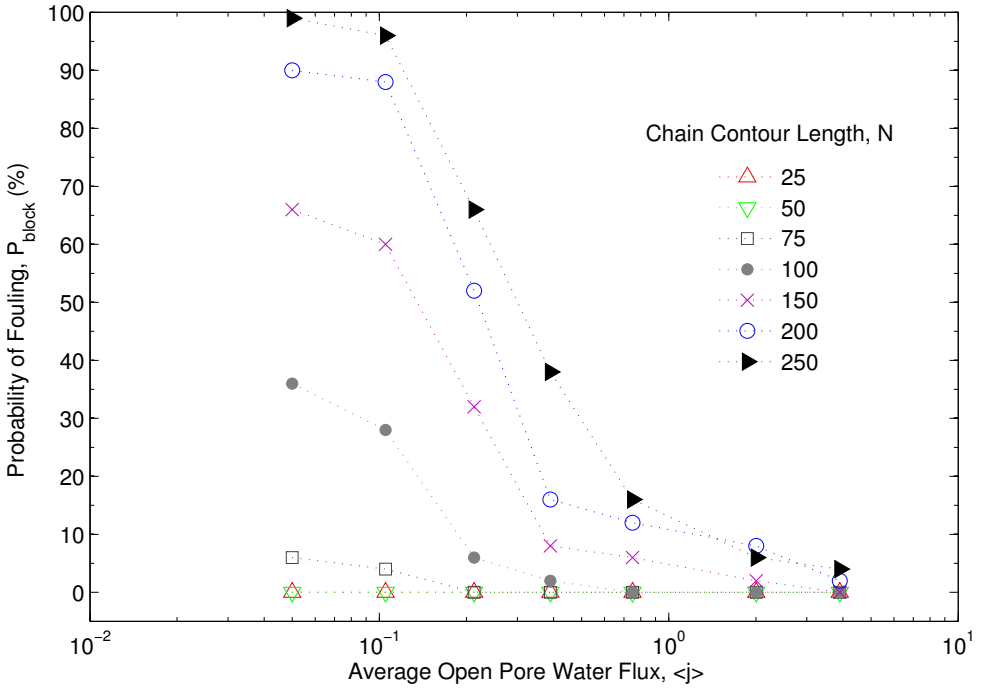

Figure 7.5: Pore blocking probability, P_{block}, at different system conditions, i.e. pore convective flux and polymer chain length.

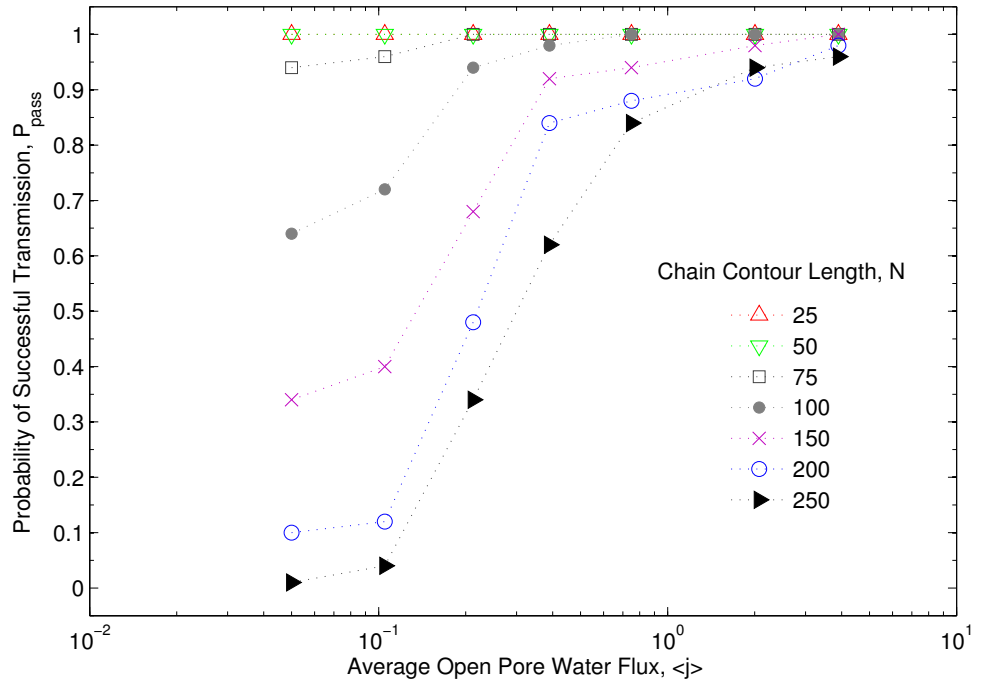

Figure 7.6: The probability of successful translocation of the polymer chain, P_{pass}, versus the average pore convective flux for various polymer chain lengths.

few observed blockages in those cases with chains of length 200 and 250. For other smaller chains, the high flow field allows a completely successful passing through the pore.

When the blocking is reduced at higher fluxes, more successful cases of translocation of a long chain through a small pore is observed correspondingly. By conjugating the blocking probability, the probability of the successful transmission is plotted in Fig. 7.6. The state of high is, in general, at high permeate fluxes while the state of low pass at low fluxes. Between these two states, the transitional phase is when fluxes are between 0.1 to 1.0 with reduced DPD units. For large polymer chains, the shape of the curves resembles that of the sieving curves obtained in the laboratory experiments in Fig. 6.5. When the flux is higher than certain values which are highly likely within the transitional range, the high probability of transmission of the polymer essentially contributes to the increased sieving rate. Hence, the simulation results prove the flux-dependent transmission during UF of macromolecules and support the theory of the threshold flux, of which the value lies within the transitional range.

However, the sharp decay of the sieving coefficients in Fig. 6.1 and the high irreversible fouling of DB at high TMPs (corresponding to high permeate fluxes) also indicate that, controversially, the high transmission probability in the simulation may relate to the eventual formidable macromolecular fouling in reality. This is not a problem of divergence between simulations and observations but it rather reflects on the limitation of the present model. The confinement of the length and time scales in the DPD method limits its capability to model the complete UF fouling event, currently. Our model only represents a tiny portion on the membrane skin. The pore length in the simulation is not in proportion to that in the reality. Nevertheless, the simulated transmission event can precisely represent the transfer of the polymer from the surface into the inside of the pore structure, which is likely a phenomenon existing during the initial state in the UF of dilute macromolecules. Therefore, the probability of the chain transmission can be related to the probability of successful translocations of a polymer into the pore structure. As for what happens next, the present model cannot simulate that.

The detailed translocation of large polymers ($N > 100$) in the simulation is discussed following. The event starts when the chain approaches the pore entrance, where the flow converges. The converging flow is known to be elongational, possessing extensional strain components in the velocity gradient. For a polymer chain

within the gradient, the hydrodynamic drag forces (i.e., the dissipative force) experienced by different chain beads are of different magnitude depending on the relative distance of a particular bead to the pore opening. Theory [248] suggests that once the velocity gradient reaches a critical value, the difference between the drag forces on the two ends of the chain becomes large enough to stretch it. The simulation results have confirmed this. It appears that, at a close distance to the pore entrance, one end (closest to the pore opening) of the chain is pulled into the pore first, while the other parts of the chain are still on the outside of the pore. The chain then undergoes a conformational deformation from a randomly coiled shape to an elongated state due to the space confinement in the small pore. At intermediate degrees of penetration, the part of the chain that remains out of the pore struggles to retain the coiled conformation. This phenomenon was also observed in previous Monte-Carlo simulations [287, 288]. These polymer translocations have also been studied elsewhere recently [271, 276].

The theory [249] also predicts the 'coil-to-stretch' transition to be sharp, but this does not apply here. For polymers of length 250 and 200, before they can be largely predicted for successful transmission, the probability is at intermediate values over a noticeable range of fluxes as Fig. 7.6 shows. The reason for the gradual increase of the probability in the simulation is first that the pore geometry used in the simulation causes a more complex velocity gradient, having other components besides the elongational strain rate. This causes more unpredictable movements of the chain beads. Secondly, the polymer bead has a finite size comparable to the pore radius and the chain is not pre-directed towards the pore centre. The transmission somehow depends on which parts of the chain reach the pore first. When the end of the chain is first dragged into the pore, the chain will be stretched out into a single chain of beads through the pore. In this case, the chain can go through the pore channel more smoothly. In other cases when the middle part of the chain penetrates into the pore first, the chain will enter the pore in a double-folded shape. In this situation, the chain beads are more squeezed in the confined pore region so that the polymer experiences more resistance from the pore channel. The flux may be adequate to elongate the chain but not high enough to further push the beads down the channel. Hence, the polymer may just be stopped at the pore entrance while the majority of its beads is still outside of the pore to form a surface blocking.

7.3.3 Mapping Simulated Results to Physical Scales

There is not yet a direct connection between the model parameters used in DPD and actual molecular parameters, such as molecular weight. Therefore, only a rough mapping strategy, which tries to link the simulation results to the empirically obtained quantities [289], has been used in the current study. Since the actual pores in the UF membranes discussed in Chapter 6 have been estimated to possess an average pore radius of 4.4 nm, the length scale in the DPD simulation can then be assigned accordingly using the relationship, i.e. $r_p = 2.0r_c \equiv 4.4nm$. Thus, the radii of gyration of the unperturbed polymers determined in Fig. 7.4 correlate to the physical sizes ranging from 3.12 nm ($N = 25$) to 10.0 nm ($N = 250$). Assuming the neutral, linear, and flexible polymer chain considered here can represent a generic group of macromolecules such as dextran and PEO, the longest chain used in the simulation ($\lambda \approx 2.0$) may in fact represent the DB samples used in the experiments.

Since the threshold flux was estimated at approximately 50 μm/s in Fig. 6.5 for DB experiments, the threshold flux for high probability of transmission occurring in the simulation with the chain of $N = 250$ can similarly be estimated to about 1.0 with a unit of $r_c/\hat{t}$. Assuming a linkage between these two values, the time unit in the simulation can then be approximated at 4.4×10^{-5} s.

7.4 Conclusions

In this chapter, the macromolecular pore blocking phenomenon has been studied using a particle-based DPD model. The simulation system consists of a fraction of a membrane surface containing a single pore in the middle, filled with a large number of solvent fluid particles. The flow field is generated by imposing external body forces on the solvent particles. The Poiseuille flow is formed in the pore channel when the body force is higher than 0.01 k_BT/r_c. Further increase in the strength of the body force leads to higher fluxes in the pore channel. The results show that a power-law relationship exists between the average pore flux and the strength of the body force.

The macromolecule is modelled as a freely jointed chain with different sizes. The chain is added to the pore flow system individually. When there is no flow, the model chain naturally coils up in the simulation, faithfully representing the conformation of a linear flexible polymer in reality. When the flow is created, the polymer chain is dragged by the hydrodynamic force imposed by the solvent around towards the pore convergence. At low fluxes, large chains are retained on the pore opening, forming

surface blockage. However, when the flux becomes higher than a certain value, the chain starts to be pulled into the pore channel and stretched out to pass through the pore into the permeate side. This translocation event occurs more and more frequently when the pore flux further increases. Correspondingly, the probability of surface blocking is reduced . Shortly, almost all the simulation runs obtain the polymer transmission even for the largest chain when the pore flux reaches a certain high value. The simulation results have been compared with the sieving results from the macromolecular experiments in Chapter 6. The transmission curves in the two studies resemble with each other. Both show the gradual transition from low to high macromolecular transmission when the permeate fluxes increase.

These findings demonstrate that DPD as a mesoscopic simulation method is an effective (relatively fast) simulation technique for studying the fouling phenomenon at the pore entrance. In future work, it may be extended to study more complex phenomenon such as the semi-dilute case where more than one polymer molecule exists or even internal fouling.

Chapter 8

Concluding Remarks and Future Work

8.1 Concluding Remarks

The objective of this research was to gain a better understanding of the macromolecular fouling in ultrafiltration. Firstly, the work started with a comprehensive literature review in order to identify the type of the macromolecules for UF fouling of interest. This involved the study of an existing knowledge on membrane fouling related to macromolecular ultrafiltration and the study of membrane cleaning, particularly with regard to the cleaning of UF membranes subject to macromolecular fouling. Secondly, a comprehensive theoretical approach to the modelling of fouling resulted in combined models for two complex fouling scenarios. The experimental studies of macromolecular fouling in UF were carried out to observe the influence of the feed types, the feed bulk concentration, and the effect of TMP. The combined models were then used as appropriate to examine the mechanisms involved in the fouling process of these macromolecules at various TMPs and bulk concentrations. The overall fouling behaviour, the initial fouling behaviour, and the predominant fouling mechanism were identified. The switch point between one fouling mechanism and another, as well as the parameters used in the model were also determined. Thirdly, the effect of deformability of a macromolecule on membrane fouling was examined. Firstly, the sieving and reversibility results from the experiments were investigated. And furthermore, a mesoscopic model using Dissipative Particle Dynamics (DPD) was de-

veloped to simulate the pore blocking event at the pore entrance in the presence of a deformable linear macromolecule. The hydrodynamic force which may be linked to the threshold flux at which there is an onset of severe fouling was determined. This corresponds to whether a chain is sufficiently stretched or not to enable it to engage in pore plugging.

Fouling in UF is very complicated and far from being fully understood. The underlying physics are difficult to identify, whereas the widely accepted analysis method is to consider the four extreme cases of fouling, i.e., the four classical blocking models. The main advantage of using the classical blocking laws to determine the fouling mechanisms is their simplicity. They only need the time-volume-TMP data, which can be easily measured in experiments, to predict the flux decline behaviour. However, in many macromolecular fouling cases, studies have shown the flux decline in membrane filtration consists of multiple steps. These simple laws cannot satisfactorily fit to the data in these cases. However, the use of a combination of various fouling laws to construct more comprehensive models to predict the flux decline has been attempted in some recent studies [83, 88]. These models should account for the complex nature of fouling where multiple processes may develop either simultaneously or sequentially during filtration.

A multi-scale framework for developing complex fouling models was developed in Chapter 4. This approach assumes that the membrane consists of independent pores and the overall behaviour can be statistically summarised or averaged over all its pores. Thence, the average fouling behaviour can be analysed first at the pore scale. Based on the knowledge of the four classical blocking laws, two likely scenarios were considered. In the first case where particles have larger sizes than the pores, pore blocking takes place first, followed by the cake growth. In the second case where the feed contains a mixture of small and large particles, the consecutive pore blocking and cake filtration is still held valid and, in addition, smaller particles can engage in internal fouling until the pores are sealed. The mathematical model for the fouling dynamics in a single pore was deduced from the classical blocking laws as appropriate. In these two scenarios, the blocking time is an important parameter, which determines the time for the flux behaviour changing from one mode to the other. By analysis, the blocking time has a statistical distribution over all the pores constituting the whole membrane area. Therefore, by averaging the fluxes over all the pores with the distribution function, the mean permeate flux was determined for each time steps in the membrane filtration. The flux represents the predicted macroscopic permeation that one can compare with that measured in a filtration experiment.

The developed macroscopic models were then tested to study the flux decline behaviour in a lab-scale UF experiment as reported in Chapter 5. Three macromolecular feeds of different sizes and characteristics were chosen to generate primary data for the models. Model A (pore blocking and cake filtration) was found to be appropriate for UF (MWCO = 100 kDa) of dextran blue (DB, 2000 kDa) and UF of polyethylene oxide (PEO, 100 kDa), respectively, since these two polymers had large sizes compared to the membrane used. The third model macromolecule, HA, was chosen for its practical importance. HA is a mixture of natural occurring humic substances having a broad range of size and containing different functional groups, which has been identified as the major foulant in water and wastewater industries. Since HA samples were determined having large fractions smaller than the pore dimensions, Model B (pore constriction, blocking and cake filtration) was found to fit to its flux-decline data. Comparing with the experimental results on the profile of flux decline under different filtration conditions (varying bulk concentration or TMPs), the model accurately described the fouling behaviour over the whole filtration course with model parameters determined from the best-fit results. The values of the resultant parameters were consistent over different conditions and this gave further validation of the models.

The use of integral and differential methods to explicitly determine the temporal evolution of fouling mechanisms has confirmed confirmed that cake filtration was the dominant fouling mechanism at the long term of the filtration for all conditions. On the contrary, these methods were found to be too simplistic for the early stage of fouling. Due to the interplay of different mechanisms at the same time, the overall fouling can not be predicted by a single classical fouling law.

In Chapter 6, the sieving results from the experiments were revealed, along with the fouling irreversibility results. There were strong evidences of flow-induced deformation of macromolecules in the DB case of high TMPs. This phenomenon is also likely to cause a more severe and irreversible fouling.

A mesoscopic model using DPD method was developed to model such flow-induced deformation of a polymer chain at the pore entrance in Chapter 7. By varying the strength of the hydrodynamic forces in the model, the threshold flux at which a polymer can be stretched and has higher probabilities to enter the pore was obtained.

8.2 Future Work

There exist many exciting possibilities for future work stemming from this thesis.

- Experiments of cleaning methods on macromolecular fouling. Based on the critical review on membrane cleaning, physical cleaning of macromolecular fouling is often of limited effect, while chemical cleaning is often time consuming and not economical. Therefore, either improvement on chemical cleaning or finding novel methods to clean the macromolecular foulants, such as HA, is of practical interest.

- Development of physical model for fouling parameters. In the present work, these fouling parameters including pore blocking rate, additional pore blockage resistance, specific cake resistance and pore constriction rate were determined statistically best-fitting to the experimental data. However, these parameters have their own physical meanings, and therefore, may be determined independently prior to fouling results. Studies on them should be of great interest.

- Further theoretical work on pore-scale models. The present pore-scale model in the combined fouling model has simply adopted the foundation of the classical fouling laws. However, when other effects other than pure steric, such as electrostatic interaction or other specific forces, existing between the solute and the pores, more realistic and of course more complex models need to be developed. Under the multi-scale analytical framework developed in this document, a more extensive macroscopic fouling model is possible to be constructed for more complex situations.

- Enlarged range of foulants and membrane choices. In the sieving tests, only one type of membrane is used here. In a more comprehensive study, membranes with several different sizes and dextrans with different dimensions may be used in a scaled-up experiments.

- Extension of DPD model. DPD method is relatively new method to simulate the hydrodynamics at the mesoscale and itself is still an ongoing research topic. There are many potentials to employ this method in fouling study especially to obtain the nature of the complex fluids in the membrane matrix, which can not easily be observed by the usual techniques. For the particular work, the model can be extended to investigate both the effect of the size of the molecules and the rigidity in its shape on the macromolecular capture by the pore structure.

Nomenclature

Symbols

A membrane area, $[m^2]$

a_{ij} pairwise conservative force coefficient in DPD, $[kg\ m^2\ s^{-2}]$

C_b bulk concentration of the feed solutes, $[kg\, m^{-3}]$

D_e well depth in Morse potential, [-]

d_p equivalent diameter of the pore cross-section. $[m]$

d_s equivalent diameter of the solute, $[m]$

$\hat{\mathbf{e}}$ unit vector, [-]

J permeate flux, $[m\, s^{-1}]$

J_n normalised permeate flux, [-]

J^* steady state flux, $[m\, s^{-1}]$

$k(n)$ filtration constant in eqn 2.2, its form depending on the constant n

k_B Boltzmann constant, $[J\, K^{-1}]$

M consistency index for power-law model, $[Pa\, s^N]$

N exponent of the shear rate in power-law model, [-]

N_b number of beads in a polymer chain in DPD, [-]

N_p number of pores, [-]

n filtration constant in eqn 2.2, [-]

p permeability of a membrane, which is reciprocal to membrane resistance, $[m]$

p_n the normalised permeability of a membrane, [-]

Q flow rate of permeation, $[m^3\, s^{-1}]$

R resistance of a porous medium, $[m^{-1}]$

R_c fouling cake resistance, $[m^{-1}]$

R_m clean membrane resistance, $[m^{-1}]$

R_t total membrane resistance, $[m^{-1}]$

r_0 equilibrium distance of a bond in DPD, $[m]$

r_c cutoff distance of DPD model, $[m]$

r_e equilibrium distance in Morse potential used in DPD, [-]

r_p pore radius, $[m]$

T absolute temperature, $[K]$

$\hat{t}$ unit time in DPD, $[s]$

v flow velocity, $[m\,s^{-1}]$

Greek Symbols

α specific cake resistance, $[m\,kg^{-1}]$

β pore constriction constant, $[kg^{-1}]$

ΔP pressure difference across a porous medium, also transmembrane pressure, $[Pa]$

δ_m membrane thickness, $[m]$

γ_{ij} pairwise dissipative force coefficient in DPD, $[kg\,s^{-1}]$

$\dot{\gamma}$ shear rate, $[s^{-1}]$

η non-Newtonian viscosity, $[Pa\,s]$

μ Newtonian viscosity, $[Pa\,s]$

ν well width in Morse potential, [-]

σ blocked area per unit mass of particles being filtered, $[m^2\,kg^{-1}]$

σ_{ij} stochastic coefficient in the pairwise random force of DPD, $[kg\,m\,s^{-3/2}]$

ϕ volume of particles deposited onto the pore surface per unit weight of solutes being filtered, $[m^3\,kg^{-1}]$

Abbreviations

CEB chemically enhanced backwashing

CFV crossflow velocity

CIP cleaning in place

CMC critical micelle concentration

COP cleaning off place

DPD dissipative particle dynamics

EDL electrical double layer

EPS extracellular polymer substances

LHS left hand side

MBR membrane bioreactor

MF mircrofiltration

MPM multiple photon microscopy

MW molecular weight

MWCO molecular weight cutoff

NF nanofiltration

NOM natural organic matter

RO reverse osmosis

TMP trans-membrane pressure

UF ultrafiltration

Bibliography

[1] G. Geise, H.-S. Lee, D. Miller, B. Freeman, J. McGrath, D. Paul, Water purification by membranes: The role of polymer science, *Journal of Polymer Science, Part B: Polymer Physics* 48 (2010) 1685–1718.

[2] R. L. Wershaw, J. A. Leenheer, L. Cox, *Characterization of dissolved and particulate natural organic matter (NOM) in Nevenrsink Reservoir, New York*, Technical Report, U.S. Department of the Interior and U.S. Geological Survery, 2005.

[3] R. W. Baker, *Membrane technology and applications*, Chichester : Wiley, 2nd edition, 2004.

[4] E. Gaudichet-Maurin, F. Thominette, Ageing of polysulfone ultrafiltration membranes in contact with bleach solutions, *Journal of Membrane Science* 282 (2006) 198 – 204.

[5] F. Thominette, O. Farnault, E. Gaudichet-Maurin, C. Machinal, J.-C. Schrotter, Ageing of polyethersulfone ultrafiltration membranes in hypochlorite treatment, *Desalination* 200 (2006) 7 – 8.

[6] E. Arkhangelsky, D. Kuzmenko, V. Gitis, Impact of chemical cleaning on properties and functioning of polyethersulfone membranes, *Journal of Membrane Science* 305 (2007) 176 – 184.

[7] K. Yadav, K. Morison, M. P. Staiger, Effects of hypochlorite treatment on the surface morphology and mechanical properties of polyethersulfone ultrafiltration membranes, *Polymer Degradation and Stability* 94 (2009) 1955 – 1961.

[8] M. Rubinstein, R. H. Colby, *Polymer Physics*, Oxford University Press, 2003.

[9] R. W. Field, Fundamentals of fouling, in: K.-V. Peinemann, S. P. Nunes (Eds.), *Membranes for Water Treatment: Volume 4*, WILEY-VCH Verlag, 2010, pp. 1–22.

[10] M. Pilutti, J. E. Nemeth, *Technical and cost review of commercially available MF/UF membrane products*, Technical Report, Harn R/O, 2003.

[11] I. E. McAliley, P. D'Adamo, Advances in membrane treatment lead to more cost-effective options for drinking water providers, in: *2009 Annual Conference Technical Papers*, North Carolina American Water Works Association and the North Carolina Water Environment Association.

[12] Millipore, *Ultrafiltration Membranes Opetrating Instructions*, Millipore Corporation, 2011.

[13] M. Cheryan, *Ultrafiltration handbook*, Technomic Publishing Company, Inc., 1986.

[14] B. Van Der Bruggen, C. Vandecasteele, T. Van Gestel, W. Doyen, R. Leysen, A review of pressure-driven membrane processes in wastewater treatment and drinking water production, *Environmental Progress* 22 (2003) 46–56.

[15] D. Hughes, T. Taha, Z. Cui, Mass Transfer: Membrane Processes, in: S. S. Sablani (Ed.), *Handbook of food and bioprocess modeling techniques*, CRC, Boca Raton, Fla., 2007, pp. 145–177.

[16] G. Foley, *Membrane Filtration: A Problem Solving Approach with MATLAB*, Cambridge University Press, 2013.

[17] J. M. M. Peeters, *Characterization of Nanofiltration Membranes*, Ph.D. thesis, University of Twente, 1997.

[18] A. I. Schäfer, A. G. Fane, T. D. Waite, *Nanofiltration: Principles and Applications*, Elsevier, 2005.

[19] G. Belfort, R. Davis, A. Zydney, The behavior of suspensions and macromolecular solutions in crossflow microfiltration, *Journal of Membrane Science* 96 (1994) 1–58.

[20] S. Kommineni, J. Bryck, C. Stringer, C. Stevens, N. Meyers, B. Karnik, R. Hoffman, L. Sullivan, Evaluation of an emerging water treatment technology: Ceramic membranes, *Water Science and Technology: Water Supply* 10 (2010) 765–770.

[21] P. Bacchin, P. Aimar, R. Field, Critical and sustainable fluxes: Theory, experiments and applications, *Journal of Membrane Science* 281 (2006) 42 – 69.

[22] A. L. Zydney, Stagnant film model for concentration polarization in membrane systems, *Journal of Membrane Science* 130 (1997) 275 – 281.

[23] S. S. Vasan, *Analysis of mass transfer in ultrafiltration*, Ph.D. thesis, University of Oxford, 2005.

[24] N. M. D'Souza, A. J. Mawson, Membrane Cleaning in the Dairy Industry: A Review, *Critical Reviews in Food Science and Nutrition* 45 (2005) 125–134.

[25] K. Kimura, Y. Hane, Y. Watanabe, G. Amy, N. Ohkuma, Irreversible membrane fouling during ultrafiltration of surface water, *Water Research* 38 (2004) 3431–3441.

[26] S. C. Tu, V. Ravindran, M. Pirbazari, A pore diffusion transport model for forecasting the performance of membrane processes, *Journal of Membrane Science* 265 (2005) 29–50.

[27] K. L. Jones, C. R. O'Melia, Protein and humic acid adsorption onto hydrophilic membrane surfaces: Effects of pH and ionic strength, *Journal of Membrane Science* 165 (2000) 31–46.

[28] A. E. Childress, M. Elimelech, Effect of solution chemistry on the surface charge of polymeric reverse osmosis and nanofiltration membranes, *Journal of Membrane Science* 119 (1996) 253 – 268.

[29] L. J. Zeman, A. L. Zydney, *Microfiltration and ultrafiltration : principles and applications*, New York : Dekker, 1996.

[30] J. Hermia, Constant pressure blocking filtration laws - application to power-law non-newtonian fluids., *Transactions of The Institution of Chemical Engineers* 60 (1982) 183–187.

[31] R. W. Field, J. J. Wu, Modelling of permeability loss in membrane filtration: Re-examination of fundamental fouling equations and their link to critical flux, *Desalination* 283 (2011) 68 – 74.

[32] C. Güell, P. Czekaj, R. H. Davis, Microfiltration of protein mixtures and the effects of yeast on membrane fouling, *Journal of Membrane Science* 155 (1999) 113–122.

[33] D. Hughes, R. Field, Crossflow filtration of washed and unwashed yeast suspensions at constant shear under nominally sub-critical conditions, *Journal of Membrane Science* 280 (2006) 89 – 98.

[34] D. Jermann, W. Pronk, R. Kgi, M. Halbeisen, M. Boller, Influence of interactions between NOM and particles on UF fouling mechanisms, *Water Research* 42 (2008) 3870–3878.

[35] D. Jermann, W. Pronk, M. Boller, Mutual influences between natural organic matter and inorganic particles and their combined effect on ultrafiltration membrane fouling, *Environmental Science and Technology* 42 (2008) 9129–9136.

[36] Q. Li, M. Elimelech, Synergistic effects in combined fouling of a loose nanofiltration membrane by colloidal materials and natural organic matter, *Journal of Membrane Science* 278 (2006) 72–82.

[37] M. C. Porter, Concentration Polarization with Membrane Ultrafiltration, *Product R&D* 11 (1972) 234–248.

[38] A.-S. Jönsson, B. Jönsson, Colloidal Fouling during Ultrafiltration, *Separation Science and Technology* 31 (1996) 2611–2620.

[39] D. Jermann, W. Pronk, S. Meylan, M. Boller, Interplay of different NOM fouling mechanisms during ultrafiltration for drinking water production, *Water Research* 41 (2007) 1713 – 1722.

[40] G. Amy, Fundamental understanding of organic matter fouling of membranes, *Desalination* 231 (2008) 44 – 51.

[41] W.-Y. Ahn, A. Kalinichev, M. Clark, Effects of background cations on the fouling of polyethersulfone membranes by natural organic matter: Experimental and molecular modeling study, *Journal of Membrane Science* 309 (2008) 128–140.

[42] R. W. Field, G. K. Pearce, Critical, sustainable and threshold fluxes for membrane filtration with water industry applications, *Advances in Colloid and Interface Science* 164 (2011) 38 – 44.

[43] X. Shi, R. Field, N. Hankins, Review of fouling by mixed feeds in membrane filtration applied to water purification, *Desalination and Water Treatment* 35 (2011) 68–81.

[44] Z. Cui, Protein separation using ultrafiltration – an example of multi-scale complex systems, *China Particuology* 3 (2005) 343–348.

[45] S. T. Kelly, A. L. Zydney, Protein fouling during microfiltration: Comparative behavior of different model proteins, *Biotechnology and Bioengineering* 55 (1997) 91–100.

[46] C. Jucker, M. M. Clark, Adsorption of aquatic humic substances on hydrophobic ultrafiltration membranes, *Journal of Membrane Science* 97 (1994) 37 – 52.

[47] M. Kulovaara, S. Metsämuuronen, M. Nyström, Effects of aquatic humic substances on a hydrophobic ultrafiltration membrane, *Chemosphere* 38 (1999) 3485 – 3496.

[48] W. Yuan, A. Zydney, Humic acid fouling during microfiltration, *Journal of Membrane Science* 157 (1999) 1–12.

[49] A. I. Schäfer, *Natural organics removal using membranes: principles, performance and cost*, Technomic Publishing Company, Inc., 2001.

[50] I. Sutzkover-Gutman, D. Hasson, R. Semiat, Humic substances fouling in ultrafiltration processes, *Desalination* 261 (2010) 218 – 231.

[51] E. Aoustin, A. I. Schäfer, A. G. Fane, T. D. Waite, Ultrafiltration of natural organic matter, *Separation and Purification Technology* 22-23 (2001) 63–78.

[52] S. D. Richardson, The role of GC-MS and LC-MS in the discovery of drinking water disinfection by-products, *Journal of Environmental Monitoring* 4 (2002) 1–9.

[53] A. Zularisam, A. Ismail, R. Salim, Behaviours of natural organic matter in membrane filtration for surface water treatment – a review, *Desalination* 194 (2006) 211 – 231.

[54] L. Fan, J. L. Harris, F. A. Roddick, N. A. Booker, Influence of the characteristics of natural organic matter on the fouling of microfiltration membranes, *Water Research* 35 (2001) 4455 – 4463.

[55] A. I. Schäfer, A. G. Fane, T. D. Waite, Nanofiltration of natural organic matter: Removal, fouling and the influence of multivalent ions, *Desalination* 118 (1998) 109–122.

[56] J. Hanemaaijer, T. Robbertsen, T. van den Boomgaard, J. Gunnink, Fouling of ultrafiltration membranes: the role of protein adsorption and salt precipitation, *Journal of Membrane Science* 40 (1989) 199 – 217.

[57] K. Scott, *Handbook of Industrial Membranes*, Elsevier, New York, 1995.

[58] S. Li, S. Heijman, J. Verberk, P. L. Clech, J. Lu, A. Kemperman, G. Amy, J. van Dijk, Fouling control mechanisms of demineralized water backwash: Reduction of charge screening and calcium bridging effects, *Water Research* 45 (2011) 6289 – 6300.

[59] P. Le-Clech, V. Chen, T. Fane, Fouling in membrane bioreactors used in wastewater treatment, *Journal of Membrane Science* 284 (2006) 17–53.

[60] V. Chen, J. Mansouri, T. Charlton, Biofouling in Membrane Systems, in: K.-V. Peinemann, S. P. Nunes (Eds.), *Membranes for Water Treatment*, WILEY-VCH Verlag, 2010, p. 25.

[61] E. Tombácz, Z. Libor, E. Ills, A. Majzik, E. Klumpp, The role of reactive surface sites and complexation by humic acids in the interaction of clay mineral and iron oxide particles, *Organic Geochemistry* 35 (2004) 257 – 267.

[62] E. Tombácz, M. Szekeres, Surface charge heterogeneity of kaolinite in aqueous suspension in comparison with montmorillonite, *Applied Clay Science* 34 (2006) 105 – 124.

[63] K. L. Chen, S. E. Mylon, M. Elimelech, Aggregation Kinetics of Alginate-Coated Hematite Nanoparticles in Monovalent and Divalent Electrolytes, *Environmental Science & Technology* 40 (2006) 1516–1523.

[64] K. L. Chen, M. Elimelech, Influence of humic acid on the aggregation kinetics of fullerene (C60) nanoparticles in monovalent and divalent electrolyte solutions, *Journal of Colloid and Interface Science* 309 (2007) 126–134.

[65] A. E. Contreras, A. Kim, Q. Li, Combined fouling of nanofiltration membranes: Mechanisms and effect of organic matter, *Journal of Membrane Science* 327 (2009) 87 – 95.

[66] R. S. Faibish, M. Elimelech, Y. Cohen, Effect of Interparticle Electrostatic Double Layer Interactions on Permeate Flux Decline in Crossflow Membrane Filtration of Colloidal Suspensions: An Experimental Investigation, *Journal of Colloid and Interface Science* 204 (1998) 77 – 86.

[67] M. Wiesner, Morphology of Particle Deposits, *Journal of Environmental Engineering* 125 (1999) 1124–1132.

[68] W. Yuan, A. L. Zydney, Humic Acid Fouling during Ultrafiltration, *Environmental Science & Technology* 34 (2000) 5043–5050.

[69] K. Howe, M. Clark, Fouling of microfiltration and ultrafiltration membranes by natural waters, *Environmental Science and Technology* 36 (2002) 3571–3576.

[70] A. I. Schäfer, U. Schwicker, M. M. Fischer, A. G. Fane, T. D. Waite, Microfiltration of colloids and natural organic matter, *Journal of Membrane Science* 171 (2000) 151–172.

[71] Q. Li, M. Elimelech, Organic fouling and chemical cleaning of nanofiltration membranes: Measurements and mechanisms, *Environmental Science and Technology* 38 (2004) 4683–4693.

[72] K. Katsoufidou, S. Yiantsios, A. Karabelas, An experimental study of UF membrane fouling by humic acid and sodium alginate solutions: the effect of backwashing on flux recovery, *Desalination* 220 (2008) 214 – 227.

[73] S. Allgeier, B. Alspach, J. Vickers, *Membrane filtration guidance manual*, USEPA, 2005.

[74] P. H. Hermans, H. L. Bredée, Principles of the mathematical treatment of constant-pressure filtration, *J. Soc. Chem. Ind.* 55 (1936) 1–4.

[75] H. P. Grace, Structure and performance of filter media II. Performance of filter media in liquid service, *AIChE Journal* 2 (1956) 316–336.

[76] R. W. Field, D. Wu, J. A. Howell, B. B. Gupta, Critical flux concept for microfiltration fouling, *Journal of Membrane Science* 100 (1995) 259 – 272.

[77] E. Iritani, A Review on Modeling of Pore-Blocking Behaviors of Membranes During Pressurized Membrane Filtration, *Drying Technology* 31 (2013) 146–162.

[78] M. Hlavacek, F. Bouchet, Constant flowrate blocking laws and an example of their application to dead-end microfiltration of protein solutions, *Journal of Membrane Science* 82 (1993) 285 – 295.

[79] S. Chellam, W. Xu, Blocking laws analysis of dead-end constant flux microfiltration of compressible cakes, *Journal of Colloid and Interface Science* 301 (2006) 248 – 257.

[80] C. Tien, B. V. Ramarao, Revisiting the laws of filtration: An assessment of their use in identifying particle retention mechanisms in filtration, *Journal of Membrane Science* 383 (2011) 17 – 25.

[81] W. Bowen, J. Calvo, A. Hernndez, Steps of membrane blocking in flux decline during protein microfiltration, *Journal of Membrane Science* 101 (1995) 153 – 165.

[82] K.-J. Hwang, C.-Y. Liao, K.-L. Tung, Analysis of particle fouling during microfiltration by use of blocking models, *Journal of Membrane Science* 287 (2007) 287 – 293.

[83] C. C. Ho, A. L. Zydney, A combined pore blockage and cake filtration model for protein fouling during microfiltration, *Journal of Colloid and Interface Science* 232 (2000) 389–399.

[84] M. Taniguchi, J. Kilduff, G. Belfort, Modes of natural organic matter fouling during ultrafiltration, *Environmental Science and Technology* 37 (2003) 1676–1683.

[85] G. Bolton, D. LaCasse, R. Kuriyel, Combined models of membrane fouling: Development and application to microfiltration and ultrafiltration of biological fluids, *Journal of Membrane Science* 277 (2006) 75 – 84.

[86] Y.-L. Cheng, D.-J. Lee, J.-Y. Lai, Filtration blocking laws: Revisited, *Journal of the Taiwan Institute of Chemical Engineers* 42 (2011) 506 – 508.

[87] J. de Bruijn, F. Salazar, R. Brquez, Membrane Blocking In Ultrafiltration: A New Approach to Fouling, *Food and Bioproducts Processing* 83 (2005) 211 – 219.

[88] C. Duclos-Orsello, W. Li, C. C. Ho, A three mechanism model to describe fouling of microfiltration membranes, *Journal of Membrane Science* 280 (2006) 856–866.

[89] N. Porcelli, S. Judd, Chemical cleaning of potable water membranes: A review, *Separation and Purification Technology* 71 (2010) 137 – 143.

[90] X. Shi, G. Tal, N. P. Hankins, V. Gitis, Fouling and cleaning of ultrafiltration membranes: A review, *Journal of Water Process Engineering* 1 (2014) 121 – 138.

[91] G. Tragärdh, Membrane cleaning, *Desalination* 71 (1989) 325 – 335.

[92] P. Blanpain-Avet, J. Migdal, T. Bénézech, Chemical cleaning of a tubular ceramic microfiltration membrane fouled with a whey protein concentrate suspension - Characterization of hydraulic and chemical cleanliness, *Journal of Membrane Science* 337 (2009) 153 – 174.

[93] C. Shorrock, M. Bird, Membrane cleaning: chemically enhanced removal of deposits formed during yeast cell harvesting, *Food and Bioproducts Processing* 76 (1998) 30 – 38.

[94] S. Hong, T. Bae, T. Tak, S. Hong, A. Randall, Fouling control in activated sludge submerged hollow fiber membrane bioreactors, *Desalination* 143 (2002) 219 – 228.

[95] S. Hong, R. S. Faibish, M. Elimelech, Kinetics of permeate flux decline in crossflow membrane filtration of colloidal suspensions, *Journal of Colloid and Interface Science* 196 (1997) 267 – 277.

[96] H. Chua, T. Arnot, J. Howell, Controlling fouling in membrane bioreactors operated with a variable throughput, *Desalination* 149 (2002) 225 – 229.

[97] J. Verberk, H. van Dijk, Reserach on AirFlush : distribution of water and air in tubular and capillary membrane modules, *Water Science and Technology: Water Supply* 03 (2003) 409 – 414.

[98] H. Liang, W. Gong, J. Chen, G. Li, Cleaning of fouled ultrafiltration (UF) membrane by algae during reservoir water treatment, *Desalination* 220 (2008) 267 – 272.

[99] W. Gao, H. Liang, J. Ma, M. Han, Z. lin Chen, Z. shuang Han, G. bai Li, Membrane fouling control in ultrafiltration technology for drinking water production: A review, *Desalination* 272 (2011) 1 – 8.

[100] J. Chen, S. Kim, Y. Ting, Optimization of membrane physical and chemical cleaning by a statistically designed approach, *Journal of Membrane Science* 219 (2003) 27 – 45.

[101] J. G. Jacangelo, R. K. Noack, System Concepts, in: *AWWA Manual 53: Microfiltration and Ultrafiltration Membranes for Drinking Water*, American Water Works Association, 2005, pp. 51–64.

[102] S. Li, S. Heijman, J. Verberk, A. Verliefde, A. Kemperman, J. van Dijk, G. Amy, Impact of backwash water composition on ultrafiltration fouling control, *Journal of Membrane Science* 344 (2009) 17 – 25.

[103] A. Abrahamse, C. Lipreau, S. Li, S. Heijman, Removal of divalent cations reduces fouling of ultrafiltration membranes, *Journal of Membrane Science* 323 (2008) 153 – 158.

[104] S. Li, S. Heijman, J. Verberk, J. van Dijk, Influence of Ca and Na ions in backwash water on ultrafiltration fouling control, *Desalination* 250 (2010) 861 – 864.

[105] R. Villarroel, S. Delgado, E. Gonzlez, M. Morales, Physical cleaning initiation controlled by transmembrane pressure set-point in a submerged membrane bioreactor, *Separation and Purification Technology* 104 (2013) 55 – 63.

[106] P. Lipp, State of the art in drinking water treatment by MF/UF in Germany - A survey among MF/UF plants, *Water Science and Technology: Water Supply* 8 (2008) 377–381.

[107] A. Maartens, E. Jacobs, P. Swart, UF of pulp and paper effluent: membrane fouling-prevention and cleaning, *Journal of Membrane Science* 209 (2002) 81 – 92.

[108] C. Psoch, S. Schiewer, Direct filtration of natural and simulated river water with air sparging and sponge ball application for fouling control, *Desalination* 197 (2006) 190 – 204.

[109] H. Nagaoka, A. Tanaka, Y. Toriizuka, Measurement of effective shear stress working on flat-sheet membrane by air-scrabbling, *Water Science & Technology: Water Supply* 3 (2003) 423 – 428.

[110] C. Guigui, M. Mougenot, C. Cabassud, Air sparging backwash in ultrafiltration hollow fibres for drinking water production, *Water Science & Technology: Water Supply* 3 (2003) 415 – 422.

[111] C. Psoch, S. Schiewer, Critical flux aspect of air sparging and backflushing on membrane bioreactors, *Desalination* 175 (2005) 61 – 71.

[112] Z. Cui, T. Taha, Enhancement of ultrafiltration using gas sparging: a comparison of different membrane modules, *Journal of Chemical Technology & Biotechnology* 78 (2003) 249–253.

[113] S. Laborie, C. Cabassud, L. Durand-Bourlier, J. Lain, Flux enhancement by a continuous tangential gas flow in ultrafiltration hollow fibres for drinking water production: Effects of slug flow on cake structure, *Filtration & Separation* 34 (1997) 887 – 891.

[114] C. Cabassud, S. Laborie, J. Lainé, How slug flow can improve ultrafiltration flux in organic hollow fibres, *Journal of Membrane Science* 128 (1997) 93 – 101.

[115] T. Y. Wu, N. Guo, C. Y. Teh, J. X. W. Hay, *Advances in Ultrasound Technology for Environmental Remediation*, Springer, 2013.

[116] M. Kallioinen, M. Mänttäri, Influence of Ultrasonic Treatment on Various Membrane Materials: A Review, *Separation Science and Technology* 46 (2011) 1388–1395.

[117] H. Kyllönen, P. Pirkonen, M. Nyström, Membrane filtration enhanced by ultrasound: a review, *Desalination* 181 (2005) 319 – 335.

[118] A. L. Ahmad, N. F. Che Lah, S. Ismail, B. S. Ooi, Membrane Antifouling Methods and Alternatives: Ultrasound Approach, *Separation and Purification Reviews* 41 (2012) 318–346.

[119] M. O. Lamminen, H. W. Walker, L. K. Weavers, Mechanisms and factors influencing the ultrasonic cleaning of particle-fouled ceramic membranes, *Journal of Membrane Science* 237 (2004) 213 – 223.

[120] S. Muthukumaran, K. Yang, A. Seuren, S. Kentish, M. Ashokkumar, G. Stevens, F. Grieser, The use of ultrasonic cleaning for ultrafiltration membranes in the dairy industry, *Separation and Purification Technology* 39 (2004) 99 – 107.

[121] A. Mirzaie, T. Mohammadi, Effect of ultrasonic waves on flux enhancement in microfiltration of milk, *Journal of Food Engineering* 108 (2012) 77 – 86.

[122] X. Chai, T. Kobayashi, N. Fujii, Ultrasound-associated cleaning of polymeric membranes for water treatment, *Separation and Purification Technology* 15 (1999) 139 – 146.

[123] T. Kobayashi, X. Chai, N. Fujii, Ultrasound enhanced cross-flow membrane filtration, *Separation and Purification Technology* 17 (1999) 31 – 40.

[124] T. Kobayashi, T. Kobayashi, Y. Hosaka, N. Fujii, Ultrasound-enhanced membrane-cleaning processes applied water treatments: influence of sonic frequency on filtration treatments, *Ultrasonics* 41 (2003) 185 – 190.

[125] J. H. Gibson, H. Hon, R. Farnood, I. G. Droppo, P. Seto, Effects of ultrasound on suspended particles in municipal wastewater, *Water Research* 43 (2009) 2251 – 2259.

[126] S. Muthukumaran, S. Kentish, S. Lalchandani, M. Ashokkumar, R. Mawson, G. W. Stevens, F. Grieser, The optimisation of ultrasonic cleaning procedures for dairy fouled ultrafiltration membranes, *Ultrasonics Sonochemistry* 12 (2005) 29 – 35.

[127] X. Li, J. Yu, A. A. Nnanna, Fouling mitigation for hollow-fiber UF membrane by sonication, *Desalination* 281 (2011) 23 – 29.

[128] I. Masselin, X. Chasseray, L. Durand-Bourlier, J.-M. Lain, P.-Y. Syzaret, D. Lemordant, Effect of sonication on polymeric membranes, *Journal of Membrane Science* 181 (2001) 213 – 220.

[129] M. O. Lamminen, H. W. Walker, L. K. Weavers, Cleaning of particle-fouled membranes during cross-flow filtration using an embedded ultrasonic transducer system, *Journal of Membrane Science* 283 (2006) 225 – 232.

[130] X. Chai, T. Kobayashi, N. Fujii, Ultrasound effect on cross-flow filtration of polyacrylonitrile ultrafiltration membranes, *Journal of Membrane Science* 148 (1998) 129 – 135.

[131] A. Simon, N. Gondrexon, S. Taha, J. Cabon, G. Dorange, Low-Frequency Ultrasound to Improve Dead-End Ultrafiltration Performance, *Separation Science and Technology* 35 (2000) 2619–2637.

[132] G. Rios, H. Rakotoarisoa, B. T. de la Fuente, Basic transport mechanisms of ultrafiltration in the presence of an electric field, *Journal of Membrane Science* 38 (1988) 147 – 159.

[133] H. Huotari, G. Trgrdh, I. Huisman, Crossflow Membrane Filtration Enhanced by an External {DC} Electric Field: A Review, *Chemical Engineering Research and Design* 77 (1999) 461 – 468.

[134] A. Saxena, B. P. Tripathi, M. Kumar, V. K. Shahi, Membrane-based techniques for the separation and purification of proteins: An overview, *Advances in Colloid and Interface Science* 145 (2009) 1 – 22.

[135] W. Bowen, R. S. Kingdon, H. A. Sabuni, Electrically enhanced separation processes: the basis of in situ intermittent electrolytic membrane cleaning (IIEMC) and in situ electrolytic membrane restoration (IEMR), *Journal of Membrane Science* 40 (1989) 219 – 229.

[136] L. Liu, J. Liu, B. Gao, F. Yang, Minute electric field reduced membrane fouling and improved performance of membrane bioreactor, *Separation and Purification Technology* 86 (2012) 106 – 112.

[137] P. von Zumbusch, W. Kulcke, G. Brunner, Use of alternating electrical fields as anti-fouling strategy in ultrafiltration of biological suspensions Introduction of a new experimental procedure for crossflow filtration, *Journal of Membrane Science* 142 (1998) 75 – 86.

[138] A. Ahmad, N. Ibrahim, Automated electrophoretic membrane cleaning for dead-end microfiltration and ultrafiltration, *Separation and Purification Technology* 29 (2002) 105 – 112.

[139] J.-P. Chen, C.-Z. Yang, J.-H. Zhou, X.-Y. Wang, Study of the influence of the electric field on membrane flux of a new type of membrane bioreactor, *Chemical Engineering Journal* 128 (2007) 177 – 180.

[140] N. Mameri, S. Oussedik, R. Yeddou, D. Piron, D. Belhocine, H. Lounici, H. Grib, Enhancement of ultrafiltration flux by coupling static turbulence promoter and electric field, *Separation and Purification Technology* 17 (1999) 203 – 211.

[141] N. Mameri, S. Oussedik, A. Khelifa, D. Belhocine, H. Ghrib, H. Lounici, Electric fields applied in the ultrafiltration process, *Desalination* 138 (2001) 291.

[142] C. C. Tarazaga, M. E. Campderrs, A. P. Padilla, Physical cleaning by means of electric field in the ultrafiltration of a biological solution, *Journal of Membrane Science* 278 (2006) 219 – 224.

[143] K. Akamatsu, W. Lu, T. Sugawara, S. Nakao, Development of a novel fouling suppression system in membrane bioreactors using an intermittent electric field, *Water Research* 44 (2010) 825 – 830.

[144] B. Sarkar, S. DasGupta, S. De, Application of external electric field to enhance the permeate flux during micellar enhanced ultrafiltration, *Separation and Purification Technology* 66 (2009) 263 – 272.

[145] J. M. Arnal, B. Garcia-Fayos, M. Sancho, Membrane cleaning, in: R. Y. Ning (Ed.), *Expanding issues in desalination*, InTech, 2011.

[146] S. Strugholtz, K. Sundaramoorthy, S. Panglisch, A. Lerch, A. Brgger, R. Gimbel, Evaluation of the performance of different chemicals for cleaning capillary membranes, *Desalination* 179 (2005) 191 – 202.

[147] J. C.-T. Lin, D.-J. Lee, C. Huang, Membrane Fouling Mitigation: Membrane Cleaning, *Separation Science and Technology* 45 (2010) 858–872.

[148] T. Mohammadi, S. Madaeni, M. Moghadam, Investigation of membrane fouling, *Desalination* 153 (2002) 155 – 160.

[149] L. Paugam, D. Delaunay, N. W. Diagne, M. Rabiller-Baudry, Cleaning of skim milk PES ultrafiltration membrane: On the real effect of nitric acid step, *Journal of Membrane Science* 428 (2013) 275 – 280.

[150] X. Li, J. Li, X. Fu, R. Wickramasinghe, J. Chen, Chemical cleaning of PS ultrafilters fouled by the fermentation broth of glutamic acid, *Separation and Purification Technology* 42 (2005) 181 – 187.

[151] R. Naim, I. Levitsky, V. Gitis, Surfactant cleaning of UF membranes fouled by proteins, *Separation and Purification Technology* 94 (2012) 39 – 43.

[152] I. Levitsky, A. Duek, E. Arkhangelsky, D. Pinchev, T. Kadoshian, H. Shetrit, R. Naim, V. Gitis, Understanding the oxidative cleaning of UF membranes, *Journal of Membrane Science* 377 (2011) 206 – 213.

[153] H. Petrus, H. Li, V. Chen, N. Norazman, Enzymatic cleaning of ultrafiltration membranes fouled by protein mixture solutions, *Journal of Membrane Science* 325 (2008) 783 – 792.

[154] I. Levitsky, A. Duek, R. Naim, E. Arkhangelsky, V. Gitis, Cleaning UF membranes with simple and formulated solutions, *Chemical Engineering Science* 69 (2012) 679 – 683.

[155] I. Levitsky, R. Naim, A. Duek, V. Gitis, Effect of Time in Chemical Cleaning of Ultrafiltration Membranes, *Chemical Engineering & Technology* 35 (2012) 941–946.

[156] D. Wu, M. R. Bird, The fouling and cleaning of ultrafiltration membranes during the filtration of model tea component solutions, *Journal of Food Process Engineering* 30 (2007) 293–323.

[157] H. Lee, G. Amy, J. Cho, Y. Yoon, S.-H. Moon, I. S. Kim, Cleaning strategies for flux recovery of an ultrafiltration membrane fouled by natural organic matter, *Water Research* 35 (2001) 3301 – 3308.

[158] X. Guo, H. Shao, W. Hu, H. Shen, Fouling potential and cleaning characteristics of PVC ultrafiltration membrane during ultrafiltration of hydrophilic dissolved organic matter, *Desalination and Water Treatment* 33 (2011) 231–239.

[159] X. Guo, Q. Li, W. Hu, W. Gao, D. Liu, Ultrafiltration of dissolved organic matter in surface water by a polyvinylchloride hollow fiber membrane, *Journal of Membrane Science* 327 (2009) 254 – 263.

[160] S. Pavlova, Study on the cleaning of new ultrafiltration spiral-woundmodules to prevent membrane fouling (including biological fouling), *Desalination* 172 (2005) 267 – 270.

[161] Y. Zhang, J. Tian, H. Liang, J. Nan, Z. Chen, G. Li, Chemical cleaning of fouled PVC membrane during ultrafiltration of algal-rich water, *Journal of Environmental Sciences* 23 (2011) 529 – 536.

[162] S. T. Nguyen, F. A. Roddick, Chemical cleaning of ultrafiltration membrane fouled by an activated sludge effluent, *Desalination and Water Treatment* 34 (2011) 94–99.

[163] A. Weis, M. R. Bird, M. Nyström, The chemical cleaning of polymeric UF membranes fouled with spent sulphite liquor over multiple operational cycles, *Journal of Membrane Science* 216 (2003) 67 – 79.

[164] E. Plett, Cleaning of fouled surfaces, in: D. Lund, E. Plett, C. Sandu (Eds.), *Fouling and Cleaning in Food Processing*, University of Wisconsin-Madison Ext Dup, Wisconsin, 1985, p. 286.

[165] American Water Works Association (Ed.), *Microfiltration and Ultrafiltration Membranes for Drinking Waters*, AWWA Manual 53, first edition, 2005.

[166] A. Al-Amoudi, R. W. Lovitt, Fouling strategies and the cleaning system of NF membranes and factors affecting cleaning efficiency, *Journal of Membrane Science* 303 (2007) 4 – 28.

[167] S. S. Razavi, J. Harris, F. Sherkat, Fouling and cleaning of membranes in the ultrafiltration of the aqueous extract of soy flour, *Journal of Membrane Science* 114 (1996) 93 – 104.

[168] C. Brepols, K.Drensla, A. Janot, M. Trimborn, N. Engelhardt, Strategies for chemical cleaning in large scale membrane bioreactors, *Water Science and Technology* 57 (2008) 457–463.

[169] R. Krack, *Fouling and cleaning in pressure driven membrane processes*, International Dairy Federation,, pp. 151–174.

[170] M. F. Cox, *Detergents and cleaners: a handbook for formulators*, 1994.

[171] N. G. Marriott, R. B. Gravani, *Principles of Food Sanitation*, Springer, New York, 2006.

[172] K. H. Kroner, W. Hummel, J. Volkel, M.-R. Kula, *Membranes and Membrane Processes*, Plenum, New York, p. 223.

[173] M. Munoz-Aguado, D. Wiley, A. Fane, Enzymatic and detergent cleaning of a polysulfone ultrafiltration membrane fouled with BSA and whey, *Journal of Membrane Science* 117 (1996) 175 – 187.

[174] M. A. Argüello, S. Alvarez, F. A. Riera, R. Alvarez, Enzymatic Cleaning of Inorganic Ultrafiltration Membranes Fouled by Whey Proteins, *Journal of Agricultural and Food Chemistry* 50 (2002) 1951–1958.

[175] S. Li, *A New Concept of Ultrafiltration Fouling Control: Backwashing with Low Ionic Strength Water*, Ph.D. thesis, Technische Universiteit Delft, 2011.

[176] S. K. Lateef, B. Z. Soh, K. Kimura, Direct membrane filtration of municipal wastewater with chemically enhanced backwash for recovery of organic matter, *Bioresource Technology* 150 (2013) 149 – 155.

[177] C. Astudillo, J. Parra, S. Gonzlez, B. Cancino, A new parameter for membrane cleaning evaluation, *Separation and Purification Technology* 73 (2010) 286 – 293.

[178] K. G. Tay, L. Song, A more effective method for fouling characterization in a full-scale reverse osmosis process, *Desalination* 177 (2005) 95 – 107.

[179] D. J. Hughes, *Novel tools for the analysis of fouling in microfiltration*, Ph.D. thesis, University of Oxford, 2006.

[180] V. Chen, H. Li, A. Fane, Non-invasive observation of synthetic membrane processes a review of methods, *Journal of Membrane Science* 241 (2004) 23 – 44.

[181] P. Wang, Z. Wang, Z. Wu, Q. Zhou, D. Yang, Effect of hypochlorite cleaning on the physiochemical characteristics of polyvinylidene fluoride membranes, *Chemical Engineering Journal* 162 (2010) 1050 – 1056.

[182] E. Arkhangelsky, D. Kuzmenko, N. Gitis, M. Vinogradov, S. Kuiry, V. Gitis, Hypochlorite Cleaning Causes Degradation of Polymer Membranes, *Tribology Letters* 28 (2007) 109–116.

[183] M. Rabiller-Baudry, L. Bégoin, D. Delaunay, L. Paugam, B. Chaufer, A dual approach of membrane cleaning based on physico-chemistry and hydrodynamics: Application to PES membrane of dairy industry, *Chemical Engineering and Processing: Process Intensification* 47 (2008) 267 – 275.

[184] M. Rabiller-Baudry, M. L. Maux, B. Chaufer, L. Begoin, Characterisation of cleaned and fouled membrane by ATRFTIR and EDX analysis coupled with SEM: application to UF of skimmed milk with a PES membrane, *Desalination* 146 (2002) 123 – 128.

[185] P. Väisänen, M. Bird, M. Nyström, Treatment of UF Membranes with Simple and Formulated Cleaning Agents, *Food and Bioproducts Processing* 80 (2002) 98 – 108.

[186] L. Bégoin, M. Rabiller-Baudry, B. Chaufer, M.-C. Hautbois, T. Doneva, Ageing of PES industrial spiral-wound membranes in acid whey ultrafiltration, *Desalination* 192 (2006) 25 – 39.

[187] Y. Hao, A. Moriya, T. Maruyama, Y. Ohmukai, H. Matsuyama, Effect of metal ions on humic acid fouling of hollow fiber ultrafiltration membrane, *Journal of Membrane Science* 376 (2011) 247 – 253.

[188] R. Chan, V. Chen, Characterization of protein fouling on membranes: opportunities and challenges, *Journal of Membrane Science* 242 (2004) 169 – 188.

[189] D. J. Hughes, Z. Cui, R. W. Field, U. K. Tirlapur, In Situ Three-Dimensional Characterization of Membrane Fouling by Protein Suspensions Using Multiphoton Microscopy, *Langmuir* 22 (2006) 6266–6272.

[190] R. W. Field, D. Hughes, Z. Cui, U. Tirlapur, Some observations on the chemical cleaning of fouled membranes, *Desalination* 227 (2008) 132 – 138.

[191] Z. Reich, R. Kapon, R. Nevo, Y. Pilpel, S. Zmora, Y. Scolnik, Scanning force microscopy in the applied biological sciences, *Biotechnology Advances* 19 (2001) 451 – 485.

[192] X. Melamane, B. Pletschke, W. Leukes, C. Whiteley, Cleaning fouled membranes using sludge enzymes, *Water SA* 28 (2002) 100–104.

[193] A. Maartens, P. Swart, E. Jacobs, Characterisation techniques for organic foulants adsorbed onto flat-sheet UF membranes used in abattoir effluent, *Journal of Membrane Science* 119 (1996) 1 – 8.

[194] S. Platt, M. Nyström, Amido black staining of ultrafiltration membranes fouled with BSA, *Desalination* 214 (2007) 177 – 192.

[195] C.-H. Wei, X. Huang, R. B. Aim, K. Yamamoto, G. Amy, Critical flux and chemical cleaning-in-place during the long-term operation of a pilot-scale submerged membrane bioreactor for municipal wastewater treatment, *Water Research* 45 (2011) 863 – 871.

[196] M. R. Bird, M. Bartlett, CIP optimisation for the food industry: relationships between detergent concentration, temperature, and cleaning time, *Food and Bioproducts Processing, Transactions of the Institution of Chemical Engineers, Part C* 73 (1995) 63 – 70.

[197] A. Makardij, X. Chen, M. Farid, Microfiltration and Ultrafiltration of Milk: Some Aspects of Fouling and Cleaning, *Food and Bioproducts Processing* 77 (1999) 107 – 113.

[198] V. Puspitasari, A. Granville, P. Le-Clech, V. Chen, Cleaning and ageing effect of sodium hypochlorite on polyvinylidene fluoride (PVDF) membrane, *Separation and Purification Technology* 72 (2010) 301 – 308.

[199] M. Kazemimoghadam, T. Mohammadi, Chemical cleaning of ultrafiltration membranes in the milk industry, *Desalination* 204 (2007) 213 – 218. Conference on Desalination Strategies in South Mediterranean Countries, 2006.

[200] C. Liu, S. Caothien, J. Hayes, T. Caothuy, T. Otoyo, T. Ogawa, Membrane chemical cleaning: from art to science, in: *Proc. AWWA 2000 Water Quality Technology Conference, Denver Co.*, pp. 1 – 25.

[201] M. Bartlett, M. Bird, J. Howell, An experimental study for the development of a qualitative membrane cleaning model, *Journal of Membrane Science* 105 (1995) 147 – 157.

[202] M. Bird, M. Bartlett, Measuring and modelling flux recovery during the chemical cleaning of {MF} membranes for the processing of whey protein concentrate, *Journal of Food Engineering* 53 (2002) 143 – 152.

[203] M. O. Nigam, B. Bansal, X. D. Chen, Fouling and cleaning of whey protein concentrate fouled ultrafiltration membranes, *Desalination* 218 (2008) 313 – 322.

[204] A.-S. Jönsson, G. Trägårdh, Ultrafiltration applications, *Desalination* 77 (1990) 135 – 179. Proceedings of the Symposium on Membrane Technology.

[205] N. Porcelli, P. Hillis, S. Judd, Microfiltration membrane plant start up: A case study with autopsy and permeability recovery analysis, *Environmental Technology* 30 (2009) 629–639.

[206] N. Porcelli, S. Judd, Chemical cleaning of potable water membranes: The cost benefit of optimisation, *Water Research* 44 (2010) 1389 – 1398.

[207] M. Cheryan, *Ultrafiltration and microfiltration handbook*, Lancaster, Pa. : Technomic Pub. Co., 1998.

[208] H. Kyllönen, P. Pirkonen, M. Nyström, J. Nuortila-Jokinen, A. Grönroos, Experimental aspects of ultrasonically enhanced cross-flow membrane filtration of industrial wastewater, *Ultrasonics Sonochemistry* 13 (2006) 295 – 302.

[209] D. Chen, L. K. Weavers, H. W. Walker, Ultrasonic control of ceramic membrane fouling: Effect of particle characteristics, *Water Research* 40 (2006) 840 – 850.

[210] A. Gijsbertsen-Abrahamse, E. Cornelissen, J. Hofman, Fiber failure frequency and causes of hollow fiber integrity loss, *Desalination* 194 (2006) 251 – 258.

[211] S. Rouaix, C. Causserand, P. Aimar, Experimental study of the effects of hypochlorite on polysulfone membrane properties, *Journal of Membrane Science* 277 (2006) 137 – 147.

[212] C. Causserand, S. Rouaix, J.-P. Lafaille, P. Aimar, Ageing of polysulfone membranes in contact with bleach solution: Role of radical oxidation and of some dissolved metal ions, *Chemical Engineering and Processing: Process Intensification* 47 (2008) 48 – 56.

[213] J.-J. Qin, Y.-M. Cao, Y.-Q. Li, Y. Li, M.-H. Oo, H. Lee, Hollow fiber ultrafiltration membranes made from blends of PAN and PVP, *Separation and Purification Technology* 36 (2004) 149 – 155.

[214] K. Yadav, K. R. Morison, Effects of hypochlorite exposure on flux through polyethersulphone ultrafiltration membranes, *Food and Bioproducts Processing* 88 (2010) 419 – 424.

[215] V. Gitis, R. C. Haught, R. M. Clark, J. Gun, O. Lev, Application of nanoscale probes for the evaluation of the integrity of ultrafiltration membranes, *Journal of Membrane Science* 276 (2006) 185 – 192.

[216] J. C. Morris, The acid ionization constant of HOCl from 5 to 35 celcius, *The Journal of Physical Chemistry* 70 (1966) 3798–3805.

[217] B. Pellegrin, R. Prulho, A. Rivaton, S. Thrias, J.-L. Gardette, E. Gaudichet-Maurin, C. Causserand, Multi-scale analysis of hypochlorite induced PES/PVP ultrafiltration membranes degradation, *Journal of Membrane Science* 447 (2013) 287 – 296.

[218] I. M. Wienk, E. E. B. Meuleman, Z. Borneman, T. van den Boomgaard, C. A. Smolders, Chemical treatment of membranes of a polymer blend: Mechanism of the reaction of hypochlorite with poly(vinyl pyrrolidone), *Journal of Polymer Science Part A: Polymer Chemistry* 33 (1995) 49–54.

[219] J.-J. Qin, F.-S. Wong, Hypochlorite treatment of hydrophilic hollow fiber ultrafiltration membranes for high fluxes, *Desalination* 146 (2002) 307 – 309.

[220] J.-J. Qin, Y.-M. Cao, Y. Li, Effect of hypochlorite concentration on properties of posttreated outer-skin ultrafiltration membranes spun from cellulose acetate/poly(vinyl pyrrolidone) blends, *Journal of Applied Polymer Science* 97 (2005) 227–231.

[221] R. Prulho, S. Therias, A. Rivaton, J.-L. Gardette, Ageing of polyethersulfone/polyvinylpyrrolidone blends in contact with bleach water, *Polymer Degradation and Stability* 98 (2013) 1164 – 1172.

[222] F. Wang, V. V. Tarabara, Pore blocking mechanisms during early stages of membrane fouling by colloids, *Journal of Colloid and Interface Science* 328 (2008) 464 – 469.

[223] B. Sarkar, A combined complete pore blocking and cake filtration model during ultrafiltration of polysaccharide in a batch cell, *Journal of Food Engineering* 116 (2013) 333 – 343.

[224] K. Katsoufidou, S. Yiantsios, A. Karabelas, A study of ultrafiltration membrane fouling by humic acids and flux recovery by backwashing: Experiments and modeling, *Journal of Membrane Science* 266 (2005) 40 – 50.

[225] E. Iritani, Y. Mukai, M. Furuta, T. Kawakami, N. Katagiri, Blocking resistance of membrane during cake filtration of dilute suspensions, *AIChE Journal* 51 (2005) 2609–2614.

[226] M. G. Davidson, W. M. Deen, Hydrodynamic theory for the hindered transport of flexible macromolecules in porous membranes, *Journal of Membrane Science* 35 (1988) 167 – 192.

[227] G. Belfort, J. M. Pimbley, A. Greiner, K. Y. Chung, Diagnosis of membrane fouling using a rotating annular filter. 1. Cell culture media, *Journal of Membrane Science* 77 (1993) 1 – 22.

[228] K.-L. Tung, C.-J. Chuang, Effect of pore morphology on fluid flow and particle deposition on a track-etched polycarbonate membrane, *Desalination* 146 (2002) 129 – 134.

[229] D. Gassara, P. Schmitz, A. Ayadi, M. Prat, Modelling the Effect of Particle Size in Microfiltration, *Separation Science and Technology* 43 (2008) 1754–1770.

[230] K.-J. Kim, P. Sun, V. Chen, D. E. Wiley, A. G. Fane, The cleaning of ultrafiltration membranes fouled by protein, *Journal of Membrane Science* 80 (1993) 241 – 249.

[231] G. R. Aiken, Evaluation of ultrafiltration for determining molecular weight of fulvic acid, *Environmental Science & Technology* 18 (1984) 978–981.

[232] J. Cho, G. Amy, J. Pellegrino, Membrane filtration of natural organic matter: initial comparison of rejection and flux decline characteristics with ultrafiltration and nanofiltration membranes, *Water Research* 33 (1999) 2517 – 2526.

[233] K. M. Yunos, R. Field, Rejection amplification in the ultrafiltration of binary protein mixtures using sandwich configurations, *Chemical Engineering and Processing: Process Intensification* 47 (2008) 1053 – 1060.

[234] A. Savitzky, M. J. E. Golay, Smoothing and Differentiation of Data by Simplified Least Squares Procedures., *Analytical Chemistry* 36 (1964) 1627–1639.

[235] T. Perkins, D. Smith, S. Chu, Single polymer dynamics in an elongational flow, *Science* 276 (1997) 2016–2021.

[236] F. Jin, C. Wu, Observation of the First-Order Transition in Ultrafiltration of Flexible Linear Polymer Chains, *Phys. Rev. Lett.* 96 (2006) 237801.

[237] D. R. Latulippe, K. Ager, A. L. Zydney, Flux-dependent transmission of supercoiled plasmid DNA through ultrafiltration membranes, *Journal of Membrane Science* 294 (2007) 169 – 177.

[238] A. Morao, J. C. Nunes, F. Sousa, M. T. P. de Amorim, I. C. Escobar, J. A. Queiroz, Development of a model for membrane filtration of long and flexible macromolecules: Application to predict dextran and linear DNA rejections in ultrafiltration, *Journal of Membrane Science* 336 (2009) 61 – 70.

[239] L. Beguin, B. Grassl, F. Brochard-Wyart, M. Rakib, H. Duval, Suction of hydrosoluble polymers into nanopores, *Soft Matter* 7 (2011) 96–103.

[240] D. R. Latulippe, J. R. Molek, A. L. Zydney, Importance of Biopolymer Molecular Flexibility in Ultrafiltration Processes, *Industrial & Engineering Chemistry Research* 48 (2009) 2395–2403.

[241] W. M. Deen, Hindered transport of large molecules in liquid-filled pores, *AIChE Journal* 33 (1987) 1409–1425.

[242] W. Opong, A. L. Zydney, Diffusive and convective protein transport through asymmetric membranes, *AIChE Journal* 37 (1991) 1497–1510.

[243] P. Dechadilok, W. M. Deen, Hindrance Factors for Diffusion and Convection in Pores, *Industrial & Engineering Chemistry Research* 45 (2006) 6953–6959.

[244] J. C. Giddings, E. Kucera, C. P. Russell, M. N. Myers, Statistical theory for the equilibrium distribution of rigid molecules in inert porous networks. Exclusion chromatography, *The Journal of Physical Chemistry* 72 (1968) 4397–4408.

[245] I. Teraoka, Polymer solutions in confining geometries, *Progress in Polymer Science* 21 (1996) 89 – 149.

[246] W. Sparreboom, A. Van Den Berg, J. Eijkel, Principles and applications of nanofluidic transport, *Nature Nanotechnology* 4 (2009) 713–720.

[247] Q. T. Nguyen, J. Neel, Characterization of ultrafiltration membranes. : Part IV. Influence of the deformation of macromolecular solutes on the transport through ultrafiltration membranes., *Journal of Membrane Science* 14 (1983) 111 – 127.

[248] S. Daoudi, F. Brochard, Flows of flexible polymer solutions in pores, *Macromolecules* 11 (1978) 751–758.

[249] P. G. de Gennes, Coil-stretch transition of dilute flexible polymers under ultrahigh velocity gradients, *The Journal of Chemical Physics* 60 (1974) 5030–5042.

[250] D. Smith, H. Babcock, S. Chu, Single-polymer dynamics in steady shear flow, *Science* 283 (1999) 1724–1727.

[251] T. Hirasaki, T. Sato, T. Tsuboi, H. Nakano, T. Noda, A. Kono, K. Yamaguchi, K. Imada, N. Yamamoto, H. Murakami, S. ichi Manabe, Permeation mechanism of DNA molecules in solution through cuprammonium regenerated cellulose hollow fiber (BMMtm), *Journal of Membrane Science* 106 (1995) 123 – 129.

[252] D. Latulippe, A. Zydney, Elongational flow model for transmission of supercoiled plasmid DNA during membrane ultrafiltration, *Journal of Membrane Science* 329 (2009) 201 – 208.

[253] S. Rao, A. L. Zydney, Controlling protein transport in ultrafiltration using small charged ligands, *Biotechnology and Bioengineering* 91 (2005) 733–742.

[254] A. L. Zydney, A. Xenopoulos, Improving dextran tests for ultrafiltration membranes: Effect of device format, *Journal of Membrane Science* 291 (2007) 180 – 190.

[255] A. N. de Belder, *Dextran Handbook*, Amersham Biosciences, 2003.

[256] K. Devanand, J. C. Selser, Asymptotic behavior and long-range interactions in aqueous solutions of poly(ethylene oxide), *Macromolecules* 24 (1991) 5943–5947.

[257] X. Fan, N. Phan-Thien, N. T. Yong, X. Wu, D. Xu, Microchannel flow of a macromolecular suspension, *Physics of Fluids* 15 (2003) 11–21.

[258] M. Allen, D. Tildesley, *Computer simulation of liquids*, Oxford : Clarendon Press, 1987.

[259] D. Frenkel, B. Smit, *Understanding Molecular Simulation From Algorithms to Applications*, Academic Press, 2nd edition edition, 2002.

[260] J. C. Phillips, R. Braun, W. Wang, J. Gumbart, E. Tajkhorshid, E. Villa, C. Chipot, R. D. Skeel, L. Kal, K. Schulten, Scalable molecular dynamics with NAMD, *Journal of Computational Chemistry* 26 (2005) 1781–1802.

[261] H. Bruus, *Theoretical Microfluidics*, Oxford University Press, 2008.

[262] C. Marsh, *Theoretical Aspects of Dissipative Particle Dynamics*, Ph.D. thesis, University of Oxford, 1998.

[263] R. D. Groot, P. B. Warren, Dissipative particle dynamics: Bridging the gap between atomistic and mesoscopic simulation, *The Journal of Chemical Physics* 107 (1997) 4423–4435.

[264] U. Frisch, B. Hasslacher, Y. Pomeau, Lattice-Gas Automata for the Navier-Stokes Equation, *Phys. Rev. Lett.* 56 (1986) 1505–1508.

[265] D. D'humires, P. Lallemand, Lattice gas automata for fluid mechanics, *Physica A: Statistical Mechanics and its Applications* 140 (1986) 326 – 335.

[266] P. J. Hoogerbrugge, J. M. V. A. Koelman, Simulating Microscopic Hydrodynamic Phenomena with Dissipative Particle Dynamics, *EPL (Europhysics Letters)* 19 (1992) 155.

[267] J. Backer, *Bridging time and length scales in Dissipative Particle Dynamics*, Ph.D. thesis, University of Amsterdam, 2006.

[268] P. Espanol, P. Warren, Statistical mechanics of Disspative Particle Dynamics, *Europhysics Letters* 30 (1995) 191–196.

[269] S. Willemsen, H. Hoefsloot, P. Iedema, Mesoscopic Simulation of Polymers in Fluid Dynamics Problems, *Journal of Statistical Physics* 107 (2002) 53–65.

[270] T. F. Clarke, *Rheological Characterisation of Polymers via Dissipative Particle Dynamics*, Ph.D. thesis, Massachusetts Institute of Technology, 2008.

[271] J. Guo, X. Li, Y. Liu, H. Liang, Flow-induced translocation of polymers through a fluidic channel: A dissipative particle dynamics simulation study, *The Journal of Chemical Physics* 134 (2011).

[272] M. A. Seaton, R. L. Anderson, S. Metz, W. Smith, DL MESO: highly scalable mesoscale simulations, *Molecular Simulation* 39 (2013) 796–821.

[273] R. D. Groot, T. J. Madden, Dynamic simulation of diblock copolymer microphase separation, *The Journal of Chemical Physics* 108 (1998) 8713–8724.

[274] I. Pagonabarraga, M. H. J. Hagen, D. Frenkel, Self-consistent dissipative particle dynamics algorithm, *EPL (Europhysics Letters)* 42 (1998) 377.

[275] C. A. Marsh, J. M. Yeomans, Dissipative particle dynamics: The equilibrium for finite time steps, *EPL (Europhysics Letters)* 37 (1997) 511.

[276] A. K. Das, P.-D. Hong, Forced translocation of polymer chains through a nanotube: A case of ultrafiltration, *Polymer* 51 (2010) 2244 – 2254.

[277] P. Español, Hydrodynamics from dissipative particle dynamics, *Phys. Rev. E* 52 (1995) 1734–1742.

[278] R. Cracknell, D. Nicholson, N. Quirke, Direct Molecular Dynamics Simulation of Flow Down a Chemical Potential Gradient in a Slit-Shaped Micropore, *Phys. Rev. Lett.* 74 (1995) 2463–2466.

[279] T. Steiner, C. Cupelli, R. Zengerle, M. Santer, Simulation of advanced microfluidic systems with dissipative particle dynamics, *Microfluidics and Nanofluidics* 7 (2009) 307–323.

[280] J. Li, D. Liao, S. Yip, Coupling continuum to molecular-dynamics simulation: Reflecting particle method and the field estimator, *Phys. Rev. E* 57 (1998) 7259–7267.

[281] R. Feng, M. Xenos, G. Girdhar, W. Kang, J. Davenport, Y. Deng, D. Bluestein, Viscous flow simulation in a stenosis model using discrete particle dynamics: a comparison between DPD and CFD, *Biomechanics and Modeling in Mechanobiology* 11 (2012) 119–129.

[282] P. Nikunen, I. Vattulainen, M. Karttunen, Reptational dynamics in dissipative particle dynamics simulations of polymer melts, *Phys. Rev. E* 75 (2007) 036713.

[283] G. Pan, C. W. Manke, Developments toward simulation of entangled polymer melts by dissipative particle dynamics (DPD), *International Journal of Modern Physics B* 17 (2003) 231–235.

[284] H. Liu, Y.-H. Xue, H.-J. Qian, Z.-Y. Lu, C.-C. Sun, A practical method to avoid bond crossing in two-dimensional dissipative particle dynamics simulations, *The Journal of Chemical Physics* 129 (2008) 024902.

[285] W. Pan, I. V. Pivkin, G. E. Karniadakis, Single-particle hydrodynamics in DPD: A new formulation, *EPL (Europhysics Letters)* 84 (2008) 10012.

[286] M. M. Nardai, G. Zifferer, Simulation of dilute solutions of linear and star-branched polymers by dissipative particle dynamics, *The Journal of Chemical Physics* 131 (2009) 124903.

[287] G. F. Hermsen, B. A. de Geeter, N. F. A. van der Vegt, M. Wessling, Monte Carlo Simulation of Partially Confined Flexible Polymers, *Macromolecules* 35 (2002) 5267–5272.

[288] L. I. Klushin, A. M. Skvortsov, H.-P. Hsu, K. Binder, Dragging a Polymer Chain into a Nanotube and Subsequent Release, *Macromolecules* 41 (2008) 5890–5898.

[289] N. Ileri, S. E. Letant, A. Palazoglu, P. Stroeve, J. W. Tringe, R. Faller, Mesoscale simulations of biomolecular transport through nanofilters with tapered and cylindrical geometries, *Phys. Chem. Chem. Phys.* 14 (2012) 15066–15077.